

**“Geochemical characterisation of the Pliensbachian-Toarcian
boundary during the onset of the Toarcian Oceanic Anoxic Event.
North Yorkshire, UK”**

Najm-Eddin Salem

A thesis submitted to Newcastle University
In partial fulfilment of the requirements for the degree of
Doctor of Philosophy in the Faculty of Science and Agriculture

School of Civil Engineering and Geosciences,
Newcastle University, UK.

February 2013

ABSTRACT

The lower Whitby Mudstone Formation of the Cleveland Basin in North Yorkshire (UK) is a world renowned location for the Early Toarcian (T-OAE). Detailed climate records of the event have been reported from this location that shed new light on the forcing and timing of climate perturbations and associated development of ocean anoxia. Despite this extensive previous work, few studies have explored the well-preserved sediments below the event that document different phases finally leading to large-scale (global) anoxia, which is the focus of this project. We resampled the underlying Grey Shale Member at cm-scale resolution and conducted a detailed multi-proxy geochemical approach to reconstruct the redox history prior to the Toarcian OAE.

The lower Whitby Mudstone Formation, subdivided into the Grey Shale Member overlain by the Jet Rock (T-OAE), is a cyclic transgressive succession that evolved from the relatively shallow water sediments of the Cleveland Ironstone Formation. The Grey Shale Member is characterised by three distinct layers of organic rich shales (~10-60 cm thick), locally named as the 'sulphur bands'. Directly above and below these conspicuous beds, the sediments represent more normal marine mudstones. Further upwards the sequence sediments become increasingly laminated and organic carbon rich (up to 14 wt %) representing a period of maximum flooding that culminated in the deposition of the Jet Rock (T-OAE).

Detailed analyses of the Grey Shale Member, with a focus on the sulphur bands, for TOC and total sulfur concentrations, microscopy, iron speciation (FeHR/FeT, FePyrite/FeHR), trace element concentrations, molecular biomarkers, and bulk carbon and sulphur isotopes confirm highly variable redox conditions prior to the Toarcian OAE, with repeated anoxia/euxinia during periods of sulphur band deposition. Cm-scale geochemical records from the lower sulphur band actually suggest significant, short term variations in redox within the bed, with one full cycle from anoxia/euxinia to oxic conditions and back. We speculate that these cyclic variations in redox during and possibly also between sulphur band formation were driven by orbital forcing, however, better chronological information is necessary to validate this interpretation. The bioturbated mudstones between and below the sulphur bands show less enrichment of TOC, reactive iron and trace elements, but still suggest conditions close to the Fe-proxy threshold characteristic of anoxia (FeHR/FeT = 0.38). Further up the section in the bioturbated mudstones, highly reactive iron and trace elements are significantly depleted, indicating a return to more oxic conditions, which persisted up the top laminated unit of the Grey Shale. This observation challenges the general concept that anoxia/euxinia was limited to the Toarcian OAE, at least in the Cleveland Basin of North Yorkshire.

This thesis discusses the detailed dynamics of redox variations and biogeochemical elemental cycling in the run-up to this major event in Earth history. The mechanisms behind the short redox events documented in the sulphur bands may have had some similarities to those proposed for the small hyperthermals post-dating the Paleocene-Eocene thermal maximum (PETM) and other OAE's. Enhancement of run off from land via enhanced hydrological cycling could have temporarily created conditions in the Jurassic Cleveland

Basin that favoured stratification, high productivity, and development of extreme (euxinic) redox condition with high sulphur and carbon burial. The increasing amplitude of perturbations from the first sulphur band to the T-OAE, and their progressive spatial expansion from proximal to global, may argue for a unifying causal connection, orbital forcing. Further work will have to validate these conclusions and assumption.

DECLARATION

I hereby certify that the work described in this thesis is my own, except where otherwise acknowledged, and has not been submitted previously for a degree at this or any other university.

Najm-Eddin Salem

ACKNOWLEDGEMENTS

I thank family and friends who have been very supportive throughout the entire PhD. Without you all, it would not have been possible to juggle the extensive work which this PhD entailed. I especially thank my parents and my lovely wife for their unfailing support throughout the duration of this PhD.

I would like to express my appreciation and gratitude to my supervisors, Professor Simon Poulton and Professor Tom Wagner, for their guidance during the entire PhD. I would also like to thank Al-Zawia University and the Libyan Cultural affairs department (London) for their funding and support of this project.

I would like to acknowledge the technical assistance provided by several people at Newcastle University, namely Phil Green, Paul Donohoe, Ian Harrison, Bernie Bowler and Rob Hunter

TABLE OF CONTENTS

CHAPTER 1 – INTRODUCTION

1.1 General Overview	1
1.2 Overview of the Lower Jurassic	6
1.2.1 Paleogeography and Geological Framework	6
1.3 Toarcian Oceanic Anoxic Event	11
1.3.1 Causes and mechanisms for the Toarcian Carbon Isotopic Excursions	15
1.3.1.2 Locally driven mechanisms	15
1.3.1.1 Globally driven mechanisms	16
1.4 Aims and Objectives	18

CHAPTER 2 – TRACKING OCEANIC REDOX CONDITIONS

2.1 Overview	19
2.2 Existing models for anoxia	22
2.2.1 The silled basin model	22
2.2.2 The upwelling model	27
2.3 Characteristics of euxinic environments	28
2.4 An overview of palaeoredox indicators	30
2.4.1 Sedimentological and palaeoecological indicators of anoxia	30
2.4.2 Carbon–sulphur relationships	33
2.4.3 Framboidal pyrite distributions	34
2.4.4 Iron geochemistry	36
2.4.4.1 Determining highly reactive iron content (FeHR)	38
2.4.4.2 Iron recycling, enrichment, and the shelf-to-basin iron shuttle	39
2.4.5 Redox-sensitive trace metals	45

2.4.5.1 Trace metal sources and fixation mechanisms	45
2.4.5.1 Mo geochemistry	46
2.4.6 Molecular palaeoredox indicators	47
2.4.6.1 Pristane/Phytane ratio	47
2.4.6.2 Isorenieratane.....	48

CHAPTER 3 – GEOLOGICAL SETTING, MATERIALS AND METHODS

3.1 Geological setting	51
3.2 Sampling	58
3.3 Analytical Methods	61
3.3.1 Bulk Geochemistry.....	63
3.3.1.1 Total Organic Carbon (TOC) Determination	63
3.3.1.2 Total Carbon and Total Sulphur (TC & TS) Determination	63
3.3.1.3 Isotopic analysis	64
3.3.1.4 Rock- Eval Pyrolysis	66
<i>Procedure</i>	66
3.3.2 Microscopy.....	66
3.3.2.1 Palynological Preparation Technique	66
3.3.2.2 Transmitted White Light (TWL) analysis	67
3.3.2.3 Fluorescence Microscopy	68
3.3.3 Organic molecular chemistry.....	68
3.3.3.1 Bitumen Extraction.....	68
3.3.3.2 Thin Layer Chromatography (TLC)	68
3.3.4 Sequential Extraction Procedure for Iron Speciation	70
3.3.4.1 Pyrite extraction.....	71
3.3.4.2 Sequential iron extractions	72
3.3.4.3 Boiling HCl extractable iron.....	73

3.3.5 Total Sediment Dissolutions	73
---	----

**CHAPTER 4 - AN ORGANIC GEOCHEMICAL PROFILE OF THE
PLIENSBACHIAN-EARLY TOARCIAN OF STAITHES AND PORT MULGRAVE
(NORTH EAST YORKSHIRE, UK)**

4.1 Introduction	75
4.2 Results	75
4.2.1 Bulk Geochemistry.....	76
4.2.1.1 Total Organic Carbon (TOC), Total Carbon (TC) and Total Sulphur (TS).	76
4.2.1.2 Rock- Eval pyrolysis	84
<i>Rock-Eval Quality Indices</i>	87
4.2.2 Molecular biomarkers	89
4.2.2.1 <i>n</i> -alkanes distribution	89
4.2.2.2 Acyclic isoprenoids	93
4.2.2.3 Steranes and diasteranes biomarkers	95
4.2.2.4 Hopane biomarkers.....	97
4.2.2.5 Homohopane Index.....	99
4.2.2.6 Isorenieratane.....	103
4.2.3 Organic petrological results	106
4.2.3.1 Transmitted light microscopy	106
4.2.3.2 Blue light fluorescent microscopy	108
4.2.4 Detailed geochemical profile across the Sulphur Band at the Pliensbachian-Toarcian boundary.....	115
4.2.4.1 Solid bitumen assemblages within the Lower Sulphur Band.	117
4.3.1 Thermal maturity of the organic matter	122
4.3.2 Source of Organic Matter	124
4.3.3 The palaeoenvironment of deposition	127

4.3.4 Comparison of Sulphur Bands (Grey Shale Member) basal transgressive black shales and Jet Rock (maximum flooding) black shales	130
4.3.5 Hydrocarbon potential.....	133
4.4 Conclusions	134

CHAPTER 5 - WATER COLUMN REDOX DYNAMICS DURING THE ONSET OF THE TOARCIAN OCEANIC ANOXIC EVENT

5.1 Introduction	135
5.2 Results	136
Lateral geochemical variation of the Sulphur Bands.	147
5.3 Discussion.....	151
5.3.1 Redox dynamic throughout the study section	151
5.3.1.1 Iron data.....	151
5.3.1.2 Biomarkers.....	155
5.3.1.3 Sulphur isotope record.....	155
5.3.1.4 Trace elements	156
5.3.2 Detailed iron geochemistry across the Sulphur Bands.....	162
5.3.3 Regional redox of the Sulphur Bands	169
5.3.4 Carbon isotopic excursion before the T-OAE.....	170
5.3.5 Conceptual model.....	173
5.4 Conclusions	175

CHAPTER 6 - FT-NIRS ANALYSIS OF MARINE ROCK SAMPLES FROM A RANGE OF DEPOSITIONAL ENVIRONMENTS

6.1 Introduction	176
6.1.1 Principles of Near Infra-Red Spectroscopy.....	177
6.1.2 Fourier Transform Infrared Spectroscopy.....	181

6.1.3 Partial Least Square Regression	184
6.1.4 Sample material.....	184
6.1.5 Aims of the study	186
6.2 Methodology	186
6.2.1 Sample Preparation	187
6.2.2 Instrumentation and Analyses	187
6.2.3 NIR Data Pre-Treatment.....	188
6.2.3.1 Multiplicative Scatter Correction	188
6.2.3.2 Savitzky-Golay smoothing	188
6.2.4 Development of the calibration models	189
6.3	Results and discussion
.....	192
6.3.1 Sediment TOC, TS and Organic S Distribution.....	192
6.3.2 PCA Score plots	195
6.3.3 Calibrated Validation Models.	196
6.3.4 External Cross Validation	200
6.4 Conclusion	205
 CHAPTER 7 – SUMMARY AND OUTLOOK	
Future work.....	209

LIST OF FIGURES

Figure 1.1: Early Toarcian black shale distribution (dark grey colour) in Western Europe epicontinental basins.	3
Figure 1.2: Stratigraphic distribution of the Oceanic Anoxic Events (OAE) with some examples of organic rich formation	4
Figure 1.3: Early Jurassic palaeogeographical map illustrating the global distribution of previously reported lower Toarcian bituminous black shales.....	5
Figure 1.4: A) Global lower Toarcian paleogeography. B) Lower Toarcian paleogeography of Northwest European region.	7
Figure 1.5: A) map shows the reconstruction of the extent of organic-rich sedimentation for the Lower Toarcian of north-western Europe	10
Figure 1.6: Ammonite zonal schemes (after Howarth, 1992; Jakobs et al., 1994), and generalized isotope profiles (after Hesselbo et al., 2007; McArthur et al., 2000) for the Early and Middle Toarcian.	12
Figure 1.7: Comparison of the PETM and Toarcian CIEs.	14
Figure 2. 1: depth distribution of common electron acceptors, chemical zonation which accompanies respiration processes in the environment	21
Figure 2.2: Conceptual models for the formation of basin anoxia in the silled basin setting. after Armstrong et al. (2005)	24
Figure 2.3: Schematic diagram of the main features of the dissolved and particulate inorganic Fe and S chemical structure of the Black Sea.....	25
Figure 2.4: Chemical data from the Black Sea.	26
Figure 2.5: An oxygen profile at an oceanic location with an oxygen minimum zone.	27
Figure 2.6: A classification scheme for black shale biofacies derived from data on the fauna and lithologies of the British Jurassic.	32
Figure 2.7: TOC and TS relationship by Berner, 1984.....	33
Figure 2.8: SEM images for samples from the Grey shale member at North Yorkshire (Newton, 2001)..	35
Figure 2.9: Diagrammatic representation of the overall process of sedimentary pyrite formation (after Berner et al., 1984).....	37

Figure 2.10: Schematic of the shelf-to-basin shuttle that results in iron enrichment in sediments deposited under euxinic conditions.....	40
Figure 2.11: Conceptualization of the iron-speciation parameters for evaluating ocean redox condition.	43
Figure 2.12: The most reliable redox trace element parameters (Ni/Co, V/Cr, U/Th and authigenic uranium) calibrated against DOP (<i>After Jones and Manning, 1994</i>).....	44
Figure 2.13: The mean and range of molybdenum concentrations observed at a large number of modern oxic, suboxic, and euxinic environments, Euxinic settings are subdivided as a function of persistence of euxinia and Mo availability in the basin (<i>After Loyns and Anbar, 2009</i>).....	46
Figure 2.14: A schematic diagram of the diagenesis of the phytol side chain of chlorophyll (IGI Ltd, 2009).....	48
Figure 2.15: Schematic diagram of the isorenieratane produced by green-pigmented bacteria that thrive in presence of sun light and free hydrogen sulphide (<i>After Summons and Powell, 1987</i>).....	49
Figure 3. 1: A) North Yorkshire coast, view ESE towards Port Mulgrave , B) the three laminated sulphur beds at the base of Gray shale Member, C) Zooming in to show the lower Sulphur Bed.	53
Figure 3.2: Boundary beds between the Cleveland Ironstone and Grey shales Formations, Port Mulgrave, North Yorkshire	53
Figure 3.3: Photographic picture of the LSB illustrating its yellowish appearance at Staithes outcrop.	54
Figure 3.4: Chondrites and Diplocraterion burrows developed in the top of the Sulphur Band at Brachenberryt Wytke, North Yorkshire.....	55
Figure 3.5: Areal extent of the LSB (yellow band) along the coastal exposures of Staithes, Kettlewell and the Hawsker Bottoms. Note that the LSB does not grade into any near-shore facies (<i>after Howard, 1985</i>).....	57
Figure 3.6: Location map of the north Yorkshire coast fieldwork sites	59
Figure 3.7: Lithological column of the studied section at Port Mulgrave showing the position and heights of the analysed samples from the base of the Grey Shale Member.....	60
Figure 3.8: Flow chart showing the order of methods	62

Figure 4. 1: Variation of total organic carbon content throughout the study section at Port-Mulgrave section. LSB = Lower Sulphur Band; MSB= Middle Sulphur Band; USB= Middle Sulphur Band	78
Figure 4. 2: Variation of total sulphur TS content throughout the study section at Port Mulgrave section.....	79
Figure 4. 3: Cross plot of the TOC% versus the TS% of the studied samples. Regression lines for the average S and C relationships in sediments deposited under normal marine and euxinic conditions, supplied by Berner (1984) and Leventhal (1995), are shown.	80
Figure 4. 4: Variation of the $\delta^{13}\text{C}$ and $\delta^{34}\text{S}$ values through the study section at Port Mulgrave.....	81
Figure 4. 5: Cross plot between $\delta^{13}\text{C}_{\text{TOC}}$ and % TOC for the study section at Port Mulgrave	82
Figure 4. 6: S ₂ and T _{max} variation throughout the study section at Staithes. Note the suppressed T _{max} values for the Sulphur Bands	84
Figure 4. 7: S ₂ versus TOC relationship for the Port Mulgrave samples	85
Figure 4.8: HI versus TOC % wt for the study section at Port Mulgrave	87
Figure 4.9: Production index profile cross the study section at Port Mulgrave. $\text{PI}=\text{S}_1/(\text{S}_1+\text{S}_2)$	88
Figure 4.10: Variation of the Carbon Preference index CPI and $\sum (\text{C}_{21} - \text{C}_{31})/ (\text{C}_{15} - \text{C}_{20})$ ratio throughout the study section at Port Mulgrave.....	90
Figure 4.11: Chromatograms showing n-alkanes and isoprenoids of two representative samples. Number by the peaks give the number of carbon atoms in n-alkanes (Pr = Pristane, Ph = Phytane).....	92
Figure 4.12: showing the relationship between degree of waxiness and Pr/Ph ratio for the study section.....	93
Figure 4. 13: Variation of Pr/C17, Ph/C18 and Pr/Ph ratio throughout the study section at Port Mulgrave.	94
Figure 4.14: Mass chromatograms showing the distributions of steranes and diasteranes (m/z 217) for a representative sample from the Lower Sulfur Band at Port Mulgrave section.	95
Figure 4.15: Mass chromatograms showing the distribution of steranes and diasteranes (m/z 217) for selected samples from Jet Rock and Grey shale at Port Mulgrave (note the relative abundance of C ₂₉ 5 α (H) 14 α (H) 17 α (H) 20R-sterance). Refer to figure 4.14 for peak label.	96
Figure 4.16: Mass chromatograms (m/z 191) showing the hopanoid hydrocarbon distribution for representative sample from the Lower Sulfur Band at Port Mulgrave section.	97

Figure 4.17: Mass chromatograms (m/z 191) showing the hopanoid hydrocarbon distribution for selected samples from Jet Rock and Grey shale at Port Mulgrave section.	98
Figure 4.18: Homohopane index and 22S/22(S+R) AB hopanes cross the study section at Port Mulgrave.	99
Figure 4.19: Sterane/hopane plotted against the height (Cm) above the base of the Grey Shale at Port Mulgrave section showing the inferred changes in organic matter input.....	101
Figure 4.20: A ternary diagram showing the distributions of C27, C28 and C29 $\alpha\alpha\alpha$ (20R) steranes within the studied samples at Port Mulgrave section.....	101
Figure 4.21: A ternary diagram showing the distribution of C31, C33 and C35 $\alpha\beta$ (22 S&R) homohopanes within the studied samples at Port Mulgrave section.	102
Figure 4.22: (A) GC-MS ion chromatogram of m/z 133 of aromatic hydrocarbon fraction of representative sample (from the Jet Rock Shale) showing presence of a diagenetic product of isorenieratane (first identified by Koopmans et al. 1996). (B) Is mass spectrum of isorenieratane from sample JET4.....	103
Figure 4.23: Stratigraphic records of isorenieratane abundances in $\mu\text{g/g}$ TOC across the study section.....	104
Figure 4.24: Stratigraphical variation of % Phytoclasts and the fluorescent scale throughout the study section at Port Mulgrave.....	107
Figure 4.25: Amorphous organic matter-Palynomorphs-Phytoclast "APP" ternary diagram of relative abundance of palynofacies parameters after Tyson (1995)..	109
Figure 4.26: Stratigraphic variation in the character of the woody phytoclast fraction and of TOC.....	110
Figure 4.27: Well preserved 'AOM' seen in transmitted white light, amorphous matrix rich in small unidentifiable fragments (fluorescent under the blue light; equivalent to the maceral liptodetrinite) plus other inclusions (palynomorphs, pyrite and small phytoclasts) (Magnification X20).	111
Figure 4.28: relative dominance of phytoclast mixed with poorly preserved AOM and Palynomorous. (Magnification X20).	111
Figure 4.29: stratigraphic variation in the bulk geochemistry parameters: depth versus TOC wt% and HI of the lower Grey shale member at Port Mulgrave (Staithe) and Hawsker Bottom outcrops.....	115
Figure 4.30: Cm-scale analysis of the TOC, TS and isotopic analysis for the organic carbon and pyrite sulfur cross the Lower Sulfur Bed at Port Mulgrave section.....	116

Figure 4.31: Cm-scale molecular biomarker analysis cross the Lower Sulfur Band at Port Mulgrave section includes Pr/Ph, Isorenaraten concentration ($\mu\text{g/gTOC}$), Steranes over Hopanes ration and the Homohopanes index.....	116
Figure 4.32: Thin layer of bitumen within the Lower sulfur band at Port Mulgrave section.	117
Figure 4.33: bitumen accumulation within the Lower Sulfur Bed. The picture shows the elongated structure casted on the shale rock.	118
Figure 4.34: GC trace of the bitumen from the Lower sulfur Bed at Port Mulgrave.	119
Figure 4.35: Cross plot of Pr/ $n\text{-C}_{17}$ versus Ph/ $n\text{-C}_{18}$ ratios from extracted bitumen gas chromatograms showing organic matter type, biodegradation and maturation conditions for the Lower Sulfur Band and the bitumen layer included compare to the Jet Rock Shale.....	120
Figure 4. 36: Ternary diagram showing the relative abundances of C_{31} , C_{33} and C_{35} 17α (H) 21β (H) hopanes $22\text{R} + 22\text{S}$ isomers.	121
Figure 4.37: Ternary diagram showing the relative abundances of C_{27} , C_{28} and C_{29} -regular steranes 5α (H) 14α (H) 17α (H) 20 R isomer.	121
Figure 4.38: Cross plot of HI and Tmax showing the thermal maturity state of the samples at Port Mulgrave section.	123
Figure 4.39: S2 versus TOC diagram with Kerogen type fields indicating that all of the Jet Rock samples do fall in Kerogen type II while the Grey shale fall in Kerogen types II and III region.	125
Figure 5. 1: Outline lithostratigraphy, and profile of concentrations TOC, TS, $\delta^{13}\text{C}$ of the organic matter and $\delta^{34}\text{S}$ of the pyrite sulphur through the Lower Toarcian strata of Port Mulgrave section.....	136
Figure 5.2: Cross plot of $\delta^{13}\text{C}_{\text{TOC}}$ and TOC wt% show negative correlation. Samples from the Jet Rock shale and Lower sulphur bands are the most depleted in $\delta^{13}\text{C}_{\text{TOC}}$	137
Figure 5. 3: Ternary TOC-TS-FeT diagram showing the relative distribution of the three elements. Construction and principles of interpretation of the diagram based on Dean and Arthur (1989) and Arthur and Sageman (1994).....	138
Figure 5.4: Composite stratigraphy with iron speciation data. The total Fe content (in wt%) and the relative proportion of Fe residing in unreactive and reactive phases at Port Mulgrave section	139
Figure 5.5: Composite stratigraphy with iron speciation data of the Port Mulgrave section	140

Figure 5.6: Stratigraphic records of isorenieratane abundances in $\mu\text{g/g}$ TOC across the study section at Port Mulgrave.	141
Figure 5.7: Sedimentary content of Mo/Al (10^4), V/Al (10^4) and Zn (10^4) plotted versus height from base of Gray Shale Members at Port Mulgrave section.	143
Figure 5.8: Mean enrichment factors (E.F) of Cu, Zn, Mn, V and Mo relative to average shale for the study section at Port Mulgrave.....	144
Figure 5.9: Mean enrichment factors (E.F) of Cu, Zn, Mn, V and Mo relative to average shale for the Sulphur bands at Port Mulgrave.....	144
Figure 5.10: Cross-plots of element/Al against TOC for the study section at Port Mulgrave.	146
Figure 5. 11: TOC and Iron speciation profile of section at Hawsker Bottoms.	147
Figure 5. 12: iron speciation of section at Hawsker Bottoms.	148
Figure 5. 13: Cross-plot of MO ppm and TOC %wt for the Lower Sulphur Band at Port-Mulgrave (empty triangles) and the Hawsker Bottoms (grey squares).	150
Figure 5. 14: TOC and Iron redox proxies of the lower Grey Shale at Hawsker Bottoms section.	150
Figure 5.15: Composite stratigraphy with iron Paleoredox indicators for the study section at Port Mulgrave.	152
Figure 5.16: Composite stratigraphy with iron speciation data at Port Mulgrave section....	153
Figure 5.17: A) Cross-plot of MO ppm and TOC %wt from this study; B) Cross-plot of MO ppm and TOC %wt from McArthur et al., 2008	159
Figure 5.18: Mo/TOC versus FePy/FeHR for the study section at Port Mulgrave.	160
Figure 5.19: Detailed iron speciation profile across the Lower Sulphur Band at Port Mulgrave.....	162
Figure 5.20: Detailed chemostratigraphic plots of $\delta^{34}\text{S}_{(\text{Pyrite})}$ and $\delta^{13}\text{C}$ isotopes, Mo/Al ratio and maxima of isorenieratane abundances across the Lower Sulphur Band at Port Mulgrave section.....	163
Figure 5.21: Cross plot of Mo/TOC versus FePy/FeHR through the three sulphur beds at Port Mulgrave section.....	164
Figure 5. 22: Detailed iron speciation profile across the Middle sulphur Band at Port Mulgrave.	165
Figure 5.23: Detailed chemostratigraphic plots of $\delta^{34}\text{S}_{(\text{Pyrite})}$ and $\delta^{13}\text{C}$ isotopes , Mo/Al ratio and maxima of isorenieratane abundances across the Middle Sulphur Band.....	166
Figure 5.24: Detailed iron speciation profile across the USB at Port Mulgrave section.....	167

Figure 5.25: Detailed chemostratigraphic plots of $\delta^{34}\text{S}$ (Pyrite) and $\delta^{13}\text{C}$ isotopes , Mo/Al ration and maxima of isorenieratane abundances across the Upper Sulphur Band at Port Mulgrave section.....	168
Figure 5. 26: Cross-plot of MO ppm and TOC %wt for the Sulphur Bands at Port Mulgrave section showing the different Mo/TOC of the Lower Sulphur Bands compare to the Upper and Middle once.....	168
Figure 5.27: Schematic W-E cross section of the Cleveland Ironstone Formation and the lowest part of the overlying Grey Shale (Rob Newton PhD thesis, after Howard, 1985).	169
Figure 5.28: Comparison between carbon-isotope records of Port Mulgrave section in North Yorkshire and Peniche section in Portugal.	172
Figure 5.29: Schematic paleoceanographic model of the lowermost Early Toarcian. Showing the development of the driving mechanism for the Sulphur Bands which then accumulates in the T-OAE. Biozone duration from McArthur et al. (2000).....	174
Figure 6. 1: the vibrational behaviour of bond stretching and bending in a molecule	178
Figure 6. 2: Internal workings of an FT-IR/NIR spectrometer ((www.chromatography-online.org).....	180
Figure 6. 3: Schematic illustration of FTIR system (www.norhtwestern.edu).....	182
Figure 6. 4: schematic map of the sampling locations: D = Lyme Regis outcrop at Dorset, P= Port Mulgrave	185
Figure 6. 5: A flow chart summarizing the 3 major steps used for the NIRS-PLSR calibration and validation procedures in this study.....	191
Figure 6. 6: Histogram representing all analyzed sediment TOC concentrations	192
Figure 6. 7: Histogram representing the analyzed sediment TS wt % concentrations.	194
Figure 6. 8: Histogram representing the analysed sediment TOS %wt concentrations.....	194
Figure 6. 9: PCA scores plot of NIR spectra of all samples	195
Figure 6. 10: Combustion technique measured and FT-NIRS predicted TOC for the Blue Lias samples plotted against the stratigraphic height at the study section.....	196
Figure 6. 11: The predicted and measured TOC %wt PLSR relationship for the Blue Lias samples.....	197
Figure 6. 12: The predicted and measured TS %wt PLSR relationship for the Whitby samples.....	198

Figure 6. 13: The predicted and measured TOS % wt PLSR relationship for the Whitby samples.....	199
Figure 6. 14: Plot of Leco measured TOC against PLS regressed TOC for the test (validation) set (96 samples) for the Whitby samples.	200
Figure 6. 15: Plot of Leco measured TOC against PLS regressed TOC for the test (validation) set (144 samples) for the School archived samples	201
Figure 6. 16: Plot of Leco measured TS against PLS regressed T for the test (validation) set (97 samples) for the Blue Lias samples.	202
Figure 6. 17: Combustion technique measured and FT-NIRS predicted TS for the Blue Lias samples plotted against the stratigraphic height at the study section.....	202
Figure 6. 18: Plot of Leco measured TOS against PLS regressed T for the test (validation) set (97 samples) for the Blue Lias samples.	203

LIST OF TABLES

Table 2. 1: Redox classification of depositional environments, <i>after Tyson and Pearson (1991)</i> ; the values for O ₂ concentrations in bottom waters are valid for present-day ocean. Fe _{py} = pyrite iron, Fe _{HR} = highly reactive iron (Poulton & Canfield, 2011).....	19
Table 2.2: Characteristics of modern euxinic basins (After Meyer and Kump, 2008).....	29
Table 2.3: summary of most used paleoredox indicators Wignall and Hallam, 1991; Berner, 1984; Koopmans et al. 1996a; Zheng et al., 2000; Poulton and Raiswell, 2002.	32
Table 3. 1: shows the accuracy and precision of the analytical methods.....	64
Table 3.2: Summary of fluorescence scale, where the 1 represents the lowest preservation stat of the organic matter and 6 the highest (after Tyson, 1995, p.347)	68
Table 3.3: Details of the Fe extraction scheme, with target phases (<i>After Poulton and Canfield, 2005</i>).	71
Table 3.4: Shows the accuracy and precision of the analytical method	72
Table 3.5: Shows the accuracy and precision of the iron speciation analytical method.....	73
Table 3.6: shows the accuracy and precision of the trace element analytical method.....	74
Table 4.1: Stratigraphic summary for the Lower Whitby Mudstone Formation modified from Salen et al. (2000); d (m) is the cumulative distance from the top of bed to base of the Grey Shale Member. The bed numbers are from Howarth (1962, 1973).	76
Table 4.2: Summary table of the bulk geochemistry data: TOC= total organic carbon; TC= total carbon; TIC= total inorganic carbon; TS= total sulphur.	83
Table 4. 3: Summary table for the Rock-Eval data.....	86
Table 4.4: showing the obtained normal alkanes and acyclic isoprenoids relative abundance and the calculated CPI values for the study section.....	91
Table 4.5: Biomarker-based parameters for organic matter thermal maturity and Paleoredox indicators. Homohopane index = percentage of $\alpha\beta$ -C35 Homohopane in Σ C31 – C35 $\alpha\beta$ homohopanes (Peters & Moldowan, 1991). +/- = presence/absence of isorenieratane.	105
Table 4.6: informal kerogen categories used in this study.....	109
Table 4.7: Summary of bulk geochemical data from the Jet Rock and Sulphur Bands.....	131

Table 4.8: Summary table show the similarities and the differences between MFS and basal black shales.	132
Table 4.9: Petroleum generative potential from combined Rock-Eval and TOC values (after Baskin, 1997)	133
Table 5. 1: Averages of element enrichment factor values for each interval through the study section. MST = Mudstone, LSB= Lower sulphur bed, MSB=Middle sulphur bed, USB=Upper sulphur bed, TL=Top Laminated unit, and the bed numbers follow those of Howarth (1962, 1973).....	142
Table 5. 2: Averages values for individual units showing a comparison of the elemental distribution and ratios at both Hawsker Bottoms and Port Mulgrave section.	149
Table 6. 1: Abbreviated table of group frequencies for Organic Groups (www.cem.msu.edu)	179
Table 6. 2: TOC characteristic of all analyzed sediments samples.....	193
Table 6. 3: Summary of correlated results	199

CHAPTER 1 - INTRODUCTION

1.1 General Overview

An increasing number of studies are devoted to the nature of black shale facies and assessing the changing redox and palaeoxygenation conditions in the geological record (Demaison and Moore, 1980; Pedersen and Calvert, 1990; Wignall, 1994; Tyson, 2005; Negri et al 2009). The concentration of dissolved oxygen and other oxidants in the bottom water and the uppermost part of the sediment have a great influence on the preservation and thus geochemical quality of organic matter. Therefore, understanding the frequency, amplitude and rates of past changes in marine redox conditions and carbon burial is important and critical for examining links between ocean chemistry and the evolution of the biosphere and atmosphere in the past.

The deficiency of free oxygen has been a major driver of evolution and extinction throughout Earth history. Examples of oceanic anoxia and euxinia are frequently found in the geologic record. The anoxic settings defined as those with less than 0.2 ml O₂/l H₂O (Tyson and Pearson, 1991), while the euxinic settings are those without oxygen (anoxic) and have free hydrogen sulfide (H₂S) within the water column.

Anoxia and euxinia typically go hand in hand because anoxia is a prerequisite for the bacterial metabolism that generates H₂S through reduction of sulfate, which is the second most abundant anion in seawater today (Meyer and Kump, 2008). Euxinic settings comprise less than 0.5% of the deep ocean today, with the Black Sea and Cariaco Basin off the coast of Venezuela being the largest and second largest examples, respectively. But in the geological record oxygen deficiency and euxinia occurred on a larger scale at times dominating entire ocean basins. Examples are the so-called Oceanic Anoxic Events (OAEs), intervals known most famously from the Mesozoic for abundant, widespread, organic-rich black shales that are shown to be euxinic (Schlanger and Jenkyns, 1976).

This study is devoted towards an understanding of changing palaeoredox condition across the lower Jurassic, which was accompanied by the deposition of black shales during the Lower Toarcian (early Jurassic, 183 Ma) OAE in Cleveland Basin in North Yorkshire (UK) (Jenkyns, 1988). Detailed climate records of the event have been reported from this location that shed new light on the forcing and timing of climate perturbations and associated

development of ocean anoxia. In discussing Early Toarcian events recorded in the Cleveland Basin, the focus of others has been largely on the 3 m interval in the lower *exaratum* Subzone where TOC concentrations are highest (the putative T-OAE in the strict sense), or the 7 m of the *exaratum* Subzone itself (the putative OAE in the wider sense). Moreover the start of this global event could have been earlier but at regional scale. In Cleveland Basin for small repeated intervals of anoxic conditions are developed at the Pliensbachian-Toarcian boundary preceding the main T-OAE. These events are characterised with smaller negative excursions in $\delta^{13}\text{C}_{\text{org}}$ trend. Here the focus is to explore and understand these small events at the Pliensbachian-Toarcian transition boundary and highlighting any possible like to the major T-OAE above.

The Jurassic stratigraphic record of Britain contains several black shale horizons, of which the Whitby Mudstone Formation in the Cleveland Basin (North Yorkshire, NE England) is amongst the best studied (Wignall and Hallam, 1991; Hallam, 2001; Simms et al., 2004; Powell, 2010). A lot of work has already been published providing a clear lithostratigraphic, biostratigraphic and sedimentological framework for further studies. These units, and the lateral time and facies equivalents of the Whitby Mudstone, are actual petroleum source rocks in France, SW-Germany, and the Dutch North Sea (Schouten *et al*, 2000) (figure 1.1)

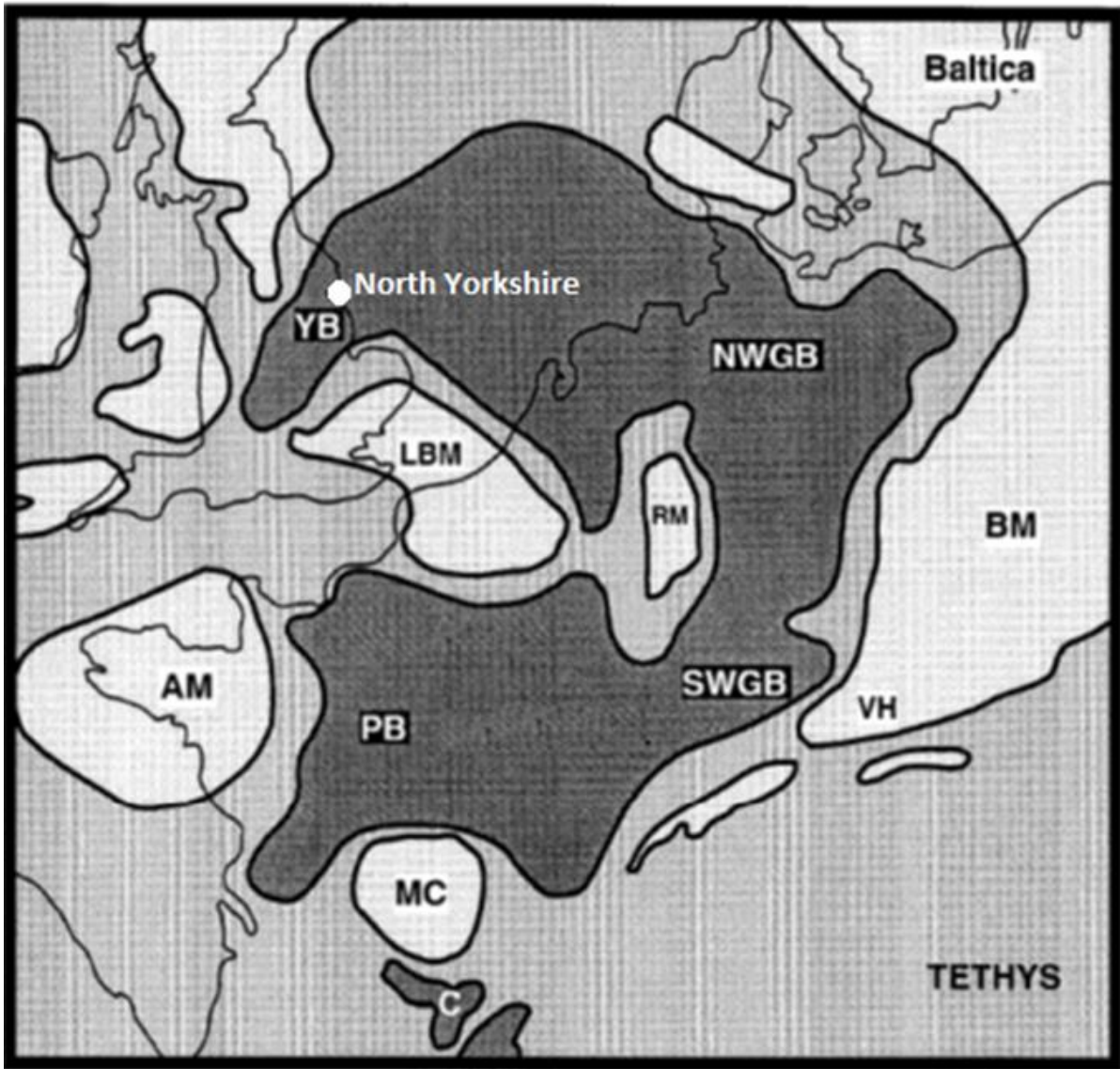


Figure 1.1: Early Toarcian black shale distribution (dark grey colour) in Western Europe epicontinental basins. YB= Yorkshire Basin, SWGB= South West Germany Basin, NWGB= North West Germany Basin and PB= Paris Basin (after McArthur et al., 2008)

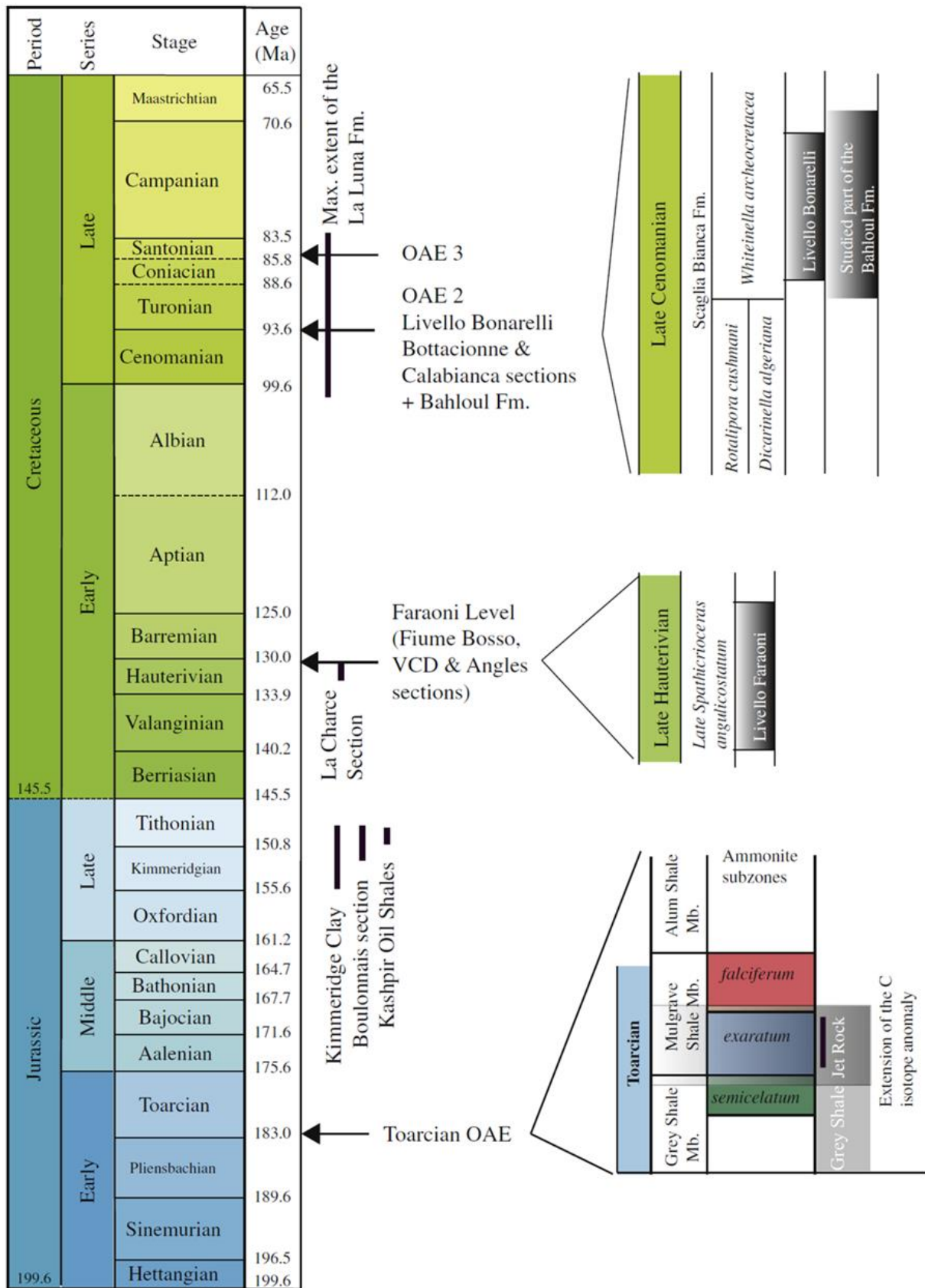


Figure 1.2: Stratigraphic distribution of the Oceanic Anoxic Events (OAE) with some examples of organic rich formation including the study section for this study (after Tribovillard et al., 2011)

In the Cleveland basin (UK), these organic-rich rocks span the upper *Dactyloceras semicelatum* ammonite Subzone and *Cleviceras exaratum* ammonite Subzone (Howarth 1992), and their presence is accompanied by major geochemical and biotic changes (Jenkyns and Clayton, 1997; McArthur et al., 2000; Little and Benton, 2005; Caswell et al., 2008).

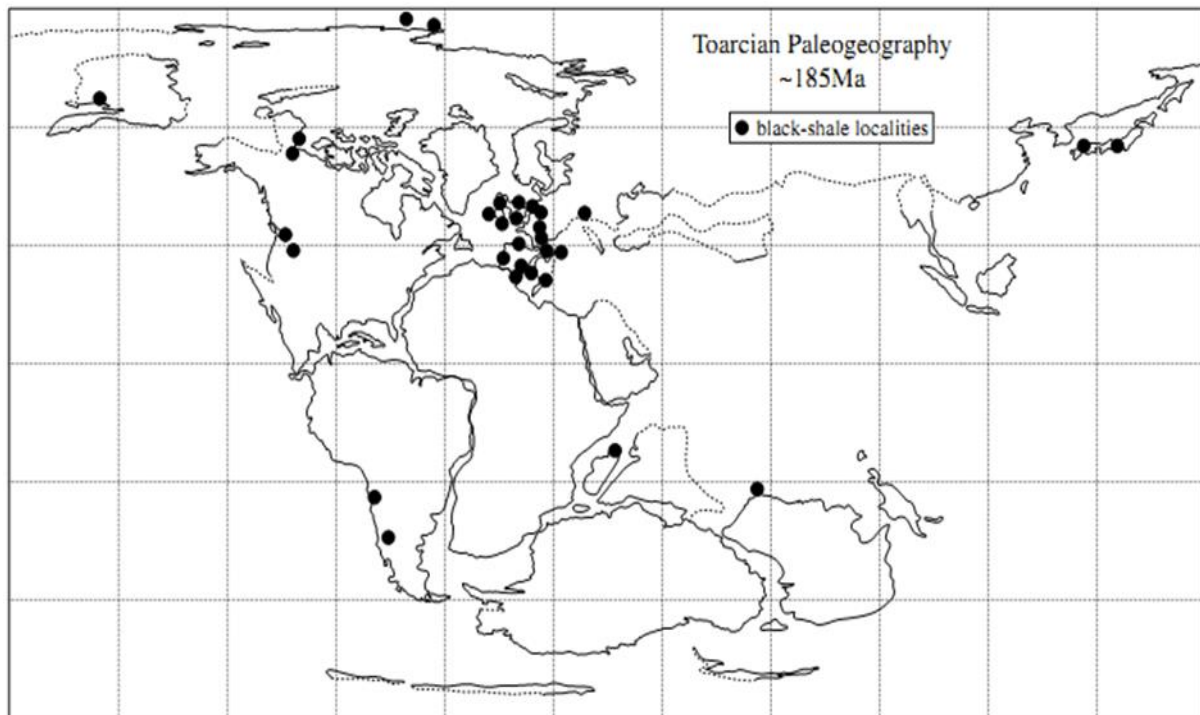


Figure 1.3: Early Jurassic palaeogeographical map illustrating the global distribution of previously reported lower Toarcian bituminous black shales (black symbols) (after Jenkyns 1988).

Subsequent work, however, revealed that the geochemical signature of the T-OAE is not so straightforward. Carbonate records show both negative and positive excursions in the $\delta^{13}\text{C}$ trend, while the organic carbon record demonstrates a negative carbon-isotope excursion (CIE) of -7‰ reported in the *falciferum* zone (Jenkyns and Clayton, 1997; Hesselbo et al., 2002; Cohen et al., 2004; Kemp et al., 2005). The conflicting carbonate signals and the large and rapid nature of the organic carbon excursion have caused much speculation as to the causes, consequences and extent of this event.

These isotopic changes possibly resulted from widespread anoxia, coinciding with a brief interval of global warming and biotic extinction (Jenkyns and Clayton, 1997) and possibly linked to a third order sea-level rise (Frimmel et al., 2004). The T-OAE is marked by a pronounced negative carbon isotope ($\delta^{13}\text{C}$) excursion in marine organic and inorganic

carbon of ~5 - 7‰ (Kemp *et al.*, 2005) which has been widely, but not universally (e.g., van de Schootbrugge *et al.*, 2005a; Wignall *et al.*, 2006), interpreted to represent a major perturbation in Early Jurassic carbon cycling. This shift to lower $\delta^{13}\text{C}$ values also affected the atmospheric and continental carbon reservoirs because the Carbon Isotopic Excursion (CIE) has also been observed in samples of fossil wood extracted from sedimentary rocks of early Toarcian age in northwest Europe (Hesselbo *et al.*, 2000; Hesselbo *et al.*, 2007a).

This project addresses the short term redox changes associated with enhanced carbon burial (black shale formation) in the Lower Toarcian from two well known lower Jurassic sections in UK (The Staithes to Port Mulgrave and Hawsker Bottoms outcrops) within the Cleveland Basin (North Yorkshire, NE England). The intent of this project is to apply a multi-proxy geochemical approach, using a combination of robust techniques, in order to produce high resolution records of ocean redox covering the transition into the T-OAE.

1.2 Overview of the Lower Jurassic

1.2.1 Paleogeography and Geological Framework

The early Jurassic paleogeography and environment were fundamentally different from the modern world (Jenkyns and Clayton, 1997). This period witnessed the continued breakup of Pangea that began with the emplacement of the Central Atlantic Magmatic Province at the Triassic-Jurassic boundary (Palfy and Smith, 2000; Powell *et al.*, 2010). The Tethys Ocean was enclosed on the north and south by a single, arid supercontinent, Pangaea, linked to the global ocean to the east (Powell *et al.*, 2010). The western side of the Tethys Ocean bordered what is now northern Europe. The region had broad, shallow epicontinental seas containing numerous small islands (Figure 1.4). Climate changes during Lower Jurassic are extensively documented by chemical proxy data from sedimentary rocks, commonly demonstrating 5–10 °C global warming lasting a few hundred thousand years (Svensen *et al.*, 2007). Lower Jurassic oceans had an average carbonate $\delta^{13}\text{C}$ isotopic composition of approximately +2‰, compared to 0‰ today (Veizer *et al.*, 1999). Organic carbon was significantly depleted in ^{13}C , averaging -30‰, for typical marine organic carbon, compared to -22‰ today (Hayes *et al.*, 1999). Thus, the average fractionation between inorganic and organic carbon was about 32‰ compared to 25‰ today.

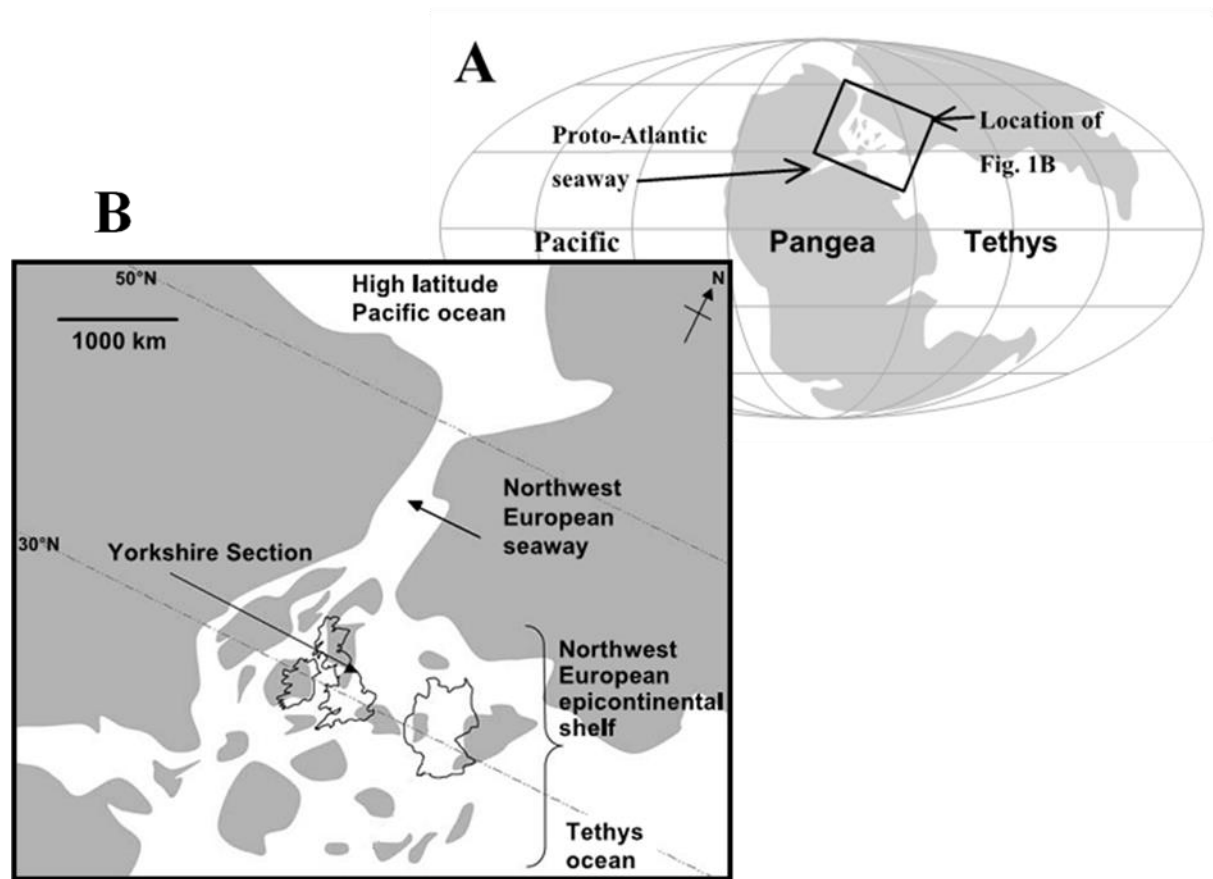


Figure 1.4: A) Global lower Toarcian paleogeography. B) Lower Toarcian paleogeography of Northwest European region (after Bailey et al., 2003).

Widespread deposition of marine organic-rich rocks known as black shales, over specific time intervals, has long received much attention in the geologic community. Such deposition of organic rich sediments, when occurring globally and accompanied by global disturbance in the carbon cycle, led to the development of the concept of Oceanic anoxic events (Schlanger and Jenkyns, 1976).

During the lower Jurassic these organic rich sediments have been found in many localities around the world in both the northern and southern hemispheres (Jenkyns 1988). Their recognition provides evidence for globally enhanced accumulation of marine organic matter during a relatively brief interval of time. The development of these organic matter-rich black shales has been a matter of intense geological, paleontological, and geochemical studies (Demaison and Moore, 1980; Pedersen and Calvert, 1990; Calvert and Pedersen, 1992, Bordenave, 1993, among many others). This is due to their often very good preservation of fossils but also because of their economic potential as hydrocarbon source rocks (Murphy et al., 1995).

Amongst the Mesozoic black shales in central Europe, those deposited during the lower Jurassic (Upper Lias), the Whitby Mudstone of Yorkshire, the Posidonia Shale in Germany, and the Schistes Cartons in France, have received special attention. The richest interval is most precisely dated in Yorkshire as belonging to the *falciferum* ammonite biozone, *exaratum* subzone. The thickest, most widespread, and most organic-rich sequences of the British Jurassic occur in the lower part of the Whitby Mudstone Formation (Jet Rock member; Lower Toarcian), the Lower Oxford Clay (*Callovian*) (Hudson and Martill, 1991) and the Kimmeridge Clay (*Kimmeridgian*) (Scotchman, 1989). In addition, minor sequences of organic rich units are found in the Blue Lias Formation and the Shales with Beef Formation (*Hettangian-Sinemurian*).

Following a relatively quiescent tectonic phase during the late Pliensbachian, the early Toarcian (*Tenuicostatum Zone*) was a period of major basin subsidence throughout England (Powell et al., 2010). Deeper water with increased sediment flux characterised the Grey Shale Member (*Tenuicostatum Subzone*). This increase in the sea level (or subsidence of the Cleveland Basin) was accompanied by fluctuating oxic and anoxic bottom water conditions throughout the Grey Shale. But increasing levels of organic carbon are present from the *Semicelatum Subzone* through the *Exaratum Subzone (Falciferum Zone)* spanning the uppermost Grey Shale (Top Laminated unit) and the Jet Rock shale member. In North Yorkshire, the lower Toarcian section was divided by Moors (1980) into three facies types (normal shale facies, restricted shale facies and the bituminous shale facies) of which each one is defined on the basis of a number of sedimentological, palaeontological and chemical criteria.

The normal shale facies belongs to the *P. paltum* and *D. clevelandicum* subzones of the Grey Shale Member and is characterised by a diverse bivalve community that included epifaunal suspension feeders and both infaunal deposit and suspension feeders. The restricted shale facies belongs to the *D. tenuicostatum*, lower *D. semicelatum subzone* and contains shallow burrowers, mainly deposit feeding protobranchs, and epifaunal bivalves with rare recognisable trace-fossils. The bituminous shale facies extends from upper *D. semicelatum* to the lower *D. commune subzone* and lacks a benthic fauna and is instead typified by epifaunal forms.

The normal grey shale facies were laid down after the deposition of shallow water deposits that included oolitic ironstones and near-shore sands of the Cleveland Ironstone

Formation. Then organic-rich laminated shales developed during the deposition of sediments from the overlying *D. Semicelatum* and *H. Exaratum* subzones, where benthic fauna is entirely absent. At this time, the most organic-rich section of the Whitby Mudstone Formation, the Jet Rock Shale was deposited in the distal part of an epicontinental sea that covered much of NW Europe. This abrupt change to deeper-water sedimentation has been linked to a rapid sea level rise during the early Toarcian (Ivimey-Cook and Powell, 1991).

Sediments become progressively less bituminous towards the top of the *H. falcifer* subzone that overlies the *H. Exaratum* subzone, with the transition from bituminous to restricted mudstones being marked by a lenticular band of limestone composed of belemnites, bivalves, fish debris and bones (Morris, 1979).

Correlation between sections of Lower Toarcian strata on the Yorkshire coast is possible at the decimeter level over a distance of several kilometers, due to numerous distinctive marker beds of (mostly) carbonate and (rare) sideritic concretions, illustrating the lateral continuity of the facies. Much of the Lower Toarcian sediment contains calcite, either cryptically as nanofossil debris and dispersed diagenetic cement, or as large discrete carbonate concretions (commonly > 15 cm diameter) commonly occurring along discrete horizons. The section is well exposed along Port Mulgrave and predominantly composed of pale to dark-grey mudstone that was deposited in fully marine conditions below storm wave-base (Salen et al. 2000).

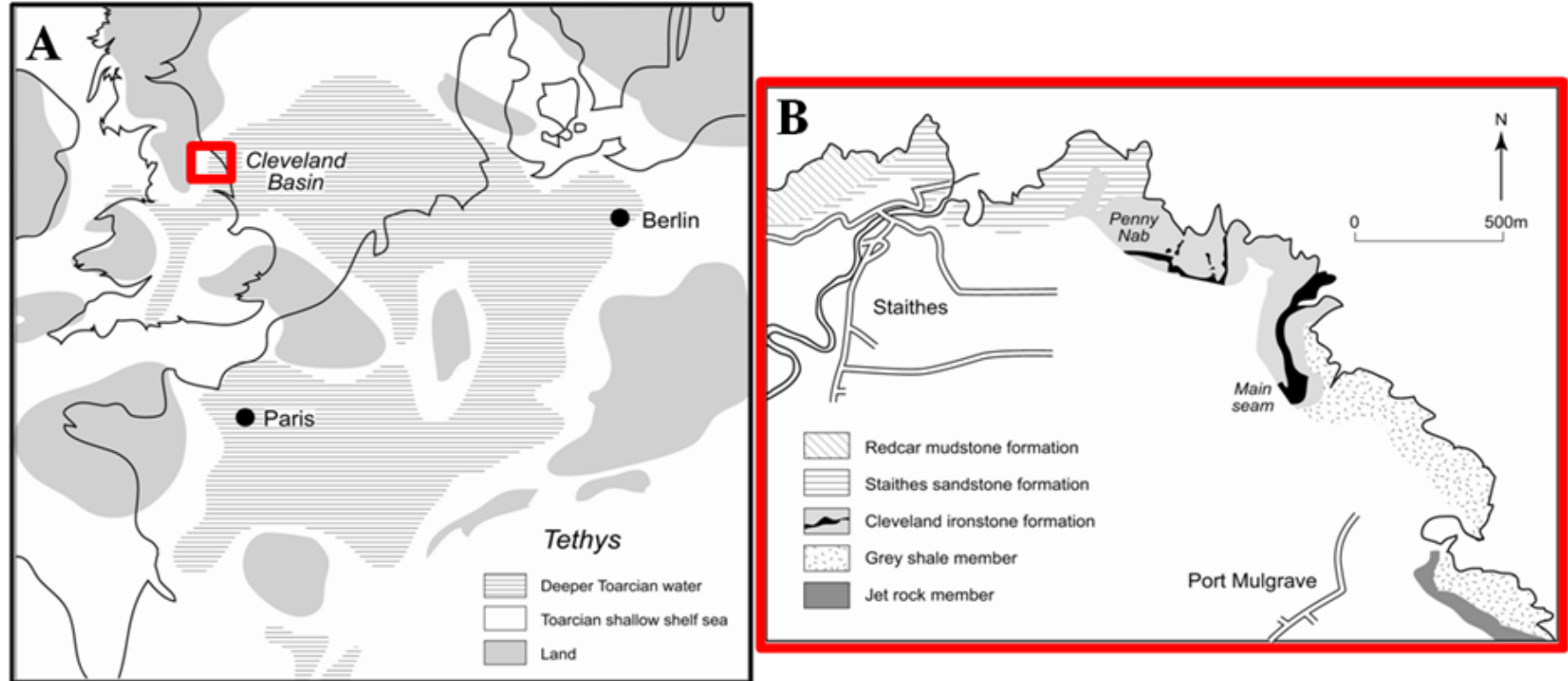


Figure 1.5: A) map shows the reconstruction of the extent of organic-rich sedimentation for the Lower Toarcian of north-western Europe, 51o 50'N, 6o 15'E. B) map shows the location of sampling site at Port Mulgrave section in North Yorkshire, UK.

1.3 Toarcian Oceanic Anoxic Event

The earliest of the OAEs occurred in the Lower Jurassic (Jenkyns, 1988). Geochemical, sedimentological and paleontological data indicate that the Early Toarcian was a period of sudden and severe global environmental change, marked by the start of a major marine transgression and global warming (Morris, 1980; Hallam, 1981, Jenkyns, 1985). These global trends were accompanied by widespread development of marine black shale characterized by a significant perturbation to the global carbon cycle (Hesselbo et al., 2000; Schouten et al., 2000; Jenkyns et al., 2001; Cohen et al., 2007) and mass extinctions (Caswell et al., 2009; Courtillot and Renne, 2003; Wignall, 2005).

Organic-rich marine rocks that are early Toarcian in age have been found in many localities in both the northern and southern hemispheres (Jenkyns 1988; Jenkyns et al. 2002). Their recognition provides a compelling case for the enhanced accumulation worldwide of marine organic matter during a relatively brief interval of time, which is now known as the Toarcian Oceanic Anoxic Event (T-OAE) (Jenkyns 1985; Jenkyns 1988). The major perturbation to the global carbon cycle during the Toarcian is marked by a substantial and abrupt carbon isotopic excursion (CIE) in organic C ($\delta^{13}\text{C}$ (org)) of about -6‰ to -7‰, that is observed in rocks of early Toarcian age from throughout Europe (Kuspert 1982; Hesselbo et al., 2000; Kemp et al., 2005).

Carbon cycle perturbations are globally recorded in sediments as carbon isotope excursions irrespective of lithology and depositional environment. Although such a globally significant organic carbon burial event apparently resulted in an overall positive excursion of the carbon isotope ratio in seawater (figure 1.6), the T-OAE is also punctuated by one of the largest negative carbon isotope excursions (CIE) of the Mesozoic, which occurred over a short period estimated to be between 300 and 1000 ka (Kemp et al., 2005; Suan et al., 2008a). This CIE is recorded in marine organic matter, marine carbonate and terrestrial material in several localities around the world (Jenkyns and Clayton, 1986, Hesselbo et al., 2000, 2007; Schouten et al., 2000; Jenkyns et al., 2001; Kemp et al., 2005).

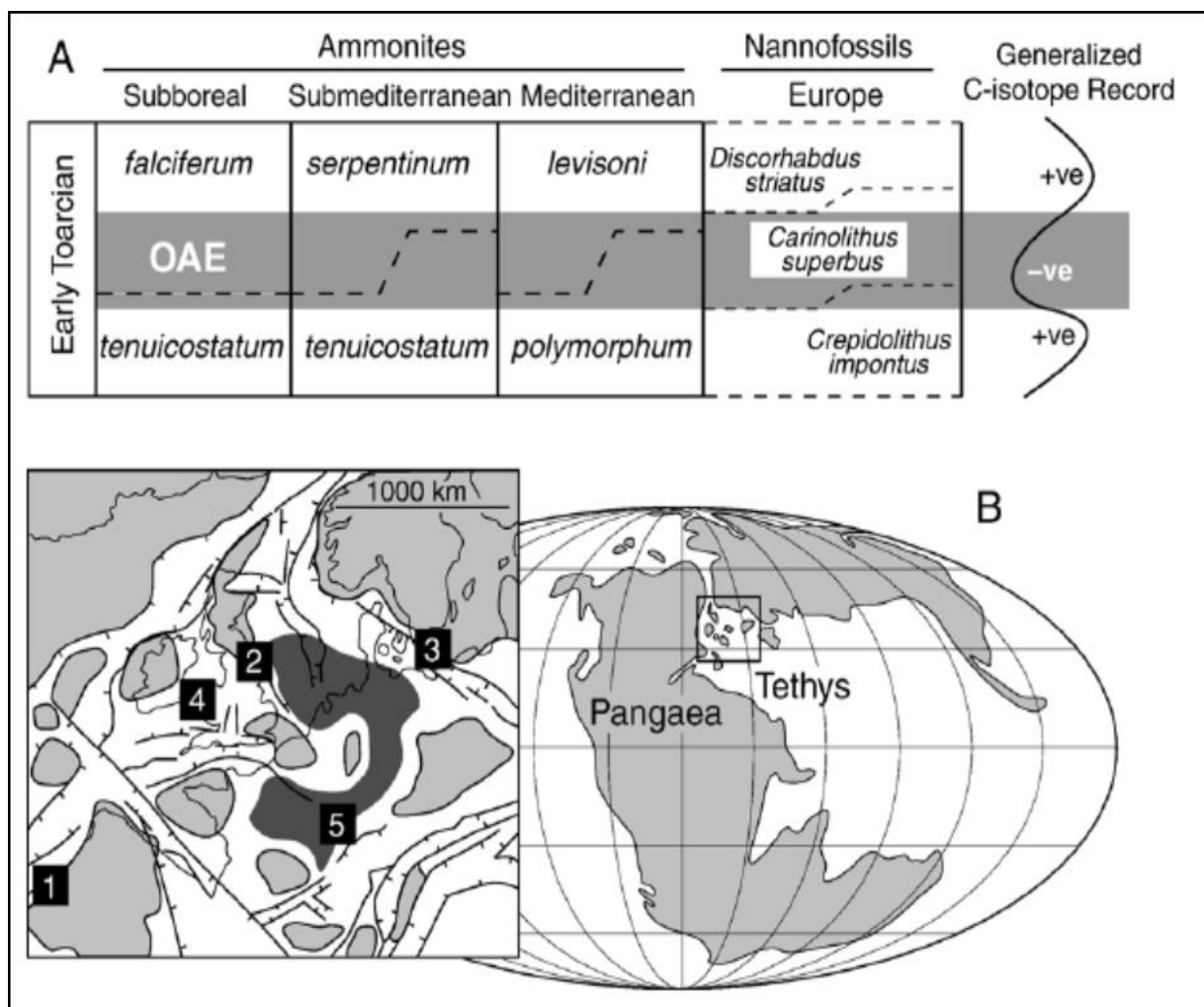


Figure 1.6: Ammonite zonal schemes (after Howarth, 1992; Jakobs et al., 1994), absolute U-Pb age data (after Palfy et al., 2000), and generalized isotope profiles (after Hesselbo et al., 2007; McArthur et al., 2000) for the Early and Middle Toarcian. B) Palaeogeographical map for the Toarcian showing the location of lower Toarcian sections with organic-rich facies (from Cohen et al., 2007).

Over the last two decades, there has been increased effort to unravel the causes and consequences of the T-OAE. These new records have documented sharp and pronounced carbon isotope excursions $\delta^{13}\text{C}_{(\text{org})}$ values which decrease abruptly from -26 to -33 ‰ (Kemp et al., 2005). The T-OAE is associated with major changes which include a threefold increase in atmospheric CO_2 levels (McElwain et al., 2005), a rise in seawater palaeotemperatures (Rosales et al., 2004; van de Schootbrugge et al., 2005), an increase in silicate weathering rates (Cohen et al., 2004; Waltham and Grocke, 2006), and a biotic crisis affecting marine invertebrates and biocalcifying microorganisms (Little and Benton, 1995; Tremolada et al., 2005).

The lithological expression of the T-OAE may be locally very different (Hesselbo et al., 2004). It has been found that the development of anoxic, organic matter rich facies did not occur everywhere in the European Neotethyan realm and, where developed, the lithology, petrology and organic matter richness of the sediments is variable. The lithological variation of the T-OAE at different localities illustrates the importance of local environmental conditions, which are ultimately more important in determining the lithology of deposits formed during an OAE (Trabucho-Alexandre et al., 2011).

It has been suggested by Hesselbo et al. (2000), that the associated perturbations in seawater temperature and chemistry, and marine and terrestrial biota were characteristic of all surficial reservoirs, and the cause of the negative carbon isotope excursion concurrent with the T-OAE was the dissociation, release and consequent oxidation of methane derived from continental slope hydrates. More recently, a high-resolution $\delta^{13}\text{C}_{(\text{org})}$ record across the T-OAE obtained from mudstones exposed in northeast England was generated by Kemp et al. (2005). These data (figure 1.7) suggest that the negative $\delta^{13}\text{C}$ excursion was not one single event, but was actually small multi events, the timing of which was interpreted as having been paced by astronomically forced climate-ocean cycles.

The sudden and major perturbations to the global carbon cycle occurred during the T-OAE is observed as well in Palaeocene–Eocene thermal maximum (PETM) about 56 million year ago (Bowen and Zachos, 2010). This sharp negative carbon isotope excursions (CIE) record at both T-OAE and PETM are globally recognized in the (marine and terrestrial) sedimentary record and characterised with decreases in the $\delta^{13}\text{C}_{(\text{org})}$ values by up to 7‰ and show broadly similar patterns of initiation and recovery (Figure 1.7).

The records of the CIEs are accompanied by other isotopic, geochemical and biotic records that show that both events were associated with the extinction of marine invertebrate species (Suan et al., 2008b), with a crisis in primary producers, with major changes in terrestrial species distributions and with sudden and substantial warming of marine surface waters as a direct physical response to atmospheric warming (Mortén and Twitchett, 2009).

The overall shift in $\delta^{13}\text{C}$ that defines the Carbon isotopic excursion at the two events was almost -2‰ (C_{carb}) for the PETM and about -7‰ (C_{org}) for the T-OAE. Moreover, the negative shifts in $\delta^{13}\text{C}$ for both events appear to have been paced by astronomical precession, where the peaks of the abrupt excursions (stage 2 in figure 1.7) lasted almost 100 ka and

involved several sudden shifts in $\delta^{13}\text{C}$ of between -1‰ to -3 ‰ within about 650 years (T-OAE) and 1 ka (PETM) (Cohen et al., 2007).

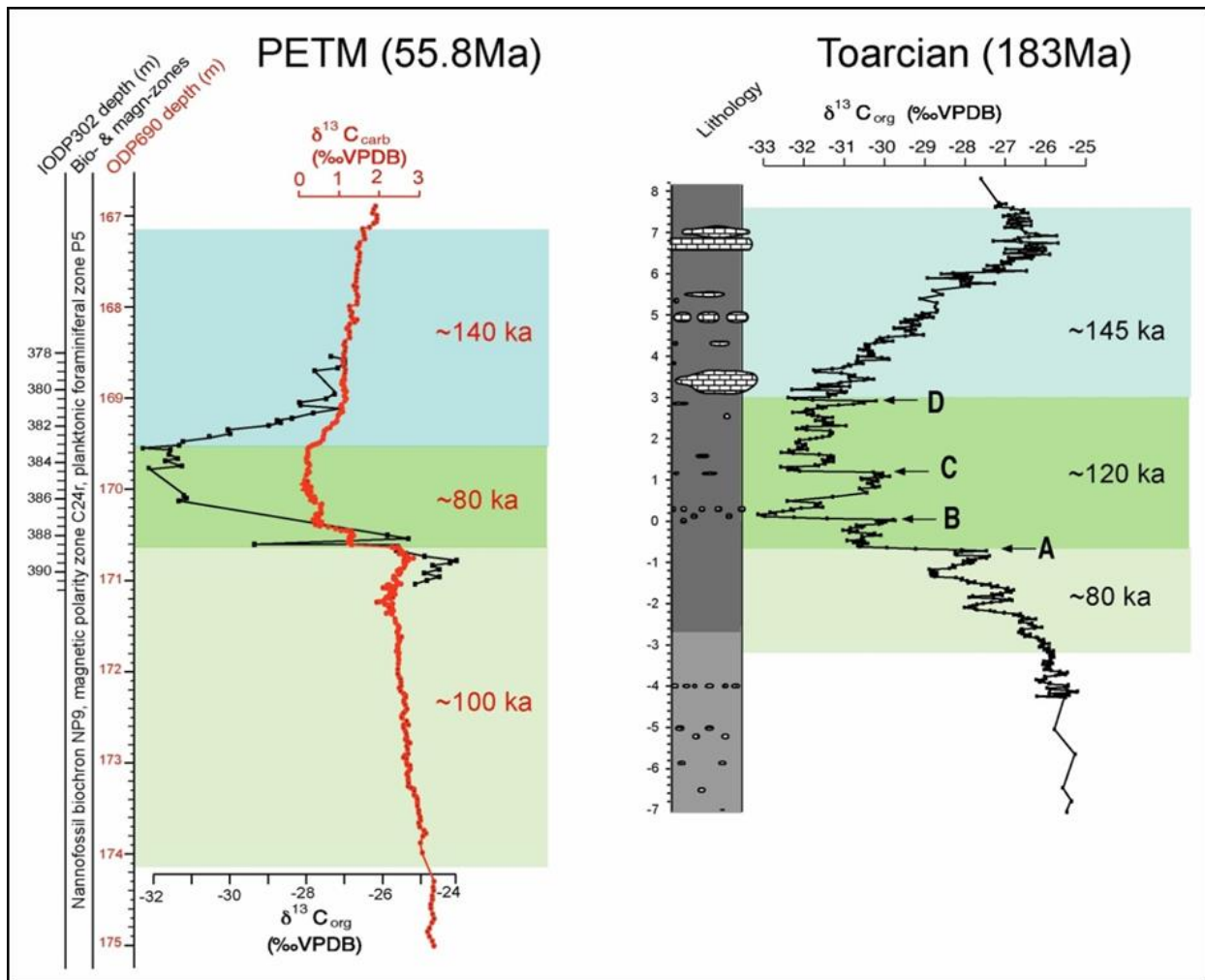


Figure 1.7: Comparison of the PETM and Toarcian CIEs. The coloured bands indicate the three distinct stages of the CIEs that can be recognized using the same criteria in each case. The A,B,C and D on the right hand column indicate the astronomical precession cycles . From Cohen et al., 2007.

The two events are associated with repetitive short lived and catastrophic event. In the case of T-OAE these small events are recorded at the Pliensbachian-Toarcian boundary preceding the main event, and characterised with negative carbon isotope excursion, that were observed at the stage boundary in the SW European section at Peniche, Portugal in $\delta^{13}\text{C}_{\text{carbonate}}$, $\delta^{13}\text{C}_{\text{wood}}$ and $\delta^{13}\text{C}_{\text{brachiopod}}$ (Hesselbo et al., 2007). The environmental change at the Pliensbachian-Toarcian boundary shares some characteristics with the T-OAE including a major drop of platform-derived carbonate accumulation, reduction in size of the pelagic carbonate producer *Schizosphaerella*, and major rise in bottom seawater temperatures as evidenced by brachiopod $\delta^{18}\text{O}$ values in Lusitanian Basin (Suan et al., 2008). This and its

widespread nature is suggested by a contemporaneous excursion of about -1.5‰ close to the Pliensbachian-Toarcian boundary recorded in belemnite and bulk carbonate in England (McArthur et al., 2000; van de Schootbrugge et al., 2005; Suan et al., 2008).

In the PETM case the repetitive short lived carbon excursions are documented following the Paleocene-Eocene thermal maximum (PETM) event, where the main PETM event is linked to four brief events recorded in marl-rich horizons characterised by low $\delta^{13}\text{C}$ and elevated sedimentation rates. The characteristics of these small events are believed to constrain explanations for the PETM as a dynamic source must have repeatedly injected large quantities of ^{13}C -depleted carbon into the ocean or atmosphere (Nicolo et al., 2007).

1.3.1 Causes and mechanisms for the Toarcian Carbon Isotopic Excursions

Across Europe, the Lower Toarcian negative carbon isotopic excursion is expressed in bulk organic matter including jet wood, organic biomarkers and in bulk nanofossil carbonate (Kuspert, 1982; Schouten et al., 2000; Hesselbo et al., 2001). Records of the Toarcian CIE based on $\delta^{13}\text{C}_{(\text{org})}$ and $\delta^{13}\text{C}_{(\text{carb})}$ analyses from a number of sections across Europe show remarkably similar patterns. All records show an overall CIE of c. -6‰ (Jenkyns et al., 2001). At Dotterhausen Quarry (Southern Germany) for instance, the $\delta^{13}\text{C}_{(\text{org})}$ and $\delta^{13}\text{C}_{(\text{carb})}$ records a decrease in the carbon isotope value of -6‰ (Rohl et al., 2001). Similarly, at the Mochras Farm borehole (Wales, UK), records of both $\delta^{13}\text{C}_{(\text{org})}$ and $\delta^{13}\text{C}_{(\text{carb})}$ show a CIE of -6‰ (Jenkyns et al., 2001). Samples from the Belluno Trough, Italy, also show a CIE of -6‰ in $\delta^{13}\text{C}_{(\text{org})}$ and -4‰ in $\delta^{13}\text{C}_{(\text{carb})}$ (Jenkyns et al., 2001). However, the causes of the carbon isotope perturbation and synchronicity in its record remain controversial. Two explanations have been given for the cause of the negative C isotope excursion, which are discussed below.

1.3.1.2 Locally driven mechanisms

The negative C isotope excursion has been attributed to the recycling of re-mineralized light carbon from the lower levels of an intermittently stratified water column into the euphotic zone and its subsequent incorporation into photosynthetic phytoplankton (Kuspert, 1982). This suggestion was made by way of comparison with the present-day Black Sea. Profiles of $\delta^{13}\text{C}_{(\text{be})}$ through the Lower Toarcian OAE in Germany and the UK presented by Van de Schootbrugge et al. (2005) supported a local driver mechanism for the CIE, whereby their data shows that the values of $\delta^{13}\text{C}$ in belemnite carbonate were actually

increase by 1.5 ‰, with no record of a negative C isotope excursion. However, the Kuspert (1982) model fails to explain more recent observations which include contemporaneous CIEs in the terrestrial and atmospheric carbon reservoirs, changes in marine and terrestrial biota, and the widespread geographical extent of the Toarcian OAE.

1.3.1.1 Globally driven mechanisms.

The methane hydrate dissociation hypothesis

More recently it has been suggested by Hesselbo et al (2000) that the negative C isotope excursion resulted from the rapid release to the ocean and atmosphere of (biogenic) methane from methane hydrate in sediments. This arises because biogenic methane is depleted in ^{13}C by ~ 60 ‰, and thus its oxidation to CO_2 in the oceans and atmosphere imparts a light carbon signal on dissolved inorganic carbon (DIC).

Although large-scale methane hydrate dissociation can explain many of the features of the Toarcian CIE as well as many of the contemporaneous environmental effects (Hesselbo et al., 2007; Cohen et al., 2004; Kemp et al., 2005), the mass of methane hydrate required to produce a global CIE does not match the mass of CO_2 required to produce the temperature increases as inferred from Mg/Ca determinations (Schmidt & Shindell 2003; Zachos et al., 2003; Higgins & Schrag 2006). A much larger mass of CO_2 (involving approximately $c.4 \times 10^3$ Gt of carbon) would have been required to produce the postulated increase in tropical sea surface temperatures.

However, it is unreasonable to reject a role for methane hydrate dissociation in the past based on the possibility that an insufficient mass was available, due to considerable uncertainty surrounding estimates for today's methane hydrate reserves, plus the fact that areas of continental shelf and epicontinental seas were substantially greater in the past (Cohen et al., 2007). Moreover, the recognition that the $\delta^{13}\text{C}_{(\text{org})}$ shifts were paced by astronomical precession (Kemp et al., 2005) provides strong support for the suggestion that a precessional trigger may have been responsible for the release of the isotopically light carbon.

Thermogenic methane release

Another hypothesis recently put forward for the cause of the T-OAE is that ^{12}C -enriched thermogenic gas (mainly methane) was released into the ocean-atmosphere system due to an igneous intrusion into coaly organic matter-rich facies in the Karro Basin, South

Africa (McElwain et al., 2005; Svensen et al., 2007). High-precision radiometric dating has established that the emplacement of the Karoo-Ferrar igneous provinces overlapped in time the Toarcian CIEs (Palfy & Smith 2000). A major issue with this mechanism is whether methane production would have been of the magnitude and rapidity required to produce the observed global CIEs and associated environmental effects (Kemp et al., 2005; Bowen et al., 2006). Gröcke et al. (2009) studied the contacts between the intrusions and organic matter facies in the Karoo Basin and indicated that the geochemical patterns within these facies suggest little or no thermogenic methane generation, which makes the thermogenic methane hypothesis questionable.

Widespread burning of terrestrial biomass

Kurtz et al. (2003) suggested that the subsequent burning and oxidation of a large proportion of terrestrial organic carbon (which is isotopically light) could have caused the CIE of the Palaeocene-Eocene thermal maximum (PETM) through the release of a large quantity of light carbon over short period of time (Cohen et al., 2007). This mechanism has also been suggested by Finkelstein et al. (2006) as a potential cause for the generation of the CIE during the Toarcian. However, Higgins & Schrag (2006) argued that insufficient biomass would have been available to produce the CIE at the PETM through burning, and that the time scales of the abrupt decreases in $\delta^{13}\text{C}$ were too short to have been compatible with this mechanism.

1.4 Aims and Objectives

This project aims to study the black shale cycles, reflecting variable redox conditions through the Lower Toarcian (Grey Shale and Jet Rock Members of the Whitby Mudstone Formation) in Cleveland Basin. In discussing Early Toarcian events recorded in the Cleveland Basin, the focus of others has been largely on the 3 m interval in the lower exaratum Subzone where TOC concentrations are highest (the putative T-OAE in the strict sense), or the 7 m of the exaratum Subzone itself (the putative T-OAE in the wider sense). Despite the extensive previous work on the T-OAE, few studies have explored the well-preserved sediments below the event that document different phases finally leading to large-scale (global) anoxia, which is the focus of this project. High-resolution multi-proxy geochemical approach (organic and inorganic) is undertaken in order to better understand the biogeochemical processes, which occurred during this event by investigating the following:

- To identify variability in organic matter composition within a small interval of the Sulphur Band at the base of the Grey Shale Member and compare with the Jet Rock shale (T-OAE interval).
- The sudden change in the nature of the depositional environment that produced the laminated Sulphur Bands at the base of the transgressive systems tract, and how the nature and geochemistry of the organic matter varies relative to that of the bituminous facies higher up the section. How the palaeo-oxygenation condition influences the quality of the organic matter within the Sulphur Bands (high organic carbon but relatively low hydrogen index).
- Understanding the trigger mechanisms that produced the laminated Sulphur Bands and to investigate whether it can be linked to the same long-lasting process that generated the T-OAE.
- To determine whether data generated by FT-NIRS can be used to estimate bulk geochemical contents of ancient sediments, such that the technique can be used to either replace or complement data measured by conventional methods. Successful application would mean that future studies on marine rocks could benefit from time and cost savings offered by FT-NIRS in comparison to other, more complex geochemical analyses.

CHAPTER 2 – TRACKING OCEANIC REDOX CONDITIONS

2.1 Overview

An increasing number of studies are devoted to the nature of organic rich mudstones and assessing the changing redox conditions in the geological record (Tyson and Pearson, 1991; Calvert et al., 1992). Oxygen deficiency has been a major driver of evolution and extinction throughout Earth history (e.g. Little and Benton, 1995; Little 1996; Wignall et al., 2005; Wignall and Bond 2008; Caswell et al., 2008). In addition, the concentrations of dissolved oxygen and other oxidants such as Mn and Fe oxides, in addition to hydrogen sulphide in the bottom waters and the uppermost part of the sediments have a great influence on the degree of preservation of organic matter (Calvert et al., 1992). Therefore, understanding past changes in redox conditions is crucial to understand the biogeochemistry of palaeo-environments.

Studies of redox conditions in marine environments trace the relative distributions of oxidizing and reducing agents through depositional and diagenetic gradients, and the biogeochemical processes that control those distributions. In more detail, the palaeo-redox conditions can be defined following the redox gradation: oxic–suboxic–anoxic–euxinic (Table 2.1).

Table 2. 1: Redox classification of depositional environments, after Tyson and Pearson (1991); the values for O₂ concentrations in bottom waters are valid for present-day ocean. Fe_{py}= pyrite iron, Fe_{HR}= highly reactive iron (Poulton & Canfield, 2011)

Redox classes	Oxic	Suboxic	Anoxic	Euxinic	Ferruginous
			No free H ₂ S in the water column	Free H ₂ S present in the water column	Fe _{py} /Fe _{HR} <0.7
O ₂ concentration in bottom waters (ml O ₂ /l H ₂ O)	(O ₂) > 2	2 > (O ₂) > 0.2	(O ₂) < 0.2	(O ₂) = 0	(O ₂) = 0
	An active calcareous benthic fauna	Weak benthic activity and formation of laminated sediments	Absence of benthic activity	Absence of benthic activity	Absence of benthic activity

Anoxic conditions may be non-sulphidic or sulphidic (sulphidic conditions also being referred to as euxinic). Euxinic water conditions develop when free H₂S occurs within the water column. In the modern world, euxinic conditions in the water column are usually restricted to semi-enclosed basins like the Black Sea (Meyer & Kump, 2008). The H₂S is produced by sulphate-reducing bacteria. In some cases, as in the Black Sea, euxinic conditions may reach the photic zone, where photosynthetic sulfide-oxidizing bacteria may develop (Koopmans et al. 1996a). However, the redox state of the ocean can vary widely (both temporally and spatially), from various levels of oxygen depletion, through anoxic and non-sulphidic (ferruginous) conditions, to fully euxinic. Anoxic, iron-rich (ferruginous) oceanic conditions are recognised recently as a dominant feature of anoxic oceanic intervals throughout much of Earth's history (Poulton and Canfield, 2011). Ferruginous conditions describe the intermediate state between the oxic and euxinic end-members, that the environmental behaviour of iron takes central stage.

Suboxic settings are characterized by extremely low but generally non-zero oxygen concentrations in the water column, where H₂S is limited to interstitial waters below the sediment–water interface. Transitional settings can occur wherein the first appearance of H₂S coincides with the sediment water interface.

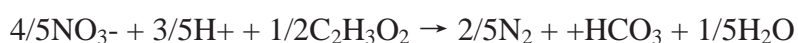
Under oxic conditions, aerobic organisms utilise dissolved O₂ from the overlying and interstitial waters for their metabolism. As dissolved oxygen becomes depleted, organic matter decomposition continues via micro-organisms using secondary oxidant sources (e.g. nitrate, iron hydroxides, manganese oxides and sulphate). Ultimately, when all free oxidants are exhausted, methanogenesis takes place (Froelich et al., 1979).

This classical early diagenetic sequence is illustrated in Figure 2.1, with the following equations representing the principle respirator pathways of organic matter mineralization:

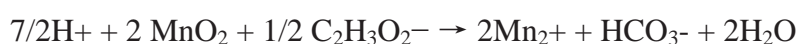
1- Oxic respiration



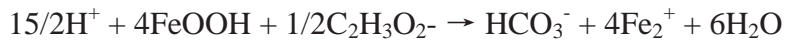
2- Denitrification



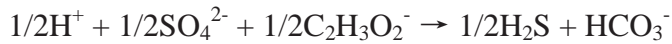
3- Dissimilatory Mn reduction



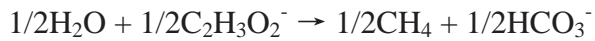
4- Dissimilatory Fe reduction



5- Sulfate reduction



6- Methanogenesis



The remineralization processes in each of these zones is dependent upon the reactivity and concentration of organic matter (Berner, 1980), and the concentration of the requisite terminal electron acceptor (e.g., O_2 , NO_3^- , SO_4^{2-}). In addition, a variety of environmental factors (e.g., temperature, accumulation of toxic substances) affect metabolism, and therefore can play a role in controlling organic matter decomposition (Wang and Chapman, 1999).

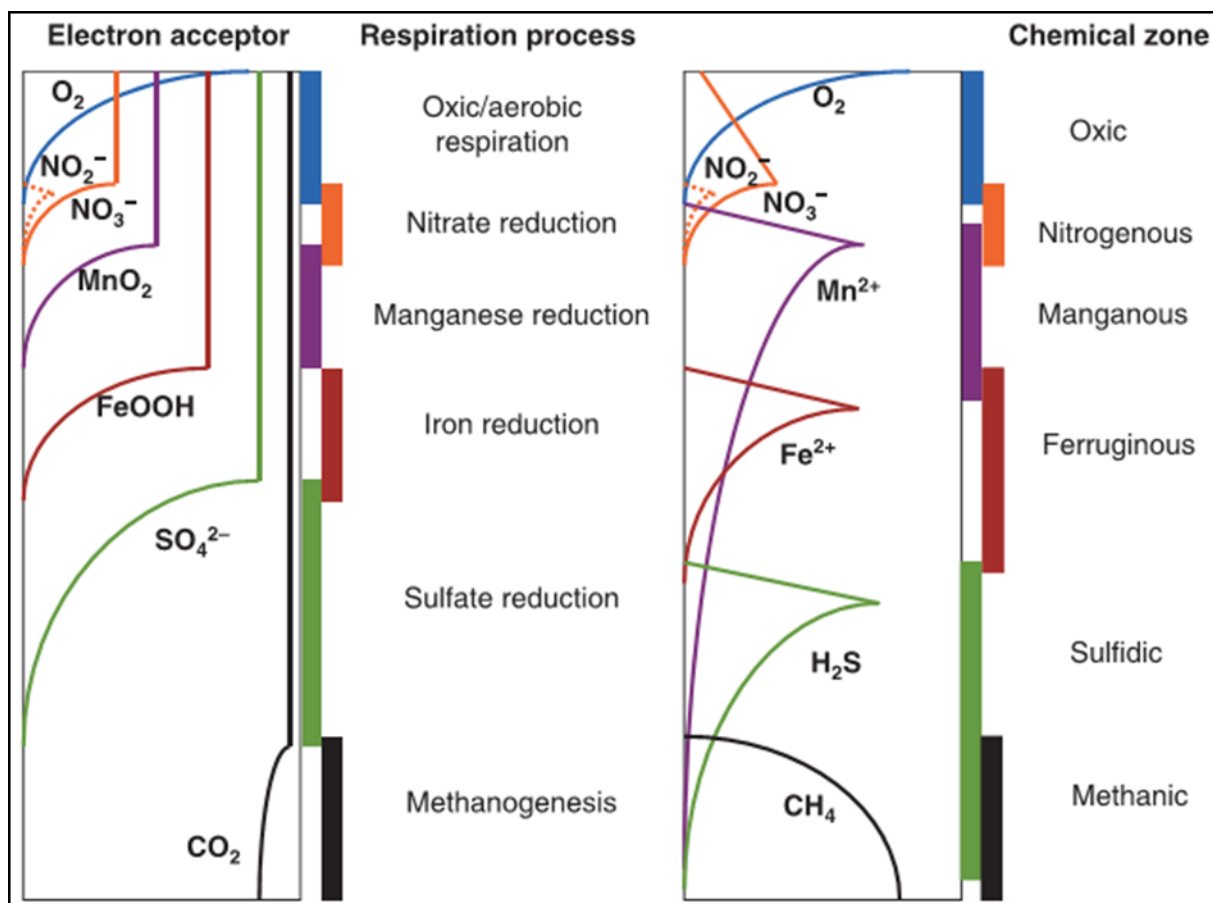


Figure 2. 1: depth distribution of common electron acceptors, chemical zonation which accompanies respiration processes in the environment, and the names used to represent the zones where different electron acceptors are used (after Canfield & Thamdrup, 2009).

Oxygen-limited conditions and ultimately anoxia may develop when the oxygen demand exceeds the supply. In the water column, anoxia may develop in stagnant or confined water masses where insufficient circulation prevents O₂ renewal, or in places where intense OM degradation consumes O₂ faster than it is replenished, even in open-marine conditions (Demaison and Moore, 1980; Pedersen and Calvert, 1990).

Euxinic settings comprise less than 0.5% of the deep ocean today, with the Black Sea and Cariaco Basin off the coast of Venezuela being the largest and second largest examples, respectively (see recent review by Meyer & Kump, 2008). In the geologic record, however, oxygen deficiencies and even euxinia occurred on much wider scales, as demonstrated by the so-called OAEs, intervals known most famously from the Mesozoic for abundant, widespread, organic-rich black shales deposited under anoxic to euxinic conditions.

2.2 Existing models for anoxia

Studies of modern oxygen-poor environments have shown that oxygen deficiency may be due to decreased oxygen supply or increased oxygen demand beneath areas of high productivity (Demaison and Moore, 1980; Jenkyns, 1988). Most models of palaeo-redox conditions are based upon observations of modern anoxic environments, which are currently limited in comparison to the much wider distribution of anoxic environments in other periods of geological time. The Black Sea is the largest landlocked body of permanently anoxic water in the world, covering roughly 4.4×10^5 km² (Meyer & Kump, 2008), and as such has been the focus of numerous studies (e.g. Vinogradov et al., 1962; Sweeney and Kaplan, 1980; Leventhal, 1983; Canfield et al., 1996; Wilkin and Arthur, 2001). Most of the formation of black shales in the present day occurs in two distinct settings, the upwelling zones and silled basins (Wignall, 1994).

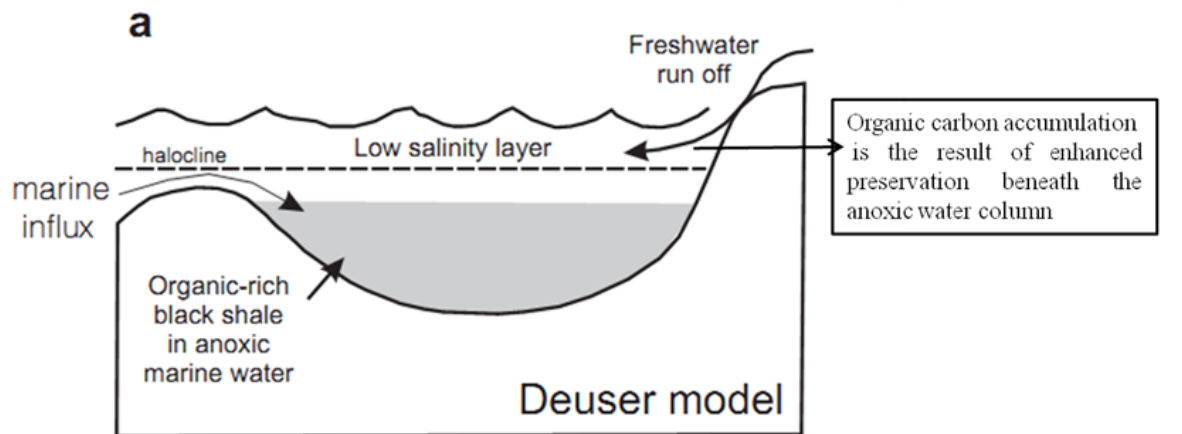
2.2.1 The silled basin model

This model uses the influx of fresh water into a basin to produce a halocline that is produced due to the different water densities. The halocline restricts oxygen rich water to lower depths in the water column. The lack of water movement and low oxygen demand due to the decaying organic matter, results in anoxia (Wignall, 1994). There are two contrasting models for the silled basin, both of which rely on the influx of marine water (Figure 2.2), and

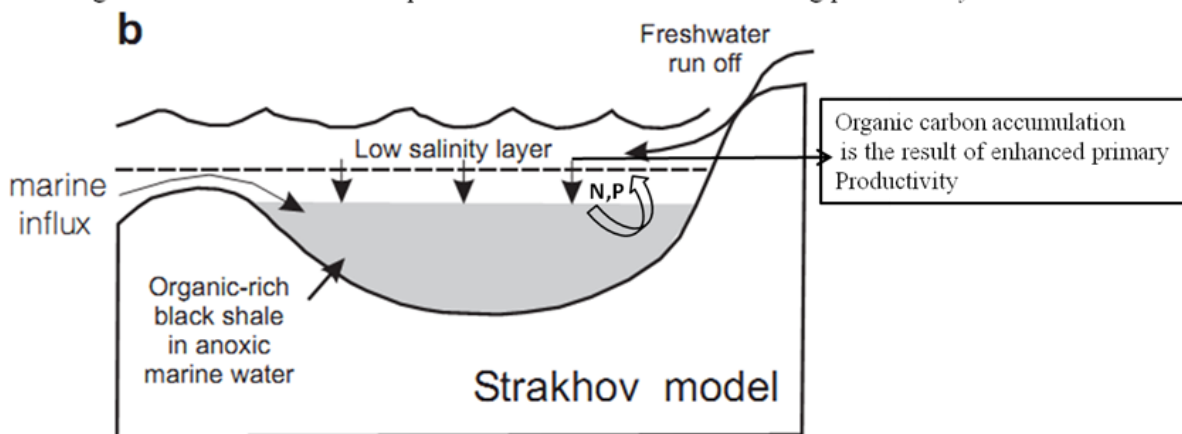
the two models are part of the productivity versus preservation argument (Armstrong et al., 2005).

In the Deuser (1974) model, marine water fills the deeper parts of the basin and gradually expands upwards. Enhanced preservation beneath the anoxic water column causes a high accumulation of organic carbon, while changes in photic zone productivity do not play an essential role in this model. Progressive restriction of the size of the oxygenated upper layer (mixolimnion) gradually prevents nutrient supply and thus leads to a decrease in productivity and hence sedimentary organic carbon production.

In contrast, the Strakhov (1971) model, invokes elevated primary productivity. During the initial stages of marine incursion, nutrients in the lower anoxic layer (monimolimnion) remain isolated from the euphotic zone by the halocline. The gradually rising monimolimnion then releases nutrients to the mixolimnion and triggers a high productivity episode, which is sustained by organic matter production in the euphotic zone. Thus, the restricted circulation characteristic in this model is important because it promotes nutrient trapping, not because it slows circulation rates which interprets the high flux of organic matter to the sediment at a time when much of the water column was fully oxygenated.



Progressive reduction in the depth of the mixolimnion = decreasing productivity



Nutrients displaced into mixolimnion (Van Cappellen effect) by rising monimolimnion
 reduction in the depth of mixolimnion = increasing productivity

Figure 2.2: Conceptual models for the formation of basin anoxia in the silled basin setting. after Armstrong et al. (2005)

In the Black Sea case, continental runoff from Eastern Europe provides a vast amount of fresh water that enters the basin via the narrow Bosphorus Strait to the south and by large rivers directly drain to the basin. These two inputs generate strong density stratification in the Black Sea, with a deep-water residence time of ~300 years (Murray et al. 2007). Therefore, the freshwater forms a layer at the surface approximately 50m thick that restricts oxygen transfer into the deep water below. An intermediate zone (free of oxygen, dissolved Fe and H₂S), separates the oxic surface fresh water from deep sulfidic waters (>100 m depth) (Figure 2.3). Dissolved H₂S is only abundant below the layer containing dissolved Fe.

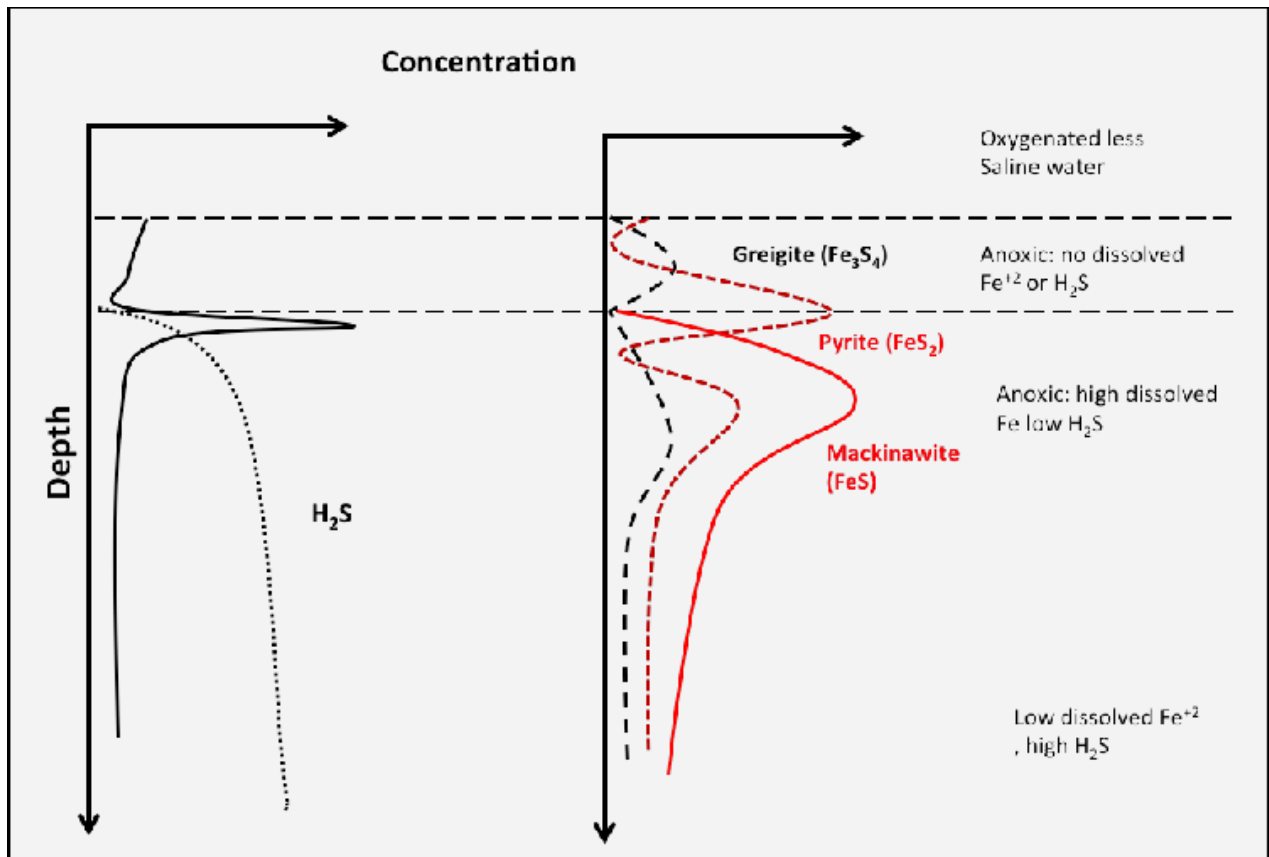


Figure 2.3: Schematic diagram of the main features of the dissolved and particulate inorganic Fe and S chemical structure of the Black Sea (after Brewer and Spencer, 1974, Cutter and Kluckhohn, 1999)

As seen in Figure 2.3, the distribution of Iron phases follows an ordered pattern. The intermediate anoxic layer contains the highest concentration of greigite (Fe_3S_4) than anywhere in the water column, and the boundary between the intermediate and Fe bearing anoxic layer is characterised by a peak in pyrite (Cutter and Kluckhohn, 1999).

The expanded suboxic zone has both low oxygen and low sulfide concentrations ($<10 \mu\text{M}$). Abiotic and microbial processes cycle nitrogen and trace metals across the chemocline. Based on Murray et al. (1989) and Murray and Izdar (1989), Canfield and Thamdrup (2009) produced depth distribution profiles of chemical zones and respiration processes deduced from the chemical data (Figure 2.4). The nitrogenous zone is restricted to the zone containing a nitrite maximum, and below this a manganous zone is designated, as here manganese begins to accumulate in the absence of other anaerobic metabolic products. The sulfidic zone is located immediately below. These respiration processes follow very closely the chemical zonations in the case of the Black Sea (Canfield & Thamdrup, 2009).

Among the chemocline microbial population there are the photosynthetic green sulfur bacteria (GSB, Chlorobiaceae) (Overmann, 2006). These anoxygenic sulfide-oxidizers can use irradiance that is just 0.0005% of the light available in surface waters (Overmann et al. 1992). Derivatives of the GSB light-harvesting carotenoid, isorenieratene, are preserved in anoxic sapropels of the Black Sea. The distribution of this molecular fossil in sediment cores from near the modern chemocline is thought to record chemocline depth oscillations over the past 8 kyr (Huang et al. 2000). Sediments accumulating at the current time in the deepest part of the Black Sea basin consist of laminated CaCO₃ rich muds (up to 80 wt%) with typically 2-5% total organic carbon (TOC) and 1-2.5 wt% pyrite (Calver and Karlin, 1991; Wilkin and Arthur, 2001).

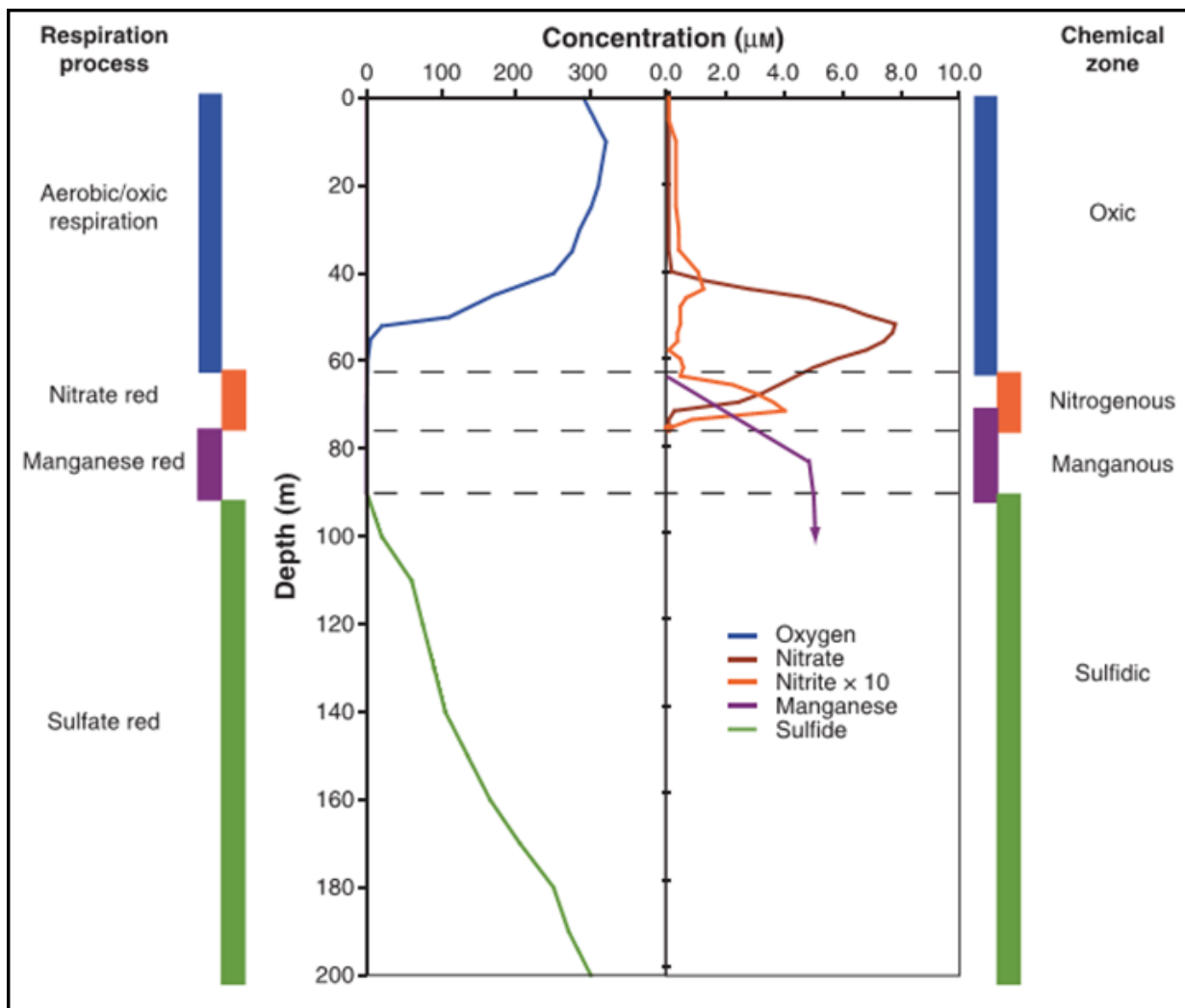


Figure 2.4: Chemical data from the Black Sea. Listed are the depth distribution of chemical zones and respiration processes deduced from the chemical data (after Canfield and Thamdrup, 2009).

2.2.2 The upwelling model

The upwelling model is where cold water from below the thermocline is moved up to compensate for the seaward movement of surface water. The water from below the thermocline is nutrient rich and, when enter the euphotic zone, high productivity stimulate or maintain in the photic zone (Demaison and Moore 1980). This high productivity allows for accumulation of organic rich shales (Armstrong *et al.*, 2005).

At the present time, anoxic and dysoxic conditions are restricted to the coastal upwelling zones at the intersection of intensified oxygen minimum zones (OMZ) and the upper slope or continental shelf break, in water depths typically >50m (e.g., the Peru Current) (Wignall, 1994). Organic rich sediment accumulation in upwelling zones is a result of elevated productivity in a region of strong circulation and high organic loading. These zones occur at water depths of about 200 to 1,000 metres, and have the potential to affect much wider areas as they develop in the open ocean, depending on local circumstances. This intensity of bio-accumulation and regeneration play an important role for trace matels accumulation, where the upwelling sediments are often enriched in Cd and P and depleted in Co and Mn (Brumsack, 2006)

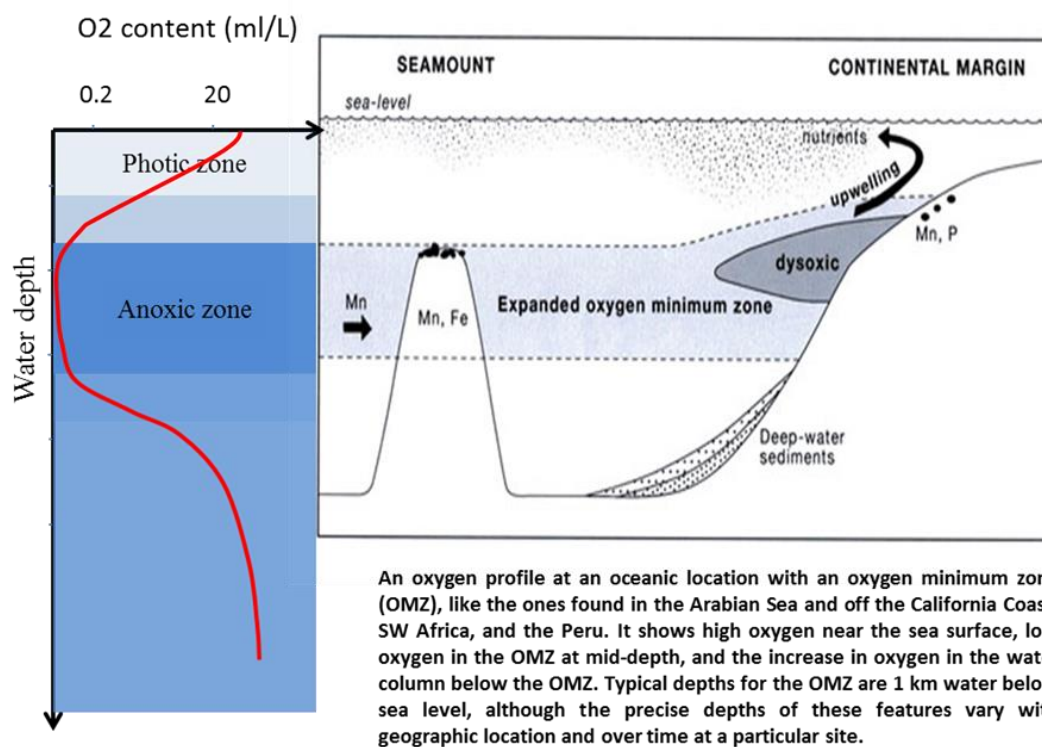


Figure 2.5: An oxygen profile at an oceanic location with an oxygen minimum zone.

One of the best studied examples is the Arabian Sea. In this case oxygen falls to below 1 mL/L between about 150 and 1500 m (Schulte et al., 1999), but no free sulphide is present. Where the oxygen minimum zone overlaps the continental margin, sediments are often laminated, and higher levels of organic carbon are preserved (Weijden et al., 1999).

Geochemical proxy data, combined with microfossil analysis, indicates that the oxygen minimum zone in the Arabian Sea has varied considerably on orbital and suborbital timescales over the past 225 Ka (Reichart et al., 1998). These changes are apparently driven by surface productivity and winter mixing patterns, whilst productivity is in turn regulated by freshwater input during the monsoon (Schulte et al., 1999). Oxygen minimum layers can be enhanced by upwelling zones at continental margins, where nutrient rich deep waters are brought to the surface by wind action. The increased oxygen demand resulting from high productivity in surface waters can lead to severe oxygen depletion. Upwelling can, itself, cause oxygen minimum zones without any pre-existing oceanic oxygen depleted layer, as is the case on the Peru margin between 12° and 13.5°S (Arthur et al., 1998). Here, the oxygen levels are lower than 0.1 mL/L in a zone between 70 and 400m depth, and sediments accumulating in this zone are frequently laminated and comparatively organic-rich (Emeis et al., 1991).

2.3 Characteristics of euxinic environments

Euxinic settings share many physical and biogeochemical characteristics (Table 2.2). Often these euxinic settings exhibit restricted circulation, deep water and high primary productivity thrived by elevated nutrient supply. Although it is conventionally agreed that sluggish circulation is a primary reason for euxinia, the argument can be made that nutrient trapping is another fundamental characteristic that promotes euxinia in such settings (Murphy et al., 2000; Meyers, 2007). Therefore, the restricted circulation characteristic of many modern euxinic basins is important because it promotes nutrient trapping, not because it slows circulation rates. In modern euxinic setting there is a strong positive correlation between deep water PO₄ and sulphide concentration (Table 2.2; Meyer and Kump, 2008). This relationship is understandable from biogeochemical relationships as decomposition of the organic matter by sulphate reducing bacteria proceeds in deep waters, oxidants are consumed and equivalent amounts of waste product (including H₂S and organic-bound N and P) are released.

Table 2.2: Characteristics of modern euxinic basins (After Meyer and Kump, 2008)

	Black Sea	Framvaren Fjord	Mariager Fjord	Fayetteville Green Lake	Lake Cadagno	Lake Mahoney	Cariaco Basin
Surface area (km ²)	420325	4.43	–	0.258	0.261043	0.198	–
Volume (km ³)	541220	0.33	–	7.236	2.41985	–	–
Surface/volume (km ⁻¹)	0.77	13.4	–	0.04	0.11	–	–
Chemocline depth (m)	120–180	18	8–18.00	21.5	8–10 m	6.5–7 m	200 m
PO ₄ (μM) surface	–	–	3	0.41	–	–	–
PO ₄ (μM) deep	7.7	100	20	3	–	–	3.7
N/P deep	12	15	30	>100	–	–	–
H ₂ S (μM) deep	310–3600	7000–8000	<400–1100	1200	175–235	3000–4000	76
δ ¹³ C gradient	6‰	17‰	–	13.1‰	–	–	–

In silled basin settings, anoxia is favoured when riverine input of nutrients is high, and recycling of P during diagenesis is high (P burial efficiency low), and when the rate of vertical mixing within the basin is suppressed relative to the deep inflow rate (Shen et al., 2002).

Silled basins with estuarine circulation, such as the Black Sea and some fjords, are efficient nutrient traps. The estuarine flow occurs in stagnant water bodies that experience a positive water balance (where the input rates exceed that lost by evaporation) (Demaison and Moore 1980). Low salinity and nutrient-depleted surface water flows out of the basin, while salty and nutrient-rich waters enter the basin at relatively deeper depths. These nutrient-rich deep waters are mixed upward, promoting biological productivity and creating high demand on oxygen as the organic matter falls through the water column (Armstrong et al., 2005). Once estuarine circulation is absent, other factors could aid to develop sulphidic conditions. For instance, the groundwater supply to meromictic lakes is sulphur replete which in such case the sulphide source allows H₂S accumulation independent of phosphate concentration (Meyer and Kump, 2008). Moreover, sulphide flux from sediments into bottom waters could play an essential role in shallow eutrophied environments, as in the Mariager Fjord, the process of sulphate reduction during the degradation of the sedimentary organic matter produces the sulphide which then diffuses upward into the water column (Weeks et al., 2004).

2.4 An overview of palaeoredox indicators

Indices which accurately record the levels of oxygen present at the time of deposition of ancient marine sediments are important for a number of reasons. In the first place the characterisation of depositional conditions is fundamental to the study of sedimentary rocks. Accurate indices of redox can also contribute to the debate on the role of redox in the preservation of organic carbon (which is still hotly contested) and the understanding of variations in oceanic oxygen levels. The latter has implications for both the timing and nature of mass extinction events as well as providing information on interactions between global climate and the oceans.

2.4.1 Sedimentological and palaeoecological indicators of anoxia

Historically, the most commonly cited fingerprints of anoxia have been organic richness and sedimentary fabrics undisturbed by burrowing organisms (Savrda and Bottjer, 1987). However, this organic enrichment is a product of complex factors, in addition to anoxia. Sedimentation rate, levels of organic input from primary production, and mineralogical controls such as clay contents that can impact organic preservation are all factors which could control organic enrichment (Pedersen and Calvert 1990). Similarly, the preservation of lamination, often but not always reflecting seasonal patterns of deposition, may not be reliable to explore the palaeo-oxygenation conditions as brief episodes of oxygenation can be marked by high-abundance, low-diversity populations of shelly pavements within otherwise microlaminated sediments (Tyson, 2005). In other words, undisturbed sediments can reveal complex histories of more or less hospitable conditions despite a preponderance of generally laminated material (Rohl et al., 2001).

Morris (1979) produced a detailed shale classification based on field analysis using sedimentological and trace-fossil observations of Toarcian sediments from North Yorkshire. He subdivided the sequence into three facies, normal, restricted and bituminous.

Normal Shale Facies

This facies is represented by the lower beds of the Grey Shale Member, and is characterised by homogeneous, bioturbated sediment with abundant benthic body-fossils and common sideritic nodules, and was deposited in an oxygenated shallow marine environment. This facies is characterised by a mixed assemblage of infaunal and epifaunal types, the infaunal bivalves being represented by both shallow and deep burrowing types (Morris, 1979).

This facies is organic-poor (TOC 0.6 to 3 wt %) with low Hydrogen Index values ranging from 83 to 134 (mg HC/g TOC).

Restricted Facies

This facies is represented by much of the Alum Shale Formation and the upper half of Grey Shale Member. The disappearance of siderite and the abundance of calcareous concretions suggest the loss of oxic layers in the sediment with reducing conditions extending close to the sediment water interface. Reducing conditions within the sediments led to an increase in the organic carbon content of the sediments. At levels of high organic carbon content (> 3% TOC; Demaison and Morris, 1980) a decrease in the diversity of the bivalves is observed with infaunal deposit-feeding becoming increasingly abundant

Bituminous Shale Facies

The bituminous shales, also commonly named bituminous mudstones, are characterized by the abundance of wavy thin lamination. According to O'Brien (1990), the laminae are commonly less than 1 mm and have smooth, parallel contacts. The microlamination indicates quiet environmental conditions and short-term alternations in the predominance of terrigenous sediment supply and plankton productivity (Oschmann, 1991; O'Brien, 1990). This facies is limited to the Jet Rock Member. The abundance of pyritic calcareous concretions and the lack of infauna suggest that reducing conditions extended up to sediment surface or even higher into the bottom waters. The Jet Rock Member at North Yorkshire is one of the most organic rich rocks in Britain (Farrimond 1988). It represents a bituminous ("inhospitable bottom") shale facies containing high values of weight percent total organic carbon (TOC) of around 20%, which occur towards the base of the Jet Rock and decline upwards to the contact with the overlying Alum Shales (Myers and Wignall 1987).

Moreover, the Palaeoecological techniques were used to derive evidence for palaeo-oxygen levels. The oxygen restricted biofacies (ORB) scheme of Wignall and Hallam (1991) is one of the well-known indicators of Palaeo-oxygen levels of ancient sediments. This scheme uses species diversity combined with sedimentological data to define 6 zones of increasing oxygenation (figure 2.1)

ORB

	1	2	3	4	5	6
	Anaerobic		Lower		Upper	
						Dysaerobic
Nekton (free swimmers)	Present					
Nekto-Benthos (sea floor living free swimmers)	Present					
No. of Benthic Species (sea floor dwellers)			1-3 (rare)	2-4	4-8	6-12
Sediment Fabric	Fissile compacted ± lamination				Bioturbated, no lamination	

Figure 2.6: A classification scheme for black shale biofacies derived from data on the fauna and lithologies of the British Jurassic. The transition from biofacies 1-6 is interpreted to reflect an increase in both the levels of bottom water oxygenation and the longevity of oxygenation events (Wignall and Hallam, 1991)

Because organic richness and benthic ecologies can fail to point uniquely to the benthic oxygen condition at the time of deposition, researchers have turned increasingly to geochemical methods (Table 2.3).

Table 2.3: summary of most used paleoredox indicators Wignall and Hallam, 1991; Berner, 1984; Koopmans et al. 1996a; Zheng et al., 2000; Poulton and Raiswell, 2002.

Levels of oxygen	Fe _{py} /Fe _{HR}	Fe _{HR} /Fe _T	C/S	Mo (µg/g)	Isorenieratane
Oxic (0.8-1 ml/l O₂)		<~0.22	Zero S intercept TOC:TS > 5.0	Terrestrial background values	Absent
Dysoxic (0.2-1.0 ml/l O₂)				<5 ppm	Absent
Deep water anoxia; a. non-sulphidic (ferruginous) b. euxinic	a. <0.7 b. >0.7	≥0.38	Non-zero S intercept TOC:TC < 1.5	>25 ppm	Absent
Photic zone euxinia	>0.7	≥0.38	Non-zero S intercept TOC:TC < 1.5	>25 ppm	Present

2.4.2 Carbon–sulphur relationships

Several approaches for evaluating the development of anoxic bottom waters are based on C/S ratios, Fe-TOC-S relationships, and framboidal pyrite size distributions (Berner, 1984; Brumsack, 1988; Wilkin *et al.*, 1996; Raiswell and Canfield (1998); Poulton and Raiswell, 2002). These techniques are used to evaluate the role of sulfate reduction in marine environments. The development of sulfate reduction is a sign of redox and occurs only under anoxic conditions, where it is mediated by bacterial reactions utilizing dissolved sulphate and organic matter as reactants, and yielding H_2S . The output of this process (H_2S) in the presence of reactive iron can be fixed in the sediments in the form of pyrite (Berner, 1984). Cross-plots of organic carbon and sulphur (figure 2.7) are commonly assigned to palaeoredox conditions in the depositional environment (Berner, 1984; Jackson and Raiswell, 1991).

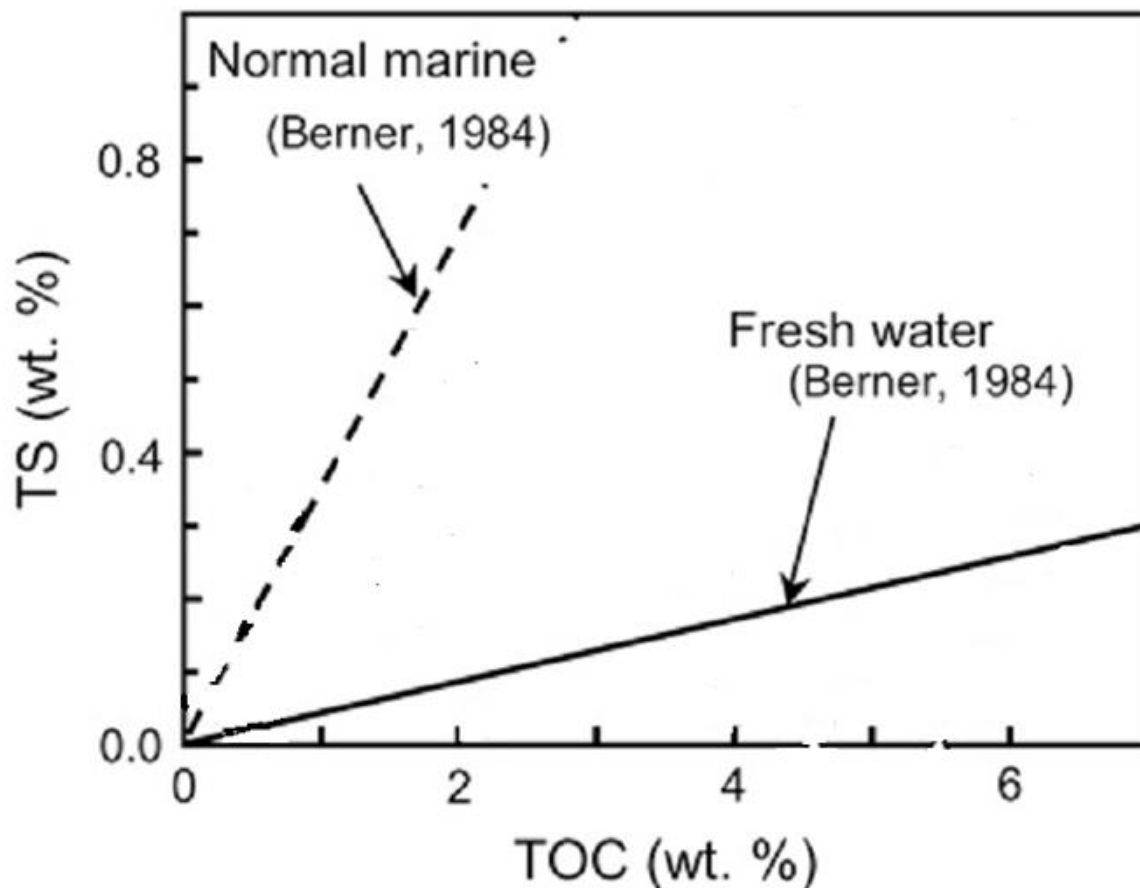


Figure 2.7: TOC and TS relationship by Berner, 1984. the dashed and solid lines are regression lines for normal marine (oxygenated bottom water) and freshwater respectively.

Sediments deposited under oxic marine conditions generally tend to display S/C ratios of less than 0.4 (Bernier and Raiswell, 1984). On the other hand, euxinic environments are either characterized by S/C ratios higher than 0.4 with positive intercepts on the S axis (Leventhal, 1983), or by a fairly constant sulfur content independent of the organic carbon content. The latter case occurs mainly in euxinic environments where sulfur fixation via pyrite formation is limited by the availability of reactive iron and, hence, pyrite formation ceases after the reactive iron reservoir is exhausted, even though sulfate reduction continues (Raiswell and Bernier, 1985). Moreover, the relationship between carbon and sulphur alters with increasing burial due to preferential carbon loss during diagenesis and thermal maturity (Jones and Manning, 1994).

The degree of pyritisation (DOP), which is defined as $DOP = (Fe_{pyrite}) / (Fe_{pyrite} + Fe_{reactive})$, eliminates the effect of variations in Fe content, and Raiswell *et al.* (1988) suggest that DOP may be used to distinguish between sediments deposited under different conditions, where values of DOP less than 0.42 indicate oxic conditions, and DOP more than 0.75 indicates anoxic conditions. Reactive iron was defined by Raiswell *et al.* (1988) as the fraction of iron that is HCl-soluble. Dean and Arthur (1989) plotted Fe, S, and TOC values in a ternary diagram, where the limiting factors for pyrite formation can be distinguished. This means that the dilution effects caused by biogenic (carbonate and opal) or siliciclastic sources are eliminated. Based on the process of pyrite formation in organic bearing sediments, a refinement of DOP has been defined, termed the Indicator of Anoxicity (IA) (Raiswell *et al.*, 2001). Here, the ratio $(FeD+FeP)/FeT$ is used, where FeD represents the iron soluble in dithionite, FeP the iron present as pyrite, and FeT represents total iron. Values of IA above 0.38 suggest anoxic conditions, while values of IA < 0.38 indicate oxic conditions (Raiswell *et al.*, 2001).

2.4.3 Framboidal pyrite distributions

Framboids are densely-packed, raspberry-like, spherical aggregates of equigranular, micron-sized crystals or microcrysts (Rickard, 1970). They are a common diagenetic feature in many shales, and are particularly abundant in strata formed under oxygen-poor depositional conditions (Raiswell and Bernier, 1985; Wilkin *et al.*, 1997; Wignall and Newton, 1998). They occur within the surface layers of sediments formed beneath oxygen-poor (dysoxic) bottom waters, where the redox boundary is located close to the sediment surface, and can occur in a range of sizes typically between 4 and 50 μm diameter (Wilkin *et al.*,

1997). As oxygen restriction intensifies the redox boundary may move above the sediment water interface into the lower water column which creates right conditions for pyrite framboids to form syngenetically (Wilkin et al., 1997).

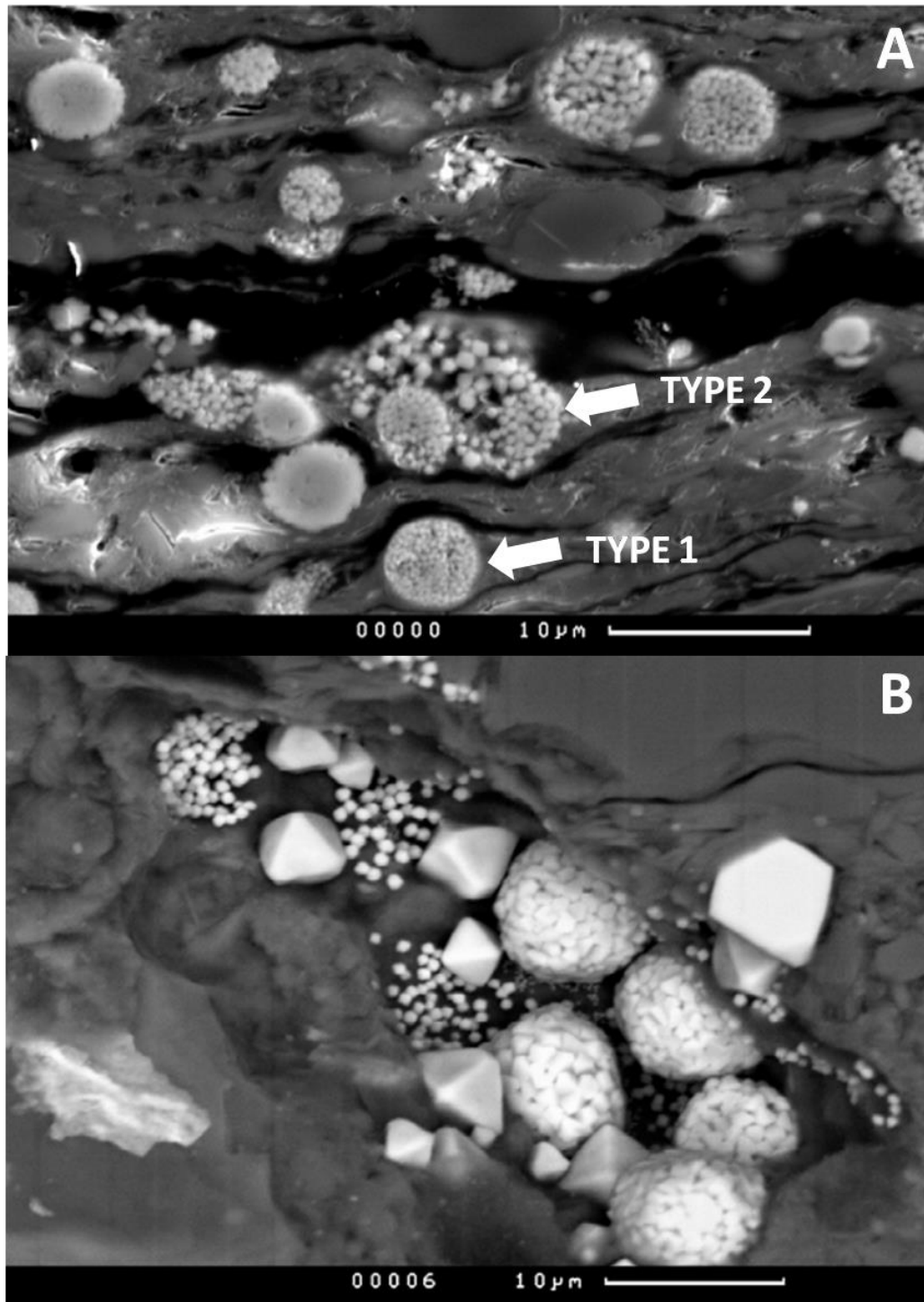


Figure 2.8: SEM images for samples from the Grey shale member at North Yorkshire (Newton, 2001). Image A (top laminated unit) showing narrow range of framboid size distribution dominated with type 1 framboids, and just one type 2 framboid appears at the centre. Image B (bioturbated mudstone) showing a mixed cluster of framboids and euhedral crystals.

A clear distinction was noted between syngenetic pyrite (pyrite formed in the water column) and diagenetic pyrite (formed within the sediment), where there are distinct differences between the average diameters and the degree of size variability of framboidal pyrites, depending on the oxygenation state of the environment of formation. In euxinic environments, framboid nucleation and growth occurs within an anoxic water column, and because of hydrodynamic effects, growth times are generally shorter than when framboid nucleation and growth occur within anoxic sediment pore waters underlying oxic water columns. As a result, syngenetic framboid populations formed in euxinic environments are characteristically small (5.0 +/- 1.7 µm) and have a narrow size distribution (Wilkin et al., 1997), while those framboid crystals formed in oxic or dysoxic are characteristically larger and have wider size range distribution (7.7 +/- 4.1µm) (Wilkin *et al.*, 1996; Wignall et al., 2005).

2.4.4 Iron geochemistry

The iron-based paleoredox proxies are an important inorganic indicators of redox conditions in ancient sediments ((Raiswell and Berner, 1987; Raiswell et al., 1994; Suits and Wilkin, 1998; Wilkin et al., 1997; Poulton and Raiswell, 2002). Its application has sharply increased in recent years as researchers have unlocked their underlying mechanisms (Rickard, 1974; Berner, 1980; Canfield et al., 1992; Yao and Millero, 1996; Poulton, 2003; Poulton et al., 2004).

Under sulphidic conditions where free hydrogen sulphide is available as output of sulphate reduction by sulphur reducing bacteria (equation 1), reactive iron associated with detrital sediments reacts with hydrogen sulfide and forms pyrite as in equation 2 (Berner, 1970). The initial product of this reaction is not, in fact, pyrite but rather a series of metastable iron monosulfides which during early, diagenesis readily transform to pyrite under most conditions.



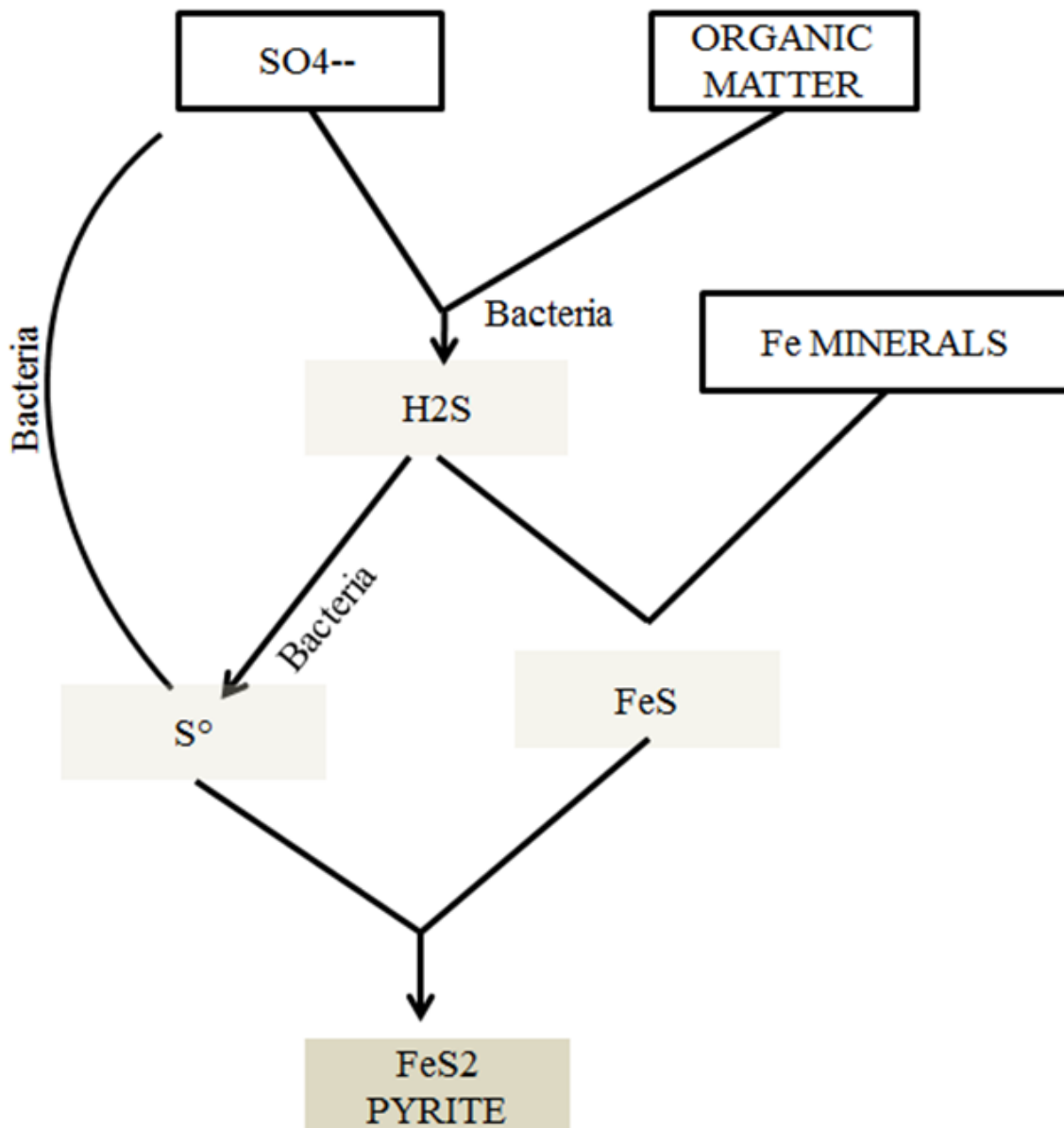


Figure 2.9: Diagrammatic representation of the overall process of sedimentary pyrite formation (after Berner et al., 1984)

This iron can limit the formation of sedimentary pyrite when abundant supplies of organic carbon and sulphate are available. Berner (1970) proposed that one minute extraction with boiling, concentrated hydrochloric acid can approximate the amount of iron remaining in sediment that is reactive to hydrogen sulphide on early diagenetic time scales, and argued that the method efficiently extracts those phases most readily reactive to H₂S (e.g., iron (oxyhydr) oxides). Berner then expanded this concept by introducing the degree of pyritization (DOP) parameter, defined as pyrite-Fe/(pyrite-Fe + HCl-extractable Fe). From this definition, it follows that sediments with ample remaining supplies of reactive iron

would have low DOP values, and degrees of pyritization for those with limited iron availability should approach one. Raiswell et al (1988) calibrated the DOP parameter using ancient shales with independent paleoecological indications, and showed that <0.42 DOP points to oxic facies, $0.46 < \text{DOP} < 0.80$ suggests dysoxic facies, while $0.55 < \text{DOP} < 0.93$ corresponds to euxinic facies, with the possibility of some overlapping. They argued that pyrite forms in euxinic environments with higher DOP due to long exposure to high levels of H_2S , resulting in sulfidation of the less reactive iron minerals. Canfield et al. (1992) found that in some settings DOP is intermediate (~ 0.4) despite exposure to pore water sulphide concentrations of up to 6 mM on time scales of 10^3 years. Therefore high DOP values that characterize the euxinic sediments must stem from another factors rather than the duration of exposure to high concentration of dissolved sulphide.

In fact, Canfield (1989) recognised that the Fe extracted during the DOP procedure did not accurately reflect the Fe reacting in marine systems. The challenge was a precise definition and efficient quantification of the reactive iron portion, particularly given that in many types of sediment only a portion of the total reactive iron pool is converted to iron sulfide. The most highly reactive iron phases in sediments, dominantly oxides and oxyhydroxides, are reactive toward H_2S on time scales of only days to weeks or less (Canfield et al., 1992; Poulton et al., 2004a).

2.4.4.1 Determining highly reactive iron content (Fe_{HR})

A buffered citrate-dithionite technique was used by Raiswell and Canfield (1996) to avoid including the poorly reactive Fe that can be leached from recalcitrant phases under the boiling HCl treatment, the approach earlier used to define reactive iron for DOP (Berner, 1970). Therefore, the highly reactive iron (Fe_{HR}) was originally redefined as the sum of pyrite Fe, iron present as acid volatile sulfide (AVS), and residual, unsulfidized dithionite-extractable Fe (representing Fe oxides, but not including magnetite; Raiswell and Canfield, 1996; 1998; Raiswell et al., 2001; Poulton and Raiswell, 2002).

However, Poulton and Canfield (2005) then refined the analytical characterization of reactive iron by introducing a new sequential extraction technique for iron, based on a refinement of existing redox proxies centred on the mineralogy and biogeochemical behaviour of iron. This technique allows full evaluation of the iron minerals that are considered to be highly reactive (Fe_{HR}) towards biological and abiological reduction under anoxic conditions. The Fe_{HR} includes four different pools of iron;

- 1) Iron associated with carbonate minerals (Fe_{carb} ; siderite FeCO_3 , ankerite $\text{Ca}(\text{Fe}, \text{Mg}, \text{Mn})(\text{CO}_3)$)
- 2) Ferric (oxyhydr)oxide minerals (Fe_{ox} ; ferrihydrite $\text{Fe}_2\text{O}_3 \cdot 0.5\text{H}_2\text{O}$, lepidocrocite $\gamma\text{-FeOOH}$, goethite $\alpha\text{-FeOOH}$, hematite Fe_2O_3 , $\alpha\text{-Fe}_2\text{O}_3$)
- 3) Magnetite (Fe_{mag}) iron(II,III) oxide (Fe_3O_4)
- 4) Fe pyrite (Fe_{py}) iron disulfide (FeS_2)

Thus, in contrast to the older technique for defining Fe_{HR} (Raiswell et al., 1994), the new scheme includes carbonate Fe and magnetite, which also react rapidly with dissolved sulphide (Poulton et al., 2004; Poulton and Canfield, 2011). The sum of these pools therefore gives the total concentration of highly reactive Fe ($\text{Fe}_{\text{HR}} = \text{Fe}_{\text{carb}} + \text{Fe}_{\text{ox}} + \text{Fe}_{\text{mag}} + \text{Fe}_{\text{py}}$).

2.4.4.2 Iron recycling, enrichment, and the shelf-to-basin iron shuttle

Canfield et al. (1996) provided the first detailed insight into how high concentrations of pyrite are produced under euxinic water column conditions. The very high enrichments of highly reactive iron (defined as Fe (oxyhydr) oxides plus pyrite) in the deep part of the Black Sea occur due to the scavenging of dissolved iron in the water column during syngenetic pyrite formation under euxinic conditions (Canfield et al., 1996; Raiswell and Canfield, 1998). By contrast, in oxic to suboxic bottom water conditions, such iron enrichment cannot occur, and this enrichment forms the basis for all Fe redox indicators (also explaining how the DOP parameter works).

The remobilization of Fe in shelf settings and its transfer to the deep part of the basin increases the ratio of highly reactive portion relative to the total Fe ($\text{Fe}_{\text{HR}}/\text{Fe}_{\text{T}}$) and the total Fe to Al ($\text{Fe}_{\text{T}}/\text{Al}$) in basinal sediments (Lyons and Severmann 2006). This and other mechanisms (including enhanced hydrothermal inputs) can enhance highly reactive iron contents of sediments. Thus, elevated $\text{Fe}_{\text{HR}}/\text{Fe}_{\text{T}}$ may be considered a characteristic indicator of anoxic conditions.

More recent work has explored in detail how the enrichments in Fe_{HR} are generated under anoxic conditions. This relates to how reactive iron is distributed and transported within sedimentary basins. Export of reactive iron from shelf sediments (Figure 2.10) results from solubilization of iron (oxyhydr) oxides during diagenesis and release of dissolved Fe(II) into the water column (Lyons and Severmann, 2007).

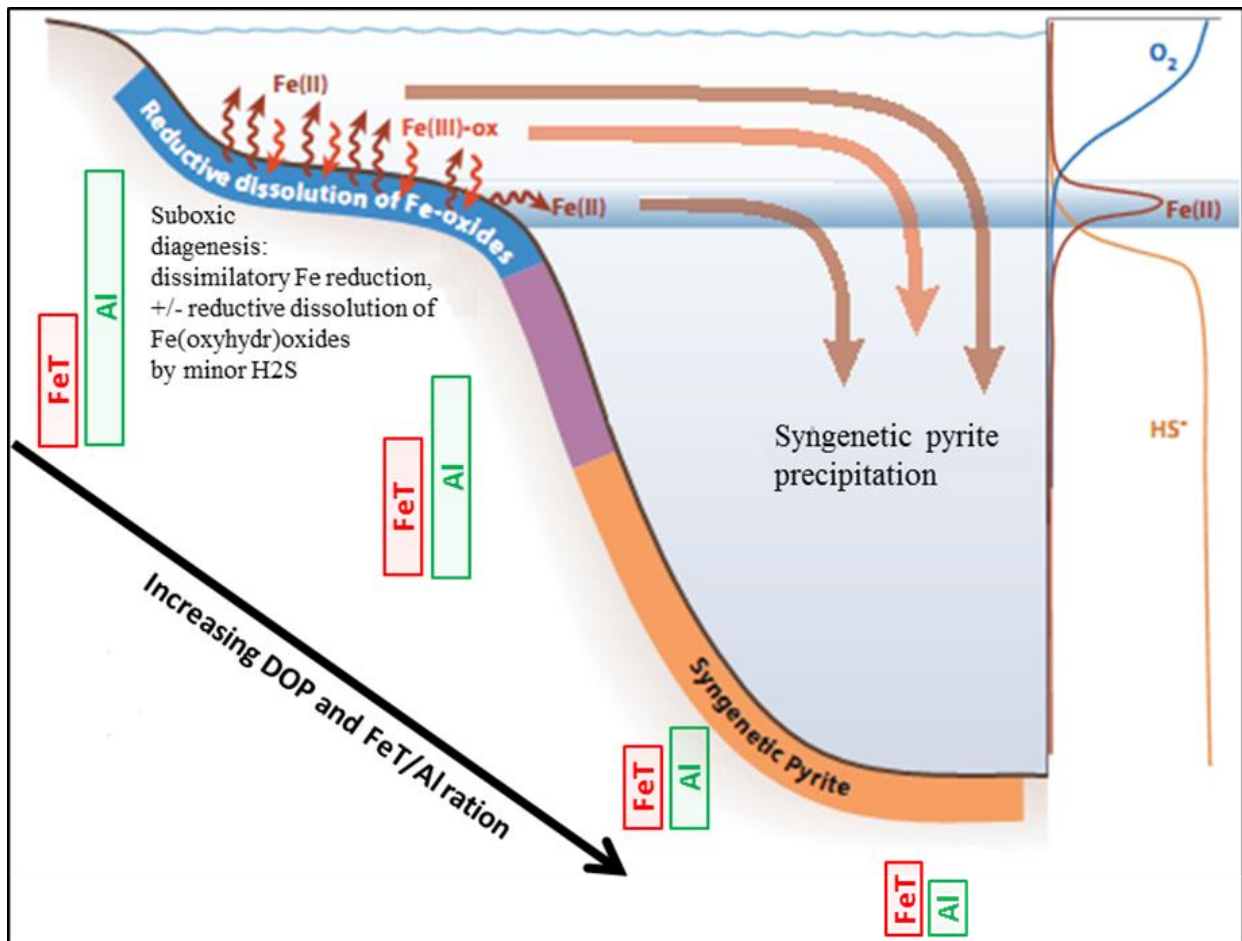


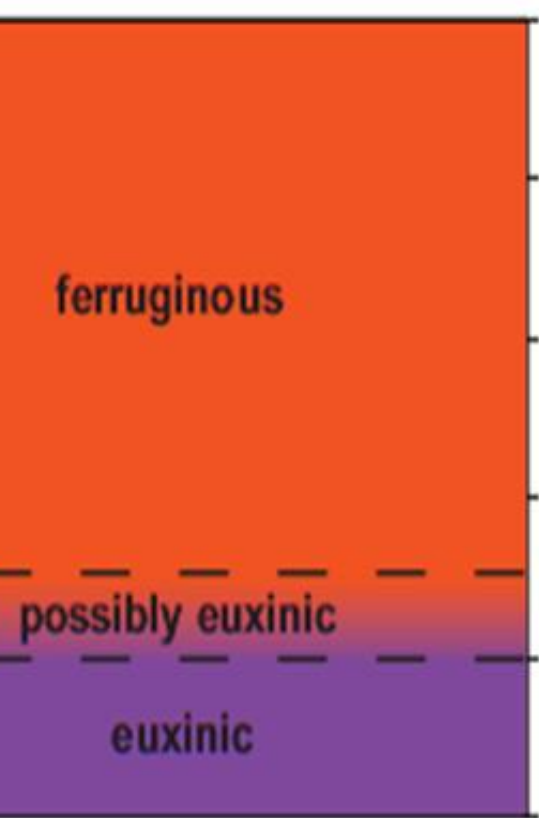
Figure 2.10: Schematic of the shelf-to-basin shuttle that results in iron enrichment in sediments deposited under euxinic conditions. Colored shading corresponds to color scheme used in Figure 4, indicating oxic deposition on the shelf, high siliciclastic accumulation (or suboxic bottom waters) on the upper slope, and euxinic deposition with low siliciclastic contribution in the deep part of the basin. After Lyons and Severmann, (2006).

At the shallow shelf area, above the chemocline, a high proportion of this Fe(II)_{aq} flux is expected to be reoxidized at the sediment water interface and redeposit again within the shelf sediments as iron (oxyhydr) oxide, where it can be recycled many times. However, a significant fraction of the benthic Fe(II)_{aq} flux appears to escape this recirculation and is transported to the deep basin, probably as Fe oxide floccs (Raiswell and Canfield, 1998; Lyons and Severmann, 2007). Shelf-to-basin reactive iron transport may thus occur through advection of either dissolved iron or fine grained particulate iron (oxyhydr) oxide (Anderson and Raiswell, 2004).

In a euxinic water column, however, the portion of iron which is transported laterally from the shelf is efficiently sequestered by iron-sulfide precipitation and thus added to the reactive pool of the basinal sediments. Euxinic iron enrichments are therefore a function of

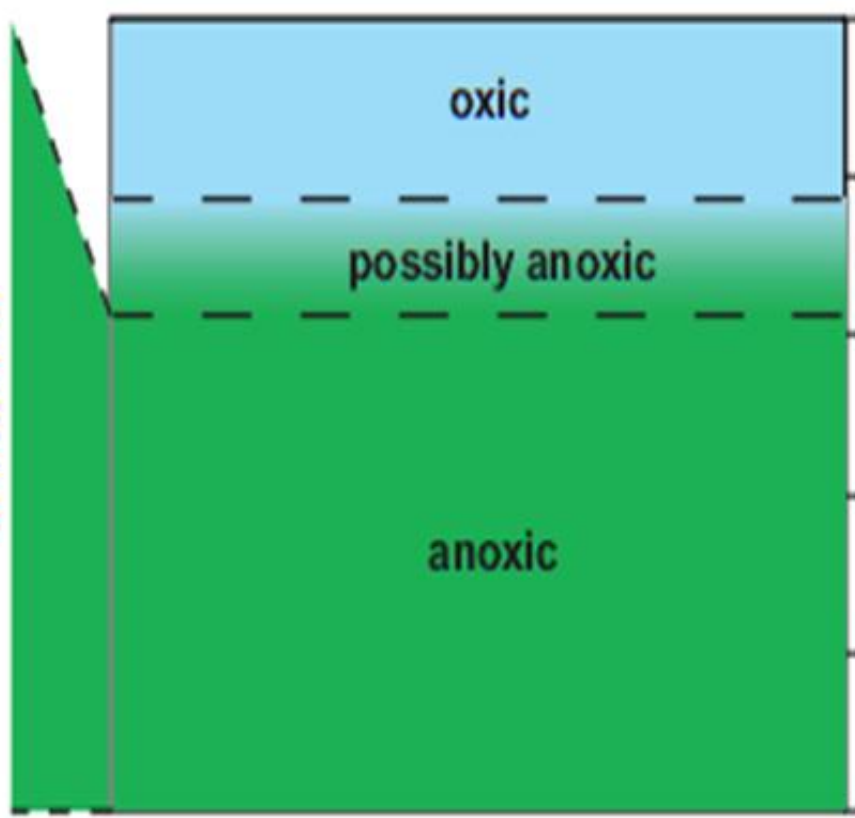
the escape efficiency of iron from benthic shelf-recycling, as well as the relative proportions of shelf area to basin area, the source to sink ratio (Raiswell and Anderson, 2005). The net escape efficiency from a continental shelf must take into account repeated cycles of benthic release (reduction) and re-deposition (oxidation) of reactive iron during its lateral advection across the shelf. Moreover, release of reactive iron from the zone where the chemocline intersects the sea floor (Figure 2.10) is an important mechanism for shelf-to-basin transport. It is also possible that the reactivity of particulate iron in the deep basin is enhanced by other mechanisms, potentially involving microbial activity or grazing by heterotrophic organism as particles settle through the sulfidic water (Lyons and Severmann, 2006).

Depth in section



$FeP/FeHR$

Depth in section



$FeHR/FeT$

Figure 2.11: Conceptualization of the iron-speciation parameters for evaluating ocean redox condition. Fe_{HR} = highly reactive iron; Fe_T = total iron; Fe_P = pyrite iron (after Poulton and Canfield, 2011).

Based on studies of modern and ancient marine sediments, it has been found that Fe_{HR}/Fe_T ratios do not exceed 0.38 in sediment deposited under oxygenated water column condition (Poulton and Raiswell 2002). On the other hand, values above this threshold are commonly indicative of deposition under anoxic conditions. Observations by Poulton and Raiswell (2002) have shown that ancient sediments deposited from an oxic ocean have average Fe_{HR}/Fe_T ratios of 0.14 ± 0.08 . This allows distinguishing anoxic condition where Fe_{HR}/Fe_T ratios ≥ 0.38 (figure 2.11) and oxic condition where Fe_{HR}/Fe_T ratios ≤ 0.22 .

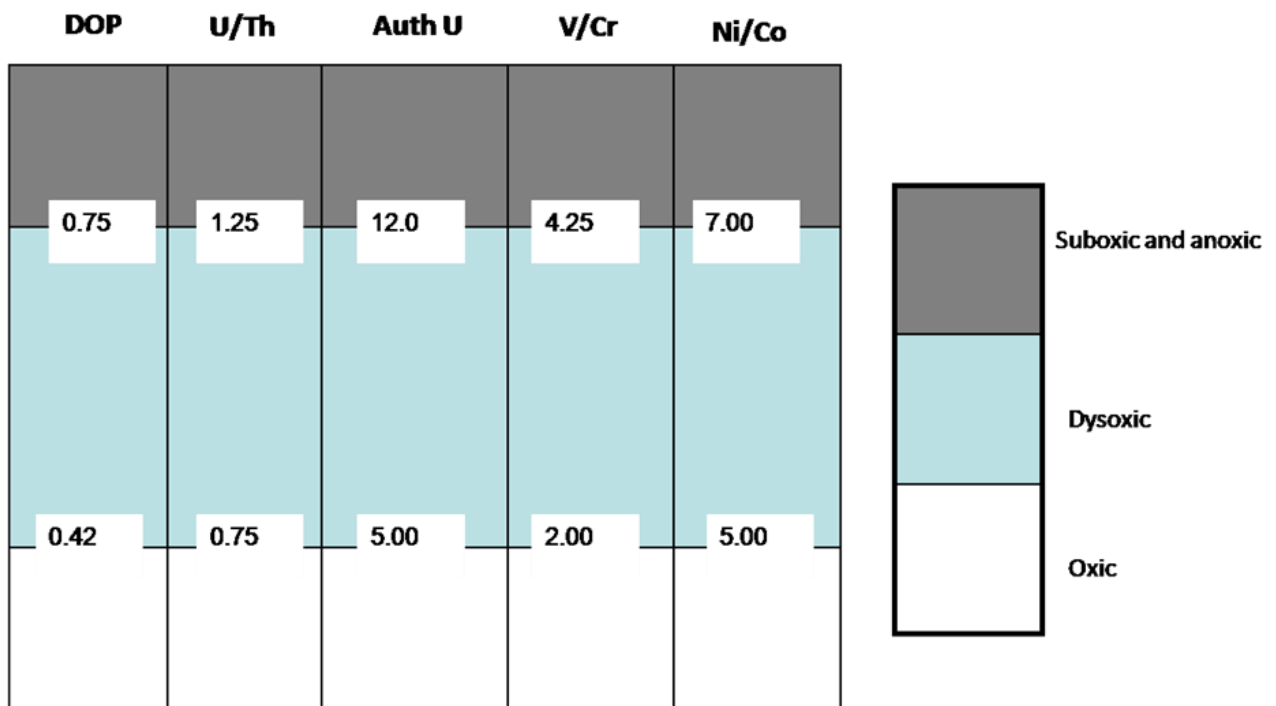


Figure 2.12: The most reliable redox trace element parameters (Ni/Co, V/Cr, U/Th and authigenic uranium) calibrated against DOP (After Jones and Manning, 1994).

Moreover, the recent iron extraction scheme enables distinguishing ferruginous conditions from euxinic condition. Observations on the extent of highly reactive iron pyritization in Black Sea sediments suggest that $Fe_{py}/Fe_{HR} = 0.8$ characterizes the upper limit for ferruginous deposition (Anderson and Raiswell 2004). This threshold could drop down to 0.7 when applying Poulton and Canfield (2005) extraction scheme which includes the Fe_{carb} and Fe_{mag} in its quantification of the highly reactive iron pool (Figure 2.11; Poulton and Canfield 2011).

2.4.5 Redox-sensitive trace metals

Redox-sensitive trace element (TE) concentrations or ratios are among the most widely used indicators of redox conditions in modern and ancient sedimentary systems (e.g., Calvert and Pedersen, 1993, Jones and Manning, 1994, Wignall, 1994). Elements providing good potential for palaeo-redox determination are those which are predicted or observed as being more insoluble in anoxic water, which can be expected to be enriched relative to detrital inputs to normal oxic sediments. Algeo and Maynard (2004) describe strong enrichments in Mo, U, V, and Zn from sediments deposited under euxinic bottom waters. Brumsack (2006) extends this list to include Cd, Cu, Tl, Ni, and Sb. These metals all have in common the tendency to form insoluble phases under anoxic sulfidic conditions.

2.4.5.1 Trace metal sources and fixation mechanisms

Under anoxic conditions, the flux and transfer rates of certain trace metals (TM) are high, and can result in significant drawdown of TM in seawater. Chemostratigraphic variations are a result of efficient organo-metallic complexation or precipitation of authigenic mineral phases (Morford and Emerson, 1999).

Suitable fixation mechanisms form an important prerequisite for any trace metal enrichment in organic rich sediments. The exposure time versus molecular oxygen seems to be an important factor determining the transfer of trace metals from the bio-cycle towards the sedimentary pool (Brumsack, 2006). Next to oxygen availability, the presence of hydrogen sulphide is an important factor (Vernadsky et al., 1998). Following the catabolic pathway of organic matter degradation, bacterial sulfate reduction and the associated presence of H₂S close to the sediment water interface or even higher up in the water column forms an important factor for trace metal fixation, as many trace metals are immobilized as sulphides (Zheng et al., 2000). The source and mediation of trace metals are difficult to differentiate due to the interrelated mechanisms through which trace metals are concentrated in fine grained sediments. Thus geochemical investigations of organic-rich sediments also require an understanding of major element (ME) distribution, which are not affected by biological or diagenetic processes and stable during thermal diagenesis. Brumsack (2006) used Al for quantifying the terrigenous-detrital fraction in near shore environments. Any deviation from average shale composition (either enrichment or depletion) can be seen in element/Al-ratios. Brumsack (2006) calculated the enrichment factor (EF) using average shale to represent

terrigenous detrital background concentrations. Any relative enrichment is then expressed by an $EF > 1$, whereas depleted elements have an $EF < 1$.

2.4.5.1 Mo geochemistry

Mo is a particularly useful redox proxy, and along with many other redox-sensitive metals, Mo enrichment occurs in sediments overlain by euxinic waters, since it is strongly affected and reduced in the presence of free hydrogen sulphide (H_2S) (Crusius *et al.*, 1996). The enrichment of Mo occurs in sediments deposited in settings with significant free hydrogen sulfide (H_2S). Beyond a threshold concentration of $\sim 11 \mu M$, direct Mo-sulfide precipitation or the switching of Mo behavior from the conservative molybdate anion (MoO_4^{2-}) to particle reactive oxythiomolybdate ions ($MoO_xS_{4-x}^{2-}$) occurs (Helz *et al.*, 1996; Erickson and Helz, 2000). Mo is then sequestered by sulphide minerals or organic matter, and as concentrations of H_2S get higher ($\sim 100 \mu M$), near quantitative removal of dissolved Mo can occur from the water column (Zheng *et al.*, 2000; Barling *et al.*, 2001; Nägler *et al.*, 2005; Neubert *et al.*, 2008). However, Helz *et al.* (2011) have suggested that the near-quantitative removal of dissolved Mo observed in some modern euxinic basins is actually due to a fortuitous combination of pH and H_2S concentration, raising doubt as to whether complete drawdown of Mo would necessarily be expected under euxinic conditions. Nevertheless, high and variable Mo concentrations are often diagnostic of deposition under euxinic conditions (figure 2.13).

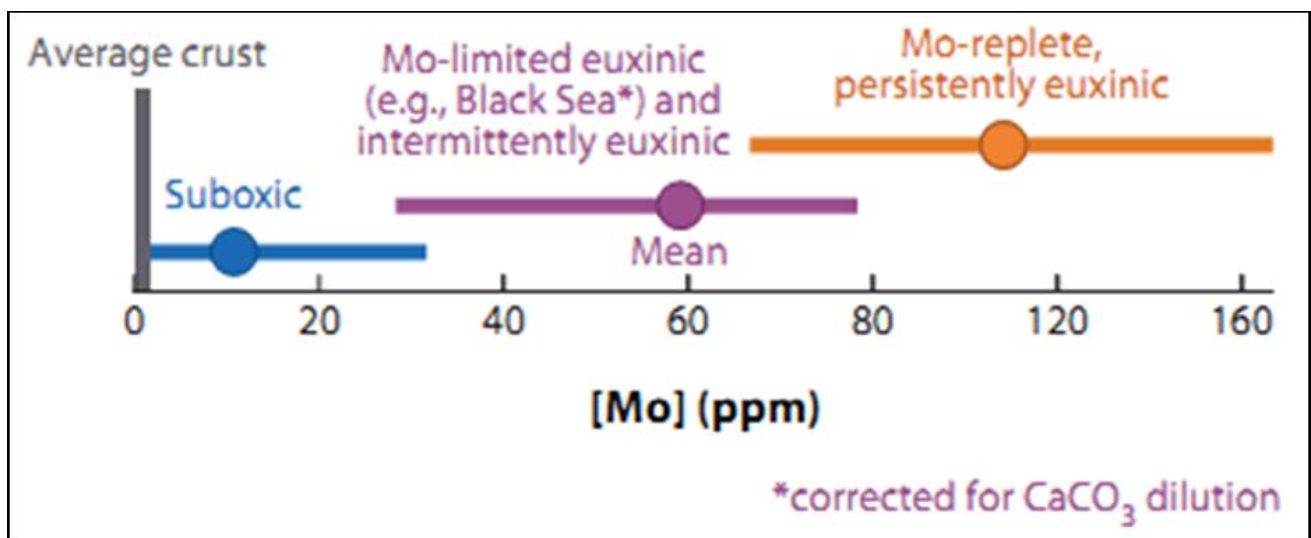


Figure 2.13: The mean and range of molybdenum concentrations observed at a large number of modern oxic, suboxic, and euxinic environments, Euxinic settings are subdivided as a function of persistence of euxinia and Mo availability in the basin (After Loyns and Anbar, 2009).

Molybdenum enrichment in sediments often tracks the organic carbon flux and availability of Mo in the basin of deposition (Lyons and Anbar, 2009). However, persistent or widespread euxinia would be expected to gradually lower the Mo concentration of seawater as expanded sinks exceed input from riverine sources (McArthur et al., 2008). Subsequent studies of modern euxinic basins have confirmed the generalization that with time, euxinic basins become depleted in Mo. For instance, the Mo contents of black shales decline with time as other indicators of euxinia (e.g., DOP) increase (Algeo, 2004).

2.4.6 Molecular palaeoredox indicators

Organic molecular geochemistry using the advanced technology of gas chromatography mass spectroscopy (GC-MS) has been used to generate biomarker data that can indicate the depositional environment. Molecular biological markers, or biomarkers, are natural products that can be assigned to a particular biosynthetic origin. For environmental and geological studies, the most useful molecular biomarkers are organic compounds with high taxonomic specificity and potential for preservation. Thus they can be used to identify organic matter inputs, as well as indicating the condition of deposition (Mackenzie, 1984a).

2.4.6.1 Pristane/Phytane ratio

Pristane/Phytane (Pr/Ph) ratio is the most common and widely used biomarker parameter for the assessment of redox conditions during sediment accumulation. According to Didyk et al. (1978), sediments deposited under an anoxic water column condition display low Pr/Ph ratios, with values less than 1.0, while values greater than 1.0 are observed under oxic conditions. The underlying rationale behind the application of Pr/Ph ratio as an indicator of oxicity is that both compounds are derived from phytol (mainly derived from the side chain of chlorophylls), with oxidation tending to promote a decarboxylation reaction (to form the C₁₉isoprenoid skeleton), and reduction tending to form phytane in preference (Figure 2.14)

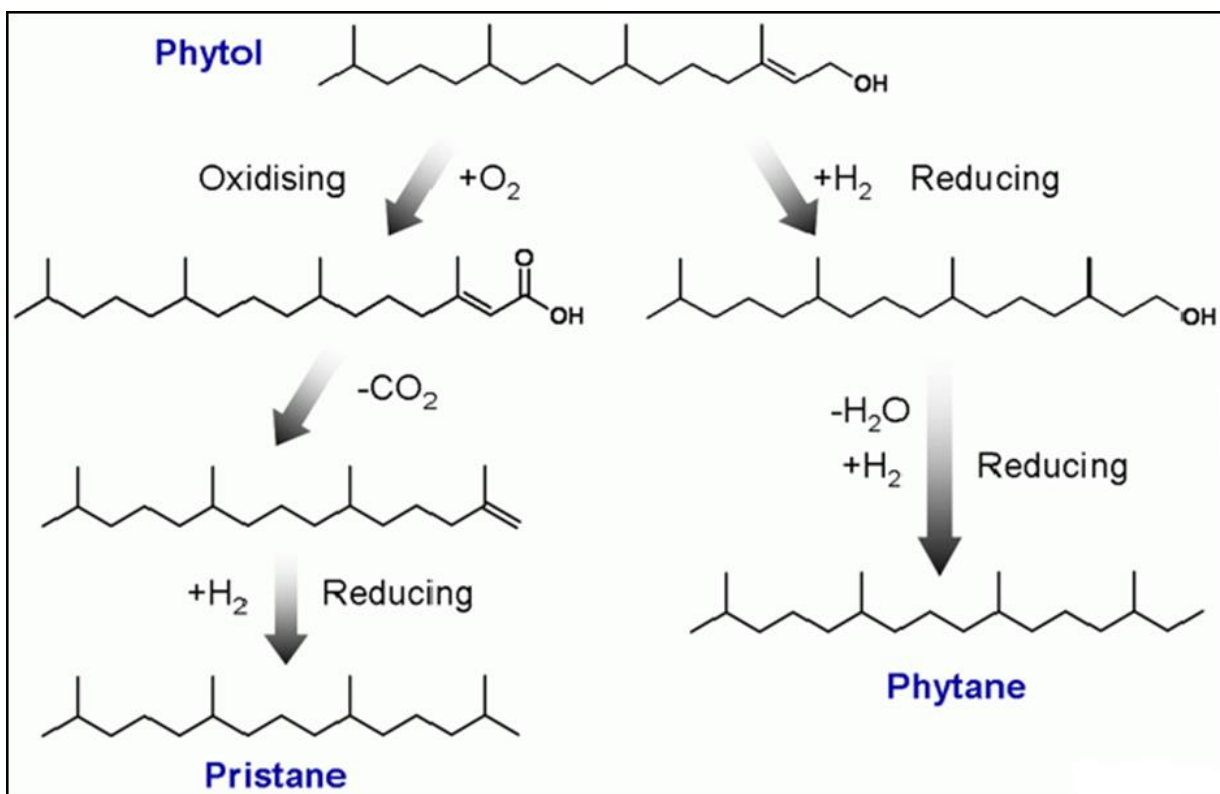


Figure 2.14: A schematic diagram of the diagenesis of the phytol side chain of chlorophyll (IGI Ltd, 2009)

Indeed, Pr/Ph is likely to become less definitive as additional data are acquired, since there are a number of influences that impact on the Pr/Ph ratio, the most important being (1) additional biological inputs of precursors of either pristane or phytane, and (2) the tendency for the ratio to increase with maturity. As a consequence, the ratio should be used with caution and in association with other indicators of redox conditions. Peters et al. (2005) recommend that the Pr/Ph ratio is not used in immature samples, and that even within the oil window, values between 0.8 and 3 are equivocal. High Pr/Ph values (>3) are common in samples with abundant terrestrial organic matter deposited under oxic conditions, whilst very low values (<0.8) are common in hypersaline environments, where anoxic conditions typically prevail.

2.4.6.2 Isorenieratane

Organic geochemical tools have recently been developed that can diagnose the occurrence of photic zone euxinia, based on specific bacterio-plankton biomarkers such as isorenieratane (Koopmans et al. 1996). These biomarkers are exclusively or primarily derived from the photosynthetic pigments of the phototrophic sulphur bacteria that proliferate in the upper part of the water column where light, nutrients and dissolved H_2S are

available (Figure 2.15). This type of bacteria produces unique and distinctive photosynthetic pigments that can be traced in ancient sediments. For instance, the Chlorobiaceae (Green Sulphur Bacteria; GSB) contains the carotenoid isorenieratene (the precursor of isorenieratane). In fact, isorenieratane is part of the carotenoid group, which are widely distributed in nature as well as ancient and modern sediments (Hartgers et al., 1994a).

During diagenesis, isorenieratene is reduced to isorenieratane which is a diaromatic C₄₀ hydrocarbon (Figure 2.15 with both aromatic rings having a 2,3,6-trimethyl substitution pattern (Hays et al., 1999). The burial products of isorenieratene, including diagenesis or catagenesis have been isolated from sedimentary rocks as old as approximately 1.64 billion years (Gyr) (Brocks et al., 2005), but they do not give any information on the duration of these conditions as they remain intact even when the conditions above the sediment have become oxic (photic zone euxinia could occur for a very short period of time).

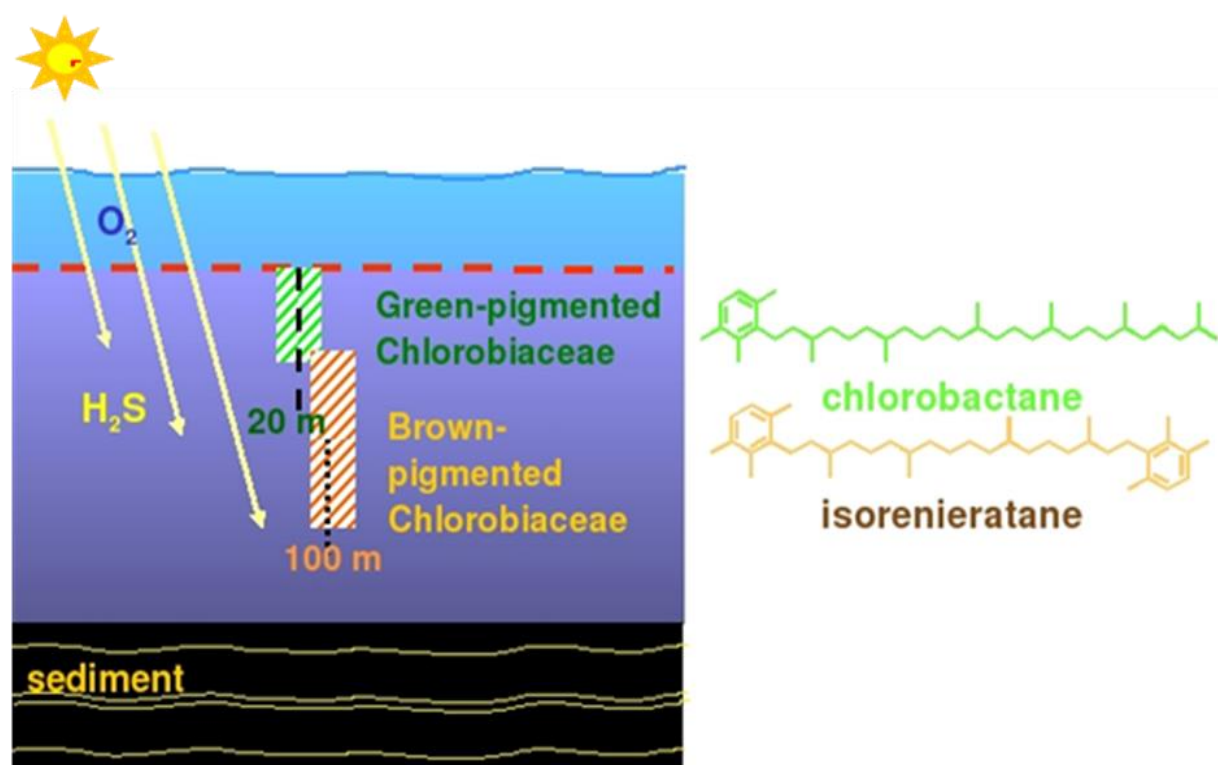


Figure 2.15: Schematic diagram of the isorenieratane produced by green-pigmented bacteria that thrive in presence of sun light and free hydrogen sulphide (After Summons and Powell, 1987).

The utility of isorenieratane is confirmed by $\delta^{13}\text{C}$ values, which are characteristically low due to the fact that Chlorobiaceae fix carbon by the reverse tricarboxylic acid cycle (Hays et al., 1999). The presence of isorenieratane, derivatives and $\delta^{13}\text{C}$ values have been used in many studies to reconstruct chemocline conditions (van Breugel et al., 2005), and for

the identification of potential source rocks (Pancost et al., 2001), as well as for evidence of euxinic conditions during Mesozoic oceanic anoxic events (Bowden et al., 2006; Van Breugel et al., 2006; Caswell et al., 2008).

CHAPTER 3 – GEOLOGICAL SETTING, MATERIALS AND METHODS

3.1 Geological setting

During Late Triassic - Early Jurassic time a shallow epicontinental sea extended throughout most of northwest Europe, following deposition of the brackish to shallow marine Penarth Group (Powell et al.1992). The Lower Jurassic was deposited as two major, upward shoaling cycles: the first cycle is Redcar Mudstone to Staithes Sandstone cycle and the second is Cleveland Ironstone to Blea Wyke Sandstone cycle (Knox et al. 1991). The first cycle has been subdivided into 3 second-order cycles by van Buchem and Knox (1998), each of the second order cycles representing a significant rise in sea-level. Hesselbo and Jenkyns (1995, 1998) recognized smaller, third-order cycles of about 300–500 Ka duration, which approximate to the estimated duration of many ammonite zones and subzones, and suggest a link between cyclicity, sea-level change and extinction or faunal turn over. Each of the third-order cycles was further subdivided into a number of smaller scale cycles or parasequences that were deposited in response to tectonic control and sediment flux.

The second major shoaling cycle represented by the Toarcian (Upper Lias) succession comprises the Whitby Mudstone to Blea Wyke Sandstone formations (Knox 1991). Following a relatively quiescent tectonic phase during the late Pliensbachian, the early Toarcian (*Tenuicostatum* zone) was a period of major basin subsidence throughout England (Powell, 2010). The rise of sea level across the Pliensbachian-Toarcian boundary, culminating in the *Falciferum* zone of the Lower Toarcian, is one of the best documented eustatic events in the Jurassic, marked by evident deepening in marine succession and marine transgression in extensive parts of the world (Hallam 1988). The period was also marked by an Early Toarcian Oceanic Anoxic Event, signified by a sharp negative excursion in the carbon isotope curve at the base of the event followed by a positive excursion (Hesselbo et al., 2000), the latter being associated with the widespread deposition of organic rich shale in the ocean (Jenkyns 1988).

The Toarcian successions of Northwest Europe comprise a well-marked cycle of sea level transgression and regression. The Early Toarcian section represents a strong transgressive system (*Tenuicostatum* tile end of *Falciferum* zone) while the Late Toarcian is strongly regressive (*Bifrons* tile *Levesquei* zone) producing pronounced large scale cyclicity

in the sediment sequences. Different from that, at the medium scale, sedimentary cycles are not well expressed (Hallam, 1997; Hesselbo and Jenkyns, 1998).

At the smaller (second order cycling) scale, sediments were deposited in progressively deeper water as manifested in the Early Toarcian section exposed on the Yorkshire coast, where the succession grades from sandstone at the top of the Cleveland Ironstone Formation, through silty mudstones to organic-rich laminated shales in a fining upward sequence (Jet Rock Shale and Alum Shale members). This trend of prominent sea level rise (deepening of the depositional environment) was interrupted by periods of slight relative sea level fall as indicated by the occurrence of hummocky cross stratified beds within the upper *tenuicostatum* zone (Wignall et al., 2005).

The bulk characteristics of each cycle indicate an upward increase in water energy and its transporting capability; such characteristics are usually attributed to an initial phase of marine transgression and deepening followed by a progressive regression and consequently shallow sea water level (Powell 2010). Sea level change or local basin subsidence fluctuations or a combination of the two are possibly the main factors explaining the observed sediment cycles (Hallam, 1981).

In most areas of north-west Europe the boundary between the Pliensbachian and Toarcian Stages of the Early Jurassic is a sequence boundary that marks the base of a major transgressive (Jenkyns, 1985). The Grey Shale Member, the Jet Rock Member and much of the overlying Alum Shale Member were deposited during this period of marine transgression (Hallam 1981). The sediments fine upwards from the base of the sequence with the deepest water conditions occurring in the middle of the Jet Rock Member. This phase of long term sea level rise resulted in the development of two distinct types of black shale. (1) A basal transgressive black shale representing in the earliest stages of transgression associated with the flooding surface, also covering the Sulphur Bands. (2) Condensed maximum flooding black shales of the Jet Rock type which sit on top of the transgressive system tract, and pass laterally into more oxygenated facies near shore (Wignall, 1994). Above this level there is a rapid increase in quartz silt content suggesting dropping down of the sea level. The overlying Peak Mudstone and Fox Cliff Siltstone Members are predominantly silty. The coarsening of the sequence probably reflects a marine regression that started toward the end of the Toarcian (Hallam 1981).

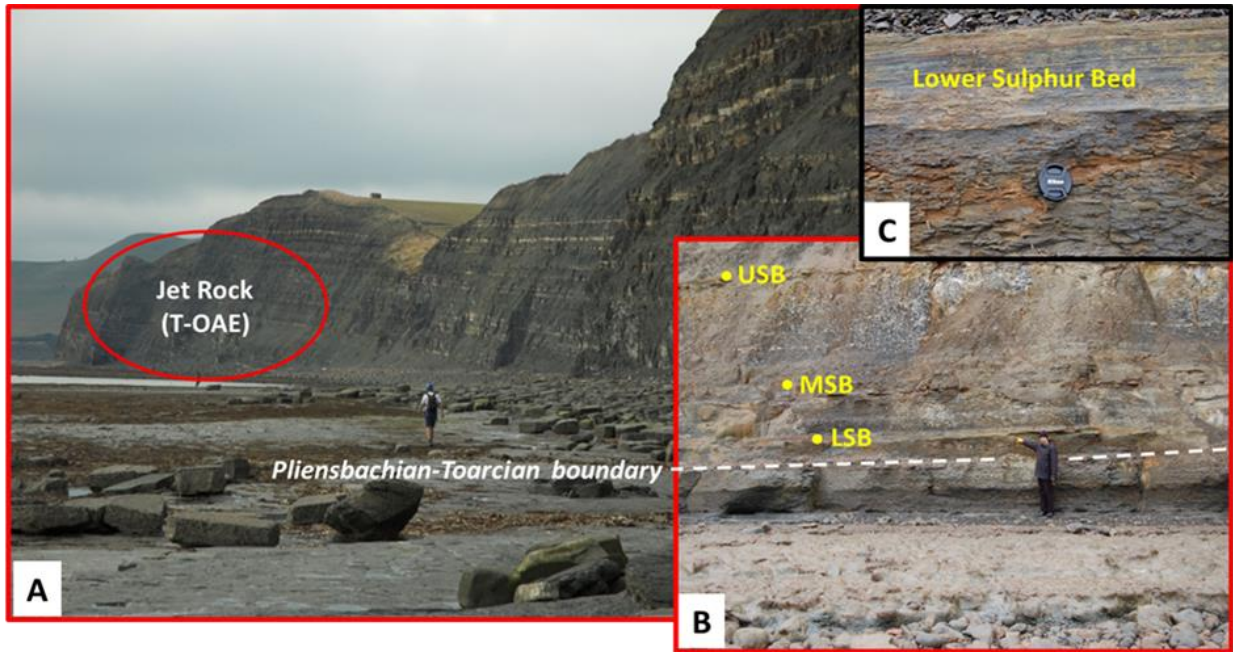


Figure 3. 1: A) North Yorkshire coast, view ESE towards Port Mulgrave , B) the three laminated sulphur beds at the base of Gray shale Member, C) Zooming in to show the lower Sulphur Bed.

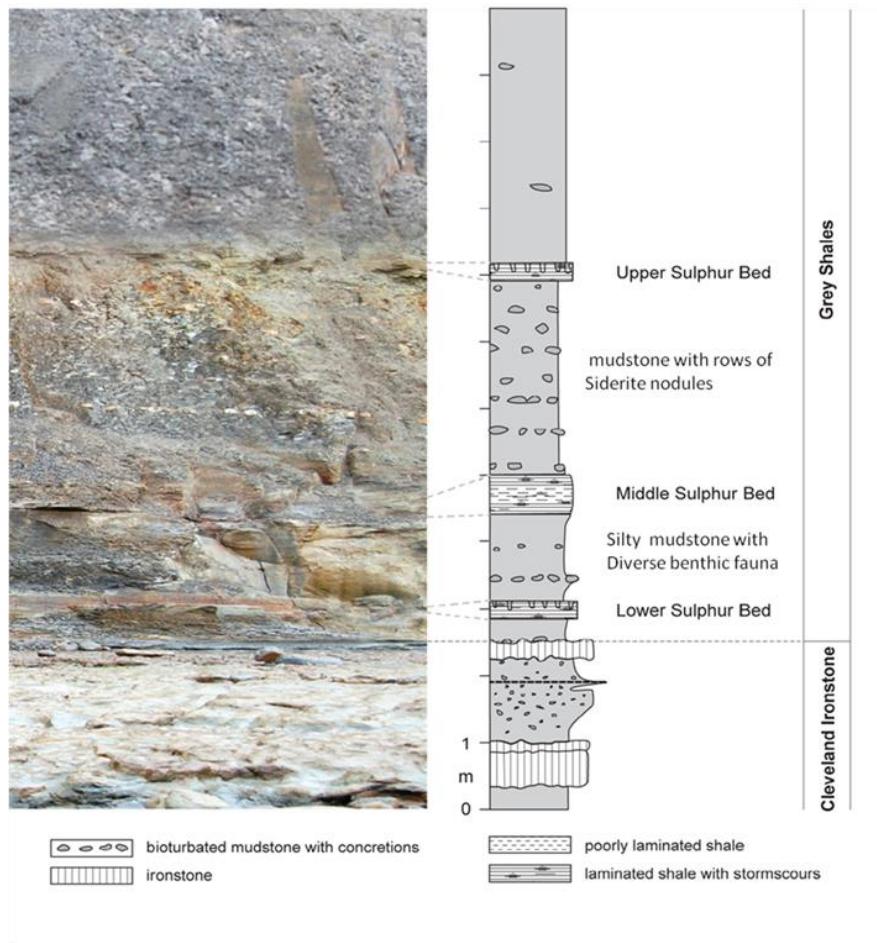


Figure 3.2: Boundary beds between the Cleveland Ironstone and Grey shales Formations, Port Mulgrave, North Yorkshire

At the base of this transgressive and half a metre from the top of the Cleveland Ironstone Formation a 15 cm thick, silty laminated black shale layer (Lower Sulphur Band) sits sharply on a siltstone with a large and diverse benthic fauna (figure 3.2). The layer corresponds to the Sulphur Band of the mining vernacular (Howard 1985). Chowns (1968) demonstrated that its formation was related to a brief episode of anoxic bottom water conditions which affected the entire area at the beginning of Toarcian times. The band gained its name from its appearance at outcrop (Figure 3.3) caused by the weathering of its abundant pyrite content.



Figure 3.3: Photographic picture of the LSB illustrating its yellowish appearance at Staithes outcrop.

The term Sulphur Band was introduced for the first time by Chowns (1968) to define this thin bed of fissile bituminous shale which corresponds to Bed 58 at Staithes, Bed 26 at Kettlewell and part of Bed 43 at Hawsker Bottoms (Figure 3.4). The silty laminations towards the top of the Sulphur Band become gently disturbed and exhibit very low angle cross lamination along with broad scour-and-fill structures (Wignall, 1994). Both pelagic and benthic fauna are absent, implying anoxic conditions extending from the sea floor into the water column but, curiously, this shale unit is not enriched in authigenic U, possibly implying oxic conditions. Chondrites and *Diplocraterion* penetrate the top of the Sulphur Band and the

overlying mudstones show vestiges of silt-lamination between the dense burrows of these two ichnogenera. There is no sequential development of burrow types and so it would appear that Sulphur Band deposition was terminated by a sudden onset of oxygenated sea floor conditions. The presence of scour and fill lamination in the Sulphur Bands, which indicate their formation above storm wave base, also suggests a more dynamic environment that was characterised by a significant degree of water column mixing. Moreover, Rob Newton (Leeds University, unpublished data) reported high DOP, contradicted by anomalously wide range of framboid sizes, suggesting that for at least some part of the sulphur band deposition the redox interface must have been located at the sediment surface. These observations provide the first evidence from ancient black shales of this mode of formation, one which has previously gone undocumented in the literature.

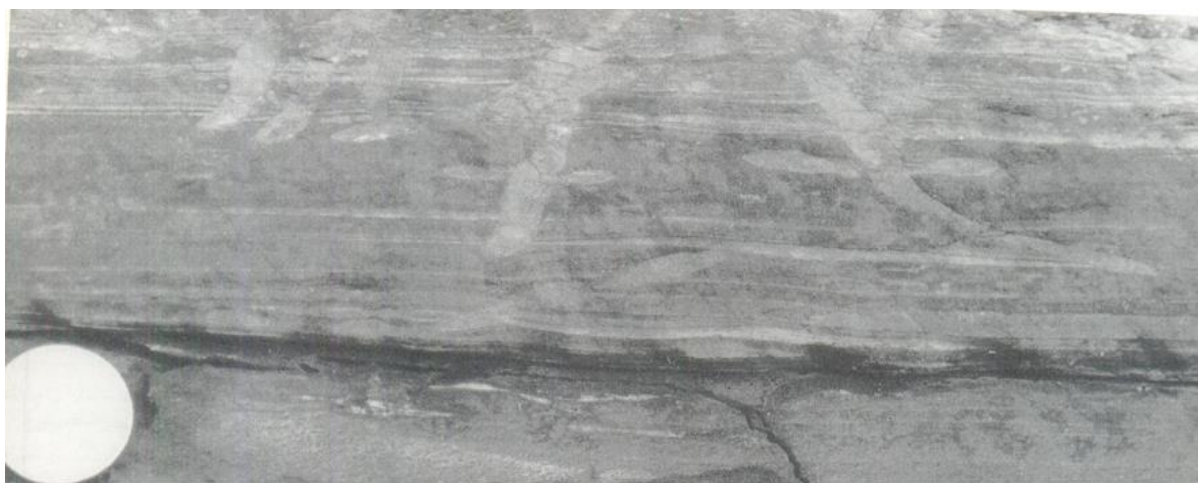


Figure 3.4: Chondrites and Diplocraterion burrows developed in the top of the Sulphur Band at Brachenberryt Wytke, North Yorkshire. Coin is 2cm in diameter (after Wingall, 1994).

A second, two decimetre-thick, pyritic unit with similar lithology to the Sulphur Band occurs at 2.3 and 5.6 m above the base of the Grey Shale. In this study, the three pyritic units are termed collectively the Lower, the Middle and the Upper Sulphur Bands, from the base upward.

The Pliensbachian–Toarcian boundary preceding the T-OAE has received less attention, but it is quite an important interval with regards to changes in carbon cycling, sea level, faunal turn-over, and, more generally, evolving Early Jurassic climate. A sea-level rise across the stage boundary of several tens of metres (Hallam, 1981) coincides with a relative minimum in seawater strontium-isotope values at this boundary interval where the $^{87}\text{Sr}/^{86}\text{Sr}$ ratios fall to the least radiogenic values seen throughout the Early Jurassic (Jones and Jenkyns,

2001). Moreover, the transition from the Pliensbachian into the Toarcian is marked by the initiation of a mass extinction event, suggesting that changes in climate and palaeoceanography started to occur well before the onset of the OAE (Little and Benton, 1995; Wignall and Bond, 2008). It has been observed that most of the well-known mass extinction events in the geological record were accompanied by perturbations to the global carbon cycle (Keller and Lindinger, 1989; Arens and Jahren, 2000; Payne et al. 2004; Hesselbo et al. 2002; Riccardi et al. 2007).

Since the Sulphur Bands at the Pliensbachian–Toarcian boundary preceding the T-OAE are interbedded as thin dark laminated shale layers in more or less normal light-colored bioturbated mudstones sediments, the formation of these layers record short-lived but catastrophic alterations in oceanographic conditions that were probably caused by a repeated mechanism that operated regionally at small scale and then developed to a major process that effected the whole ocean on a global scale. Our current understanding of these pre-TOAE small events is unconstrained. Here we present new and comprehensive geochemical analysis across the Pliensbachian-Toarcian and extending throughout the T-OAE to shed more light on these events and how could they link to the main event that linked to the T-OAE. The very high resolution (cm scale) geochemical analysis scanning this interval is the scope of this study to shed light any possible short-lived changes in the paleoredox history which may have gone undocumented before.

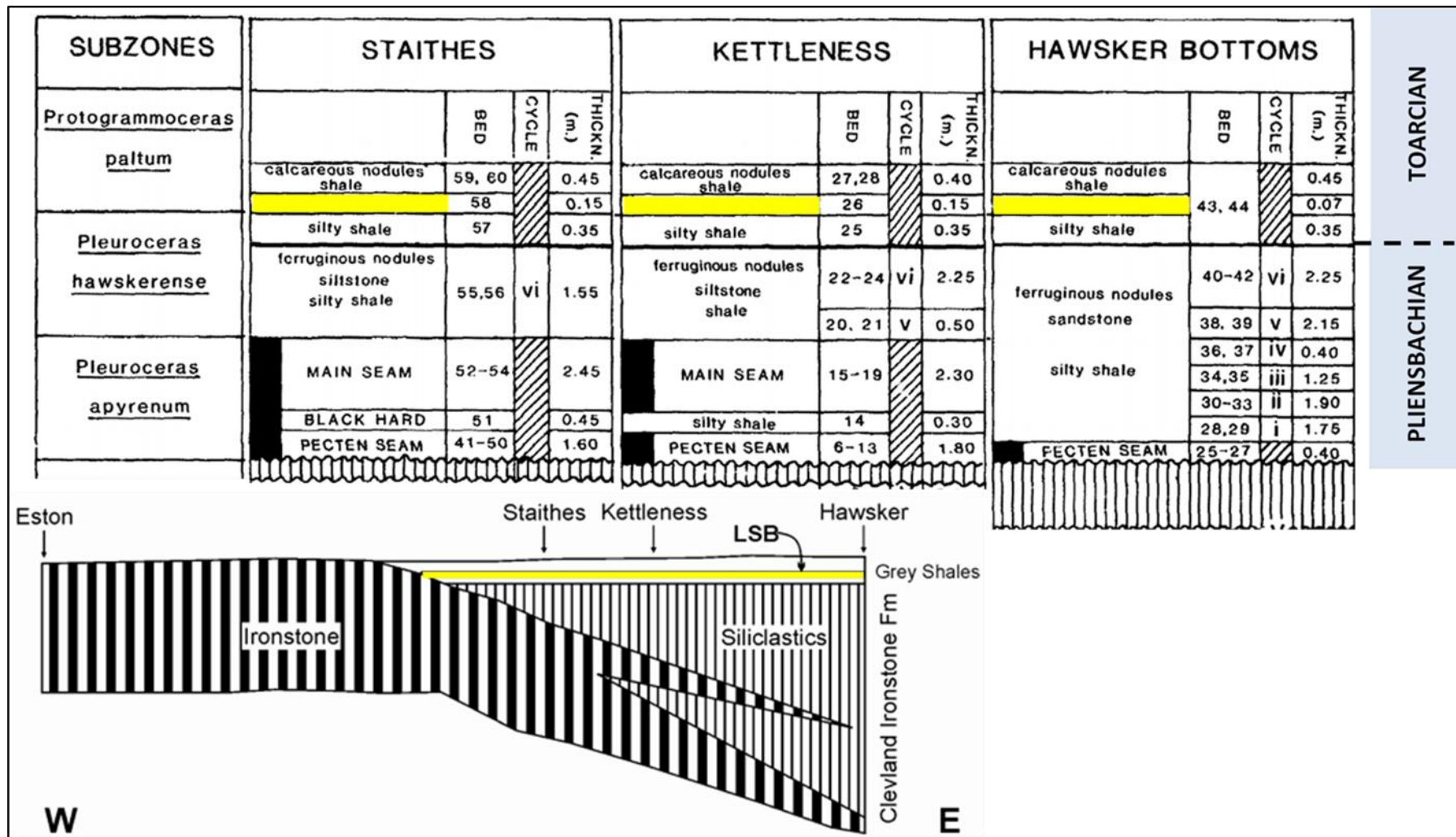


Figure 3.5: Areal extent of the LSB (yellow band) along the coastal exposures of Staithes, Kettlecess and the Hawsker Bottoms. Not that the LSB does not grade into any near-shore facies (after Howard, 1985)

3.2 Sampling

Samples used in this study were collected from two lower Jurassic exposures in the UK. The main station is at the costal exposure between Staithes and Port Mulgrave, where the sampled and logged section covers the Lower part of the Whitby Mudstone Formation. The sampled lithostratigraphic units are, in ascending order, the Grey Shale Member (beds 1 to 32) between 0 and 13.60 m above the top of the Mushroom Concretions bed which is taken as reference (all sample heights were measured from the top of this unit) and the Jet Rock Shale Member (beds 33 to 40) between 13.60 and 18.23 m. The entire section is well exposed along the coastal cliffs between Staithes and Port Mulgrave on the north east coast of Yorkshire. The other location used in this study was Hawsker Bottoms (figure 3.6), where the lower Grey Shale was sampled to investigate the geochemical variation of the Sulphur Beds.

A total of 131 rock samples were collected at decimetre and centimetre scale from both outcrops using either, a geological hammer and chisel or for some laminated units (e.g the Sulphur Bands) an electrical saw was used to cut whole sections of rock which could then be subdivided later to obtain very detailed samples at sub-cm scale. Particular attention was taken to avoid weathered material.

Samples were labelled in the field and the top and bottom of each sample were marked. Back in the lab, more detailed sub-sampling was carried out on the larger rock samples. Then samples were trimmed to remove the outer edges (about 0.5 cm or more). Prior to any geochemical and palynological analyses, the whole rock samples were described in terms of laminations, banding, bioturbation, heterogeneity, mica content and the presence of macrofossil material. The sections were sub-sampled and powdered in a Tema mill. The colour of the powdered samples was recorded using a Geological Society of America Rock Color Chart (Goddard *et al.*, 1970).

Most of the collected samples are carbon-rich, laminated black shales that are inter-bedded with layers of calcite concretions, and which are stratigraphically equivalent to similar organic-rich deposits throughout Central and Western Europe (e.g. the 'Schistes Carton' from the Paris Basin, France, and the 'Posidonia Shale' from the Posidonienschiefer Basin, Germany; Jenkyns, 1988; Röhl *et al.*, 2001).

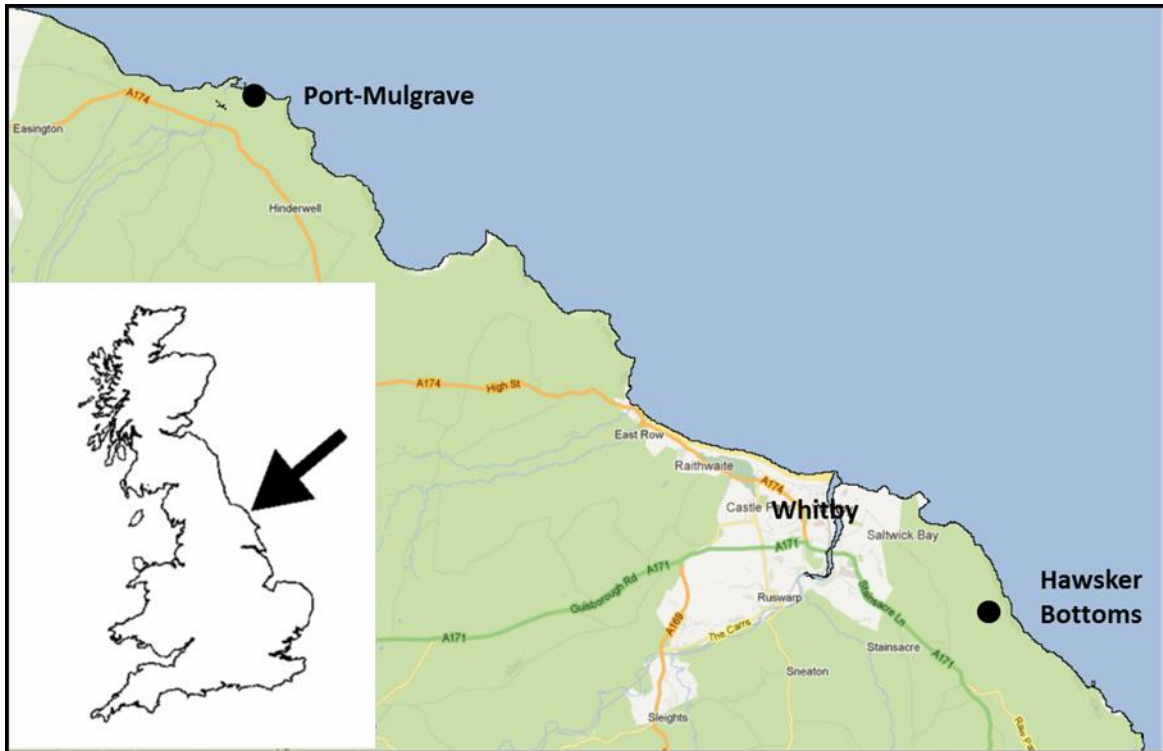


Figure 3.6: Location map of the north Yorkshire coast fieldwork sites

At the Port Mulgrave section, a total of 98 samples were collected over almost 20 m of the study interval, starting at the base of the Grey Shale Member, and ending at bed 40 of the Jet Rock Shale Member (Figure 3.7). All samples were collected from outcrop, but from a horizontal depth of > 10 cm in order to minimize the oxidative influence of subaerial weathering. Sampling was at decimetre-scale within the bioturbated mudstone of the Grey Shale and throughout the Jet Rock shale (*exaratum* subzone). The Sulphur Bands at the Pleninsbachian-Toarcian boundary were sampled at higher resolution (mm-scale).

In order to evaluate the lateral geochemical characterization of the Sulphur Bands within Cleveland basin, Lower Toarcian section at Hawsker bottoms was chosen as it represents more distal site. At Hawsker bottoms 26 samples were taken spanning the Paltum and Clevelandian subzones, which represent the stratigraphic interval of the Sulphur Beds.

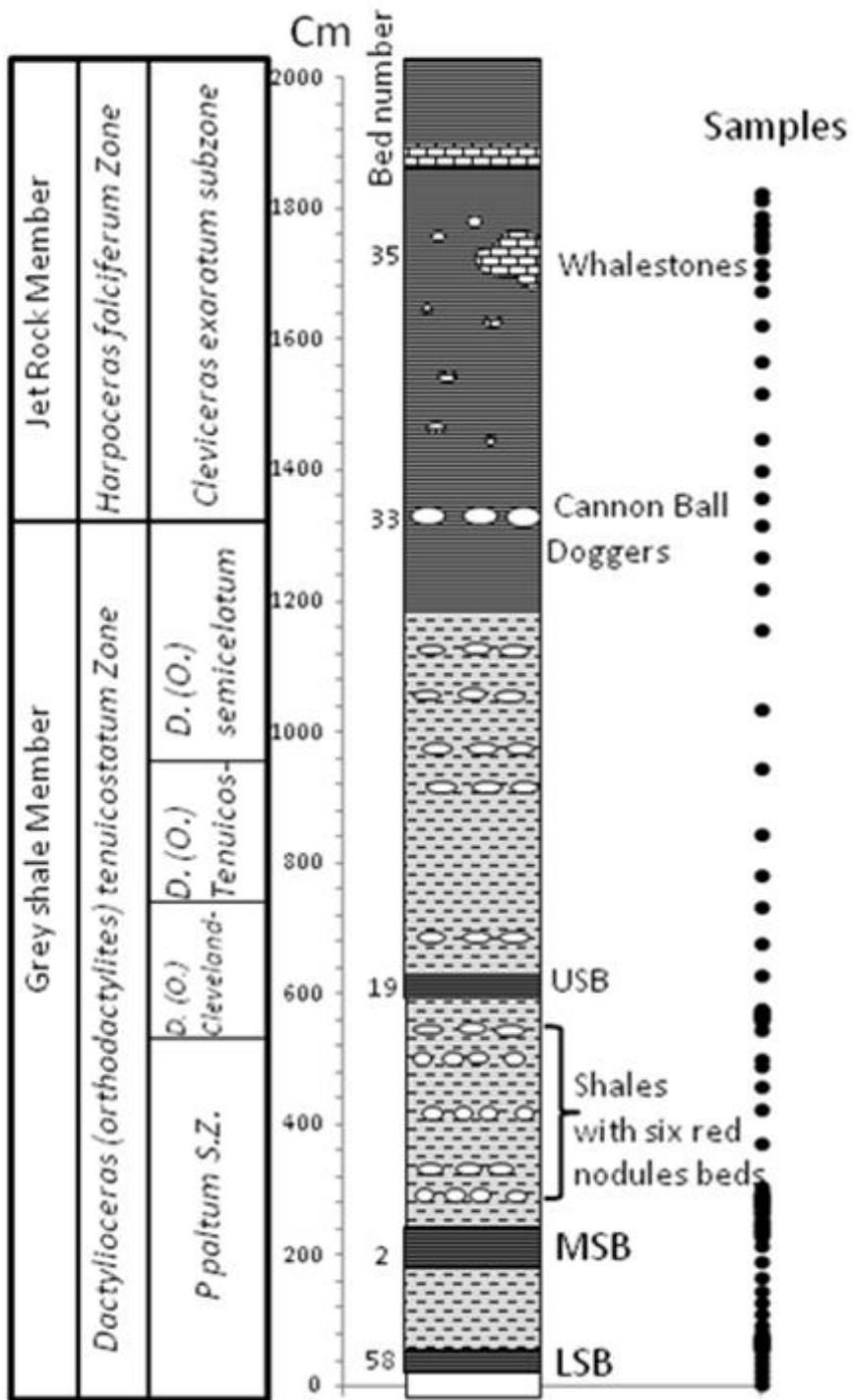


Figure 3.7: Lithological column of the studied section at Port Mulgrave showing the position and heights of the analysed samples from the base of the Grey Shale Member.

3.3 Analytical Methods

During the course of this study a variety of techniques were applied. These techniques vary from commonly applied geochemical analyses (where the whole set of samples were analysed), to some more detailed and advanced techniques (where selected samples were analysed, based on the previous results). The order of analysis is described in Figure 3.8.

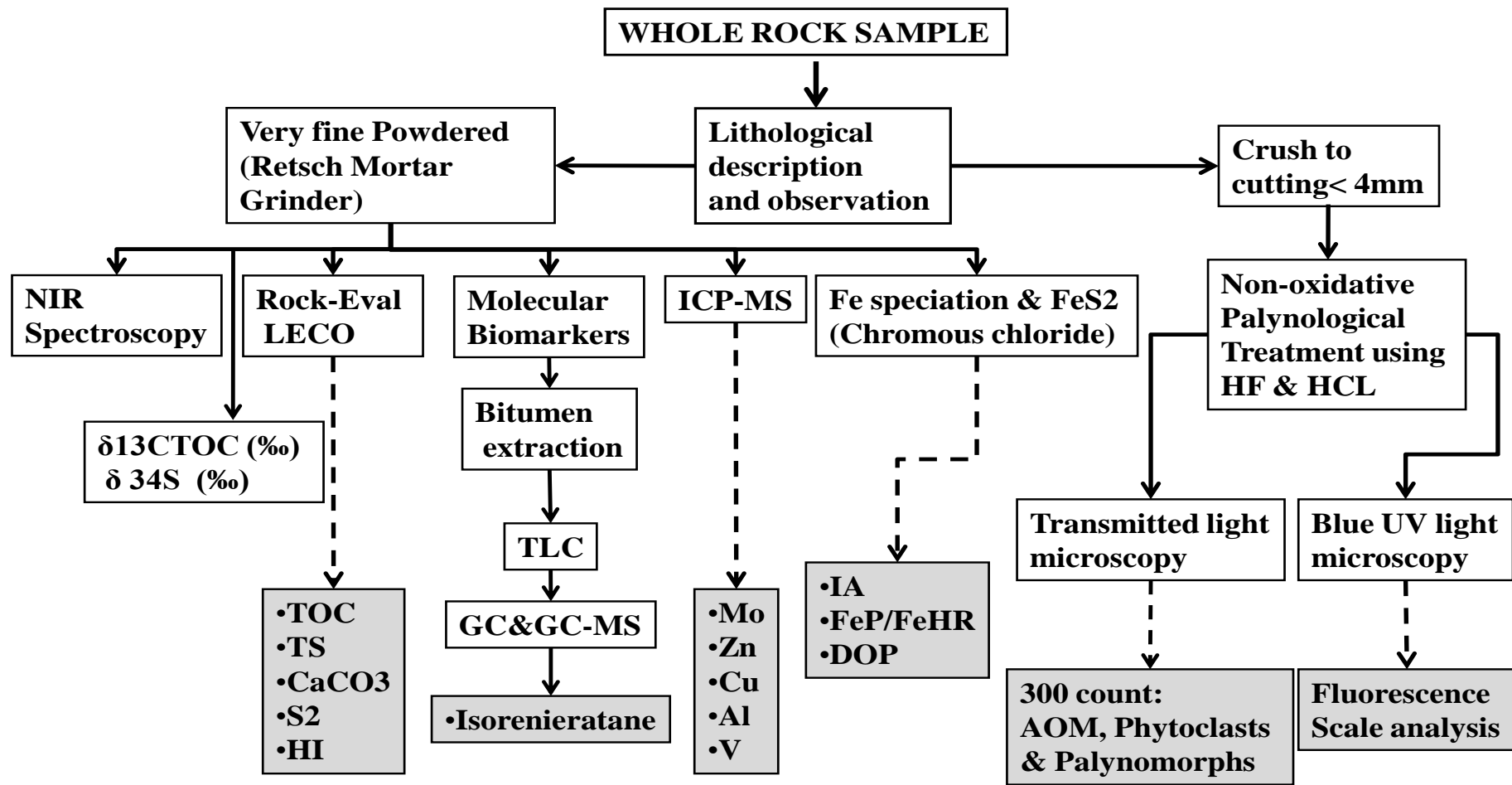


Figure 3.8: Flow chart showing the order of methods

3.3.1 Bulk Geochemistry

3.3.1.1 Total Organic Carbon (TOC) Determination

To determine total organic carbon, approximately 100 mg of the powdered rock sample was placed in a porous crucible and treated with 5 ml of 40% HCl to remove carbonate phases. The samples were washed thoroughly six times with distilled water, and placed in an oven overnight at a temperature of 60 °C. TOC was then measured using a LECO® HF-100 induction furnace attached to a LECO® LS-244 Carbon Sulphur Determinator. Prior to analysis, copper metal and iron chips were added to each crucible. Then the crucible was inserted into a furnace and combusted at 1500°C for 30 – 50 seconds. The apparatus was calibrated to known standards before any analyses were conducted, and to ensure the performance of the machine some samples were run in duplicate and some additional standards were run after every ten samples. Table 3.2 shows the results for triplicate analyses of a rock sample from the Whitby Mudstone Formation for an internal standard. The accuracy relative to the internal standard falls within 2% of certified standard value. Based on triplicate measures, the relative standard deviation (RSD) was less than 1%.

3.3.1.2 Total Carbon and Total Sulphur (TC & TS) Determination

The samples were prepared for TC and TS analysis by weighing 0.1 gram of each powdered rock sample into a crucible, and some copper metal and iron chips were added to each crucible and inserted into the LECO CS- 244 Carbon/Sulphur Analyser. Within a few seconds the oxidising reaction takes place producing CO₂ and SO₂, and these gases were quantified by a LECO® LS-244 Carbon Sulphur Determinator, as for TOC. The accuracy relative to the internal standard falls within 2% of certified standard value. Based on triplicate measures, high precision was achieved with relative standard deviation (RSD) of 0.51%.

Sample	TOC	T C
MSB24	1.722	2.166
MSB24	1.744	2.161
MSB24	1.726	2.182
Mean	1.731	2.170
%RSD	0.67	0.51
Internal Std	1.723	2.807
Internal Std	1.736	2.803
Internal Std	1.727	2.798
Mean	1.729	2.803
% RSD	0.39	0.16

Table 3. 1: shows the accuracy and precision of the analytical methods

3.3.1.3 Isotopic analysis

3.3.1.3.1 Organic carbon isotopes

Sample Preparation

Prior to carbon-13 analysis, the sediment samples were treated with hydrochloric acid to remove inorganic carbon (carbonate) as follows. About 200 mg of sample was treated with 1 M HCl. The sample and acid were mixed and left for 24 hours to allow the carbonate content of samples to be liberated as CO₂. The acid was decanted and the sediment washed several times with distilled water. The samples were completely dried at 60°C and re-ground to a powder. The sample was then weighed into a tin capsule (8 x 5 mm) and sealed ready for analysis.

Carbon-13 Analysis

The technique used for analysis was EA-IRMS (elemental analyzer isotope ratio mass spectrometry), which was performed by Iso-Analytical Ltd., UK. In this technique, samples and references are loaded into an auto-sampler on a Europa Scientific elemental analyzer. The samples are then combusted at 1000°C in the presence of oxygen. The tin capsules flash combust, raising the temperature in the region of the sample to ~1700°C. The combusted gases are swept in a helium stream over a combustion catalyst (Cr₂O₃), copper oxide wires (to oxidize hydrocarbons), and silver wool (to remove sulfur and halides). The resultant gases,

N₂, NO_x, H₂O, O₂, and CO₂ are swept through a reduction stage of pure copper wires held at 600°C. This removes any oxygen and converts NO_x species to N₂. A magnesium perchlorate chemical trap is used to remove water. Nitrogen and carbon dioxide are separated using a packed column gas chromatograph held at a constant temperature of 100 °C. The resultant carbon dioxide peak enters the ion source of the Europa Scientific 20-20 IRMS where it is ionised and accelerated. Gas species of different mass are separated in a magnetic field then simultaneously measured using a Faraday cup collector array to measure the isotopomers of CO₂ at *m/z* 44, 45, and 46. The reference material used during analysis of the samples was IA-R001 (Iso-Analytical working standard Flour, 40.2% Carbon), with a δ¹³C value of -26.43‰ (relative to V-PDB).

3.3.1.3.2 Sulphur isotopes analysis

Sulphur was collected for analysis in form of silver sulphide that was produced during the pyrite extraction process (look at 3.3.2.1 section for details). Tiny amount of the silver sulphide were placed in tin capsules and processed using continuous flow isotope ratio mass spectrometry (EA-IRMS). The tin capsules containing reference or sample material plus vanadium pentoxide catalyst were loaded into an automatic sampler. From where they were dropped, in sequence, into a furnace held at 1080° C and combusted in the presence of oxygen. Tin capsules flash combust, raising the temperature in the region of the sample to ~1700° C. The combusted gases are then swept in a helium stream over combustion catalysts (tungstic oxide/zirconium oxide) and through a reduction stage of high purity copper wires to produce SO₂, N₂, CO₂, and water. Water is removed using a Nafion™ membrane. Sulfur dioxide is resolved from N₂ and CO₂ on a packed GC column at a temperature of 45 °C. The resultant SO₂ peak enters the ion source of the IRMS where upon it is ionized and accelerated. Gas species of different mass are separated in a magnetic field then simultaneously measured on a Faraday cup universal collector array. Analysis was based on monitoring of *m/z* 48, 49 and 50 of SO⁺ produced from SO₂ in the ion source.

Reference Standards and Quality Control: The reference material used for analysis was IA-R061 (Iso-Analytical working standard barium sulphate, δ³⁴S_{CDT} = +20.33 ‰). IA-R025 (Iso-Analytical working standard barium sulphate, δ³⁴S_{V-CDT} = +8.53 ‰), IA-R026 (Iso-Analytical working standard silver sulphide, δ³⁴S_{V-CDT} = +3.96 ‰) and IA-R061 were used for calibration and correction of the ¹⁸O contribution to the SO⁺ ion beam.

3.3.1.4 Rock- Eval Pyrolysis

Procedure

About 0.1g of powdered rock sample was added to a stainless steel crucible, mounted in a carousel and progressively heated up to 550°C for about 20 min. A standard source rock sample was also analysed to enable calibration of the results. A stream of helium was passed over the sample (oxygen was excluded), then the temperature was gradually increased until 100°C and the temperature was held constant for one minute to release the free gaseous hydrocarbon (S_0 mg/g sediments). This was detected by a Flame Ionization Detector (FID), and is known as peak one (1). In the second stage, the temperature was increased by 25°C/min until 300°C, and the hydrocarbons released were quantified as peak 2, which is known as S_1 (mg/g). During the last stage the temperature was increased at a rate of 25°C/min until 550°C. This reflects the temperature where kerogen breaks down and the hydrocarbons are generated (Peak 3), and is quantified as S_2 (mg/g). T_{max} is recorded at the maximum of the S_2 peak, which is a function of thermal maturity of the organic matter.

Petroleum yield (PY) of a source rock is defined as the sum of hydrocarbons present in the rock sample and those generated during pyrolysis (S_1+S_2).

Hydrogen index (HI) corresponds to the quantity of pyrolyzable organic compound or hydrocarbons from S_2 relative to TOC (S_2/TOC).

Production Index (PI) distinguishes between the HC present in the rock and those generated by cracking during analysis ($S_1/ (S_1+S_2)$).

3.3.2 Microscopy

3.3.2.1 Palynological Preparation Technique

Based on the measured values of HI and TOC, samples were selected for palynological analysis. The selected samples represent the full range of variations in geochemical profile (not just the richest samples). Following the standard non-oxidative palynological preparation method (Barss and Williams, 1973), samples were cleaned of any contamination and gently crushed to a cutting size of >2.0 mm (wrapped in foil and hit by geological hammer, and excessive grinding was avoided). The fragments were then sieved to <2.0 mm. Then the samples were processed as follows:

- About 1 g of the crushed cutting was placed in a 600 ml plastic beaker.

- 100 ml of 40% hydrochloric acid was added to dissolve any carbonate minerals.
- Sample was left for four hours or until any reaction had stopped.
- Distilled water was added up to the rim of the beaker and then decanted after four hours; repeated three times.
- 100 ml of 40% hydrofluoric acid was added to remove any silicate material, and the beaker was allowed to stand for at least 24 hours.
- Water was added and then decanted after more than four hours or until the sediment settled; repeated two times.
- *Lycopodium* tablets were then added to each sample (the number of tablets based upon HI and TOC values).
- The residue was treated with 20% hydrochloric acid to dilute and remove any silico-fluoride compounds precipitated during the course of the treatment, and to aid dissolution of the lycopodium tablets, then washed three times with distilled water.
- About 2 L of distilled water was added to wash the residue through a ten micron sieve, and then the residue was transferred into vials.
- A thin layer of suspended kerogen was then pipetted onto a cover slip and left overnight to dry. This was then mounted on a microscope slide using Elvacite TM 2044 (ICI) and xylene mounting medium, which was produced by slowly adding 65 g of Elvacite to 100 ml xylene in a beaker, stirring occasionally until the solution was completely clear.
- The cover slip was mounted on a glass slide using 2044 acrylic resin and left overnight.

3.3.2.2 Transmitted White Light (TWL) analysis

An Olympus BH2 microscope was used for petrographic examination, with the objective to identify the source of organic matter (OM) by counting the percentages of amorphous organic matter (AOM), palynomorphs and phytoclasts, based on 300 counts per sample.

3.3.2.3 Fluorescence Microscopy

The preservation state of the kerogen was determined using blue light fluorescence microscopy, relative to the scale of Tyson (1995; see Table 3.1).

Table 3.2: Summary of fluorescence scale, where the 1 represents the lowest preservation state of the organic matter and 6 the highest (after Tyson, 1995, p.347)

Scale point	Description	Relative preservation
1	Nothing fluoresces (except rare palynomorphs or contaminants)	Poor
2	Only palynomorphs fluoresce	
3	AOM fluoresces but just detectable	
4	As 3 but AOM shows moderate fluorescence	
5	As 3 but AOM shows strong but heterogeneous fluorescence	
6	Matrix AOM shows very strong and homogeneous fluorescence	

3.3.3 Organic molecular chemistry

3.3.3.1 Bitumen Extraction

43 samples, representing a range of Rock-Eval parameters, TOC and depositional redox conditions (see below), were selected for detailed biomarker investigation. Aliquots of powdered rock (15 g) were extracted for 6 hours with 93:7 dichloromethane/methanol (DCM/MeOH) in a Dionex ASE 200 Accelerated Solvent Extraction System at 1000 psi and 100°C. Yields of extractable organic matter (EOM) were obtained.

3.3.3.2 Thin Layer Chromatography (TLC)

The extracted bitumen was concentrated by removal of solvents using a rotary evaporator, and the extract was transferred to a small vial and bellowed down under a nitrogen stream to result in slightly viscous bitumen. The traditional thin layer chromatography technique was used to separate the bitumen mixtures into the three main groups of compounds (aliphatic, aromatic and NSO compounds). The separation process was performed on a plate of unreactive glass that was coated with a thin layer (0.5 mm

thick) of silica gel as adsorbent material (stationary phase). The TLC plates were prepared by mixing the adsorbent (silica gel of standard particle size range) with a small amount of water to improve reproducibility (2 ml of water to each gram of silica gel). Then the mixture was spread as thick slurry on the glass plate. The plate was then dried and activated by heating in an oven for 24 hour at 70 °C.

About 10 mg of the extracted bitumen sample was applied to the plate using a capillary tube and spotted along a horizontal line about two centimeters from the base. The plate was then dipped in a glass jar containing light petroleum ether and placed in a sealed container. The solvent moved up the plate by capillary action and carried the sample mixture. Different compounds in the sample mixture travel at different rates due to the differences in their attraction to the stationary phase and because of differences in solubility in the solvent. Therefore, the aliphatic and aromatic fractions were separated from the bitumen and marked on the plate by the aid of a standard (squalane and anthracene). The plate was then spread with Rhodamine 6 and viewed under UV light to help identify the aliphatic and aromatic bands. These aliphatic and aromatic bands were then separately scratched out of the plate. The sample tubes were then set by adding some activated alumina, and 30 ml of DCM was used to flush the scratched sample through and the fractions were collected in small round flasks.

The saturated hydrocarbon samples were diluted to 1 mg/100 µL in DCM and transferred to a GC vial. Injections were made using an HP6890 autosampler. The column was a 60 m Chrompack CP8744 CPSil-5CB with an internal diameter of 0.32 mm and a film thickness of 0.25 µm. The carrier gas was helium with a volumetric flow rate of 1.6 mL/min. Samples were analyzed using both full scans and selected-ion monitoring methods for a more detailed analysis of specific compounds. Aromatic fractions were spiked with squalane as a standard to facilitate quantification of aromatic hydrocarbons such as isorenieratane.

Samples were analysed by gas chromatography coupled to tandem mass spectrometry using a Hewlett-Packard 6890 gas chromatograph and a Micromass Autospec Ultima operated in the metastable-reaction-monitoring (MRM) mode. A 60 m Scientific DB-1 fused silica capillary column (0.25 mm i.d.; 0.25 mm film thickness) was used with helium as the carrier gas. Samples were injected in pulsed splitless mode. The column temperature was programmed from 60 °C (held for 2 min) to 150 °C at 10 °C/min, then at 3°C/min to 250 °C, with 70 eV ionization energy and 8000 kV acceleration voltage. Peaks were identified using

previously published elution times and mass spectra. Isorenieratane peaks were identified by comparison of elution time with an authentic standard (squalene), as well as previously published mass spectra.

Quantification of GC-MS peaks

The quantification of the GC peaks was established using the integrated peaks from the GSMS and the following equation;

$$W_x = RRF * A_x * W_s / A_s$$

Where;

W_x = weight of unknown sample

RRF = is the relative response factor taken here as 1

A_x = area of unknown sample

A_s = area of known standard

W_s = weight of known standard

3.3.4 Sequential Extraction Procedure for Iron Speciation

Fe speciation is one of the most robust redox indicators currently available. It has been extensively calibrated to allow identification of oxic, anoxic non-sulfidic, and euxinic bottom water conditions. The technique is based on the reactivity of different Fe minerals towards dissolved sulphide (Canfield et al., 1992; Poulton et al., 2004). The recently developed sequential extraction technique of Poulton and Canfield (2005) allows identification of three pools of iron species of differing reactivity to dissolved sulphide, when combined with the Fe sulphide extraction procedure of Canfield et al. (1986); highly reactive Fe (Fe_{HR}), poorly reactive Fe (Fe_{PR}) and unreactive Fe (Fe_U) (Raiswell and Canfield, 1998; Poulton and Raiswell, 2002). Together, these techniques allow the recognition of five operationally-defined Fe fractions, listed in Table 3.3.

Table 3.3: Details of the Fe extraction scheme, with target phases (After Poulton and Canfield, 2005).

Extraction	Target phases	Terminology
Na Acetate, PH 4.5, 48h, 50°C	Carbonate Fe, including siderite and ankerite	Fe _{carb}
Dithionite, 2 h	Goethite, akaganeite, hematite	Fe _{ox}
Oxalate, 6h	Magnetite	Fe _{mag}
Boiling 12 N HCL	Poorly reactive sheet silicate Fe	Fe _{PRS}
Chromous chloride distillation	Pyrite Fe	Fe _{py}
Total Fe	Unreactive silicate Fe (Total Fe – sum of first 5 stages plus pyrite Fe)	Fe _U

3.3.4.1 Pyrite extraction

Sulphur geochemistry and sulphur isotopic distributions are one of the most useful techniques for elucidating depositional conditions and diagenetic histories of recent and ancient sediments and rocks. The chromium reduction method (Canfield et al., 1986) was used for the determination of total reduced S (dominantly pyrite). In this study pyrite sulphur was extracted from the rock powder using a modified version of the chromium reduction method described by Canfield et al. (1986). Approximately 300 to 1000 mg of rock powder from each sample was first treated with 8 ml of boiling 50% HCL to extract any acid volatile sulphur (AVS). Sulphur from the liberated H₂S was precipitated as Ag₂S after bubbling through a 0.1 M AgNO₃ trap (AVS-S was always below detection; <0.001 wt% S). The extraction was performed in a sealed reaction vessel and processed for 1 h under a flow of N₂ gas. The samples were then sequentially treated with a boiling CrCl₂ solution. Then the Ag₂S precipitates were filtered under vacuum, and dried overnight. The concentrations of sulphide S and Fe were then determined stoichiometrically. Based on repeated measures (five runs), acceptable precision was achieved with relative standard deviation (RSD) of 4.25 %.

Table 3.4: Shows the accuracy and precision of the analytical method

Sample	Fe as FeS₂ wt%
MSB16	1.89
MSB16	2.08
MSB16	2.11
MSB16	2.09
MSB16	2.14
Mean	2.062
% RSD	4.25

3.3.4.2 Sequential iron extractions

3.3.4.2.1 Sodium acetate

Carbonate iron in these samples is expected to be mainly present in the form of siderite (FeCO₃) and ankerite (Fe,Mg(CO₃)), with minor amounts potentially substituted within the CaCO₃ mineral lattice (Poulton and Canfield, 2005). This fraction of iron was extracted using 1 M sodium acetate solution adjusted to PH 4.5 with acetic acid. The air dried powdered sediments were packed into plastic centrifuge tubes, and 10 ml of the sodium acetate solution was carefully added to each sample to avoid any potential strong reaction due to the high carbonate contents of some samples. The tubes were left to stand for a while to release any gases. Then, sealed tubes were placed on a shaking table at 50 °C for 48 h. After that samples were centrifuged and an aliquot of the solution was diluted for subsequent analysis by flame atomic absorption spectroscopy (AAS). The remaining solution was carefully discarded and the sediment was then subjected to the next stage of the extraction.

3.3.4.2.2 Sodium dithionite

Immediately after the first pool of iron was extracted, the remaining sediment was treated with 10 ml sodium dithionite solution (50 g/L) that was buffered to pH 4.8 with 0.35 M acetic acid/0.2 M sodium citrate (the dithionite solution was always used immediately after preparation). The extraction process continued for two hours at room temperature to selectively extract highly reactive iron oxides (e.g. ferrihydrite, lepidocrocite, goethite, hematite and akaganite) and this pool is termed Fe_{ox}. Samples were then treated and analysed as above.

3.3.4.2.3 Ammonium oxalate

The third step extracts magnetite Fe (Fe_{mag}). This iron fraction was extracted using a 0.2 M ammonium oxalate/0.17 M oxalic acid solution, with 10 ml of the solution added to the remaining sediment and shaken for 6 hours, followed by treatment and analysis as described above.

3.3.4.3 Boiling HCl extractable iron

The hot HCl extraction method of Berner (1970) and Raiswell et al. (1994) was used to extract and determine the poorly reactive iron fraction. The remaining sediments after the first three sequential extractions were washed into clean quartz test tubes using distilled water and left to dry in an oven at 50°C for several days. 5 ml of concentrated HCl (12 M) was added and heated to near-boiling for the first minute and then boiled vigorously for the second minute with care to avoid any spillage during boiling. Samples were then quenched with distilled water straight away and transferred to 100 ml volumetric flasks and filled with distilled water. Prior to analysis by AAS, samples were shaken well and allowed to stand overnight.

Table 3.5: Shows the accuracy and precision of the iron speciation analytical method

sample	Fe_{carb} wt%	Fe_{ox} wt%	Fe_{mag} wt%	Fe_{PRS} wt%
LSB4	1.01	0.83	0.33	1.49
	1.14	0.79	0.27	1.32
	1.16	0.83	0.30	1.50
	1.12	0.80	0.24	1.48
mean	1.11	0.81	0.29	1.45
std	0.07	0.02	0.04	0.08
%RSD	6.03	2.50	13.77	5.78

3.3.5 Total Sediment Dissolutions

Approximately 300 mg of powdered whole-rock material was initially ashed at 550 °C overnight in porcelain crucibles. After combustion, samples were transferred into teflon beakers where the sample was completely dissolved using near-boiling hydrofluoric acid/perchloric acid/nitric acid. Once the acids had evaporated (usually overnight), 5 ml of concentrated boric acid was added to redissolve any aluminium hexafluorates that may have formed, and the samples were heated to dryness. Then 5 ml of 50% HCl was added and heated to dissolve all salts. The sample was transferred to a volumetric flask and diluted with distilled water to the required volume (100 mL). Measurement of total iron was carried out

using atomic adsorption spectroscopy (AAS). Contents of major and minor elements (Al, P, Cu, Mo, V, Zn and Mn) were measured by Inductive Coupled Plasma Optical Emission Spectrometry (ICP-OES, Perkin-Elmer Optima 3300RL), equipped with a cross-flow nebulizer for major, and with an ultra-sonic nebulizer for minor element measurements. Standard reference materials (table 2.4) were run parallel to the samples. Based on triplicate measures, very high precision was achieved with low relatively standard deviation (RSD) for the (Al, Fe, Mn, V, Zn and Cu) that is less than 1. The P and Mo showed less accuracy but still good with RSD slightly above 1.

Table 3.6: shows the accuracy and precision of the trace element analytical method

Sample	Cu µg/g	Zn µg/g	Mo µg/g	V µg/g	Mn µg/g	Al µg/g	P µg/g	Fe wt%
MSB20	26.27	99.85	4.12	127.47	295.74	100915.25	526.98	7.30
MSB20	27.16	100.11	3.24	122.87	282.65	96478.32	511.11	6.98
MSB20	25.75	98.68	4.61	128.81	296.65	101147.32	529.37	7.29
Mean	26.39	99.55	3.99	126.38	291.68	99513.63	522.49	7.19
SD	0.71	0.76	0.69	3.11	7.83	2631.21	9.92	0.18
%RSD	2.69	0.76	17.40	2.46	2.69	2.64	1.90	2.53
St 05-10	172.90	285.40	32.46	242.25	168.91	75648.06	453.37	7.76
St 05-10	171.39	285.96	32.01	243.48	168.55	75606.08	439.13	7.71
St 05-10	174.81	287.41	31.74	242.52	167.60	75591.98	460.28	7.61
Mean	173.03	286.26	32.07	242.75	168.35	75615.37	450.93	7.69
SD	1.72	1.03	0.37	0.65	0.68	29.17	10.78	0.08
%RSD	0.99	0.36	1.15	0.27	0.40	0.04	2.39	0.99

CHAPTER 4 - AN ORGANIC GEOCHEMICAL PROFILE OF THE PLIENSCHACHIAN-EARLY TOARCICAN OF STAITHES AND PORT MULGRAVE (NORTH EAST YORKSHIRE, UK)

4.1 Introduction

The development of marine organic matter-rich black shales has been a focus of geological, paleontological, and geochemical studies for many decades. This relates to their unique significance for preserving fossils and for providing economic potential as source rocks for hydrocarbons. Among the Mesozoic black shales in Central Europe, those deposited during the Early Toarcian during the Toarcian Oceanic Anoxic Event (T-OAE) have received special attention (Jenkyns, 1988; Oschmann, 1995; Baudin, 1995) in order to investigate the origins of the T-OAE and the extinction episodes associated with this event (Hesselbo and Jenkyns 1995; Salen et al 2000; Kemp et al., 2005; Wignall et al 2005; McArthur et al., 2008; Caswell et al., 2009). However, in terms of controls on source rock potential and biogeochemical processes during deposition, the nature and preservation of the organic matter in the sediments is clearly of major interest. Furthermore, organic biomarker distributions within the sediment can provide fundamental information on depositional redox conditions, allowing consideration of links between redox and organic matter quality and preservation. Thus, the geochemical properties of the organic matter deposited during the Early Toarcian on the North Yorkshire coast, and its dependence on paleoenvironmental conditions of sedimentation, are the focus of this chapter.

4.2 Results

Apart from the approximately 20 - 50 cm thick, three organic-rich, laminated silty 'sulphur beds' at its base, the lower part of the Grey Shale Member is characterised by a relatively normal benthic fauna (Salen et al., 2000). The topmost part of the Grey Shale Member is an organic rich shale that is lithologically, palaeoecologically, and geochemically more similar to the overlying Jet Rock Member. The lower 8 m of the Jet Rock Member (*H. exaratum Subzone*) is composed of the most finely, continuously laminated and most organic and sulphur-rich shales with the highest hydrogen indices and the lowest $\delta^{13}\text{C}_{\text{TOC}}$ values (Demaison and Moore, 1980)

Table 4.1: Stratigraphic summary for the Lower Whitby Mudstone Formation modified from Salen et al. (2000); d (m) is the cumulative distance from the top of bed to base of the Grey Shale Member. The bed numbers are from Howarth (1962, 1973).

Age	Subzones	Mbr.	Bed No	Lithological description
Lower Toacian	<i>H.exartum</i>	Jet Rock Member	39	Top Jet Dogger, laminated, grey limestone
			38	Shale, grey, bituminous with scattered calcitic nodules
			37	The Curling stones
			36	Shale, grey, bituminous
			35	The Whale stones, thin-bedded bituminous shale
			34	Shale, grey, bituminous
			33	The Cannon ball doggers
	<i>D.tenucostatum</i>	Grey Shale Member	32	Shale, grey, bituminous
			1-31	Shale, grey, not bituminous with occasional calcareous nodules
	Upper Pliensbachian	<i>P.apyrenum</i>	Kettleiness Member	38-56

4.2.1 Bulk Geochemistry

4.2.1.1 Total Organic Carbon (TOC), Total Carbon (TC) and Total Sulphur (TS).

The concentration of total organic carbon (TOC) of the samples is shown in Figure 4.1 as weight percent (wt %). Samples of the *Falciferum* zone contain significantly more organic material than those in the underlying and overlying zones. Geochemical analyses reveal that shales in the (lower) *Exaratum* Subzone contain more organic material than the (underlying) *tenuicostatum* zone. These results are consistent with previously reported trends (Morris 1980; Salen et.al, 2000; Jenkyns and Clayton 1997) from the same section.

Overall, the study section is characterized by fluctuating organic carbon content. Moderate to low organic matter contents of <1.5% TOC characterise the bioturbated

mudstone of the middle and lower part of the Grey shale (*upper Hawskerense* to *middle Semicelatum*) with exceptions for the laminated organic rich horizons of the Sulphur Bands, where organic carbon contents increases up to 7%. Further up section, throughout the uppermost part of the *tenuicostatum* zone and the entire *exartum* subzone (T-OAE interval), TOC tends to be consistently high with an average value of 7%. The TOC reaches its maximum values of 14% at the interval of the whale stones within the *exartum* subzone (top of Bed 34 and throughout Bed 35) beyond which TOC tends to decrease into the *Falciferum* subzone.

The higher resolution data at the Pliensbachian-Toarcian boundary interval displays repeated intervals (Sulphur Bands) where the TOC suddenly increases from background of around 1 wt% to above 3 wt% with spacing of more or less 2 m between peaks in TOC. Detailed analysis of these Sulphur Bands reveals variation in the organic carbon content at the cm scale. The Lower Sulphur Band shows the highest variation in the organic carbon. The approximately lower 8 cm have moderate TOC averaging around 1.5 wt%. TOC then increases to 6.8 wt% and decreases back to less than 1 wt% before it increases again to 6 wt% in the top part of the Lower Sulphur Band.

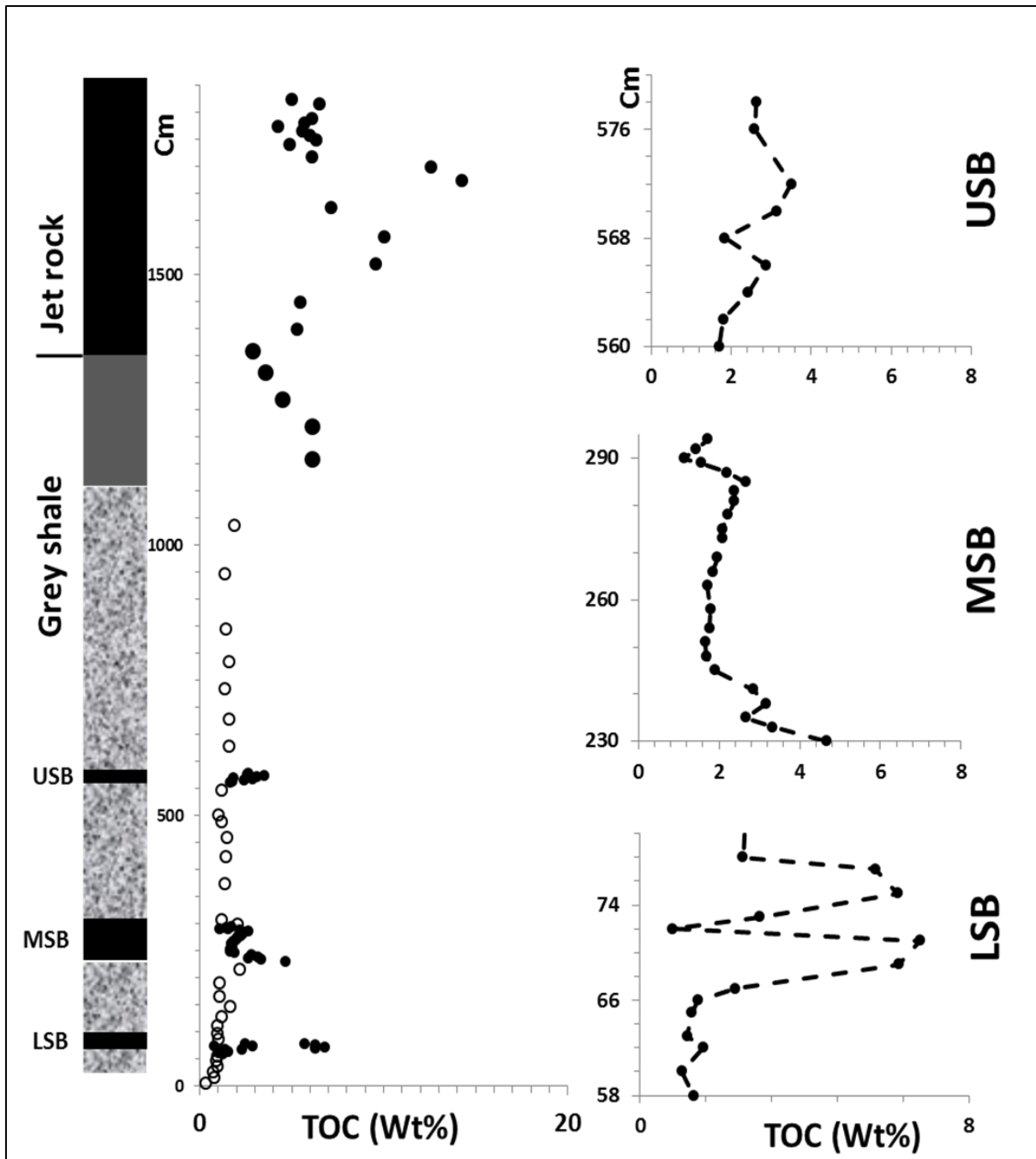


Figure 4. 1: Variation of total organic carbon content throughout the study section at Port-Mulgrave section. LSB = Lower Sulphur Band; MSB= Middle Sulphur Band; USB= Middle Sulphur Band

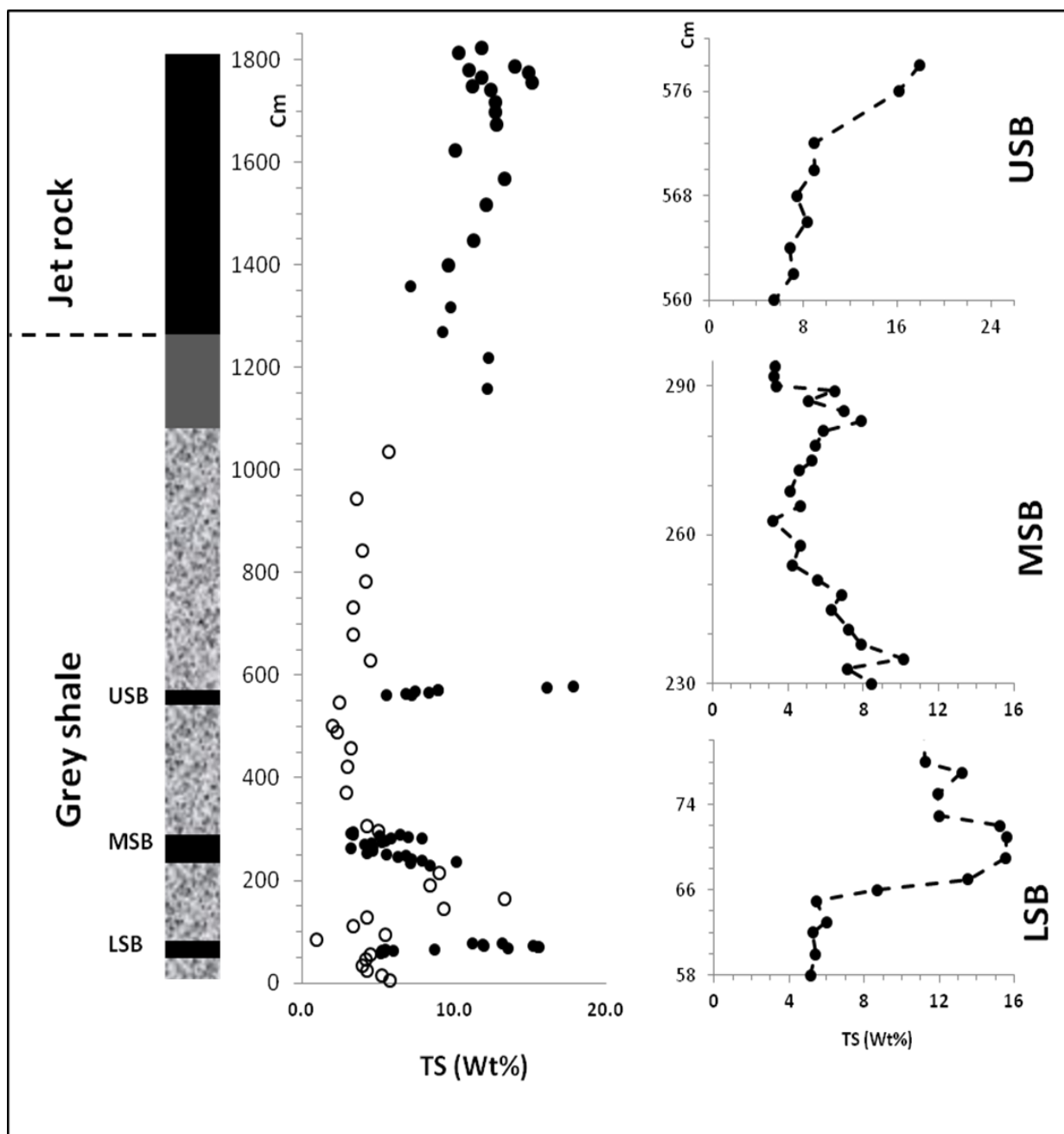


Figure 4. 2: Variation of total sulphur TS content throughout the study section at Port Mulgrave section.

The sulphur content fluctuates throughout the study section (Figure 4.2). The TS data behave similar to the TOC where it tends to be consistently high (TS >7 wt %) throughout the uppermost part of the *tenuicostatum* zone and the entire of *exartum* subzone. A cross plot of TOC versus TS (Figure 4.2.3) shows weak correlation ($r^2=0.4$). The organic content tends to decrease above the whale stone horizon (Bed 35) from values around 14 wt% to less than 5

wt%. On the other hand the TS profile shows less variation with high concentrations of TS that continues above 10 wt% throughout the Jet Rock Shale.

The bioturbated mudstones of the Grey shales are characterized by relatively low TS content with an average of 3.8 wt %. The Sulphur Bands are characterized by exceptionally high values of up to 18%, in stark contrast to less than 2% measured in the bioturbated mudstones directly above and below.

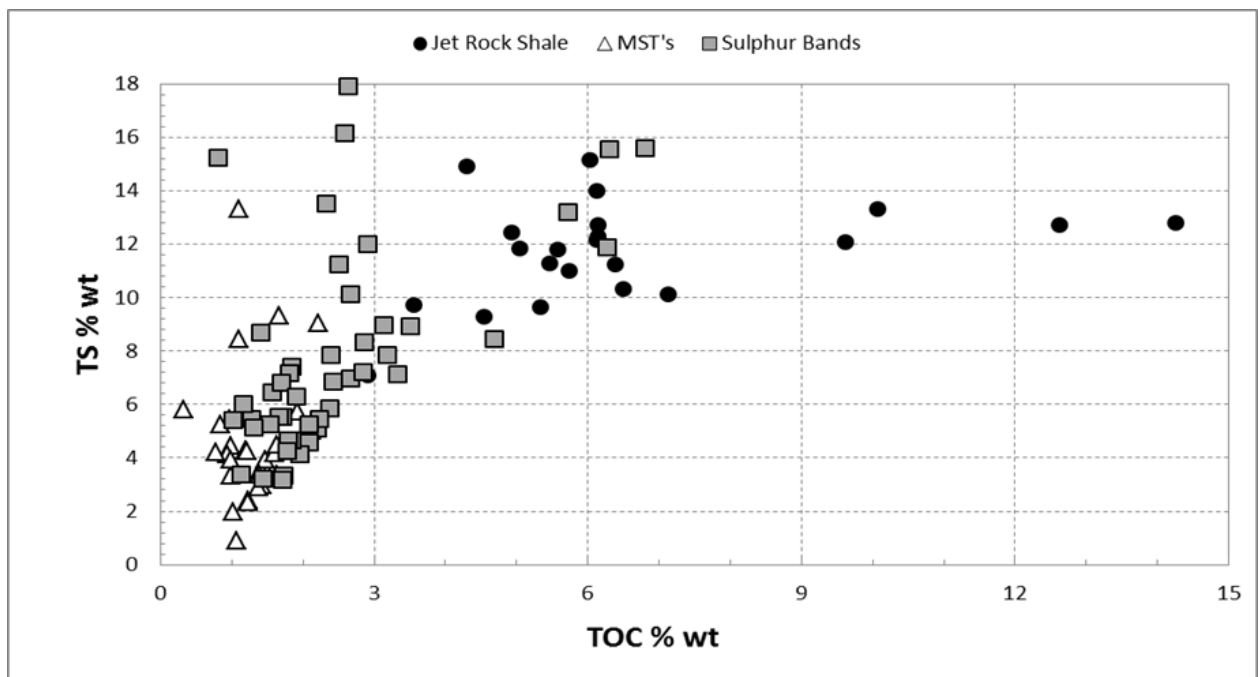


Figure 4. 3: Cross plot of the TOC% versus the TS% of the studied samples. Regression lines for the average S and C relationships in sediments deposited under normal marine and euxinic conditions, supplied by Berner (1984) and Leventhal (1995), are shown.

The $\delta^{13}\text{C}_{\text{TOC}}$ values of the study section range from about -26‰ to -32‰, clearly showing the diagnostic negative C excursions at the onset of the Toarcian-OAE (Figure 4.4). At the study site the main negative C excursion has a magnitude of approximately -7‰, consistent with previous studies (Kuspert 1982; Hesselbo et al., 2000; Cohen et al. 2004; Kemp et al. 2005). The $\delta^{13}\text{C}_{\text{TOC}}$ profile fluctuates through the section and shows a mirror image to TOC. Notably, there are three small scale negative excursions with a magnitude of almost -4‰ spanning the sulphur bands. The first peak occurs in the upper *P. hawskerense* Subzone in the latest Pliensbachian, where $\delta^{13}\text{C}_{\text{TOC}}$ culminates in values of approximately -29.5‰ within the lower sulphur band. Above, $\delta^{13}\text{C}_{\text{TOC}}$ returns to pre-excursion values of

about -25.5‰ within the base of the *P. paltum* Subzone, followed by a second peak of -28‰ at the Middle Sulphur bed. After the third peak that responds to the upper sulphur band the $\delta^{13}\text{C}_{\text{TOC}}$ returns to pre-excursion values until the onset of the larger negative carbon-isotope excursion marking the Early Toarcian OAE, in the *D. tenuicostatum* Zone.

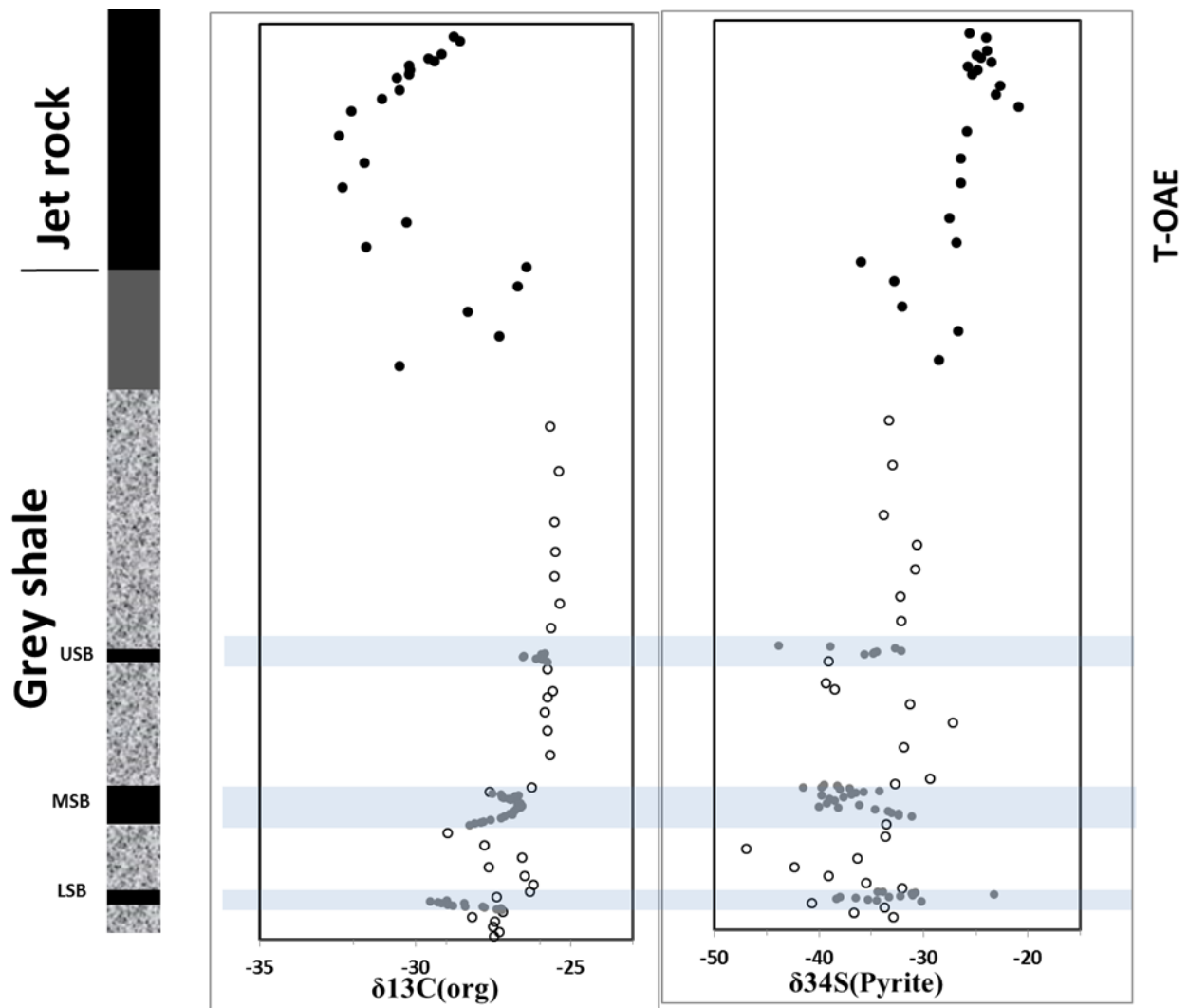


Figure 4. 4: Variation of the $\delta^{13}\text{C}$ and $\delta^{34}\text{S}$ values through the study section at Port Mulgrave.

The sulphur isotope record ($\delta^{34}\text{S}$) ranges from -46.9‰ to -20.8‰ (Figure 4.4). The Grey Shale samples including the Sulphur Beds shows lighter $\delta^{34}\text{S}$ values compare to the Jet Rock Shale with broader range of variation from -23.2 to -46.9‰ (averaging at -34.9). On the other hand, the Jet Rock Shale samples showed heavier values clustering over a narrow range from -20.8 to -27.4‰ with an average of -24.7‰.

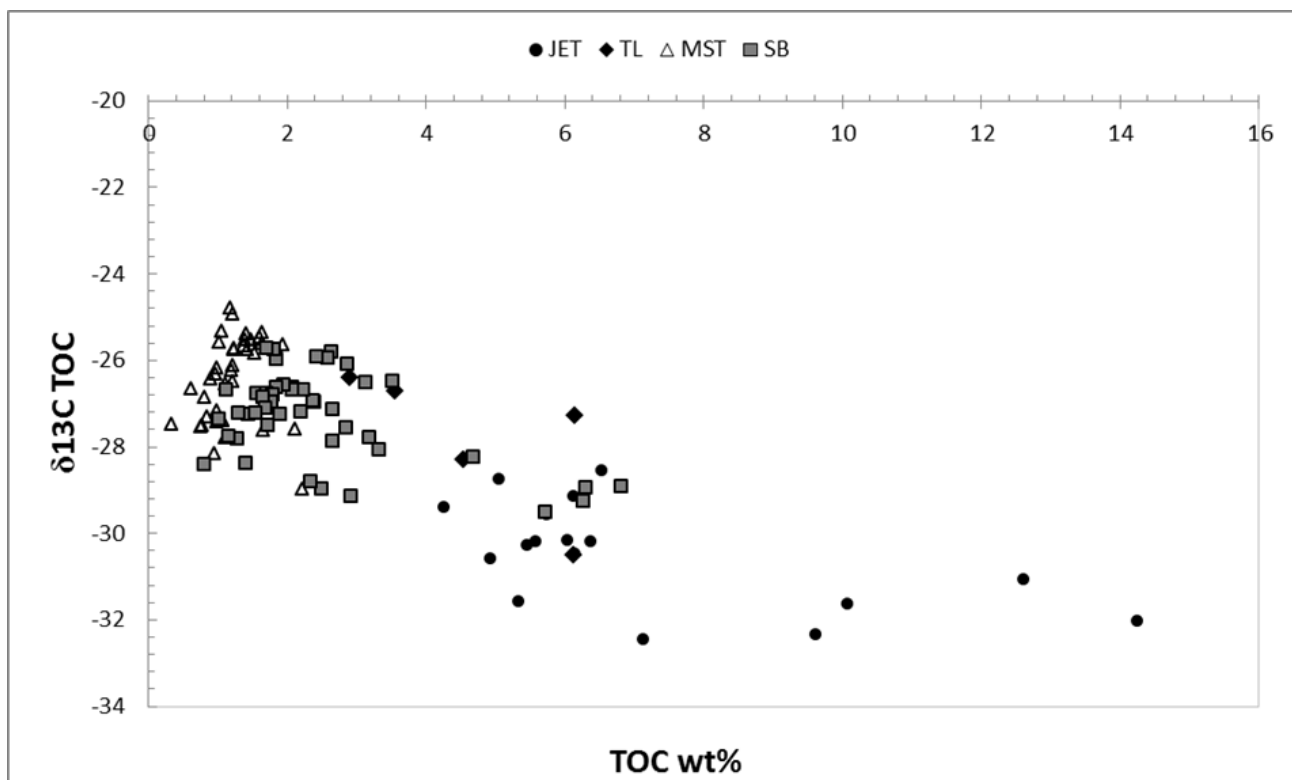


Figure 4. 5: Cross plot between $\delta^{13}C_{TOC}$ and % TOC for the study section at Port Mulgrave

Table 4.2: Summary table of the bulk geochemistry data: TOC= total organic carbon; TC= total carbon; TIC= total inorganic carbon; TS= total sulphur.

Stratigraphic unit		TOC wt %	TC wt %	TIC	CaCO₃ wt%	TS (wt%)
JET (17 samples)	Range	14.3 - 2.8	6.1 - 16.1	0.7 - 5.8	6.1 - 49.1	9.6 - 15.1
	Mean	7.1	9.2	2.0	16.5	12.2
	SD	2.8	2.9	1.3	10.9	1.6
TL (5 samples)	Range	6.1 - 1.5	3.3 - 6.7	0.2 - 0.8	1.9 - 6.7	7.1 - 12.3
	Mean	4.7	5.1	0.4	3.7	10.1
	SD	1.5	1.6	0.2	1.9	2.2
4-MST (7 samples)	Range	1.9 - 0.2	1.9 - 2.2	0.2 - 0.8	2.0 - 6.3	3.3 - 5.7
	Mean	1.6	2.1	0.5	4.0	4.1
	SD	0.2	0.1	0.2	1.4	0.8
USB (9 samples)	Range	1.7 - 3.5	1.9 - 4.1	0.1 - 0.6	0.9 - 4.9	5.5 - 17.8
	Mean	2.5	2.9	0.3	2.8	9.7
	SD	0.6	0.8	0.2	1.4	4.3
3-MST (8 samples)	Range	1.0 - 2.1	1.3 - 3.8	0.1 - 1.7	0.5 - 14	1.9 - 5
	Mean	1.4	1.8	0.3	2.8	3.1
	SD	0.3	0.8	0.5	4.5	1.0
MSB (24 samples)	Range	1.1 - 4.7	1.7 - 5.0	0.04 - 0.6	0.3 - 4.9	3.2 - 10.1
	Mean	2.2	2.5	0.3	2.1	5.7
	SD	0.8	0.8	0.2	1.3	1.8
2-MST (8 samples)	Range	0.9 - 2.2	1.3 - 4.7	0.2 - 3.6	1.8 - 30.3	0.9 - 13.3
	Mean	1.3	2.5	1.1	9.0	6.8
	SD	0.4	1.3	1.2	9.8	4.0
LSB (14 samples)	Range	0.8 - 6.8	0.8 - 7.1	0.1 - 1.6	0.7 - 13.7	5.1 - 15.5
	Mean	2.3	3.6	0.6	5.0	10.3
	SD	2.3	2.3	0.5	4.0	4.2
1-MST (6 samples)	Range	0.3 - 0.1	0.8 - 1.1	0.01 - 0.7	0.1 - 5.9	3.9 - 5.8
	Mean	0.81	0.99	0.16	1.31	4.64
	SD	0.25	0.09	0.27	2.23	0.72

4.2.1.2 Rock- Eval pyrolysis

Rock-Eval pyrolysis is the one of the standard petroleum industry screening methods to assess the source rock potential and quality of rocks. As is the case with TOC analysis, Rock-Eval pyrolysis is quick and easy to carry out, but there are also problems which must be addressed when interpreting the data, such as the mineral matrix effect, especially when dealing with organic poor sediments with TOC less than 0.3wt% (Bordenave et al., 1993).

The data collected from Rock-Eval show mobile hydrocarbons as S1. The lowest S1 value of 0.08 (mg HC/g rock) was recorded within the bioturbated mudstone units, whereas the highest value is 88 (mg HC/g rock) recorded in the Lower Sulphur Bed.

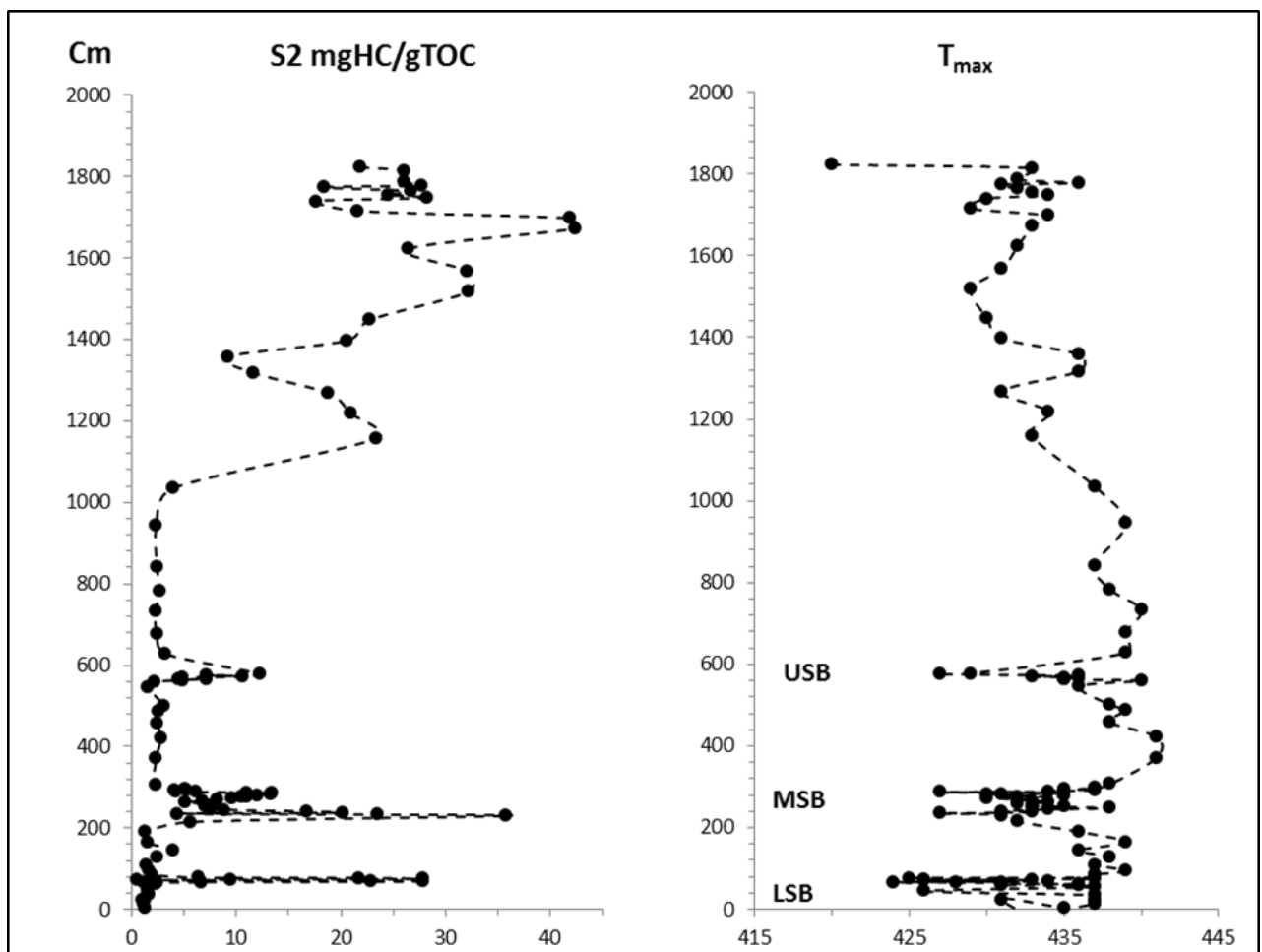


Figure 4. 6: S2 and Tmax variation throughout the study section at Staithes. Note the suppressed T_{max} values for the Sulphur Bands

The second parameter from Rock Eval Pyrolysis is the hydrocarbon potential from the kerogen fraction (S_2) as result of increasing temperature. The data is summarised in Table 4.3 Excluding the bioturbated mudstone samples, the samples show good generative potential (Peters 1986) with a S_2 average of 12.9 mg HC/g Rock. The Jet Rock and the top laminated unit of the Grey shale also show consistently good source potential (10-20 mg HC/g Rock). The crossplot of S_2 versus TOC shows that the Sulphur Band samples tend to segregate from the rest of the samples with a relatively higher slope of S_2 /TOC (corrected HI index). On the other hand, the most organically rich part of the Jet Rock (Bed 35; Whale stone) is characterized by relatively lower S_2 /TOC values (figure 4.7). A similar variation of the generative potential parameters is recorded at the cm scale within the Sulphur Bands.

The T_{max} values from Rock Eval pyrolyses range between 420 °C and 440 °C with an average of 435 °C. Notably, the sulphur beds have low mean T_{max} values of 430 °C. The relatively low Tmax within the Sulphur Bands and the Jet Rock Shale are associated with higher contents of organic sulphur.

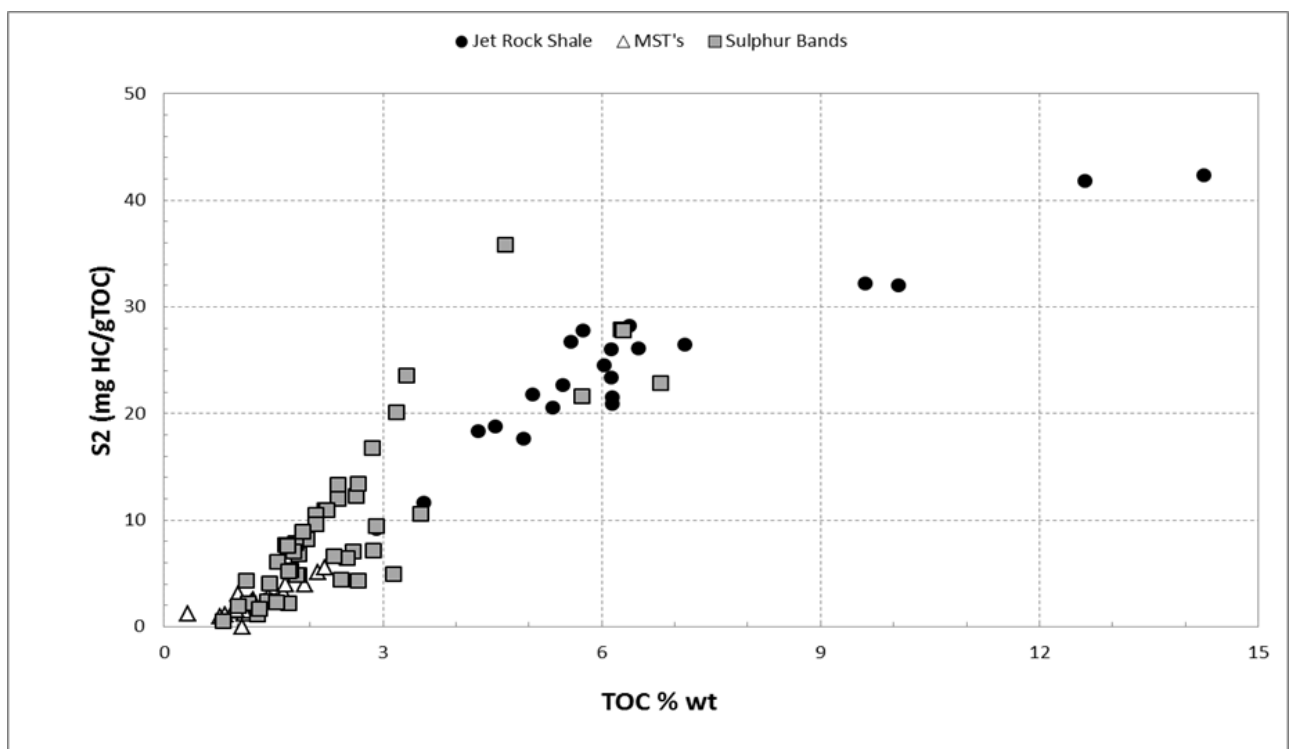


Figure 4. 7: S₂ versus TOC relationship for the Port Mulgrave samples

Table 4. 3: Summary table for the Rock-Eval data.

Sampled interval		S1 mgHC/g	S2 mgHC/g	PI	T _{max}	HI mgHC/g TOC
JET (17 samples)	Range	2.1 - 7.9	17.6 - 42.4	18.6 – 43	420 - 436	297.4 - 483.5
	Mean	4.6	26.9	27.9	431.2	392.0
	SD	1.5	7.1	7.7	3.4	55.0
TL (5 samples)	Range	0.7 - 3.8	9.2 -23.4	10.2 – 24.4	431 - 436	316.9 - 415.5
	Mean	2.2	16.8	17.8	434.0	356.7
	SD	1.3	6.1	6.1	2.1	41.2
4-MST (7 samples)	Range	0.2 - 0.4	2.3 - 4.0	3.3 – 4.98	437 - 440	146.4 - 206.5
	Mean	0.2	2.8	3.8	438.4	173.7
	SD	0.1	0.6	0.6	1.1	20.9
USB (9 samples)	Range	0.2 - 1.0	2.2 - 12.2	3.2 – 13.2	427 - 440	131.4 - 464
	Mean	0.6	6.5	7.5	434.0	255.1
	SD	0.2	3.2	3.2	3.9	98.0
3-MST (8 samples)	Range	0.2 - 0.5	1.6 - 5.2	2.6 - -6.2	436 - 441	127.6 - 301.4
	Mean	0.3	2.8	3.8	438.5	200.9
	SD	0.1	1.1	1.1	1.8	53.6
MSB (24 samples)	Range	0.3 - 3.0	4.0 - 35.8	5.1 – 36.8	427 - 438	162.0 - 765.2
	Mean	0.9	10.9	11.8	432.7	460.7
	SD	0.6	7.3	7.3	2.7	133.9
2-MST (8 samples)	Range	0.1 - 0.5	1.3 - 5.6	2.3 – 6.6	432 - 439	116.4 - 252.5
	Mean	0.3	2.6	3.6	436.8	180.0
	SD	0.1	1.6	1.6	2.3	48.4
LSB (14 samples)	Range	0.2 - 88.0	0.6 - 27.9	1.6 – 28.9	424 - 437	72.3 - 444.3
	Mean	7.1	9.6	10.6	431.1	247.1
	SD	23.3	10.5	10.5	4.6	124.2
1-MST (6 samples)	Range	0.1 - 0.3	1.0 - 1.6	2 – 2.6	426 - 437	131.2 - 387.9
	Mean	0.2	1.4	2.4	434.8	189.3
	SD	0.1	0.2	0.2	4.4	98.3

Rock-Eval Quality Indices

The Hydrogen indices (HI) range between 42 and 765 (mg HC/g TOC). Hydrogen index values over 100 indicate that organic matter is of kerogen type II and III (Tyson, 1995). The bioturbated mudstone of the Grey shale are characterized by low HI values (less than 100 mg HC/g TOC) whereas most of the low HI values occur within bioturbated mudstone. The highest HI values were recorded within the Middle sulphur bed while the Jet Rock samples characterized with relatively suppressed HI values. Figure 4.8 illustrates the relationship between HI and TOC. HI exhibits a positive linear correlation for the Sulphur Beds but a negative correlation for the Jet Rock samples where the HI values tend to be suppressed relative to TOC.

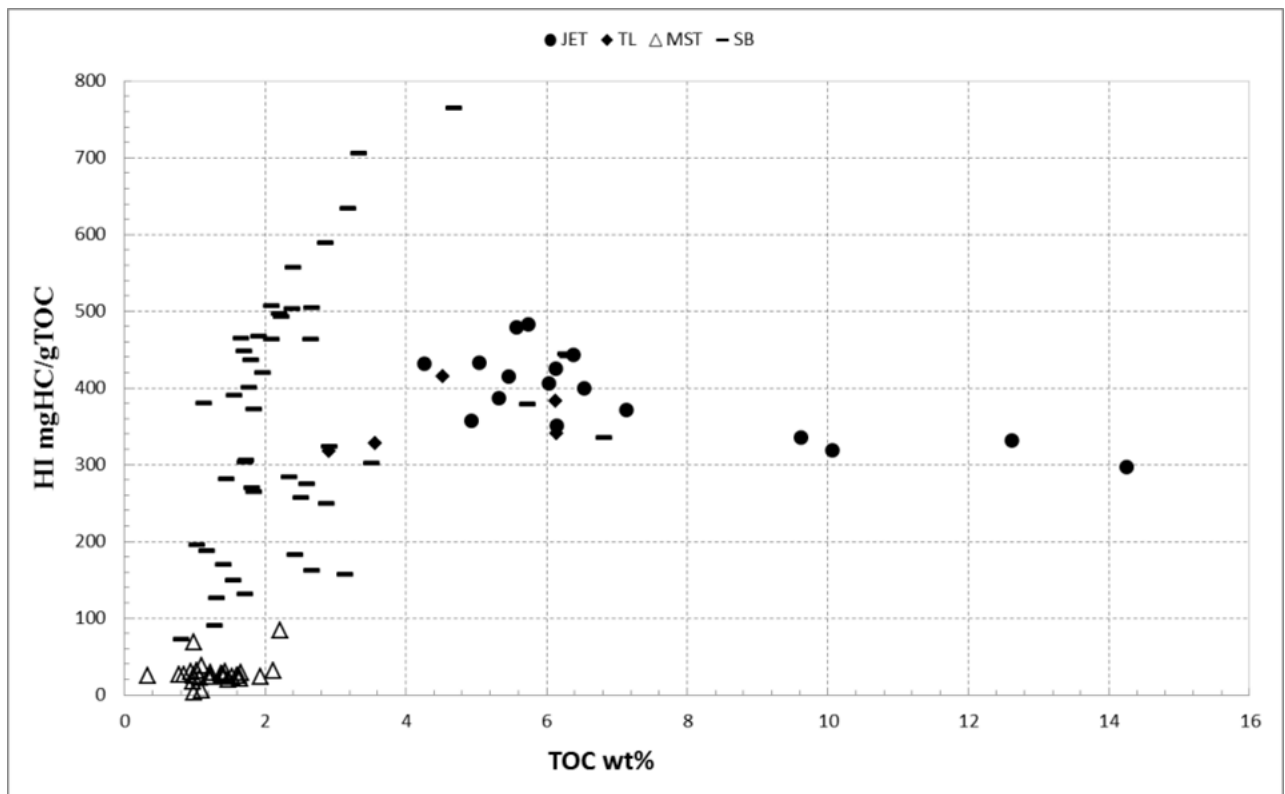


Figure 4.8: HI versus TOC % wt for the study section at Port Mulgrave

The Production index (PI) transformation ratio was calculated by using the formula $S_1 / (S_1 + S_2)$, often used as a maturation parameter (Peters, 1986). The highest values were recorded within the Jet Rock shale with a mean PI value of 27.9 and a total range between 18.6 and 43. The PI is plotted in Figure 4.9 and shows low PI for the Grey Shale, except for the Sulphur beds, which show distinctly higher values.

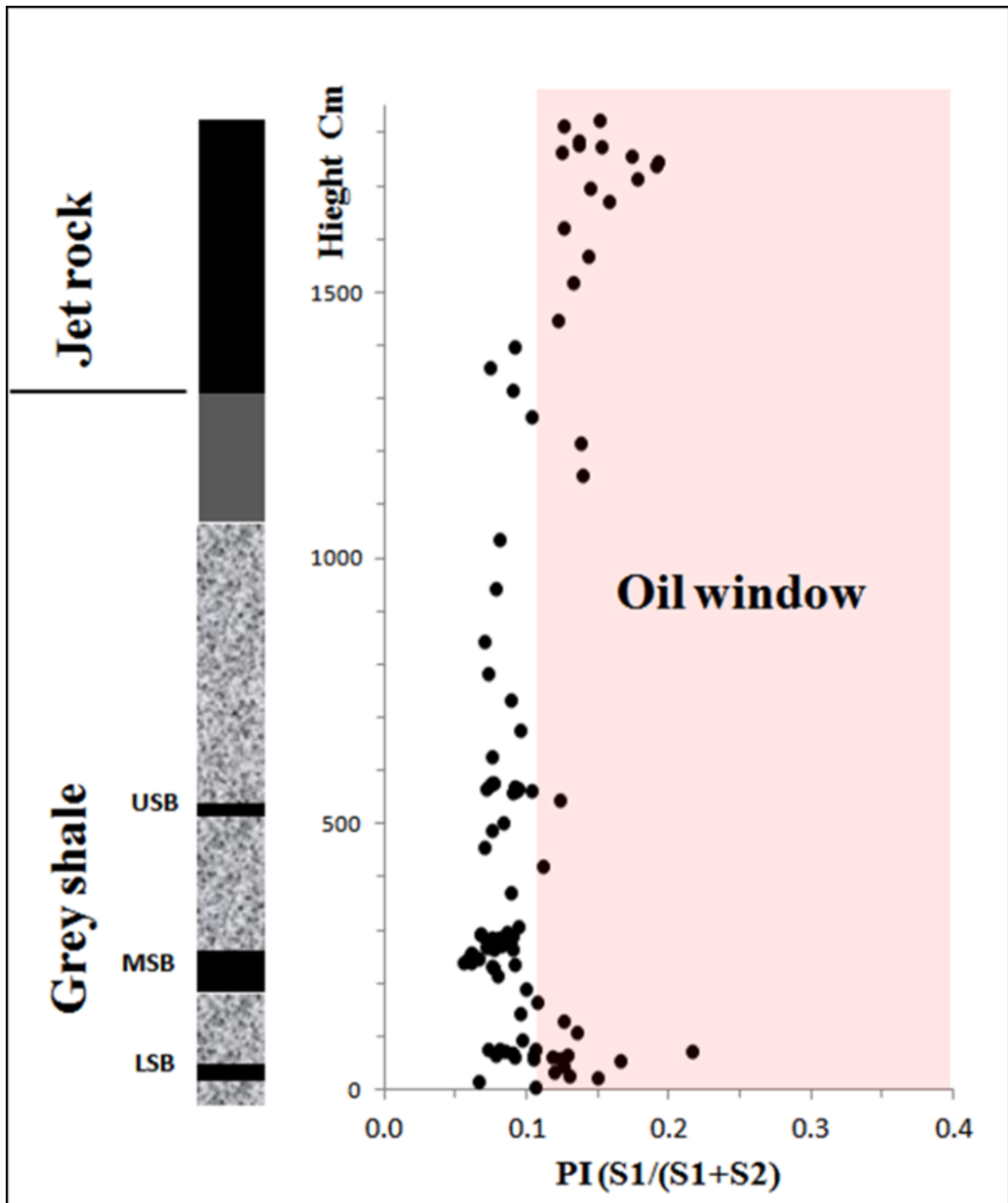


Figure 4.9: Production index profile cross the study section at Port Mulgrave. $PI = S1/(S1+S2)$

4.2.2 Molecular biomarkers

Molecular biomarker analysis of aliphatic fractions focused on three groups, normal alkanes, steranes and diasteranes, and pentacyclic triterpanes and their derivatives (Hopanes). The results based on integration of peaks in various ion chromatograms are summarized in Tables 4.4 and 4.5.

4.2.2.1 *n*-alkanes distribution

The aliphatic fractions of the extracted bitumen of 50 selected samples were analysed using Gas Chromatography (GC) in order to show the molecular variation across the study section. Figure 4.2.10 shows the aliphatic GCs of samples from the Lower sulphur, the bioturbated mudstones and the Jet Rock shale. Whole gas chromatograms show a distribution of normal alkane from *n*-C₁₁ to *n*-C₃₃ and more with maximum peak heights being *n*-C₁₅. The GC traces show similar relative abundance of *n*-alkanes distributions throughout the section.

Unimodal distribution of *n*-alkanes characterizes most samples. Normal alkanes ranging from *n*-C₁₁ to *n*-C₃₃ are present in most samples. No visible signs of an undeveloped hump or loss of *n*-C₁₅ to *n*-C₂₅ indicates that significant biodegradation has not occurred. There is an odd/even predominance in most samples.

The carbon preference index CPI represents an odd carbon preference over even, and occurs in response to chemistry in higher plant of surface waxes (an important precursor of waxy components in sedimentary organic matter). Moldowan et al. (1985) concluded that an odd carbon preference is characteristic of oils derived from source rocks deposited in non-marine depositional environment. Therefore, if the total even and odd numbers of paraffins are equally abundant the value of the CPI will be equal to one, and it goes above one with more higher plant contribution to the organic matter, but causation must be taken when interpreting the CPI as it changes with thermal maturity (Tissot and Welte, 1984). CPI values in this study were obtained using the relationship proposed by Bray and Evans (1961) formula:

$$\text{CPI} = 1/2 \left(\frac{nC_{25} + nC_{27} + nC_{29} + nC_{31} + nC_{33}}{nC_{24} + nC_{26} + nC_{28} + nC_{30} + nC_{32}} + \frac{nC_{25} + nC_{27} + nC_{29} + nC_{31} + nC_{33}}{nC_{26} + nC_{28} + nC_{30} + nC_{32} + nC_{34}} \right)$$

All CPI values obtained are greater than 1.0 and in the range between 1.0 and 1.5 with exception for the base of the Lower Sulphur Band where a 0.75 CPI value is recorded (table 4.4). Although there is small variation in the CPI values within the Sulphur bands it can be

observed that the Sulphur Bands have relatively lower CPI values compared to the bioturbated mudstone units above and below. Moreover, the calculated ratio of $\sum(C_{21} - C_{31})/(C_{15} - C_{20})$ is used as degree of waxiness indication (Roushdy et al., 2010). There is an upward decrease in the $\sum(C_{21} - C_{31})/(C_{15} - C_{20})$ ratio (Figure 4.10). Apart from the Lower Sulphur Band, the Middle and lower part of the Grey shale are characterised by higher $\sum(C_{21} - C_{31})/(C_{15} - C_{20})$ ratios (consistently above 1) with an average of 1.58, while there is variation across the Sulphur band fluctuating between 0.71 to 4.14.

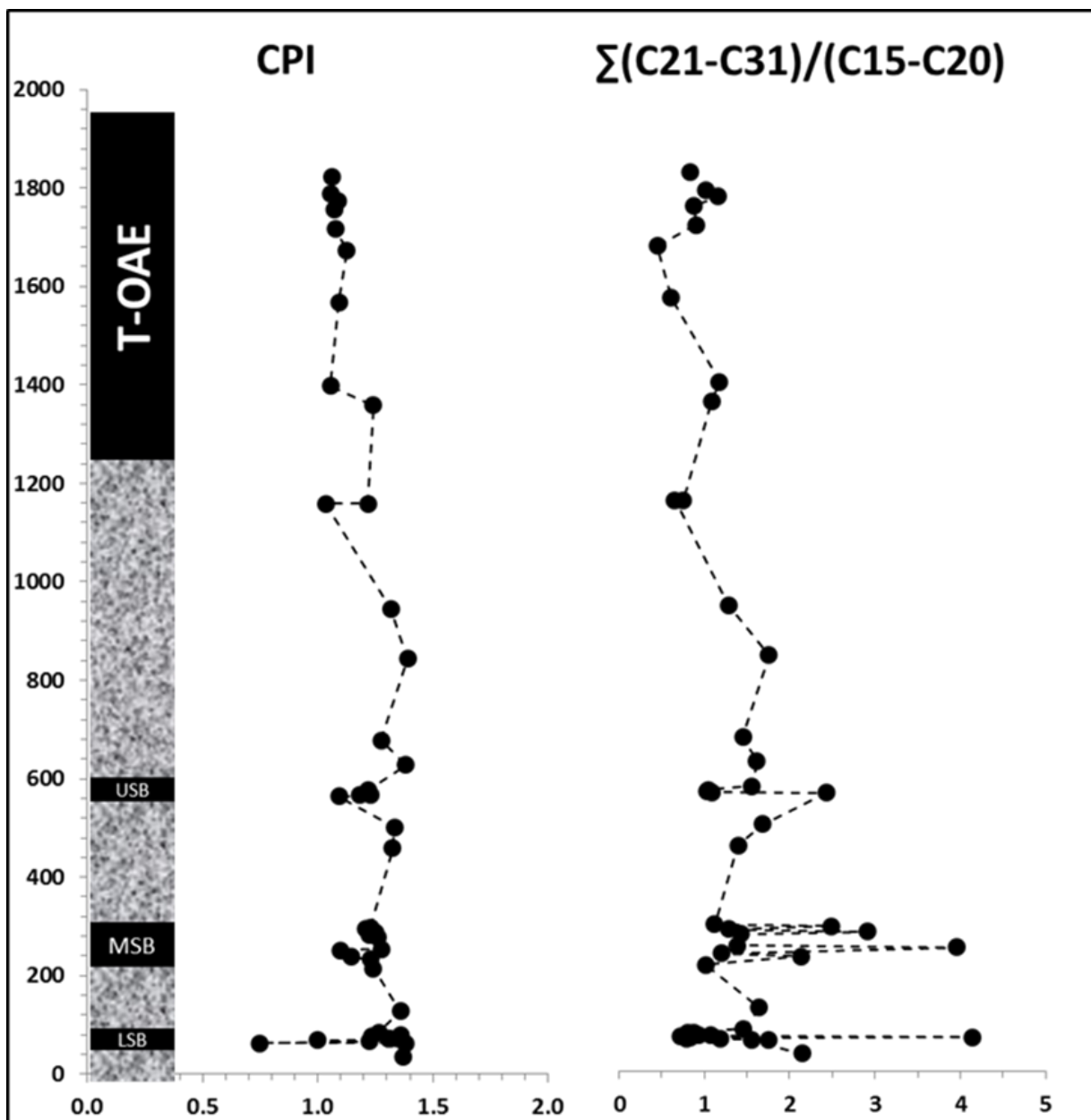


Figure 4.10: Variation of the Carbon Preference index CPI and $\sum(C_{21} - C_{31})/(C_{15} - C_{20})$ ratio throughout the study section at Port Mulgrave.

Table 4.4: showing the obtained normal alkanes and acyclic isoprenoids relative abundance and the calculated CPI values for the study section.

Sample	Height (Cm)	Pr/Ph	Pr/c17	Ph/c18	$\Sigma(C_{21}-C_{31}) / \Sigma(C_{15}-C_{20})$	CPI
Jet 17	1823	1.4	1.0	1.0	0.8	1.1
Jet15	1787	1.4	1.4	1.4	1.0	1.1
Jet 13	1774	1.3	1.3	1.3	1.2	1.1
Jet 11	1756	1.5	1.4	1.5	0.9	1.1
Jet 8	1716	1.3	1.4	1.4	0.9	1.1
Jet 6	1673	1.2	0.8	0.9	0.5	1.1
Jet 4	1568	1.3	1.3	1.3	0.6	1.1
Jet 1	1398	1.4	1.6	1.5	1.2	1.1
TL.5	1358	2.7	1.1	0.6	1.1	1.2
TL.4	1158	2.1	1.3	0.8	0.8	1.2
TL.1	1158	1.7	1.3	1.1	0.7	1.0
4-MST 6	945	4.4	0.9	0.3	1.3	1.3
4-MST 5	843	4.0	0.9	0.3	1.8	1.4
4-MST 2	678	4.3	0.9	0.2	1.5	1.3
4-MST 1	628	3.9	0.9	0.3	1.6	1.4
USB10	578	3.3	2.7	1.0	1.6	1.2
USB6	570	3.4	2.5	1.1	1.0	1.2
USB5	568	3.2	2.3	1.0	1.0	1.2
USB4	566	3.4	2.2	0.9	1.1	1.2
USB3	564	3.7	2.0	0.8	2.4	1.1
3-MST 7	501	4.6	0.9	0.2	1.7	1.3
3-MST 5	458	5.5	1.6	0.3	1.4	1.3
3-MST 1	297	3.7	1.7	0.6	1.1	1.2
MSB24	294	3.9	1.6	0.6	2.5	1.2
MSB 20	287	3.9	1.9	0.6	1.3	1.3
MSB18	283	3.3	2.0	0.9	2.9	1.2
MSB 16	278	3.5	1.9	0.7	1.4	1.3
MSB 9	254	4.1	1.5	0.5	1.4	1.3
MSB8	251	4.2	1.6	0.5	4.0	1.1
MSB 4	238	3.0	2.0	0.9	1.2	1.6
MSB2	233	2.9	2.8	1.0	2.1	1.2
2-MST 8	215	3.0	2.7	1.2	1.0	1.2
2-MST 4	128	5.0	1.2	0.3	1.7	1.4
2-MST 1	85	3.7	1.7	0.6	1.5	1.3
LSB14	78	2.9	2.7	1.2	0.9	1.4
LSB13	77	2.7	2.7	1.2	0.8	1.2
LSB11	73	2.7	2.8	1.3	0.9	1.3
LSB10	72	2.8	2.9	1.4	1.1	1.4
LSB9	71	2.9	2.8	1.3	0.7	1.3
LSB8	69	2.9	3.3	1.8	4.1	1.0
LSB4	63	1.0	2.6	1.3	0.1	0.8
1-MST 4	35	4.4	1.3	0.3	2.2	1.4

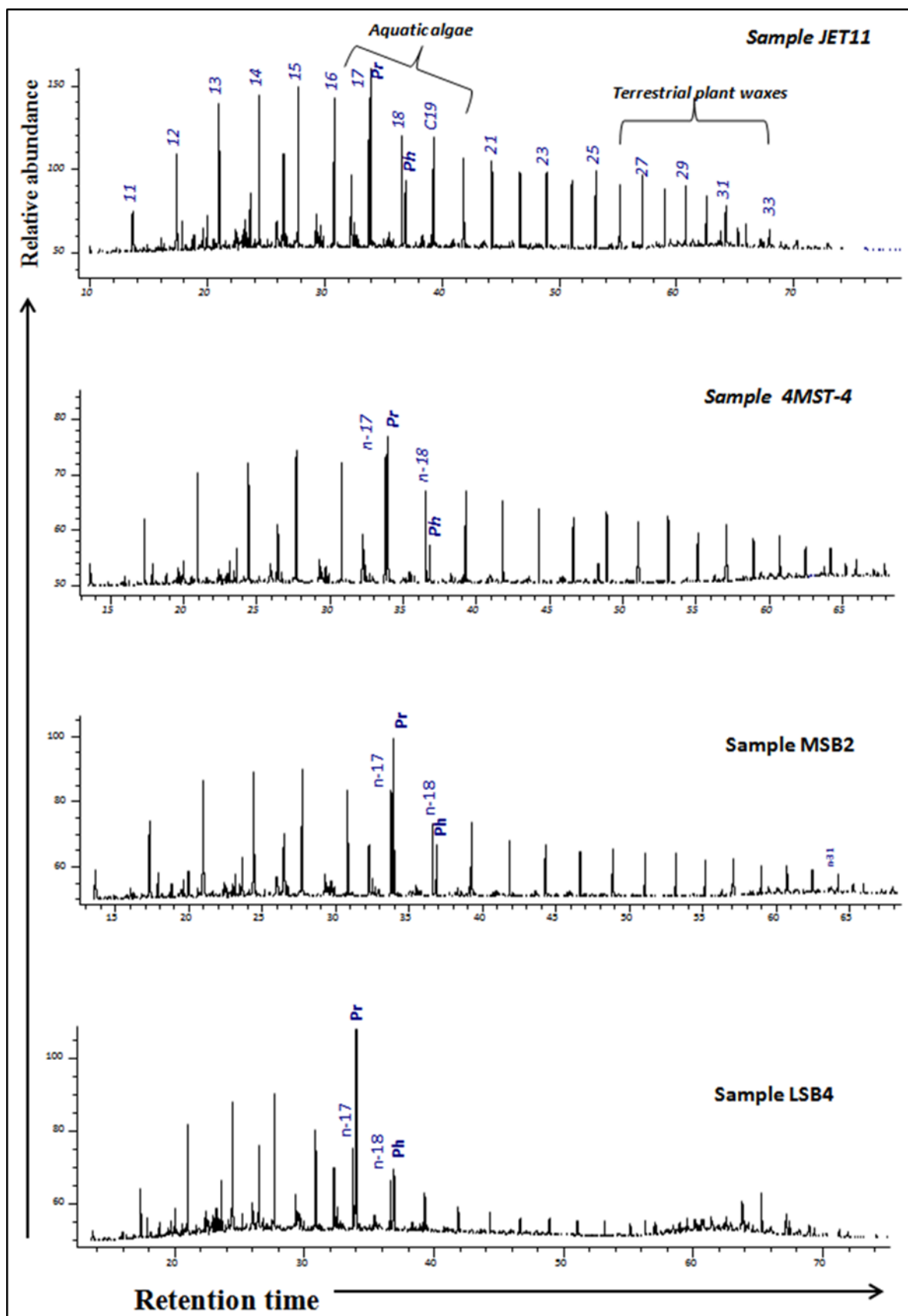


Figure 4.11: Chromatograms showing n-alkanes and isoprenoids of two representative samples. Number by the peaks give the number of carbon atoms in n-alkanes (Pr = Pristane, Ph = Phytane)

4.2.2.2 Acyclic isoprenoids

Pristane (Pr) and Phytane (Ph) were both present in all samples, the Pr/Ph ratio gradually decreases up section overall. The bioturbated mudstones and the Sulphur Bands show relatively higher Pr/Ph ratios with values above 3, while the Jet Rock samples have Pr/Ph values clustering around 1 (Figure 4.12).

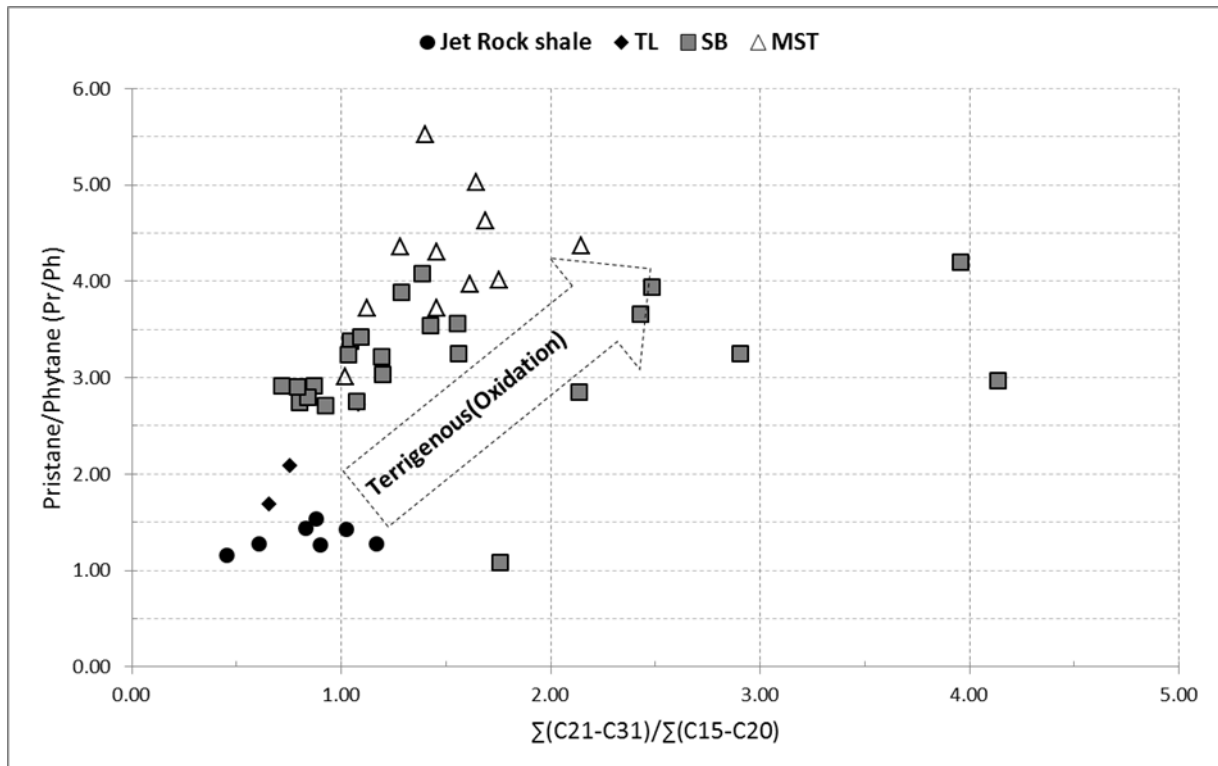


Figure 4.12: showing the relationship between degree of waxiness and Pr/Ph ratio for the study section

As shown in Figure 4.12, the Pr/n-C17 and Ph/n-C18 profiles follow the same pattern through the bioturbated mudstones. At the top laminated unit of the Grey shale and above the Pr/Ph ratio continues to decline, while the Pr/n-C17 and Ph/n-C18 tend to slightly increase.

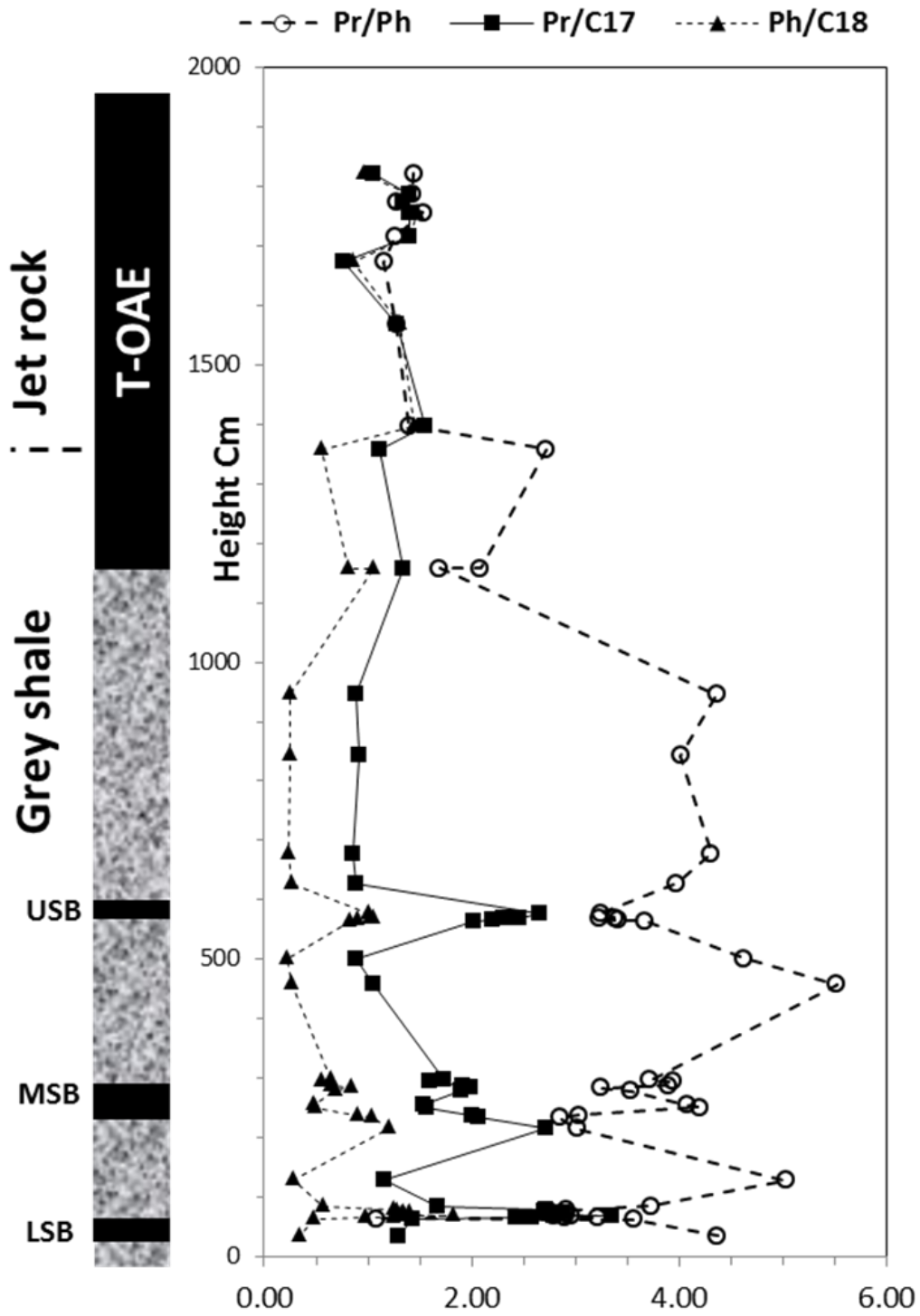


Figure 4. 13: Variation of Pr/C17, Ph/C18 and Pr/Ph ratio throughout the study section at Port Mulgrave.

4.2.2.3 Steranes and diasteranes biomarkers

The tetracyclic molecular biomarker steranes are derived from sterols in eukaryotic organisms. The distribution of steranes is best studied by monitoring the ion m/z 217, which is the characteristic fragment in the sterane series. A mass chromatogram for a representative sample is shown in Figure 4.14. The sample shows a consistent sterane pattern throughout the section, with the most abundant peak being the C27 5α (H) 14α (H) 17α (H) isomer.

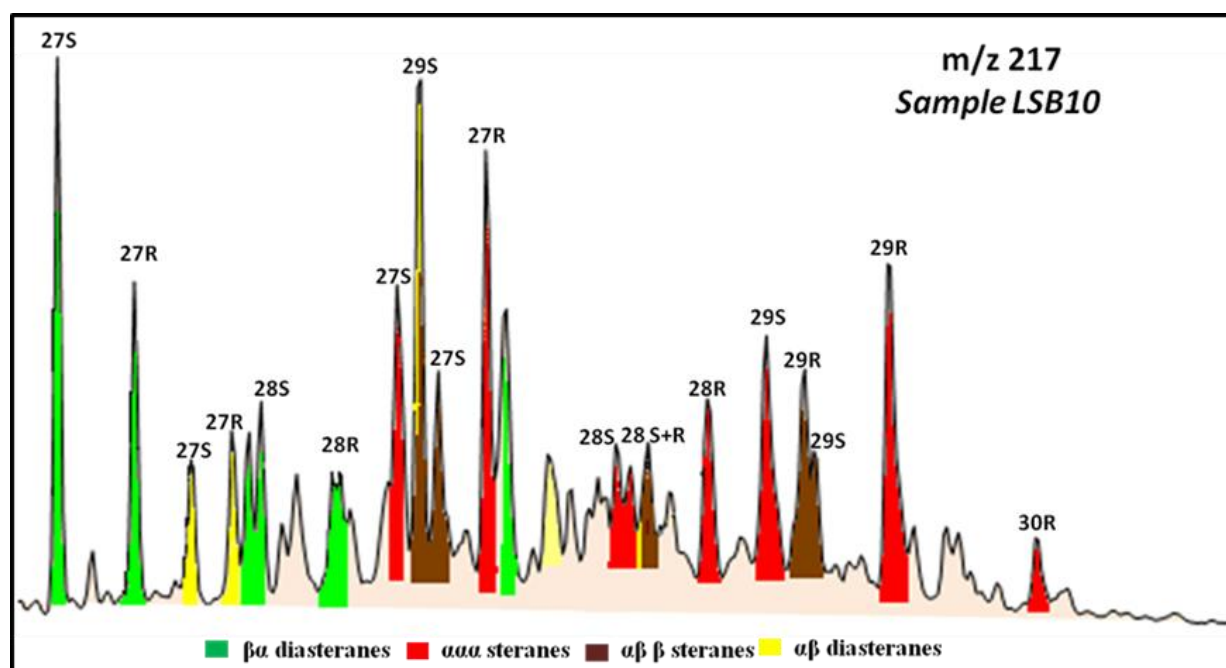


Figure 4.14: Mass chromatograms showing the distributions of steranes and diasteranes (m/z 217) for a representative sample from the Lower Sulfur Band at Port Mulgrave section.

Despite the general similarities that exist among the m/z 217 traces of the samples (Figure 4.14), some marked differences are observed. Samples from the Grey Shale zone show higher abundances of diasteranes relative to steranes, compared to samples from the Jet Rock Shale. Other main steranes present are C27 and C28 5α (H) 14α (H) 17α (H) isomers as well as C29, C28 and C27 5β (H) 14α (H) 17α (H) stereoisomers. The C30 steranes were also present in all samples. Higher proportion of steranes R isomers relative to the S isomers was observed in all samples. The ratio $20S/(20S+20R)$ of C27 13β (H), 17α (H) diasterane is around 0.6 throughout the study section (Table 4.5). The isomer distributions of the C29 steranes show some variation through the section. Whilst the $20S/(20S+20R)$ parameter for the 5α (H) 14α (H) 17α (H) steranes remains relatively fixed at around 50%. A triangular plot shows the relative abundances of C27, C28 and C29 5α (H) 14α (H) 17α (H), (20R) sterane isomers, with close grouping of all samples (Figure 4.20).

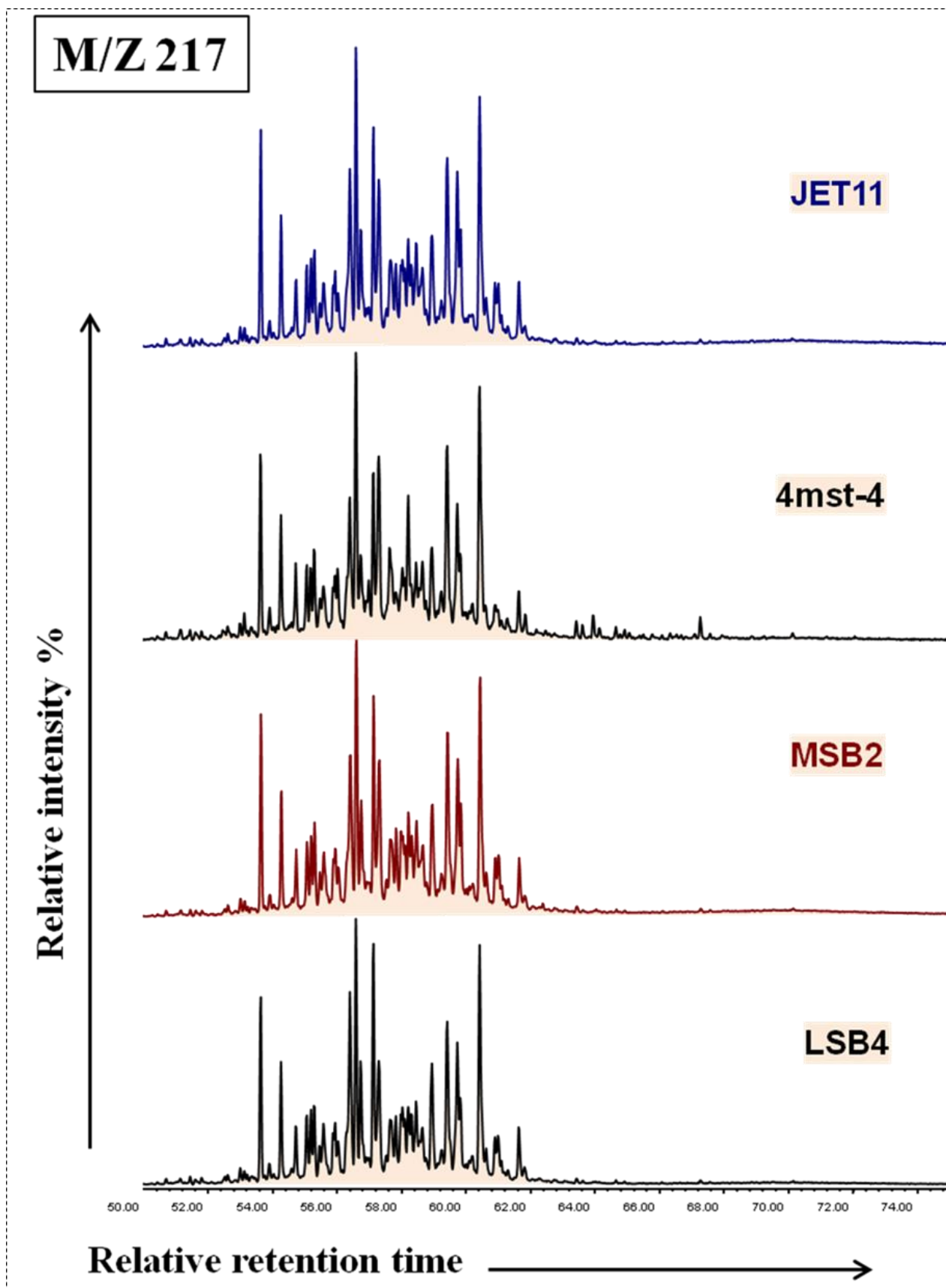


Figure 4.15: Mass chromatograms showing the distribution of steranes and diasteranes (m/z 217) for selected samples from Jet Rock and Grey shale at Port Mulgrave (note the relative abundance of C_{29} $5\alpha(H)$ $14\alpha(H)$ $17\alpha(H)$ $20R$ -sterance). Refer to figure 4.14 for peak label.

4.2.2.4 Hopane biomarkers

Together with steranes, the triterpanes are the most important petroleum hydrocarbons that retain the characteristic structure of the original biological compounds (Peter and Moldowan, 1993). Tricyclics, tetracyclics, hopanes and other compounds contribute to the terpane fingerprint (mass chromatogram m/z 191), which is commonly used to relate oils and source rocks (Peters et al., 2005). Individual components were identified by comparison of their retention times and mass spectra with a standard (North Sea oil) and published data (Peters and Moldowan, 1993; Bowden et al., 2006). The fragmentograms m/z 191 was used to detect the presence of triterpanes in the saturated hydrocarbon fractions (Figure 4.16 and 4.17). The hopane distribution pattern is similar for most samples with C30 17 α (H) 21 β (H) hopane being the dominant peak (Figure 4.16). The C29 hopane peak is generally half, or less than that of the C30 Hopane leading to a C29/C30 17 α (H) hopane ratio of one or less. This ratio and homologues of hopanes were prominent throughout the sediments analysed. The S epimers and the 17 β (H) 21 β (H) and 17 α (H) 21 β (H) isomers are present, indicating sufficient heating had occurred to isomerise the biological isomer 17 β (H) 21 β (H) to the precursor isomer 17 α (H) 21 β (H) (Mackenzie et al., 1980). As a maturity parameter the relative abundance of S and R epimers of C31 17 α (H) 21 β (H) was used (Peters and Moldowan, 1993). The average maturity (22S/(22S + 22R) in %) was 52.5 with the standard deviation of 4.8, suggesting maturity below the oil window (60% threshold).

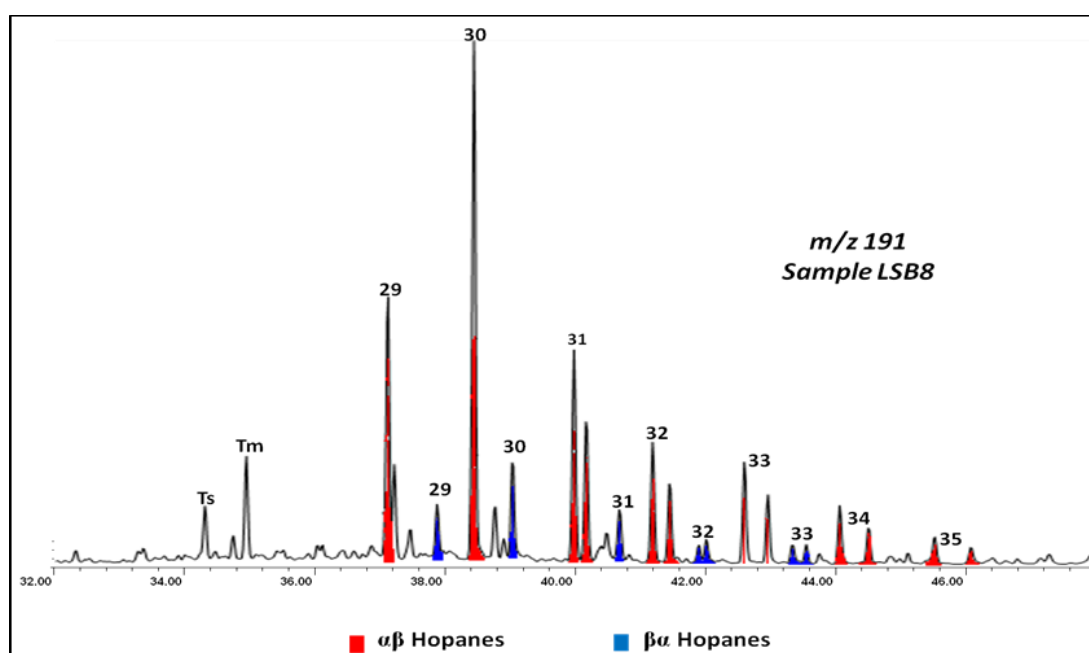


Figure 4.16: Mass chromatograms (m/z 191) showing the hopanoid hydrocarbon distribution for representative sample from the Lower Sulfur Band at Port Mulgrave section.

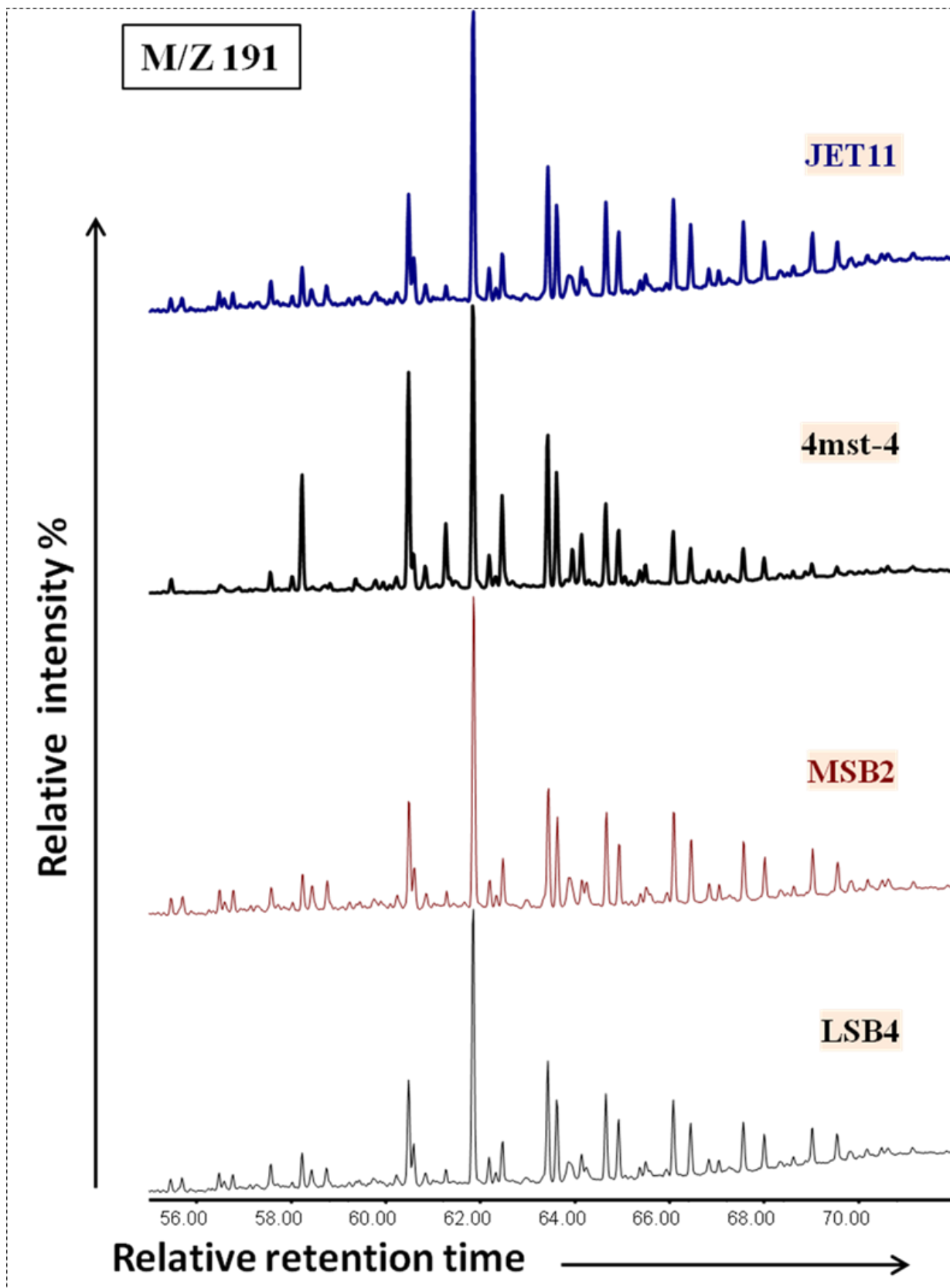


Figure 4.17: Mass chromatograms (m/z 191) showing the hopanoid hydrocarbon distribution for selected samples from Jet Rock and Grey shale at Port Mulgrave section.

4.2.2.5 Homohopane Index

The relative distribution of C31 to C35 17 α (H) 21 β (H) 22S and 22R introduced as Homohopane Index ($C_{35}/(C_{31}-C_{35})$ $\alpha\beta$ -hopanes) is often applied as an indicator of redox conditions during and immediately after deposition (Peter and Moldowan, 1991). Although high C35 homohopanes are commonly associated with marine carbonates or evaporates (Boon et al., 1983; Clark and Philp, 1989), it is widely used as a general indicator of highly reducing (low Eh) marine conditions during deposition (Peter and Moldowan, 1991). Values of Homohopane Index above 7% are regarded as high and indicative of anoxic conditions. The homohopane index values decreased slightly up section from 6.7 at the Lower sulphur bed to 2.7 in the bioturbated mudstones right below the top laminated unit of the Grey shale, after that the values sharply increase to approximately 11.0 above the Cannon Ball Doggers horizon and continue at the same level throughout the Jet Rock shale (Figure 4.18).

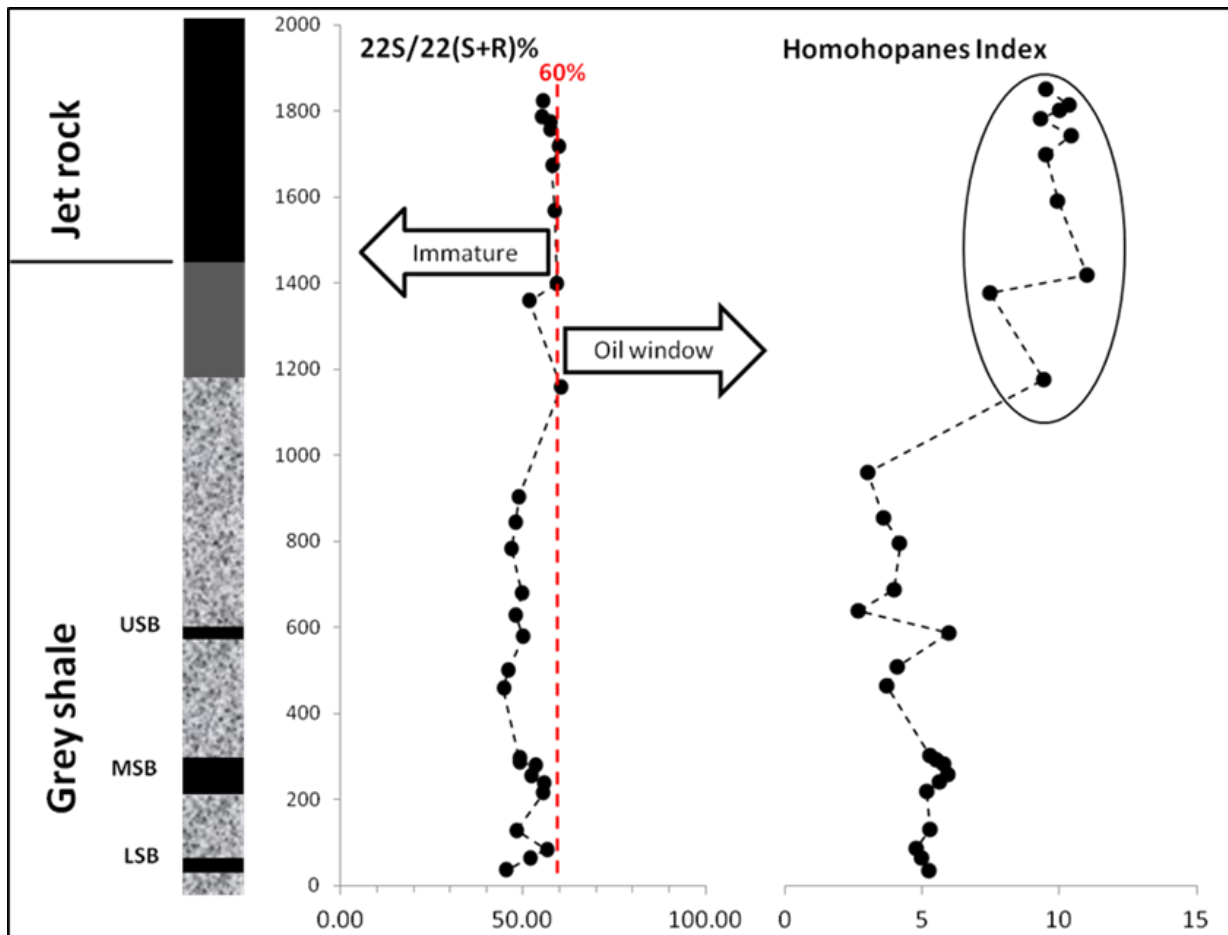


Figure 4.18: Homohopane index and 22S/22(S+R) AB hopanes cross the study section at Port Mulgrave.

Steranes commonly found in mature sediments and crude oils are derived via diagenesis from sterols which are widely dispersed in plants and microorganism, with the C27 and C28 sterols most abundant in marine organisms and the C29 sterols in higher plants. Therefore, the relative distribution of C27, C28 and C29 steranes (20S & 20R epimers) is used as indicators of depositional environment (Peters and Moldowan, 1993)

It has been proposed that the relative concentration of the diasteranes reflect the presence of clay minerals and their ability to catalyze sterane rearrangement reactions. However, it has become clear that the redox condition has an effect (Philip, 1994). Highly anoxic conditions reduces the steranes, hence reducing the amount of steranes available for the rearrangements reactions (therefore, low diasteranes to steranes ratio).

The steranes / hopanes ratio reflects input of eukaryotic (algae and higher plants) versus prokaryotic (bacteria) organisms to the source rock. To establish any changes in the organic matter input the ratio of sterane over hopanes was assessed using the following equation

$$\text{Sterane/hopane} = (\text{C27}\alpha\alpha\alpha\ 20\text{R}+20\text{S}) + (\text{C28}\alpha\alpha\alpha\ 20\text{R}+20\text{S}) + (\text{C29}\alpha\alpha\alpha\ 20\text{R}+20\text{S}) /$$

$$\text{C29} + \text{C30} + (\text{C31}\alpha\beta\ 22\ \text{R}+22\text{S}) + (\text{C32}\alpha\beta\ 22\ \text{R}+22\text{S}) \quad (\text{Peters and Moldowan, 1993})$$

This ratio was then plotted against the height above the base of the Grey Shale Member as shown in Figure 4.19.

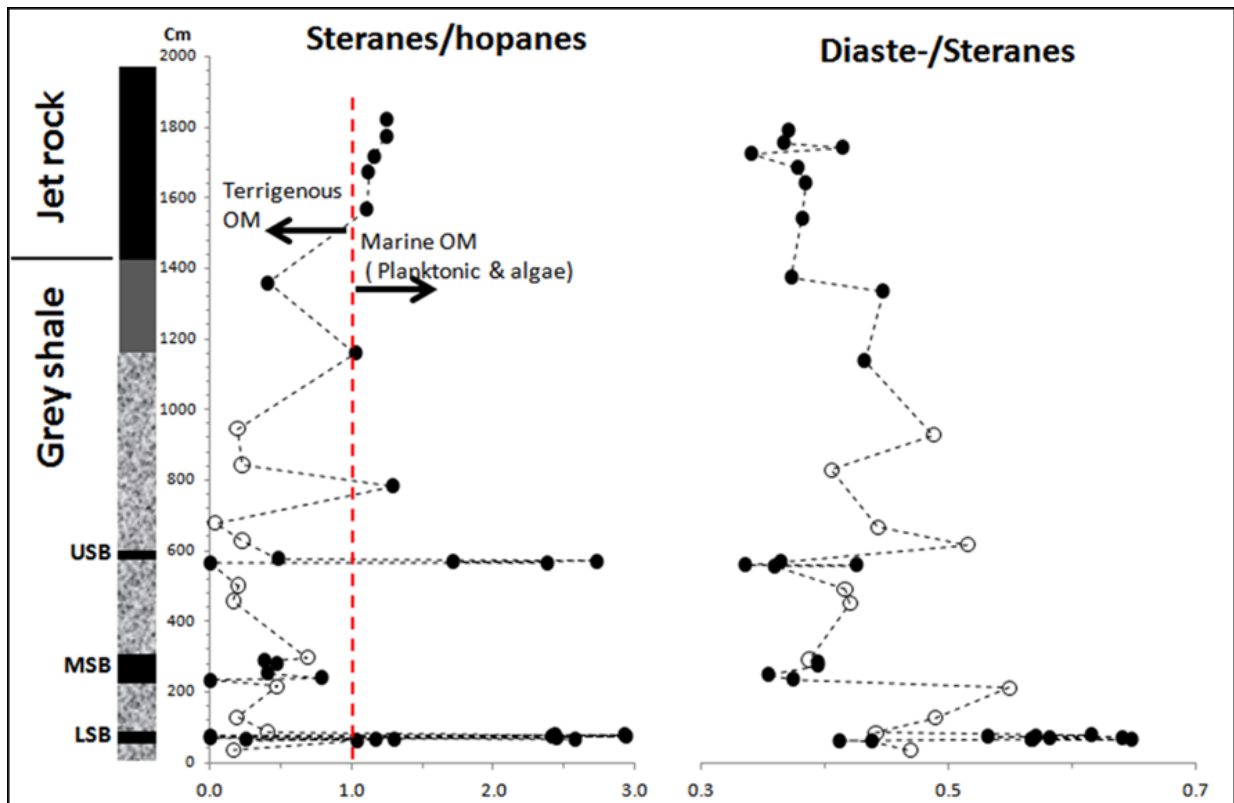


Figure 4.19: Sterane/hopane plotted against the height (Cm) above the base of the Grey Shale at Port Mulgrave section showing the inferred changes in organic matter input.

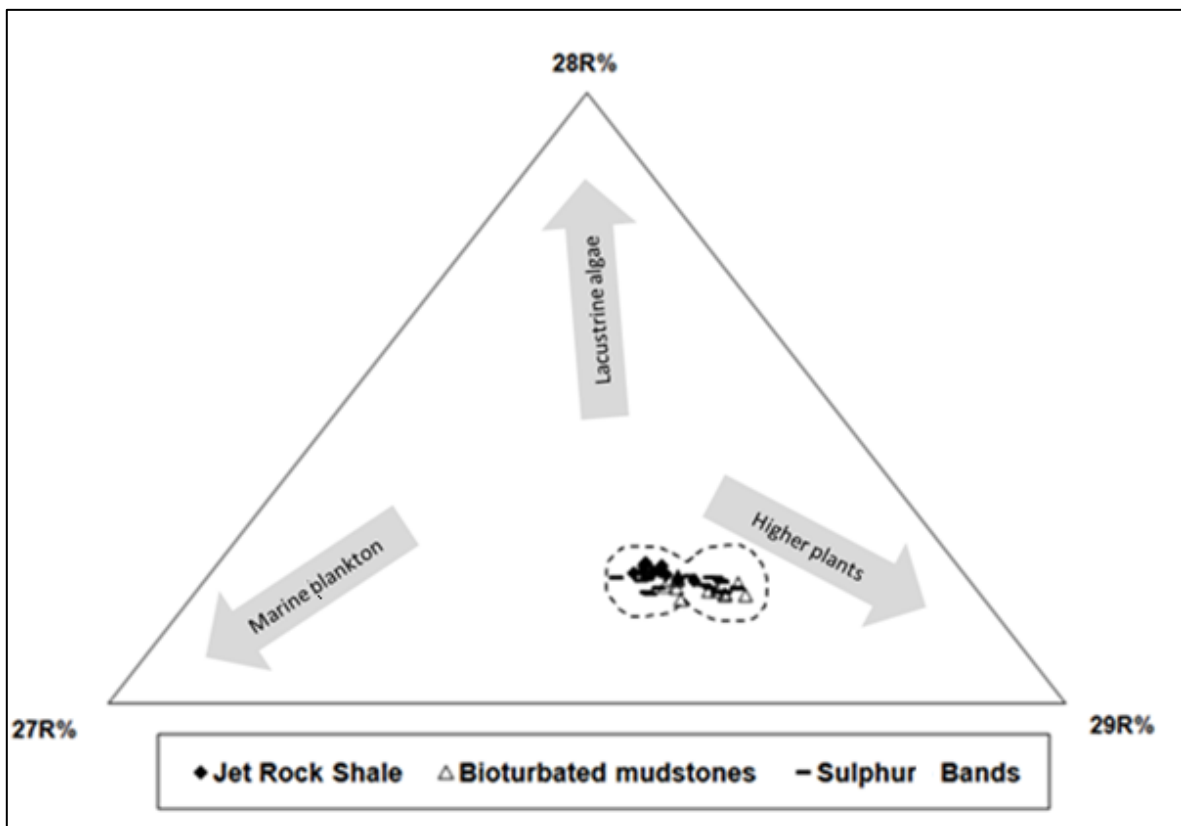


Figure 4.20: A ternary diagram showing the distributions of C27, C28 and C29 $\alpha\alpha\alpha(20R)$ steranes within the studied samples at Port Mulgrave section.

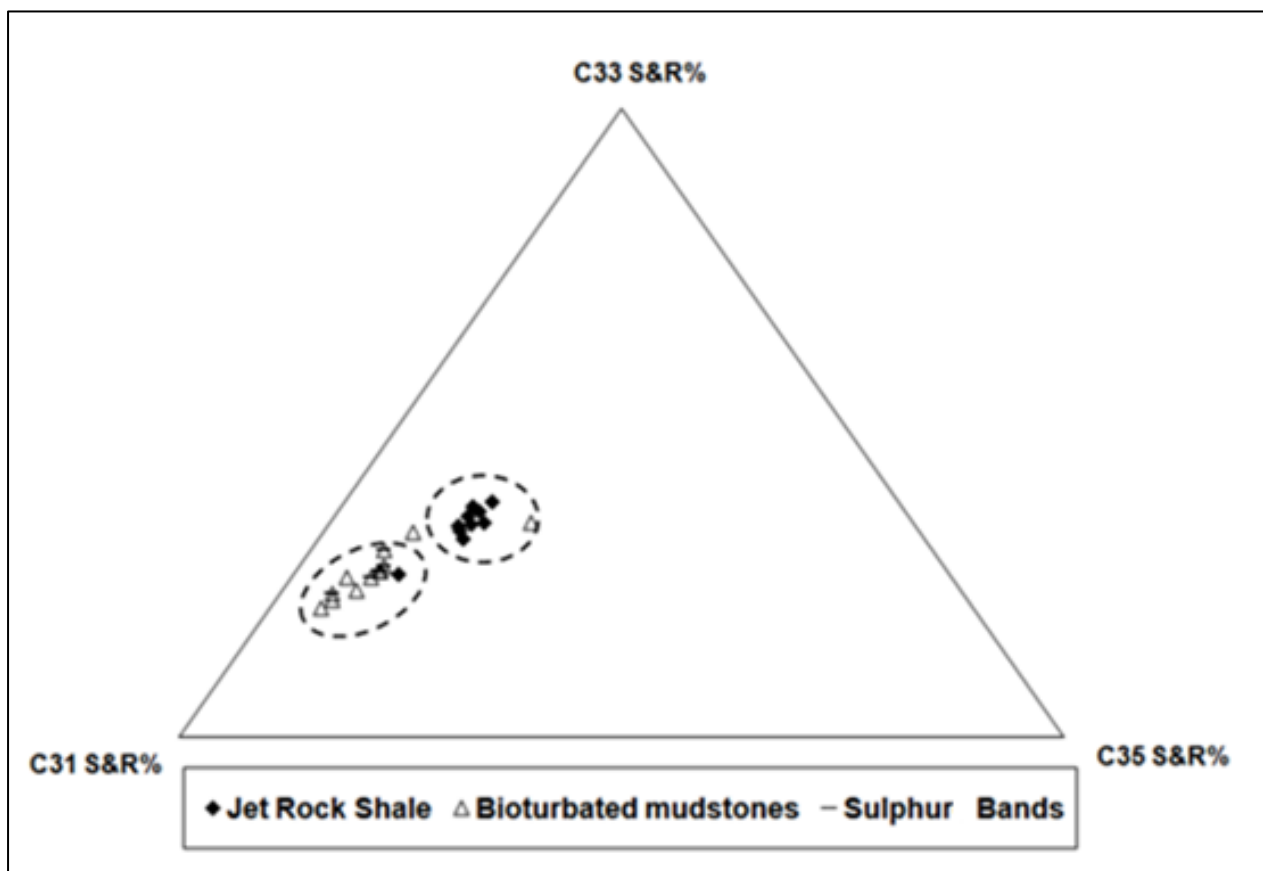


Figure 4.21: A ternary diagram showing the distribution of C31, C33 and C35 $\alpha\beta(22 \text{ S\&R})$ homohopanes within the studied samples at Port Mulgrave section.

4.2.2.6 Isorenieratane

Isorenieratane was confirmed using its diagnostic ions m/z 133, 134 and 546.5 (figure 4.22). A typical 133 chromatogram trace bearing the characteristic relative abundance pattern confirms Isorenieratane appearing at retention time of 76.1 mins.

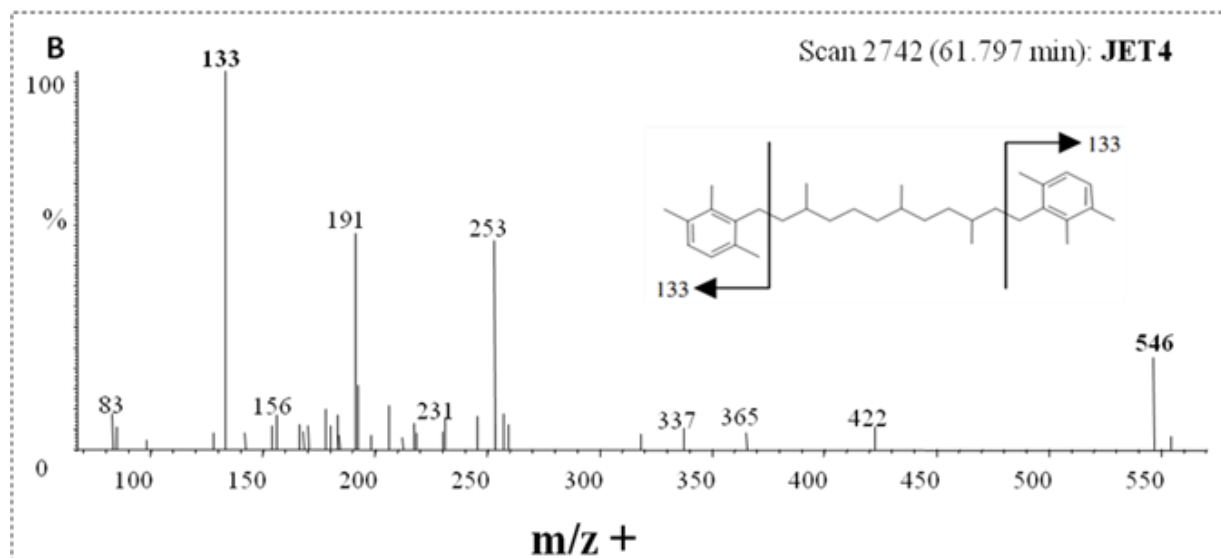
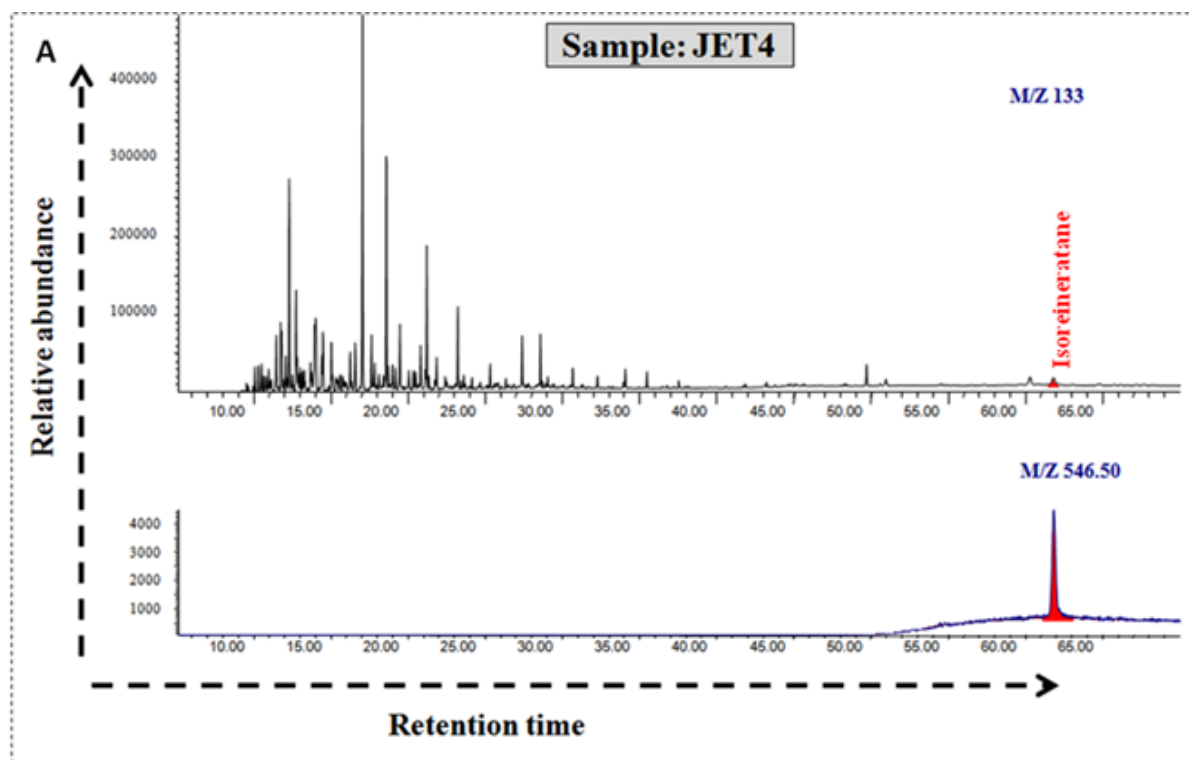


Figure 4.22: (A) GC-MS ion chromatogram of m/z 133 of aromatic hydrocarbon fraction of representative sample (from the Jet Rock Shale) showing presence of a diagenetic product of isorenieratane (first identified by Koopmans et al. 1996). (B) Is mass spectrum of isorenieratane from sample JET4.

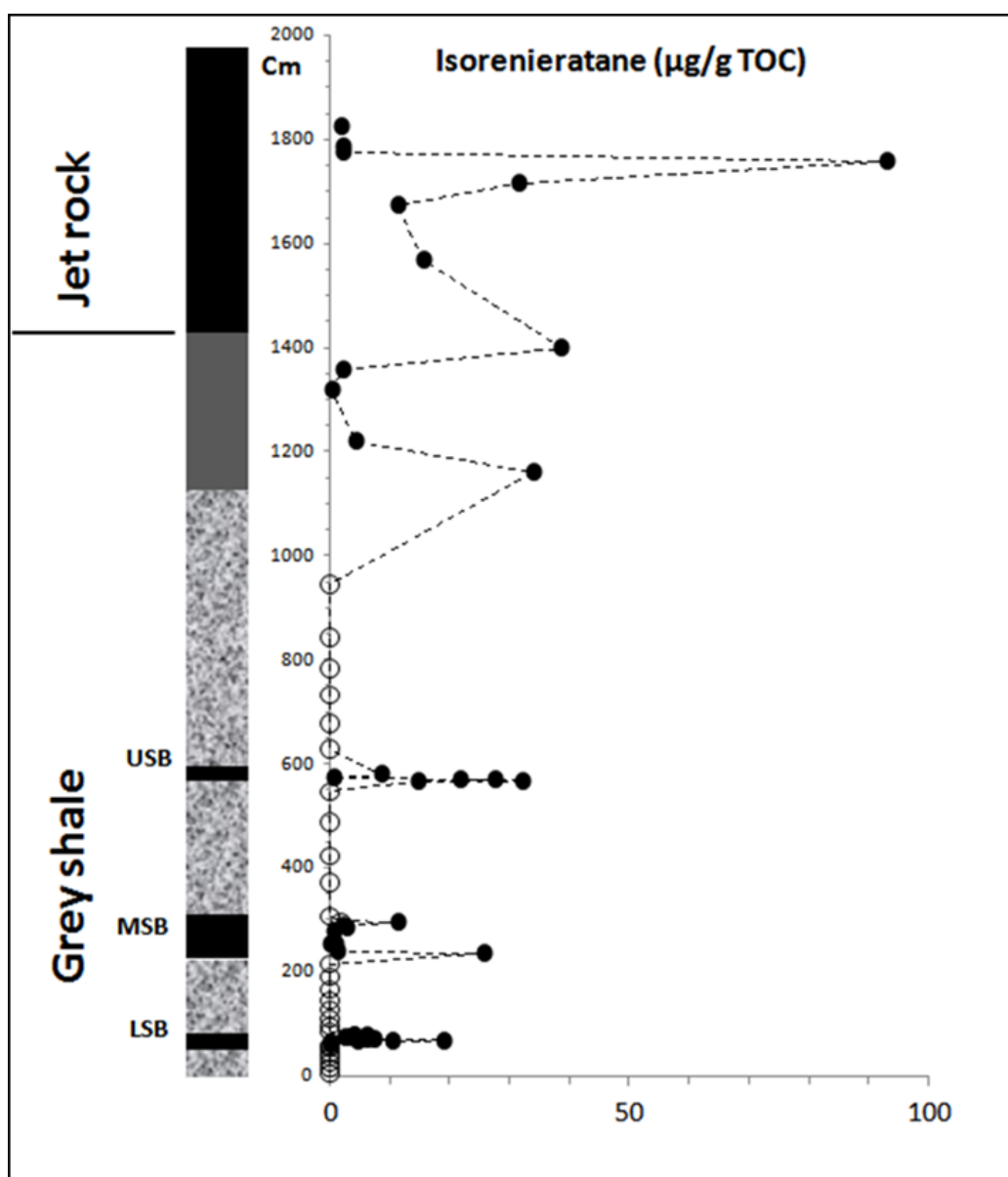


Figure 4.23: Stratigraphic records of isorenieratane abundances in $\mu\text{g/g TOC}$ across the study section

When normalised to TOC it becomes evident that samples above the boundary into the Jet Rock shale (*Exaratum subzone*) have persistently high concentrations of up to 93.1 $\mu\text{g/gTOC}$ (figure 4.23). The presence of isorenieratane within the bioturbated mudstone is negligible where it was recorded in only one sample directly above the Middle Sulphur bed (1.82 $\mu\text{g/gTOC}$). Notably, the Lower and Upper Sulphur Beds are characterized by prominent peaks in isorenieratane with an average concentration of 12.98 $\mu\text{g/gTOC}$. The Middle Sulphur bed is characterized by less isorenieratane (on average 5.57 $\mu\text{g/gTOC}$) especially in its central part where this compound was not detected at all.

Table 4.5: Biomarker-based parameters for organic matter thermal maturity and Paleoredox indicators. Homohopane index = percentage of $\alpha\beta$ -C35 Homohopane in Σ C31 – C35 $\alpha\beta$ homohopanes (Peters & Moldowan, 1991). +/- = presence/absence of isorenieratane.

Samples	Extract yield (mg/gTOC)	Maturity parameters		Paleo-Redox parameters			
		22(S/S+R) C ₃₂ Hopane	20(S/S+R) C ₂₉ Sterane	Dia/Reg. steranes	Homohopanes index	Sterane/ hopanes	Isoreniera tane
JET17	172.7	59.2	43.4	0.37	11.8	1.3	+
JET15	165.9	58.6	87.7	0.37	13.0		+
JET13	185.2	61.0	42.5	0.41	12.3	1.3	+
JET11	166.5	58.8	80.0	0.34	11.7		+
JET8	221.7	59.8	45.1	0.38	12.6	1.2	+
JET6	108	58.5	44.6	0.39	11.7	1.1	+
JET4	92.3	59.7	44.3	0.38	12.2	1.1	+
JET1	40.1	60.0	87.1	0.37	13.6		+
TL.5	86.1	59.6	45.8	0.45	9.8	0.4	+
TL.1	140.2	59.1	44.3	0.43	11.6	1.0	+
4-MST6	48.4	59.7	44.9	0.49	4.2	0.2	+
4-MST5	52.3	59.8	42.0	0.41	4.9	0.2	-
4-MST2	48.7	59.7	44.2	0.44	5.4	0.0	-
4-MST1	59.9	58.7	47.0	0.52	3.7	0.2	-
USB10	94.8	59.9	44.5	0.36	7.8	0.5	+
USB6	57.5	60.5	44.1	0.34	8.1	2.7	+
USB5	100.1	60.9	45.2	0.43	7.2	1.7	+
USB4	74.6	60.2	45.0	0.36	8.3	2.4	+
3-MST7	66.2	59.6	49.4	0.42	5.6	0.2	-
3-MST5	52.2	60.4	48.2	0.42	5.2	0.2	-
3-MST1	103.2	61.1	46.0	0.39	7.1	0.7	-
MSB20	92.9	62.1	43.6	0.39	7.2	0.4	+
MSB16	102.1	60.2	44.4	0.40	7.9	0.5	+
MSB9	80.8	59.9	48.0	0.35	7.6	0.4	+
MSB2	112.8	60.1		0.38	8.7	0.0	+
2-MST8	110.8	59.6	39.5	0.55	6.3	0.5	-
2-MST4	71.8	57.3	45.5	0.49	5.6	0.2	-
2-MST1	72.8	58.1	45.2	0.44	8.7	0.4	-
LSB14	175.1	61.1	46.2	0.62	8.4	2.4	+
LSB13	87.1	59.6	43.3	0.57	8.8	2.9	+
LSB11	167.5	59.5	42.9	0.53	9.0	2.9	+
LSB10	161.8	61.0	42.2	0.64	7.8	2.4	+
LSB9	95.6	60.4	44.5	0.58	8.8	2.5	+
LSB8	102.3	60.0			7.7	0.0	+
LSB7	118.5	59.6	44.5	0.57	8.8	2.6	+
LSB6	160.9	59.9	48.3	0.65	8.9	1.3	+
LSB5	145.6	60.3	55.1	0.57	7.5	1.2	+
LSB4	30.8	60.9	42.7	0.41	5.1	0.3	+
1-MST4	53.0	58.9	45.5	0.47	4.9	0.2	-

4.2.3 Organic petrological results

Although not a geochemical technique itself, the visual identification of kerogen particles (macerals) in slides can provide an independent means of determining the source of organic matter and corroborating bulk organic geochemical analyses. Kerogen is mostly derived from microscopic dispersed particles derived from terrestrial and aquatic organic matter and their degradation products (Vandenbroucke and Largeau, 2007). Kerogen sometimes preserves a specific morphology (structure of particles) that allows its source to be identified, and this in turn allows a better understanding of the depositional environment of the sediments in which it is found (e.g. marine or freshwater, onshore or offshore, oxidising or reducing, etc.) (Tyson, 1995). The aim of the optical examination was to give a general characterization of the organic matter composition with regard to the terrigenous, marine and amorphous origin, and to investigate whether this composition changes over the sequence.

Several optical classification schemes are available for the description of kerogen under the microscope (e.g Hutton et al., 1980; Waples, 1985). All classifications distinguish between oxidized, carbon-rich organic matter (inertinite), humic organic matter (vitrinite), and the lipid-rich particles of membranous material (exinite) or amorphous organic matter (liptinite). Tyson (1995) revised and reevaluated the palynofacies terms and presented a more simplified classification (Tyson, 1995, p.350).

4.2.3.1 Transmitted light microscopy

A relatively quick qualitative, semi-quantitative approach is transmitted light microscopy. The total kerogen assemblage was divided into major components phytoclasts, amorphous organic matter (AOM) and palynomorphs (Tyson, 1995). The stratigraphic distribution of these components is shown in Figure 4.24.

A selected set of samples shows a dominance of AOM over phytoclasts assemblages. The AOM forms more than 75% of the total kerogen apart of some mudstone samples where the AOM drops to approximately 65%. The overall trend shows that the amount of terrigenous input in the kerogen is extremely low in the Jet Rock (*Exaratum* subzone) contributing less than 2%. At the lower part of the Grey Shale member (including the Sulphur Bands) the contributions of terrigenous material are higher, especially within the bioturbated mudstone horizons where the phytoclasts form up to 25% of the total kerogen with dominance of black over brown woody materials.

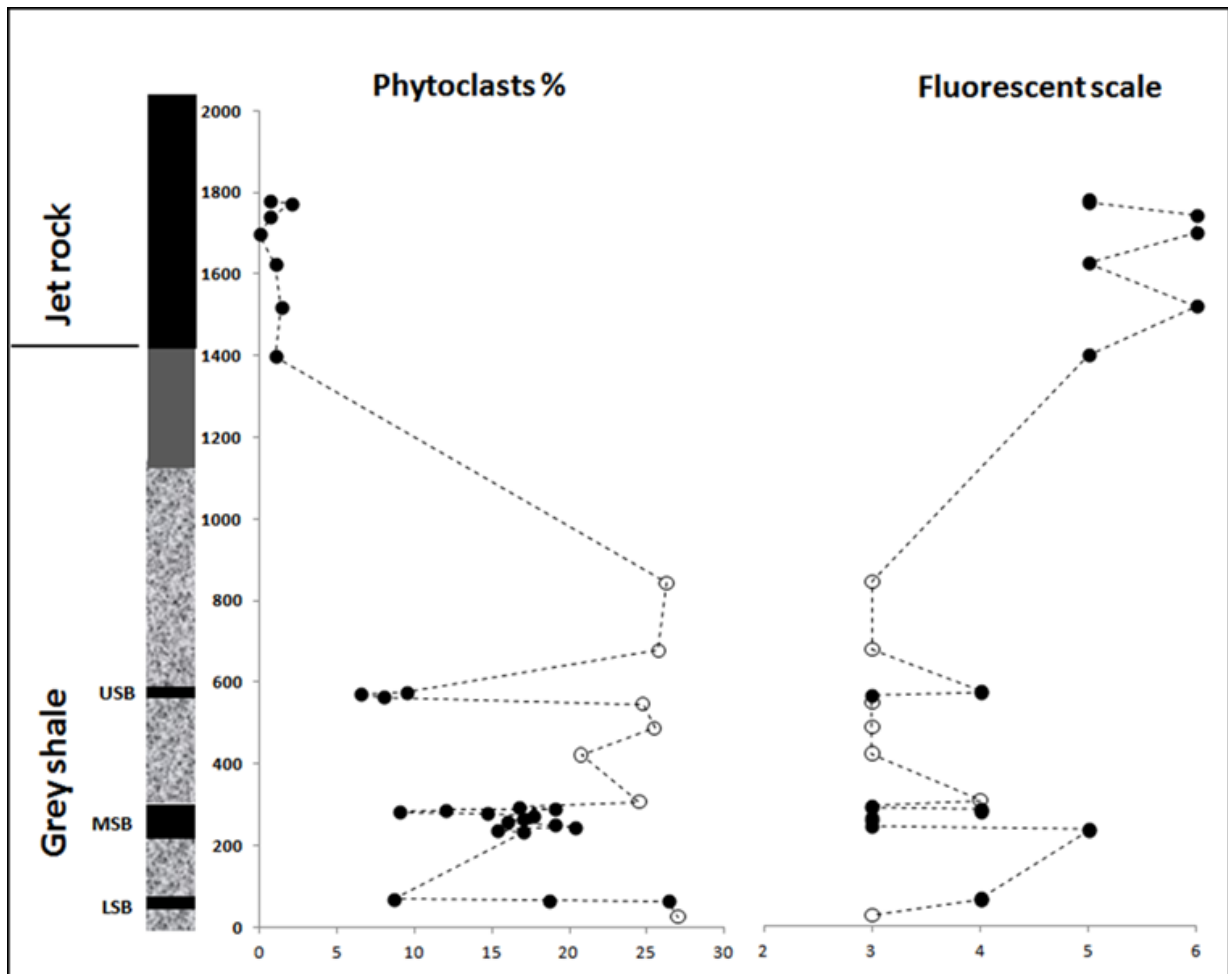


Figure 4.24: Stratigraphical variation of % Phytoclasts and the fluorescent scale throughout the study section at Port Mulgrave.

4.2.3.2 Blue light fluorescent microscopy

The palynomorphs in all samples show quite high fluorescence (e.g Plate E&F), while AOM kerogens show fluctuated fluorescence intensity from moderate to low throughout the studied section. Applying the fluorescence scale from Tyson (1995), the data shows moderate fluorescence within the Grey Shale Member which passes into very strong fluorescence in the upper part of the Grey shale and the Jet Rock member.

Total Kerogen plots

Tyson (1989) uses an AOM-phytoclast-palynomorph plot of percentage particle abundances (i.e. relative numerical particle frequency) to characterise kerogen assemblages into eleven (independently sedimentologically-defined) marine shale facies. The plot picks out differences in relative proximity to terrestrial organic matter sources, and the redox status of the depositional subenvironments that control AOM preservation. As the emphasis is on palaeoenvironment rather than source rock potential, cuticle is incorporated within the phytoclast group, not the palynomorph group.

The relative abundance of palynofacies components was plotted in an AOM-phytoclasts-palynomorphs (APP) ternary diagram to investigate the organic matter type through the section in order to determine the oxygen content of the bottom water column and the quantity of terrestrial input. In order to demonstrate correlations between different data sets, the percentage of various palynomorph categories, or geochemical values, were plotted on to this diagram (Figure 4.25)

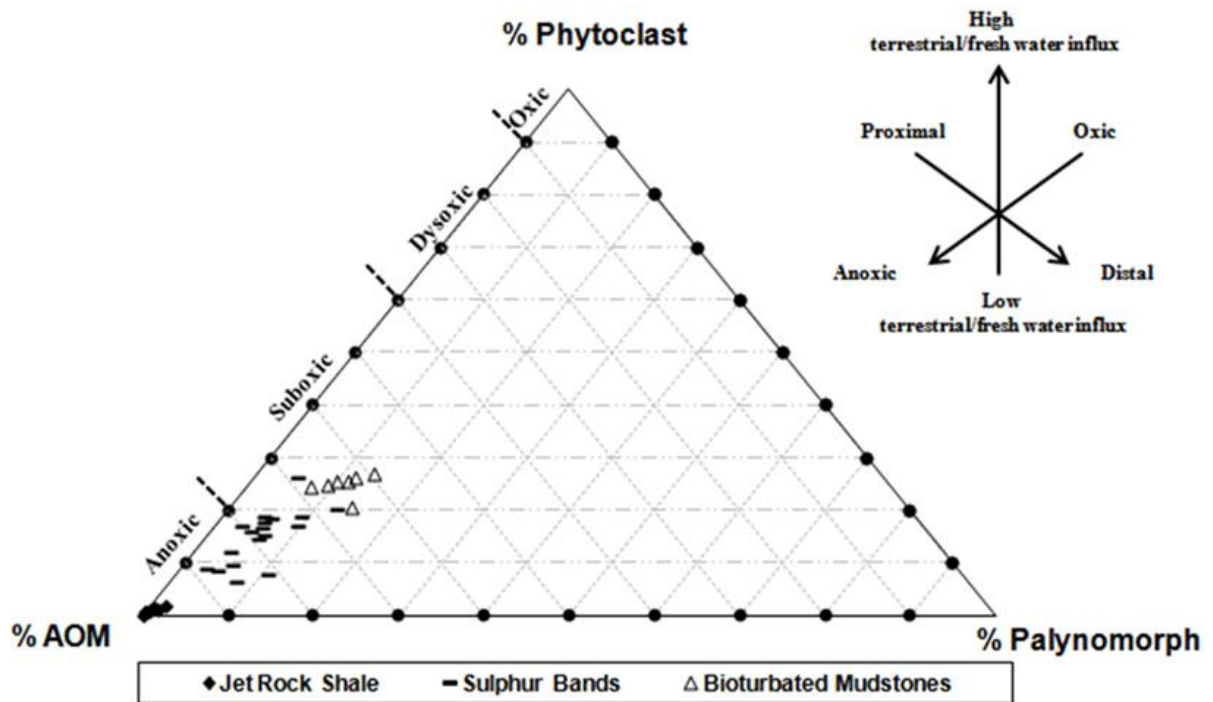


Figure 4.25: Amorphous organic matter-Palynomorphs-Phytoclast "APP" ternary diagram of relative abundance of palynofacies parameters after Tyson (1995). The percentage of each parameter is calculated in relation to the total particulate organic matter counting.

Table 4.6: informal kerogen categories used in this study.

Main category	Sub category	presence
Phytoclasts	Black wood	common
	Dark brown wood	common
	Light brown wood	common
	Cuticle	rare
	Fungal hyphae	rare
Amorphous	AOM (derived from phytoplankton and bacteria)	Dominant
Palynomorphs	Sporomorphs	Pollen (common)
		Spores (common)
	Marine microplankton	Tasmanite
	Non-marine microplankton	absent
	Marine zoomorphs	

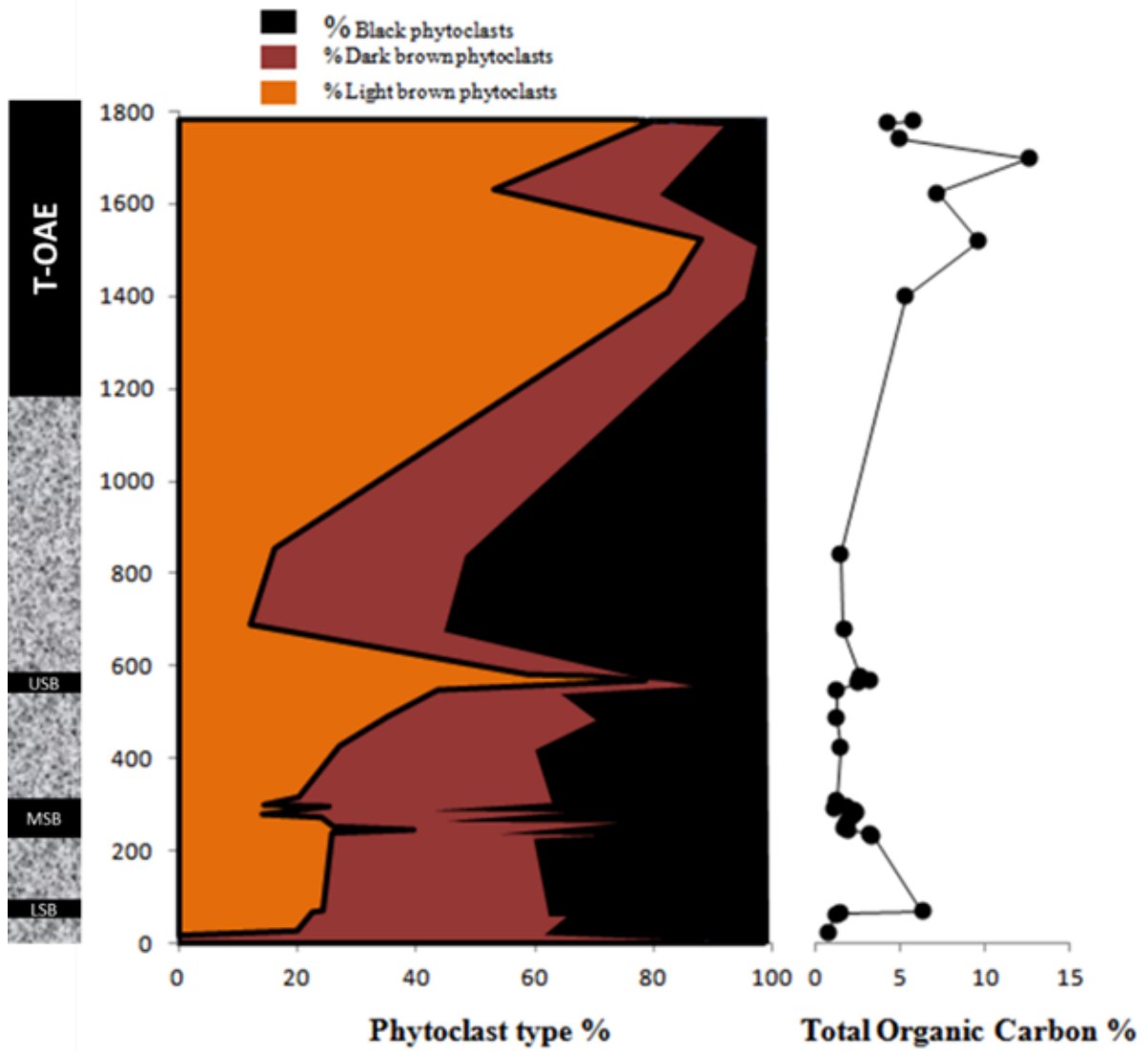


Figure 4.26: Stratigraphic variation in the character of the woody phytoclast fraction and of TOC. Connection of sample points is for diagrammatic purposes only and does not imply interpolated values. Phytoclast data are based on relative numeric particle frequencies.

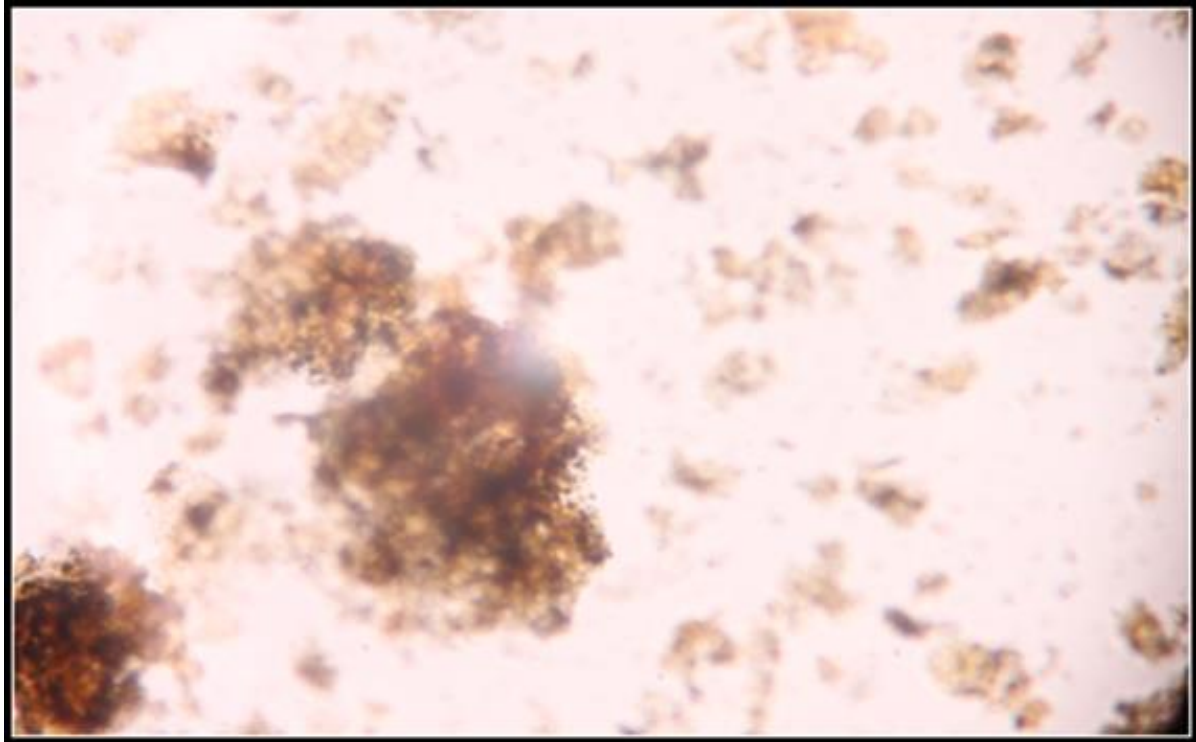


Figure 4.27: Well preserved 'AOM' seen in transmitted white light, amorphous matrix rich in small unidentifiable fragments (fluorescent under the blue light; equivalent to the maceral liptodetrinite) plus other inclusions (palynomorphs, pyrite and small phytoclasts) (Magnification X20).

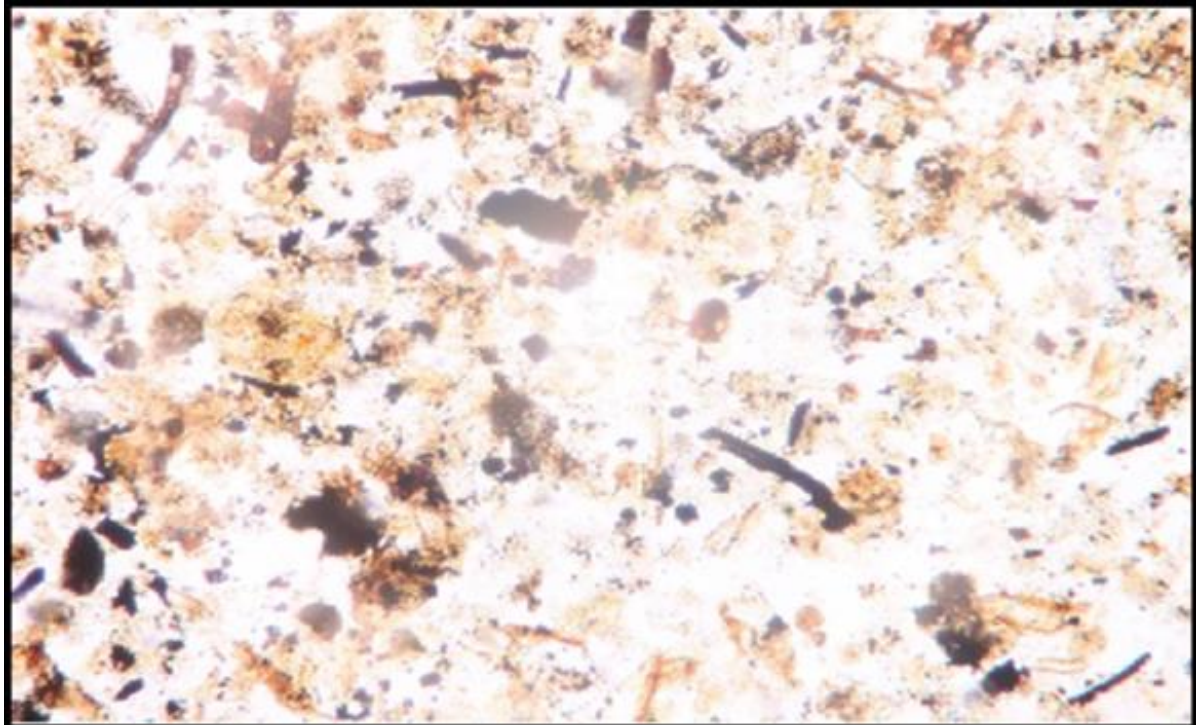


Figure 4.28: relative dominance of phytoclast mixed with poorly preserved AOM and Palynomorphous. Biostructured phytoclast (the term biostructure refers to definitive biologically-derived structure) composed of wood tissue such as gymnosperm tracheids and gymnosperm xylem ray tissue or dispersed cuticle phytoclast (Magnification X20).

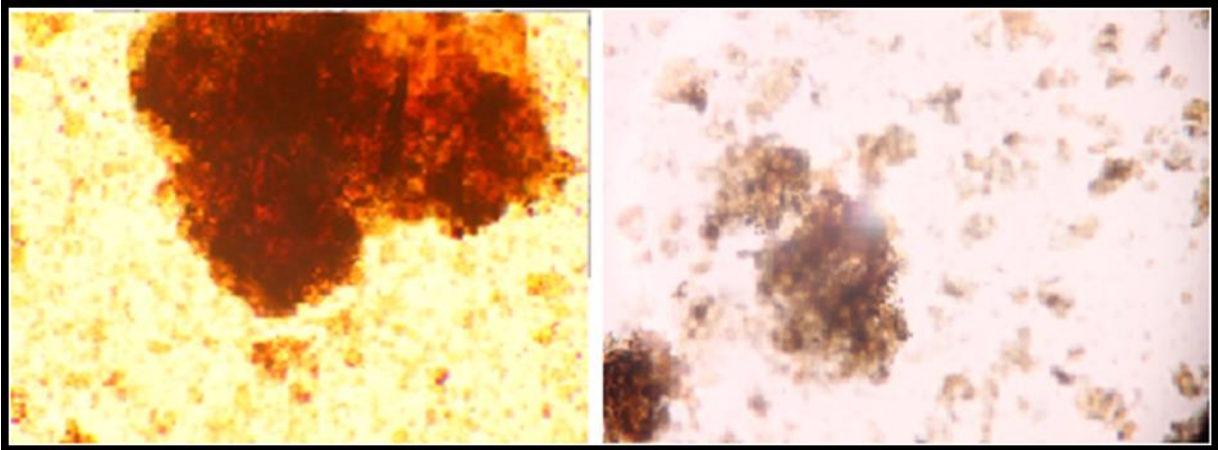


Plate A (Magnification X40)

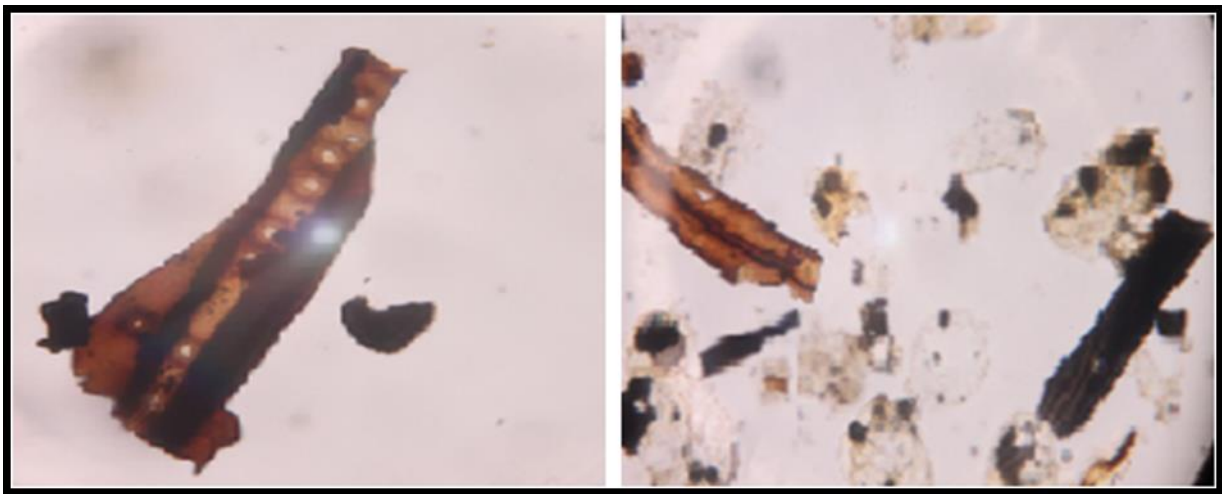


Plate B (Magnification X40)

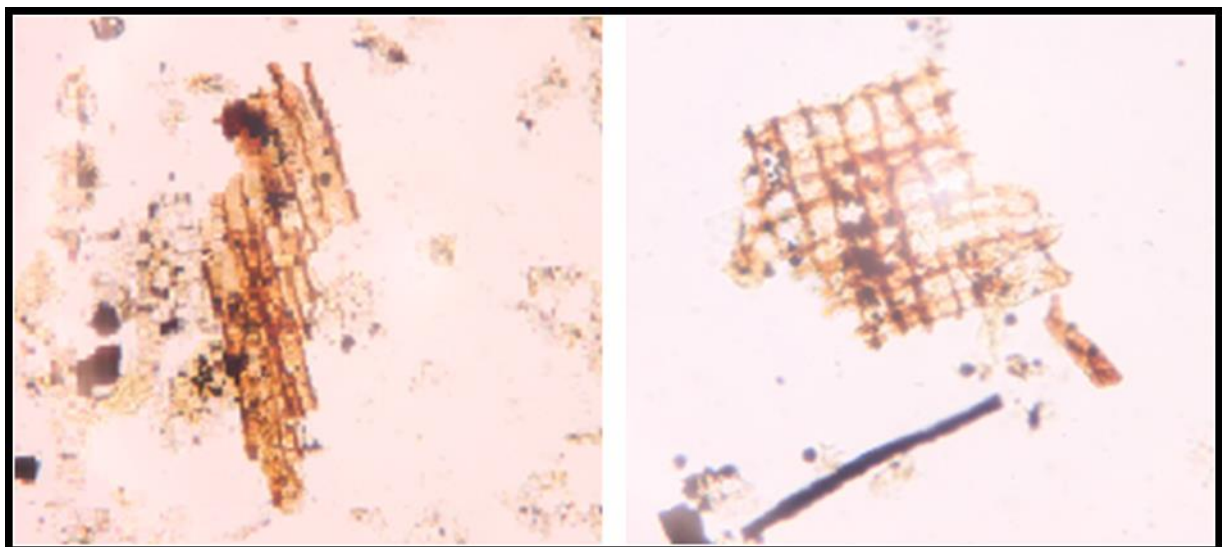


Plate C (Magnification X40)

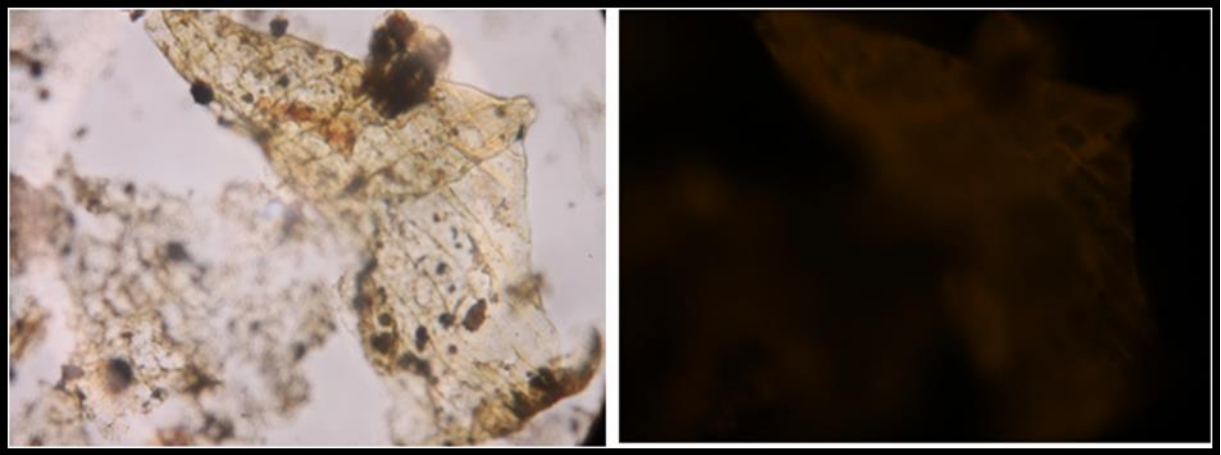


Plate D (Magnification X40)

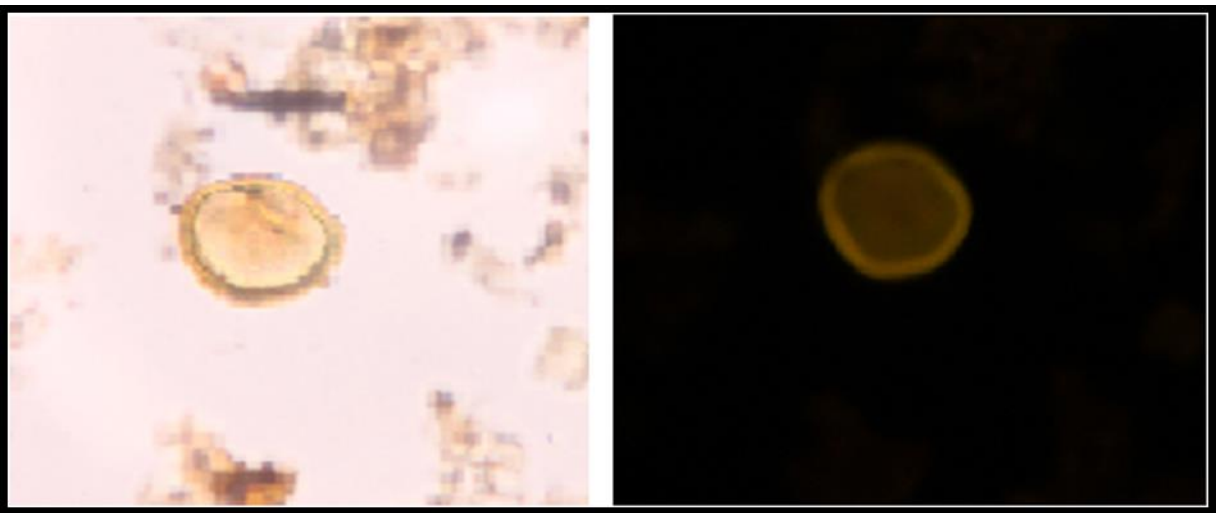


Plate E (Magnification X40)

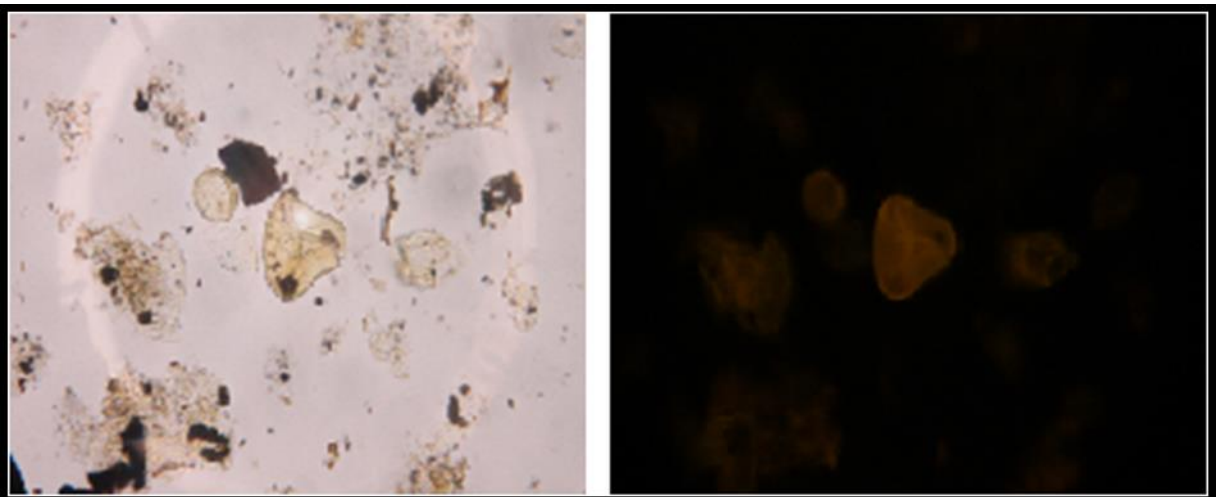


Plate F (Magnification X40)

A: Well preserved 'AOM' seen under transmitted white light. Note the diffuse edged particles. The form of the edge and the presence of the pyrite inclusions (the black spots) indicate that the particle is structureless and therefore not a phytoclast. The sample lithology is laminated black shale (Jet Rock shale; sample JET 15)

B1: Biostructured phytoclast (the term biostructure refers to definitive biologically-derived structure). The phytoclast is composed of at least two adjacent gymnosperm tracheid fragments

C: Structured phytoclast. The cross-hatch structure of the phytoclast, with thickened ribs arranged approximately at right angles to each other, indicates a derivation from ray tissues (Tyson, 1995). These are similar to cuticle tissues and distinguished by their regularly arranged columns and rows of squares or rectangles and showing no fluorescence under blue light.

D: Dispersed leaf cuticle phytoclast (Liptinite-cutinite) showing regular rectangular cell outlines (probably gymnosperm in origin). The relatively dark brownish matte colour and lack of fluorescence mainly indicate partial oxidation before or during final deposition

E: Tasmanites algae belonging to the Prasinophyte phycomata, one of the major subdivisions of the Palynomorph group. It shows intense fluorescence under the blue light.

F: Spore (Deltoidospora) with diagnostic trilete mark (Y-shaped mark) on one side, which reflects where it was joined to three neighbours on the inside of a pyramid-shaped tetrad.

4.2.4 Detailed geochemical profile across the Sulphur Band at the Pliensbachian-Toarcian boundary

The Pliensbachian–Toarcian boundary preceding the T-OAE has received special attention in this study. Intense geochemical analyses were carried out in order to understand the geochemical systematics of the Sulfur Band intervals at the base of the Grey Shale Member. Although the Sulphur Bands appears to be well laminated and generally have high organic carbon contents (average TOC ~ 2.5 wt%, Figure 4.29), the very detailed analysis at cm-scale shows that the organic content varies substantially across the Sulphur Bands. Despite the similar geochemical pattern of the Sulfur Bands of the lower Grey shale member at the Hawsker Bottoms and Staithes sections, the Hasker Bottoms section shows weaker lamination and poor organic contents (TOC average of 0.93 wt% compared with 3.0 wt% at Staithes). Moreover, the quality of the organic mattter of the Lower Sulphur Band is different at both locations as suggested by moderate Hydrogen Index (HI) with an average of 280 wt% at Staithes and lower values at at Hawsker Bottoms 191 wt%.

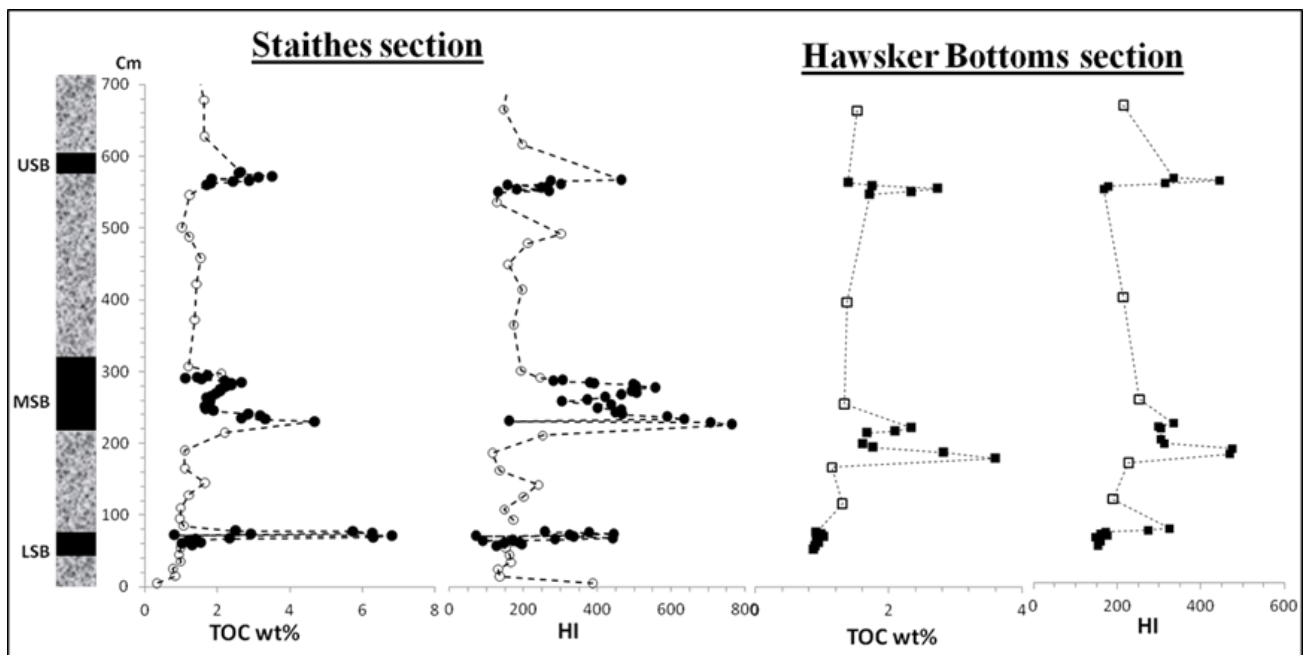


Figure 4.29: stratigraphic variation in the bulk geochemistry parameters: depth versus TOC wt% and HI of the lower Grey shale member at Port Mulgrave (Staithes) and Hawsker Bottom outcrops.

Although the Lower Sulphur Band has been described in previous studies (Wignall, 1994) as representing an anoxic environment, the new cm-scale multiproxy records reveal a more dynamic system, with distinct fluctuation in the geochemical parameters (Figure 4.30 and Figure 4.31).

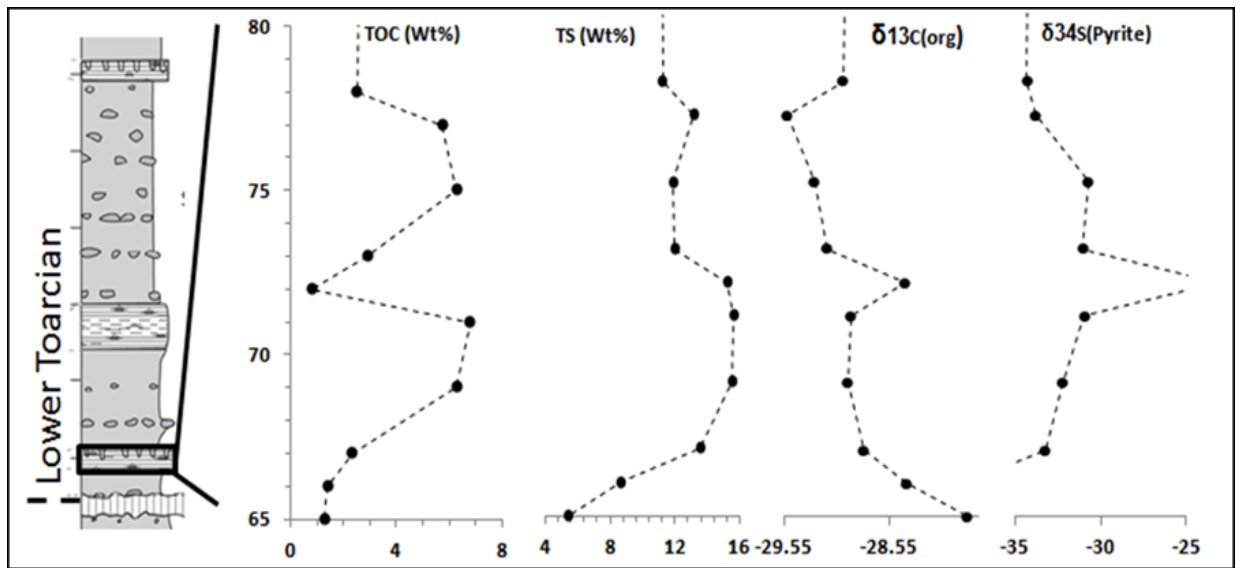


Figure 4.30: Cm-scale analysis of the TOC, TS and isotopic analysis for the organic carbon and pyrite sulfur cross the Lower Sulfur Bed at Port Mulgrave section

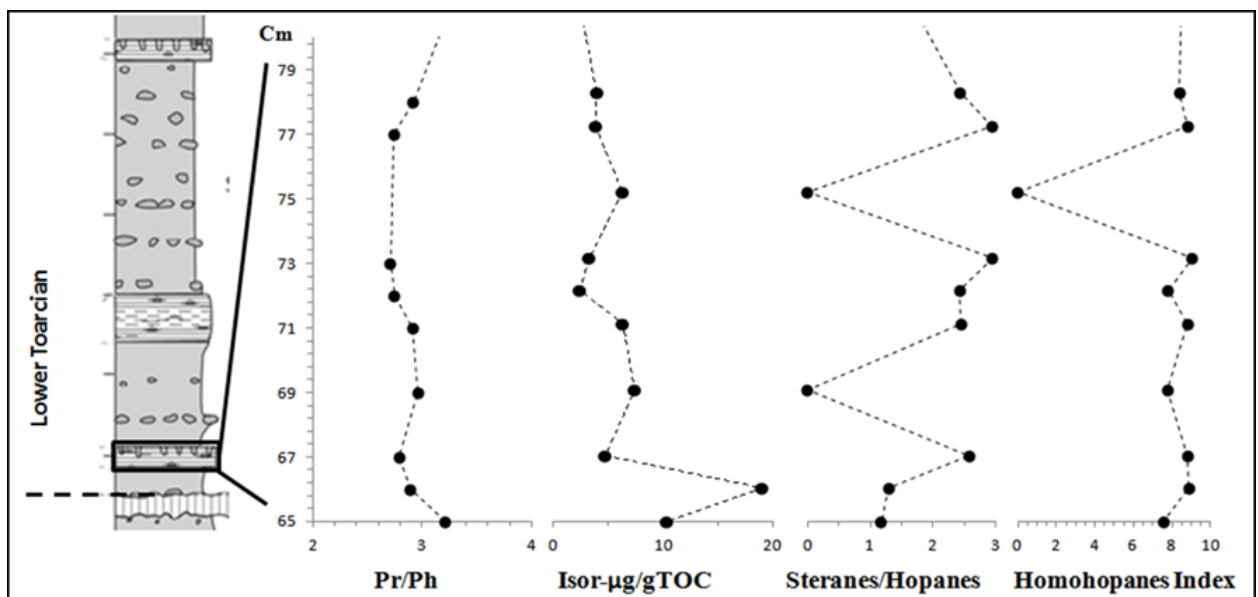


Figure 4.31: Cm-scale molecular biomarker analysis cross the Lower Sulfur Band at Port Mulgrave section includes Pr/Ph, Isorenaraten concentration ($\mu\text{g/gTOC}$), Steranes over Hopanes ration and the Homohopanes index.

4.2.4.1 Solid bitumen assemblages within the Lower Sulphur Band.

A thin layer of black material was found within the upper part of the Lower Sulphur Bed. It looks like a coal with its light weight and shiny appearance. It was traced almost 25 meters along the outcrop, is about 0.5 cm thick and extends deep in the outcrop (Figure 4.32). It is positioned between the shale laminas (Figure 4.33)



Figure 4.32: Thin layer of bitumen within the Lower sulfur band at Port Mulgrave section.

The black material was collected and subjected to hydrocarbon extraction using hot solvent (isotropic mixture of 93% DCM and 7% methanol). The hydrocarbon extractability of this material is extremely high (>95% of its weight is extractable bitumen) compare to an average hydrocarbon extractability of 1.4% for the surrounding shale of the Lower Sulphur Band and 10% for the Jet rock shale. When studied under the transmitted white light microscope no clear sings of woody material was found.



Figure 4.33: bitumen accumulation within the Lower Sulfur Bed. The picture shows the elongated structure casted on the shale rock.

4.2.4.1.1 Molecular biomarker characterisation of the bitumen layer

Normal alkanes

The distribution of *normal* alkane in the bitumen layer is similar to the extracted bitumen from the surrounded rocks. Normal alkane from $n\text{-C}_{11}$) and $n\text{-C}_{36}$ were identified (figure 4.34). The GC trace displays a unimodal distribution with a very weak predominance of odd carbon over the even carbon numbers and a low CPI of 1.9.

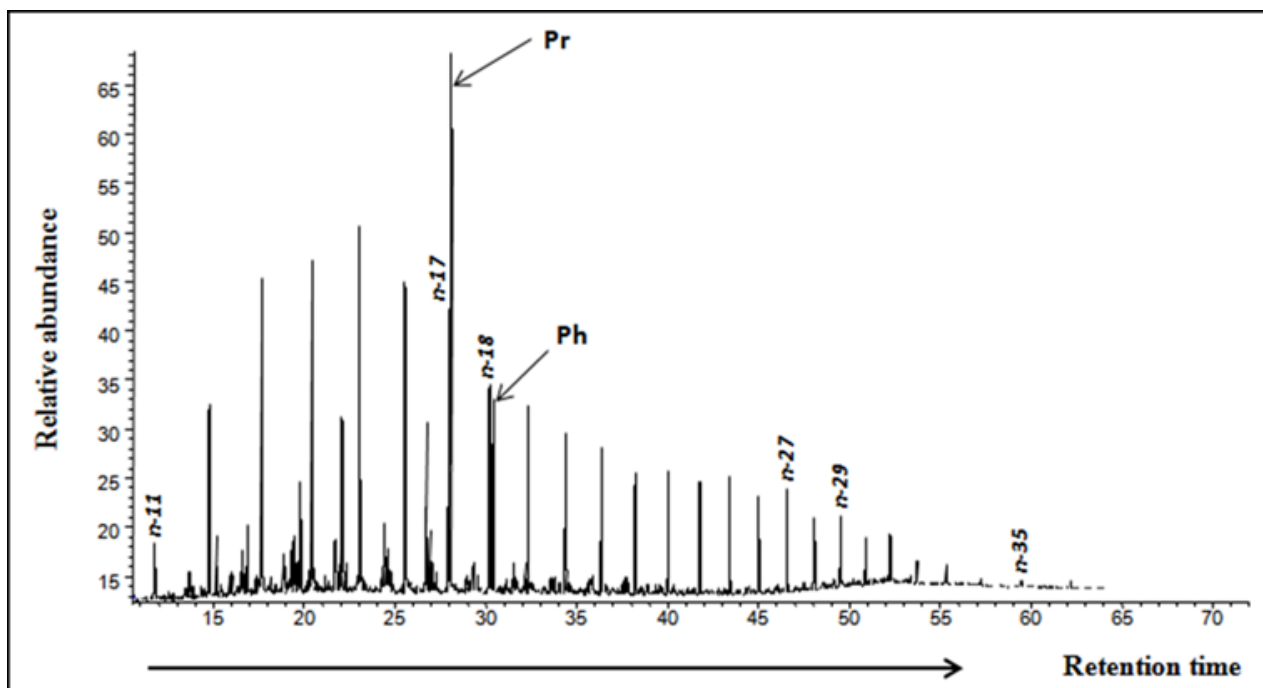


Figure 4.34: GC trace of the bitumen from the Lower sulfur Bed at Port Mulgrave.

Acyclic isoprenoids

Pristane (Pr) and Phytane (Ph) were both present in the samples, with a high Pr/Ph ratio of 3.0. The Pr/C₁₇ versus Ph/C₁₈ relationship for the whole set of samples displays that the Grey shale including the Sulphur Beds and the bitumen sample were segregated from the Jet Rock sample as seeing in figure 4.35.

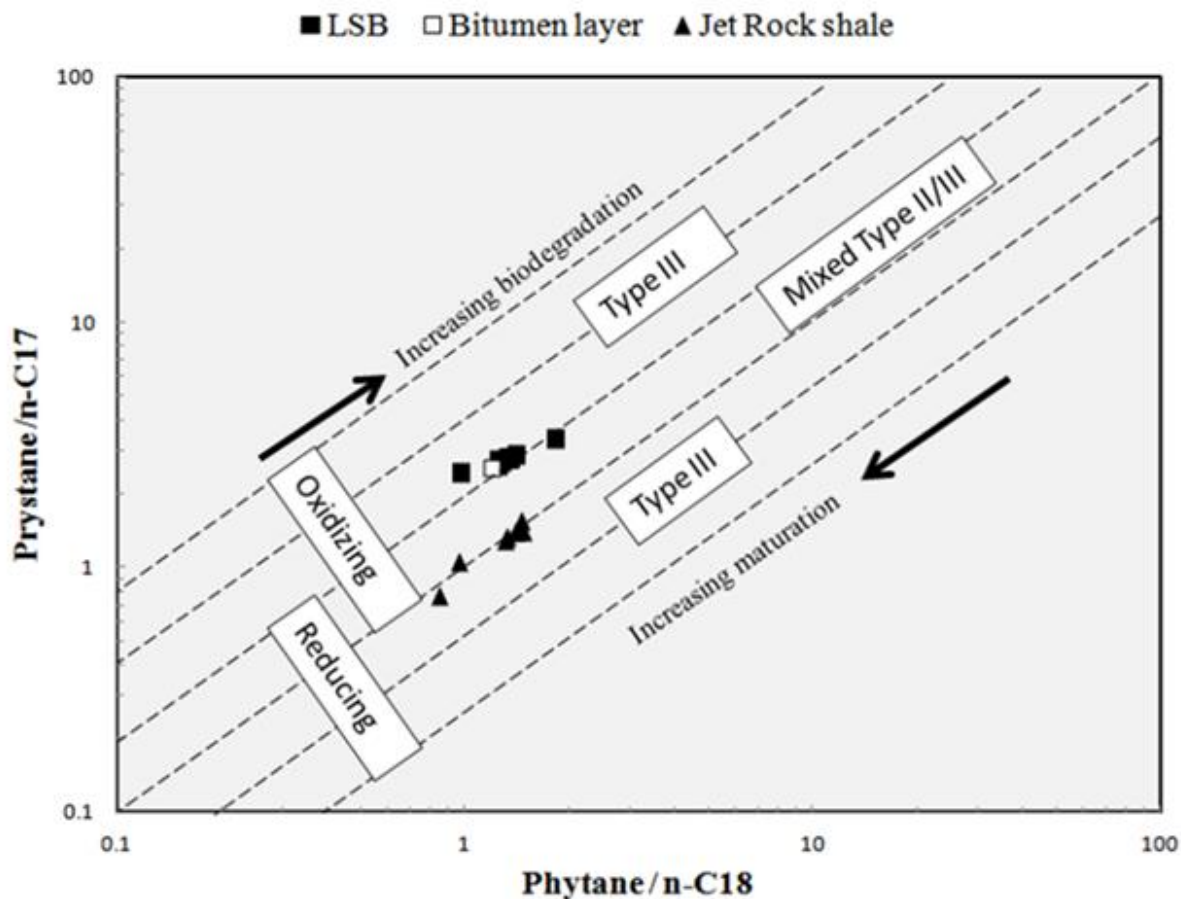


Figure 4.35: Cross plot of Pr/n-C₁₇ versus Ph/n-C₁₈ ratios from extracted bitumen gas chromatograms showing organic matter type, biodegradation and maturation conditions for the Lower Sulfur Band and the bitumen layer included compare to the Jet Rock Shale.

Hopanes and steranes distribution

Ternary plot of the 17 α (H) 21 β (H) S and R isomers for C₃₁, C₃₃ and C₃₅ $\alpha\beta$ hopanes as well as the regular 27, 28 and 29 $\alpha\alpha\alpha$ 20R Steranes (Figures 4.36 and 4.37) show a clear separation of the bitumen sample from the rest of the extracted rock samples with a dominance of C₃₁ $\alpha\beta$ hopanes.

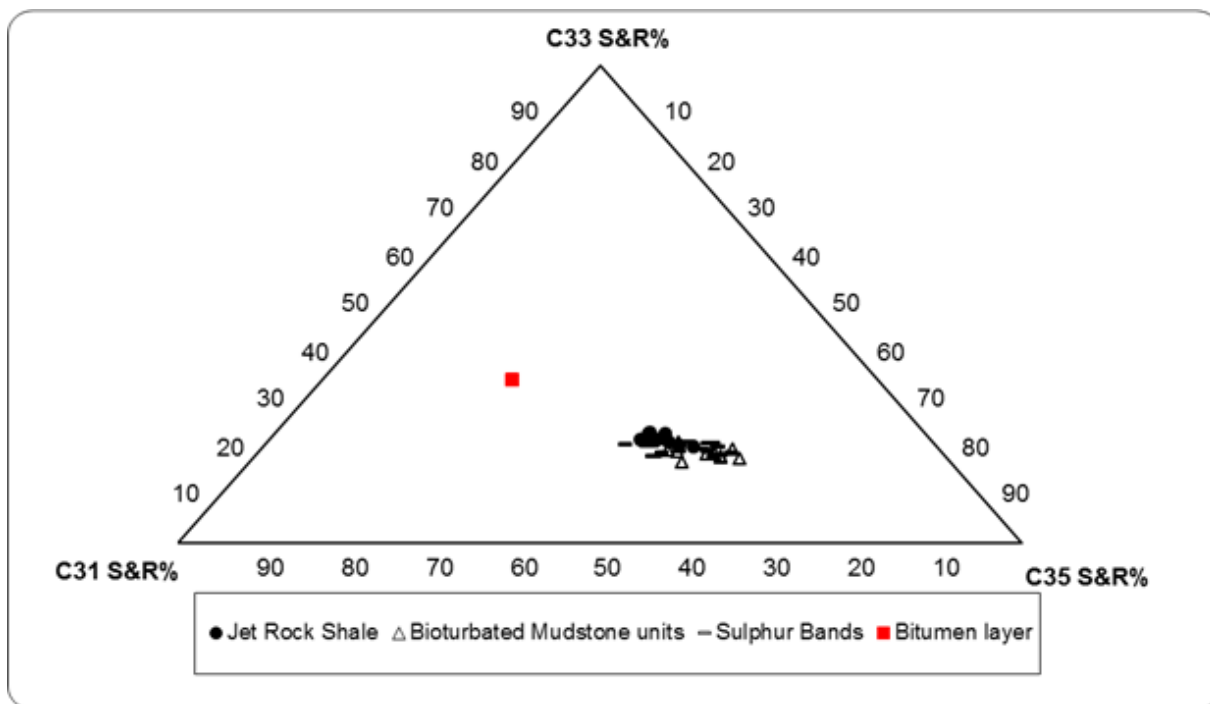


Figure 4.36: Ternary diagram showing the relative abundances of C_{31} , C_{33} and C_{35} 17α (H) 21β (H) hopanes $22R + 22S$ isomers.

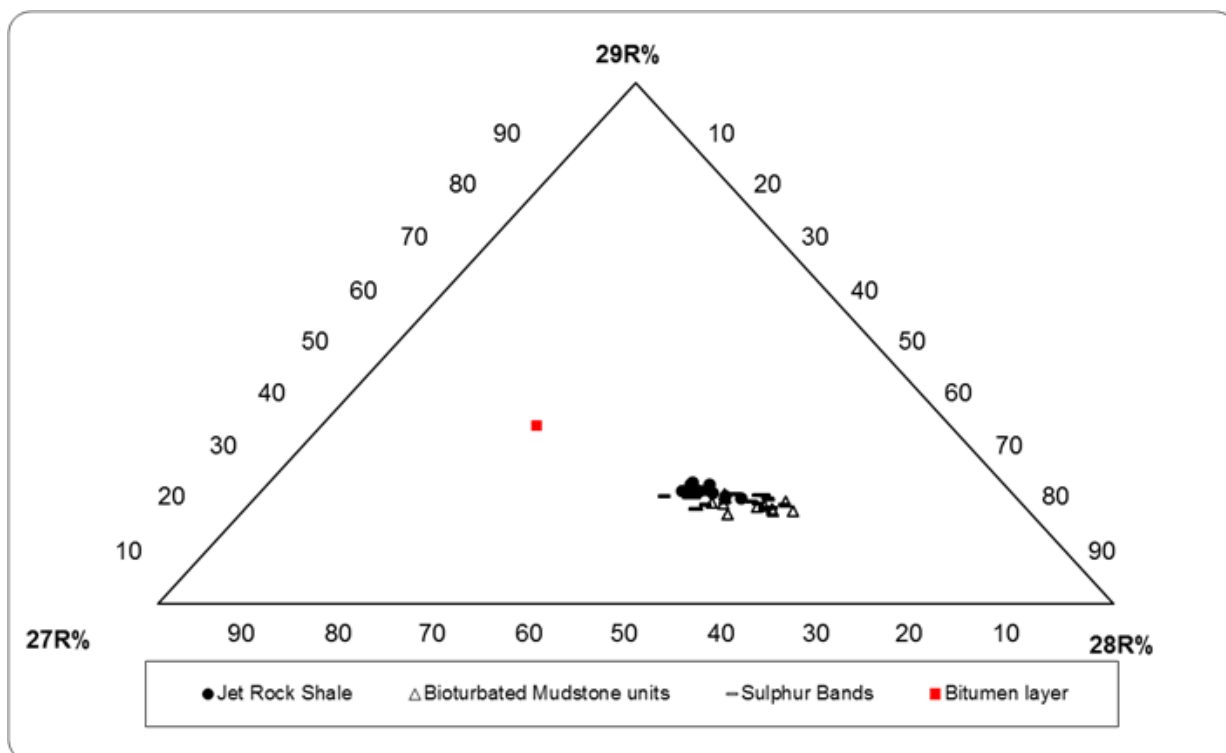


Figure 4.37: Ternary diagram showing the relative abundances of C_{27} , C_{28} and C_{29} -regular steranes 5α (H) 14α (H) 17α (H) $20R$ isomer.

4.3 Discussion

Several processes must be considered to explain the origin, preservation and distribution of organic matter. Actually the development of organic matter-rich black shales has been a matter of many geochemical studies for decades. This is due to their often perfect preservation of vital information about the geologic history and because of economic potential.

4.3.1 Thermal maturity of the organic matter

From the petroleum geochemical point of view the study section would be classified as marginally mature. The maximum burial of the Lower Toarcian section of the Cleveland basin is inferred to have been 2.2 to 2.5 km (Hemingway and Riddler, 1982). Reflectance microscopy of isolated kerogens revealed few vitrinite particles, with a consistent reflectance in the range 0.55 – 0.65% Ro (Raiswell et al., 1993; Ibrahim, 1995). Oil shows are often found in the ammonite chambers, especially the Canon ball doggers (Bed 33, sensu Howarth, 1962 and 1973) (Salen et al., 2000).

The Rock Eval data from this study confirm this maturity interpretation from previous studies, as indicated by low Tmax ranging from 420 to 441 (an average of 434 °C) and Production index (PI) ranging from 0.05 to 0.9 (an average of 0.11) reveals that early stage of thermal maturity had been achieved. Moreover, the relatively low and uniform PI that ranges between 0.06 to 0.51 and averaging around 0.13 indicates that any migrated hydrocarbons could have not indeed affected the geochemical signals (Table 4.3)

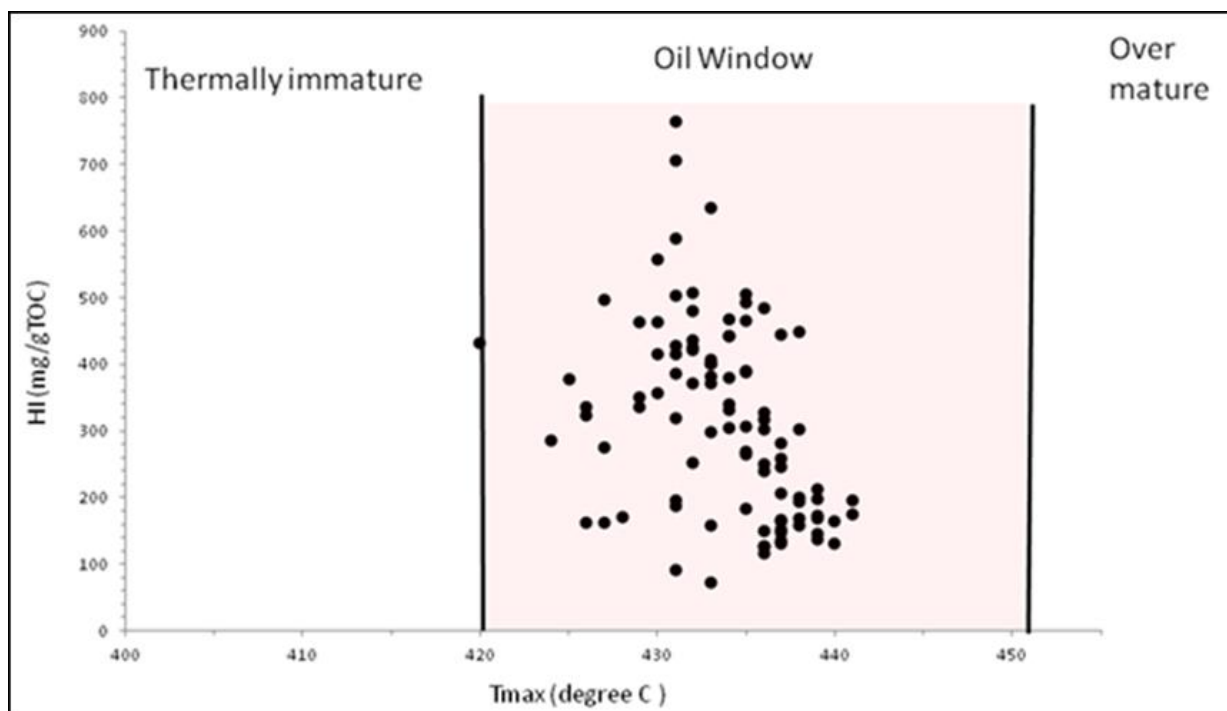


Figure 4.38: Cross plot of HI and Tmax showing the thermal maturity state of the samples at Port Mulgrave section.

Tmax values for some samples fall below the oil window ($T_{\max} \geq 430$ °C is the maturity threshold for type II according to Hunt, 1995). This suppression in the Tmax is found in the organic sulphur rich samples (e.g Sulphur bands). The low Tmax in those samples could be due to the high content of organic sulphur where the oil window for Type II-S kerogen begins earlier as the result of the breakage of weak sulphur bonds at lower temperatures (T_{\max} 390–420°C).

Molecular geochemical data also confirm an immature/marginally mature thermal maturity level. The hopanes (C_{29} to C_{35}) are dominated by the more stable $17\alpha(H)$, $21\beta(H)$ isomers with much lesser amounts of the $17\beta(H)$, $21\alpha(H)$ isomer. The biologically inherited $17\beta(H)$, $21\beta(H)$ isomers are completely absent. These isomer distributions are consistent with a relatively high thermal maturity level of the organic matter in the section (Raiswell et al., 1993). Moreover, all the samples show complete isomerisation of the $17\alpha(H)$, $21\beta(H)$ isomer at C-22 (Figure 4.18) with the $22S/(22S+22R)$ ratio corresponding to the equilibrium value of around 60 % (Peters and Moldowan, 1993). Sterane and diasterane isomerisation reactions further testify to the maturity of the organic matter of the study section as marginally mature. The $20S/(20S+20R)$ ratio for the C_{29} $5\alpha(H)$, $14\alpha(H)$, $17\alpha(H)$ sterane isomers is around 50%

for almost all samples, pointing to early matured organic matter (Peters and Moldowan, 1993).

Although most of the thermal maturity indicators used here point to thermally mature source rock, the PI are relatively low for most of the samples, particularly for the Grey Shale including the Upper and Middle Sulphur Bed (Figure 4.9). Most of these samples fall below the value of 0.1 which is the threshold of the oil window (Peters et al., 1986). This could be explained as the result of the mineral matrix effects as the Grey Shale is characterized by relatively low organic matter contents coupled with relatively high clay contents (Morris, 1979) which can retain some of the S₁ and consequently lower the production indices (Espitalie et al., 1980).

4.3.2 Source of Organic Matter

Organic matter type is an important factor in evaluating source rock potential and has an important influence on the nature of the hydrocarbon products (Tissot and Welte, 1984; Hunt, 1995 and Tyson, 1995).

Rock-Eval pyrolysis characterizes the organic matter of the *tenuicostatum* and lower *Falciferum zone (Exaratum Subzone)* as being mainly of marine origin when plotted on a S₂ vs. TOC scattered plot (Figure 4.39). The graph of S₂ versus TOC is an informative way of displaying Rock-Eval data (Langford and Valleron, 1990). The graph of S₂ vs. TOC also permits determination of the type of Kerogen without using S₃ data. The plotted data indicate that most of the samples are Kerogen type II, a part of few samples belonging to bioturbated mudstones at the lower part of the section (Grey Shale Member), which do indicate kerogen Type III OM. Moreover, the use of a linear regression curve on the S₂ versus TOC plot is the best way of calculating HI which allows identification and correction for any effects of the rock matrix (Langford and Valleron, 1990; Tyson, 1995). Despite the relatively high TOC content and the well laminated structure of the Sulphur bands, very detailed analysis across these units indicates a mixed kerogen Type II/III.

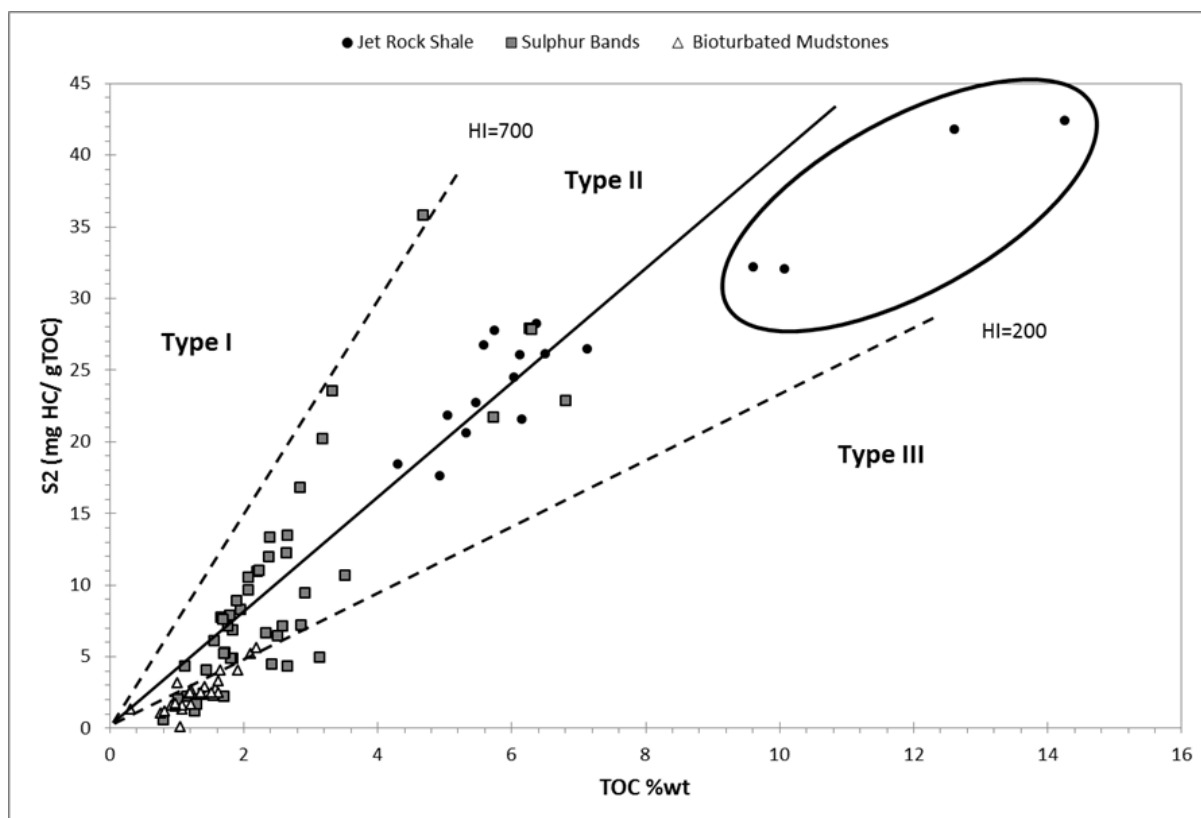


Figure 4.39: S₂ versus TOC diagram with Kerogen type fields indicating that all of the Jet Rock samples do fall in Kerogen type II while the Grey shale fall in Kerogen types II and III region.

Hydrogen index (HI) values range from 116 mg/g TOC within the bioturbated mudstones of the Grey Shale (*Tencostatum zone*) to a maximum of 484 mg/g TOC within the Jet Rock Shale (*Exartum subzone*). Despite the indication of Kerogen type II of the Jet rock samples the HI values are relatively moderate to low, especially within bed 35 where the HI values cluster around an average of 351 mg/g TOC. Generally, marine algal organic matter has higher HI values (≥ 400 ; Tyson, 1995), whereas lower values could be caused by some contribution of dispersed terrestrial material, with low hydrocarbon yields. However, microscopic examination disapproved any substantial contribution of dispersed terrestrial organic matter in the Jet Rock samples. Instead, the organic matter of the Jet Rock consists mainly of fine grained algal AOM with very rare phytoclasts (not exceeding 5%) with moderate to strong fluorescence (4-5 on the preservation scale of Tyson, 1995). These observations indicate only a minor input from higher plants. The high preservation of marine organic matter under anoxic conditions results in kerogen assemblages overwhelmingly dominated by amorphous organic matter (70-90%). On the other hand, the bioturbated mudstones (*Tencostatum zone*) apparently displayed less abundance of fine grained algal amorphous material with slightly more contribution of woody material. Therefore from

microscopic and Rock-Eval examinations and the biomarker analysis (discussed below), it can be suggested that the organic matter of the Port Mulgrave section is dominantly composed of marine-derived amorphous organic matter. Despite the powerful ability of the Rock Eval and the microscopic analysis to study the organic matter composition (Brassell et al., 1986), biomarkers can be used to further evaluate this aspect.

The *n*-alkane distributions show a unimodal distribution for all samples (Figure 4.11), maximising at C₁₅ or C₁₆ with dominance of the short chain homologues, which is generally an indication of a marine source of organic matter (Hunt, 1995). Pr/*n*-C₁₇ and Ph/*n*-C₁₈ ratios have been widely applied as indicators of source rock types, depositional environments and organic matter maturation (Peters et al., 1999; Duan et al., 2006). The high abundance of pristane and phytane compared to C₁₇ and C₁₈ *n*-alkanes respectively, for most of the samples (Table 4.13), suggest an algal or microbial source of the organic matter (Tissot and Welte, 1978). Further evidence for microbial sourced OM comes from the abundance of hopanes biomarkers.

The sterane/17 α -hopane ratio reflects input of eukaryotic (mainly algae and higher plants) versus prokaryotic (bacteria) organisms to the source rock (Peters et al., 2005). Terrigenous higher plant input is generally low (evidenced by low proportions of long-chain *n*-alkanes in the great majority of samples) indicating that dominance of steranes (in particular C₂₉ steranes) components does not reflect vascular plant contribution, but relates to the type of algal inputs (Volkman, 1986). In general, high concentrations of steranes and high steranes/hopanes (≥ 1) typify marine organic matter with major contributions from planktonic and/or benthic algae (Moldowan et al., 1985). Conversely, low steranes and low steranes/hopanes are indicative of terrigenous and/or microbially reworked organic matter (Mackenzie et al., 1984). However, sterane contents have been reported to decrease with increasing thermal maturity (Rullkotter and Marzi, 1987). The thermal maturity effect in our case is very minimum since the studied section is thin in terms of any thermal gradient to take place and it is homogeneously early matured.

However, high steranes/hopanes ratios (Figure 4.19) dominate the Jet Rock (*exartum* subzone), which is consistent with the microscopic observation pointing to mainly marine algae organic matter source (Figure 4.24). On the other hand the Grey shale member is characterized by relatively low steranes/hopanes ratios which could be indicative of a bacterial contribution associated with more terrestrial contribution of higher plant material,

which is supported by visual evidence (Figure 4.25) and higher degree of waxiness (Figure 4.10).

The relatively higher contribution of hopanes relative to steranes in the Grey Shale member may also arise from greater bacterial breakdown of the autochthonous algal material during deposition (Farrimond et al. 1986) with an associated increase in the relative proportion of bacterial biomass.

Characterisation of the organic matter source can be extracted from the distribution of regular steranes (Moldowan et al., 1985 and Philip et al., 1991). In our studied samples the distribution of regular steranes as shown in Figure 4.15 is similar throughout the section, suggesting a constant marine organic matter source with a slight preference of C29 steranes ratios over C28 and C27 for the Grey shale samples, a feature commonly seen in marine black shales with contribution of terrestrial organic matter (Peters et al., 2005). Moreover, The marine source of organic matter can be inferred (but not proven) by the ternary diagram which reflects the distributions of C27, C28 and C29, 5 α (H), 14 α (H), 17 α (H), (20R) steranes for the different shale samples of the section. All the samples, including the Grey Shale samples, show very close grouping (Figure 4.20) suggesting a constant marine source throughout the section.

Based on the above discussed parameters, a distinction can be made between the dominant types of organic matter present in the shales. It can be said that the Grey shale member seems to have received some contribution of land-derived organic matter that has been transported into a marine depositional setting and was deposited in a photosynthetic organisms-dominated environment (thereby suggesting a mixed Kerogen type II & III). Moreover, the Sulphur Bands are characterised by marine sourced organic matter with some contribution of terrestrial input. On the other hand, the Jet Rock Shale (exartum subzone) is characterised by a dominance of marine organic matter sourced mainly from planktonic and/or benthic algae.

4.3.3 The palaeoenvironment of deposition

The paleoenvironmental conditions during organic matter (OM)-rich black shale formation have been an important scientific issue to understand/reconstruct global and regional biogeochemical element cycling. The interpretation of organic matter source for any sedimentary sequence usually provides some clues for the palaeoenvironment of deposition

(Brassell et al., 1986). The well preserved, dominantly amorphous organic material, the relatively high hydrogen indices which indicate type II kerogen and the high TOC contents (Tables 4.2 and 4.3), are indicative of a dysoxic to anoxic condition of deposition (Tyson, 1995). This assumption is confirmed by the high sulphate content which shows a degree of correlation with the relatively high TOC content (Figure 4.3). All samples lie above the normal marine line and mostly fall into the euxinic consistent with euxinic condition of deposition (Raiswell and Berner, 1985) especially for those belonging to the *Exartum* subzone and the Sulphur band horizons. The well-developed lamination, which is rarely interrupted, exhibited by the shales of the Bituminous Shale zone, especially by the Jet Rock Shale of the *Exaratum* subzone (Morris, 1979), is consistent with the inferred anoxic conditions. The fluctuating TOC within the *Exaratum* subzone (Table 4.2 and Figure 4.1) might suggest that the degree of anoxia has been variable although fluctuations in productivity may be an alternative cause. The Grey Shale zone, on the other hand, consists of poorly laminated dark grey shale, but there has been inconclusive of bioturbation which suggests that during the deposition of the Grey Shale anoxic conditions prevailed below the sediment-water interface and the water column remained oxic, whereas anoxic conditions extended into the water column during the deposition of the Sulphur bands. In the present study, Pristane/Phytane ratios are greater than unity, frequently interpreted as evidence for oxic conditions prevailing during sediment deposition (Didyk et al., 1978). However, these relatively high values of pristane/phytane ratios throughout the study section (Table 4.2.4) are more likely the result of the elevated thermal maturity of the samples (Didyk et al., 1987) rather than an indication of the degree of oxicity. Although it is difficult to interpret absolute Pristane/Phytane values in terms of redox conditions, it is obvious that the ratio is higher for the Grey Shale zone than the overlying Jet rock Shale zone suggesting that more oxic conditions could have been prevailing during the deposition of the Grey Shale. Also the relatively abundant steranes compared to hopanes within the Bituminous Shale zones of the Sulphur Bands, could be interpreted as a result of less oxic conditions (Volkman, 1986) prevailing during the deposition of these shales, which is further confirmed by the low C₃₁ content compared to the C₃₅ or C₃₄ content of the 17 α (H), 21 β (H) (S+R) hopanes (Peters and Moldowan, 1991).

The presence and widespread distribution of isorenieratane indicates that a sulfidic photic zone was a common occurrence, within the Sulphur Bands at the base of the Grey Shale, and as well throughout the Jet rock shale spanning the T-OAE. Isorenieratane

maximum abundance is near the maximum in TOC, implying that strengthening euxinia was responsible for increasing in organic carbon burial. Isorenieratane signature in Toarcian black shales has been regarded as supporting evidence to point out to strong stratification during the deposition of Jet Rock shale (Kuspert, 1982). The presence of isorenieratane within short intervals of the sulphur bands before the main T-OAE indicates that euxinia was developed during short periods at the Pliensbachian-Toarcian.

The high TOC content and the distribution of the Jet Rock of Western Europe, has led Jenkyns (1985, 1988), to infer a widespread oxygen minimum zone associated with a so called Toarcian Oceanic Anoxic Event (OAE), which may have resulted from high surface productivity. In the case of the Port Mulgrave section, the well preserved algal (marine-derived) organic matter of the Jet Rock Shale, coupled with the relatively high proportion of regular steranes (table 4.5), could be consistent with high surface productivity (Farrimond et al., 1988).

The geochemical characteristics of the *Exartum* subzone reflect global geochemical change (T-OAE) and fit well with the model for deposition of the Jet Rock and its equivalents in Western Europe and elsewhere in the world. Jenkyns (1988) proposed that certain regions of the world ocean, in particular the oxygen minimum zones (OMZ) were particularly poorly ventilated due to the topographic restriction (e.g block-faulted margin) and deposition of organic-rich shales was widespread during the early part of the *Falciferum* zone (*Exaratum* subzone). This model implies high surface productivity in shallow waters rich in nutrients. The high oxygen demand, through partial microbial degradation of large quantities of the autochthonous organic matter, led to oxygen depletion in bottom waters resulting in anoxic conditions and the subsequent preservation of large quantities of the organic matter.

4.3.4 Comparison of Sulphur Bands (Grey Shale Member) basal transgressive black shales and Jet Rock (maximum flooding) black shales

It is well documented that in many epicontinental seas, the distal basin settings (settings of low and slow sedimentation rate) accumulate intervals of organic rich condensed black shales (Demaison and Moore, 1980). In such deep-water settings the benthic environment is poorly oxygenated (anoxic or suboxic) due to isolation of the bottom waters from dynamic effects such as the wind-driven vertical advection of oxygen-rich surface waters. The establishment of a very rapid density gradient in the water column and development of a pycnocline can be a factor for isolating bottom waters and therefore developing a more static state that led to water column stratification (Wignall, 1993).

Condensed sections can also extend into marginal settings at times of rapid sea level rise where they form on the maximum flooding surface, separating the transgressive from the high stand system tracts (e.g jet rock shale). This is an important mechanism for introducing black shales into areas normally characterized by shallow deposition and at the same time connecting deep and shallow water black shales. Many types of black shale are associated with sites of greatest subsidence, leading Hallam and Bradshaw (1979) to propose the model of irregular bottom topography (known as the “puddle model”). In this model the deep-water conditions essential for black shales are achieved by rapid subsidence only and potential exists for black shale formation throughout the sea level cycle. However, black shales were most likely to form on sites of rapid subsidence at the inflexion point of relative sea level rise.

Thin black shales extending from basinal into marginal settings fall into two categories: The first category is basal transgressive (BT) black shales, which show no obvious lateral facies variation and normally pass proximally into sediment-starved marginal facies (e.g the Sulphur Bands at the base of Whitby Mudstone formation at the Pliensbachian-Toarcian boundary). BT black shales are distinguished by resting directly on a transgressive surface which may coincide with a sequence boundary or it correlative conformity as is probably the case with the Sulphur Band and Lower Oxford Clay examples with no time-equivalent shoreline facies, as they most probably formed during times of non-deposition on the basin margin (Grabowski and Glaser, 1990).

The second category are maximum flooding surface black shales, which are distinguished by passing proximally into thicker sections of shallower marginal marine facies. These exhibit the most oxygen-restricted facies in the basin centre and represent a deep-water

sediment-starved condensed section. They often rest conformably on sediments of the transgressive system tract. Examples are the black shales of the Jet Rock, the G. cumbriense and G. listeri Marine Bands.

Previous studies have been concerned with boundary intervals at the Late Pliensbachian to Early Toarcian as it relates to sea level change (Hallam, 1997), paleoceanographic change (Bailey et al., 2003), as well as contrasting water mass and basinal restriction (Sælen et al., 2000; McArthur et al., 2008). All these may have affected deposition of both the Grey Shale and the overlying Jet Rock during the period of major basin subsidence characterised by deep open waters (Powell, 2010).

Despite its name, and the presence of small carbonaceous flakes and jet, the geochemical and optical analysis of this study indicate that the Jet Rock shale organic matter has been mainly derived from marine algae and comprises mostly amorphous organic matter with relatively minor terrestrial contributions (This study and Farrimond et al., 1989; Ibrahim, 1995; Sælen et al., 2000). The Jet Rock having higher TOC and HI compare with the Sulphur Bands (Table 4.8) also, the mean values of the Sulphur Beds are slightly different from the Jet Rock. The geochemical and optical data of the Jet Rock black shale show a good source rock potential and Type II kerogen, while the Sulphur Beds data indicate a lower quantity of OM and quality of kerogen.

Table 4.7: Summary of bulk geochemical data from the Jet Rock and Sulphur Bands.

Jet Rock	TOC %	S1	S2	Tmax	HI	PI
No.	17	17	17	17	17	17
Range	4.26 - 14.26	2.07 - 7.87	17.62 - 42.39	420 - 436	297 - 484	0.09 - 0.19
Mean	7.13	4.29	26.89	431	392	0.15
SD	2.82	1.48	7.06	3.43	55.01	0.03
Sulphur Beds						
No.	47	47	47	47	47	47
Range	0.80 - 6.81	0.16 - 88	0.58 - 35.81	424 - 440	72 - 765	0.06 - 0.90
Mean	2.49	2.67	9.66	432	357	0.1
SD	1.38	12.73	7.88	3.68	162	0.12

The kerogen assemblages of both samples are shown in the APP diagram (Figure 4.25). Despite the very high AOM in both intervals, the Sulphur Beds samples are clearly

separated from the Jet Rock samples with higher woody material and palynomorphs which could indicate more proximal setting and more dynamic environments relative to the Jet Rock interval. Table 4.3 summarizes the similarities and differences between the deposition conditions of the sediments in both members; the percentage of phytoclasts input in Jet Rock is either masked by AOM, or the formation was deposited further from shoreline.

Table 4.8: Summary table show the similarities and the differences between MFS and basal black shales.

Similarities	Differences
<ul style="list-style-type: none"> • All samples deposited in reducing environments. • Both have dominantly marine Amorphous Organic Matter (AOM) • Both are organic-rich shale. 	<ul style="list-style-type: none"> • Kerogen assemblages show better preserved in Jet Rock • Sulphur Bands have more variable properties and interbedded with more oxic layers. • Overall thickness of Jet Rock is much greater.

4.3.5 Hydrocarbon potential

The existing dataset indicates that the lower Toarcian sediments from the *Tenuicostatum* - *Falciferum* zones have a good source rock potential. The shale and mudstone units frequently contain above average TOC with an average of 1.3 for the mudstone units and 3.4 wt% for the laminated shales, and an average of pyrolysis S₂ yields of up to 10.9 mg/g (up to 42.4 mg/g within the bituminous shale) have been recorded pointing to very good source rock potential (table 4.2).

Table 4.9: Petroleum generative potential from combined Rock-Eval and TOC values (after Baskin, 1997)

Potential	TOC (wt %)	S1 (mg HC/g rock)	S2 (mg HC/g rock)
Poor	<0.5	<0.5	<1
Fair	0.5-1	0.5-1	1-5
good	1-2	1-2	5-10
very good	>2-4	2-4	10-20
excellent	>4	>4	>20

Kerogen is mainly oil-prone type II (marine dominant) with minor contribution of Type III kerogen. This variation in organic matter quality is also reflected in hydrogen index values which range from less than 100 to more than 480 mgHC/mgTOC; the bituminous shale (*Exartum* subzone) represent the richest horizon and the most oil-prone. Thermal maturity indicators (e.g Tmax and C₂₉ steranes biomarkers isomerisation) show that the lower Toarcian section at the study area ranges from marginally mature to peak maturity for oil. Oil and gas shows are common and are interpreted to represent hydrocarbon generation and expulsions.

4.4 Conclusions

- The application of CPI values and measurement of the stereo-isometric ratios ($22S/22S+22R$ for C_{32} hopanes and $20S/20S+20R$ for regular steranes) of the extended hopanes and steranes series indicate that the sediments studied have reached a level of thermal maturity that approaches the oil window.
- Overall, the amorphous and fluorescent nature of the organic matter of these shales, coupled with the high hydrogen indices point to a dominantly marine (algal and bacterial) origin of the organic matter. However, a slight variable terrestrial input is evidenced by a fluctuating the percentage of woody material (Phytoclasts) is observed at the base of the Grey Shale between the Sulphur Bands and the bioturbated mudstones. The terrestrial input is declined upward where very clear dominant of AOM is characterising the Jet Rock shale reflecting proximal distal trend initiated by sea level change.
- The organic matter sources do not vary significantly across the T-OAE interval (Jet Rock Shale), where it is fairly homogenous. The high TOC contents coupled with the well-developed lamination, well fluorescent nature of the organic matter and low pristane/Phytane ratios and generally consistence Isoreneratine presence are indicative of anoxic stratified water condition that prevailed during the deposition of these shales, with free sulphide being present in the photic zone.
- Despite the well laminated appearance of the Sulphur Bands, very detailed analysis indicates that there are fluctuations in the paleoredox conditions across these units, cycling between severe anoxic and sulphidic conditions extending into the photic zone and to dysoxic conditions.
- Maximum flooding black shales of the Jet Rock and the basal black shales of the Sulphur Beds both are showing to be anoxic facieses deposited in distal setting. Although both shales are characterised by relatively high level of HI, the Jet Rock shale seems to have been more stagnant with more permanent stratification perhaps because it was deposited in deeper water at the peak of the transgression.
- The bioturbated mudstone intervals surrounding the Sulphur bands, are characterized by low hydrogen index despite the relatively moderate to high AOM. The fluorescence indicates that AOM is poorly preserved in these bioturbated sediments suggesting oxic degradation with originally Type II kerogen degraded to a Type III.

CHAPTER 5 - WATER COLUMN REDOX DYNAMICS DURING THE ONSET OF THE TOARCIAN OCEANIC ANOXIC EVENT

5.1 Introduction

The North Yorkshire succession documents a gradual transition from a well-oxygenated marine environment during sea level lowstand, to a more stable, stratified water column with anoxic or even sulfidic bottom waters during the maximum flooding phase, represented by the Jet Rock Shale. Based on $\delta^{18}\text{O}$ and Mg/Ca analyses (McArthur et al. 2000; Bailey et al. 2003; van de Schootbrugge et al. 2005) it has been proposed that this transition was driven by a gradual global warming accompanied by a significant mass extinction event in the ocean (Caswell et al 2008).

The Pliensbachian–Toarcian boundary preceding the OAE has received less attention, but is quite an important interval with regards to paleoenvironmental change, including changes in carbon cycling, changes in sea level, faunal turn-over and evolving palaeoclimate. A sea-level rise across the stage boundary of several tens of metres (Hallam, 1981) coincides with a relative minimum in seawater strontium-isotope values at this boundary interval, where the $^{87}\text{Sr}/^{86}\text{Sr}$ ratios fall to the least radiogenic values seen throughout the Early Jurassic (Jones and Jenkyns, 2001).

The transition from the Pliensbachian into the Toarcian is also marked by the initiation of the mass extinction event, suggesting that changes in climate and paleoceanography started to occur well before the onset of the OAE (Little and Benton, 1995; Wignall and Bond, 2008). Moreover, an abrupt paleotemperature increase in bottom sea water is recorded at the Pliensbachian–Toarcian boundary. The changes in $\delta^{18}\text{O}_{\text{brachiopod}}$ isotope suggest approximately 6°C shift in the bottom water paleotemperature from 14°C at the late Pliensbachian to about 20°C in the earliest Early Toarcian (Suan et al., 2008a). It has been observed that most of the well-known mass extinction events in the geological record were routinely accompanied by perturbations to the global carbon cycle (Keller and Lindinger, 1989; Arens and Jahren, 2000; Payne et al. 2004; Hesselbo et al. 2002; Riccardi et al. 2007).

Our current understanding of the small events before the main T-OAE is, however, largely unconstrained. Thus this chapter focuses on new and comprehensive geochemical analyses across the Pliensbachian-Toarcian and extending throughout the T-OAE. Using a

combination of organic and inorganic geochemical techniques, including iron speciation (Poulton and Canfield, 2005), trace element enrichments, molecular biomarkers for photic zone euxinia, and bulk geochemical and isotopic analyses, new insight is provided into the detailed dynamics of depositional redox variations. This, in turn, allows consideration of the biogeochemical processes driving these rapid redox variations, and the significance of the Sulphur Bands to the T-OAE.

5.2 Results

The concentration of total organic carbon is shown in Figure 5.1. These results are consistent with previously reported trends (Salen et.al, 2000; Jenkyns and Clayton 1997). Moderate to low organic matter contents of <1.5% TOC occur in the middle and lower part of the Grey shale (*upper Hawskerense* to *middle Semicelatum*), except for the laminated organic rich horizons of the Sulphur Bands where concentrations reach up to 7%. Further up-section throughout the uppermost part of the *tenuicostatum* zone, TOC gradually increases to reach maximum values exceeding 14% within the *exartum* subzone (top of Bed 34 and throughout Bed 35) beyond which TOC tends to decrease into the *Falciferum* subzone.

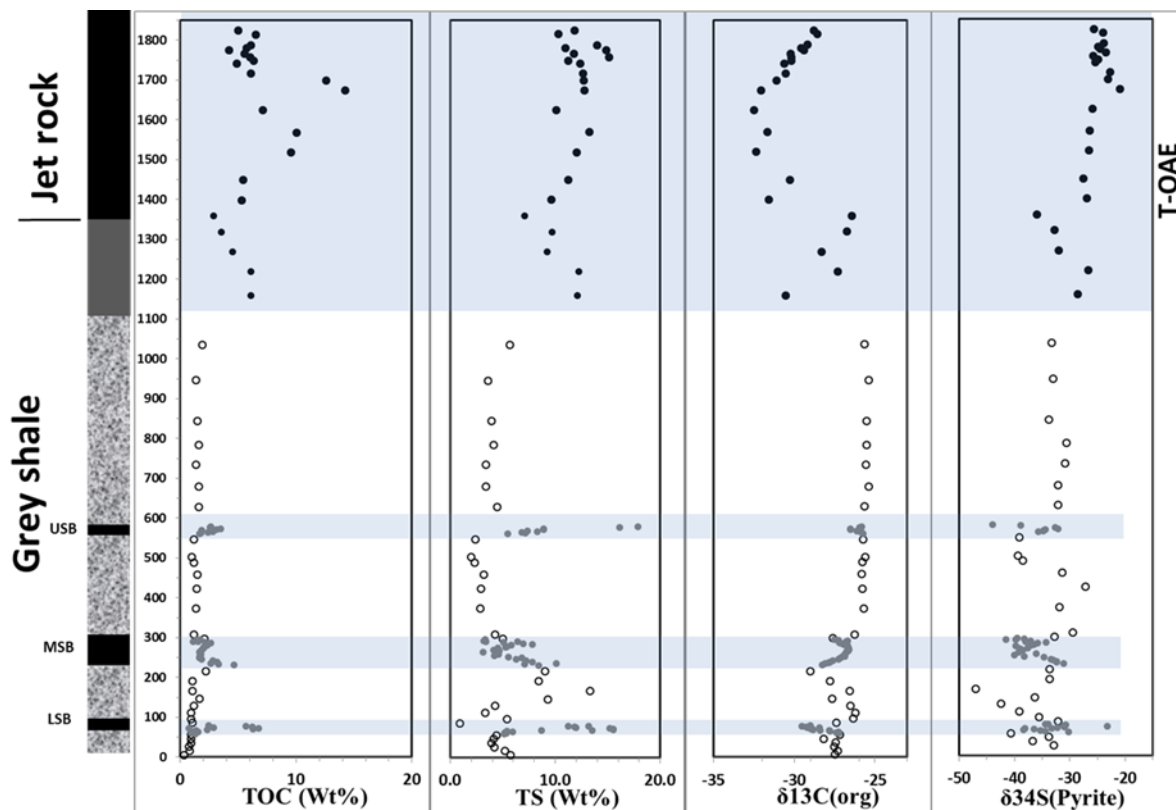


Figure 5. 1: Outline lithostratigraphy, and profile of concentrations TOC, TS, $\delta^{13}\text{C}$ of the organic matter and $\delta^{34}\text{S}$ of the pyrite sulphur through the Lower Toarcian strata of Port Mulgrave section.

The sulphur content in general changes proportional to TOC with peaks in the sulphur bands and the Jet Rock unit. Here total S approaches up to 18%, in stark contrast to less than 2% measured in the bioturbated mudstones directly above and below. Upwards in the section towards the laminated units, total S gradually increases to exceed 12% in Bed 31-32 before it decreases to less than 7% near the base of the Jet Rock unit. Within the Jet Rock, total S remains high and reaches up to 15% within bed 38, whereas TOC starts to decline above bed 35 to values of around 6%.

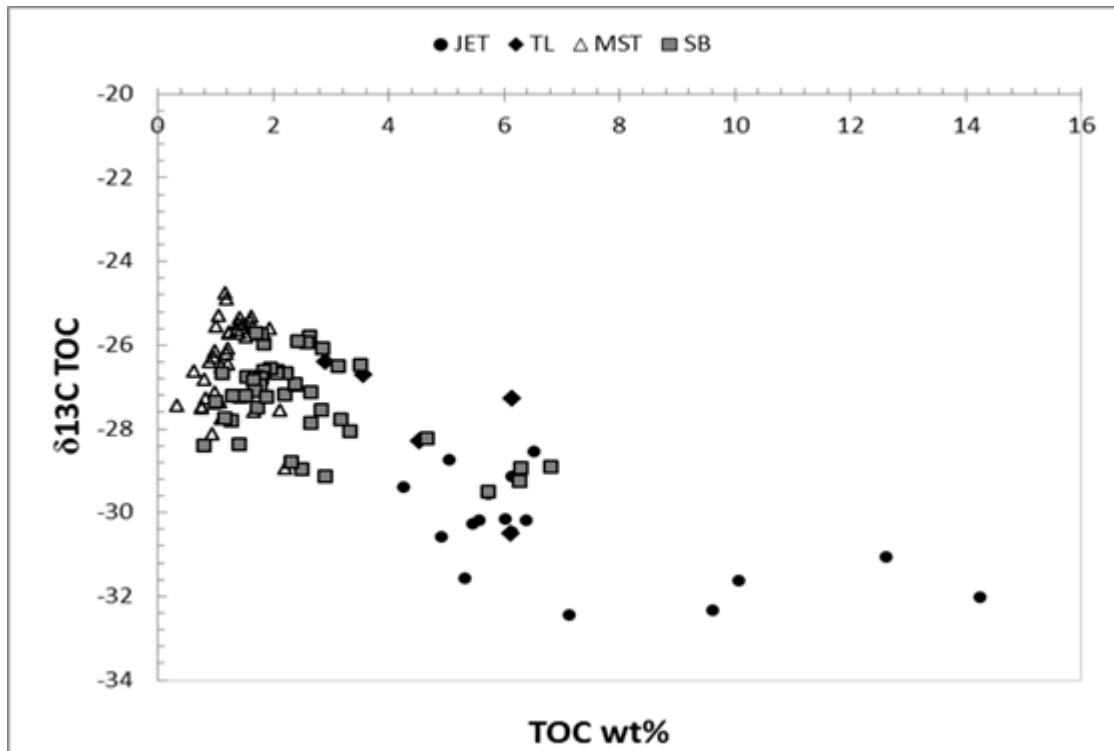


Figure 5.2: Cross plot of $\delta^{13}\text{C}_{\text{TOC}}$ and TOC wt% show negative correlation. Samples from the Jet Rock shale and Lower sulphur bands are the most depleted in $\delta^{13}\text{C}_{\text{TOC}}$.

The $\delta^{13}\text{C}_{\text{TOC}}$ values of the study section range from about -26‰ to -32‰ clearly showing the diagnostic negative C excursions marking the onset of the Toarcian-OAE. At the study site the main negative C excursion has a magnitude of approximately -7‰. Notably, there are three smaller scale negative excursions with a magnitude of almost -4‰ spanning the sulphur bands. The first peak occurs in the upper *P. hawskerense* Subzone in the latest *Pliensbachian*, where the $\delta^{13}\text{C}_{\text{TOC}}$ culminating in values of approximately -29.5‰ within the lower sulphur bed. Above, $\delta^{13}\text{C}_{\text{TOC}}$ returns to pre-excursion values of about -25.5‰ within the base of the *P. paltum* Subzone, and is then followed by a second peak of -28‰ at the middle sulphur bed. After the third peak that responds to the upper sulphur bed the $\delta^{13}\text{C}_{\text{TOC}}$

returns to pre-excursion values again and persists until the onset of the larger negative carbon-isotope excursion in the *D. tenuicostatum* Zone that is associated with the Early Toarcian OAE. TOC is negatively correlated to $\delta^{13}\text{C}_{\text{TOC}}$ with higher TOC having the most negative $\delta^{13}\text{C}_{\text{TOC}}$ signatures (Figure 5.2).

The sulphur isotope record ($\delta^{34}\text{S}$) ranges from -46.96‰ to -20.85‰ (Figure 5.1). The variability is greatest in the bioturbated mudstones and the sulphur bands in comparison to the Jet Rock unit where values cluster around a mean of -24.79‰.

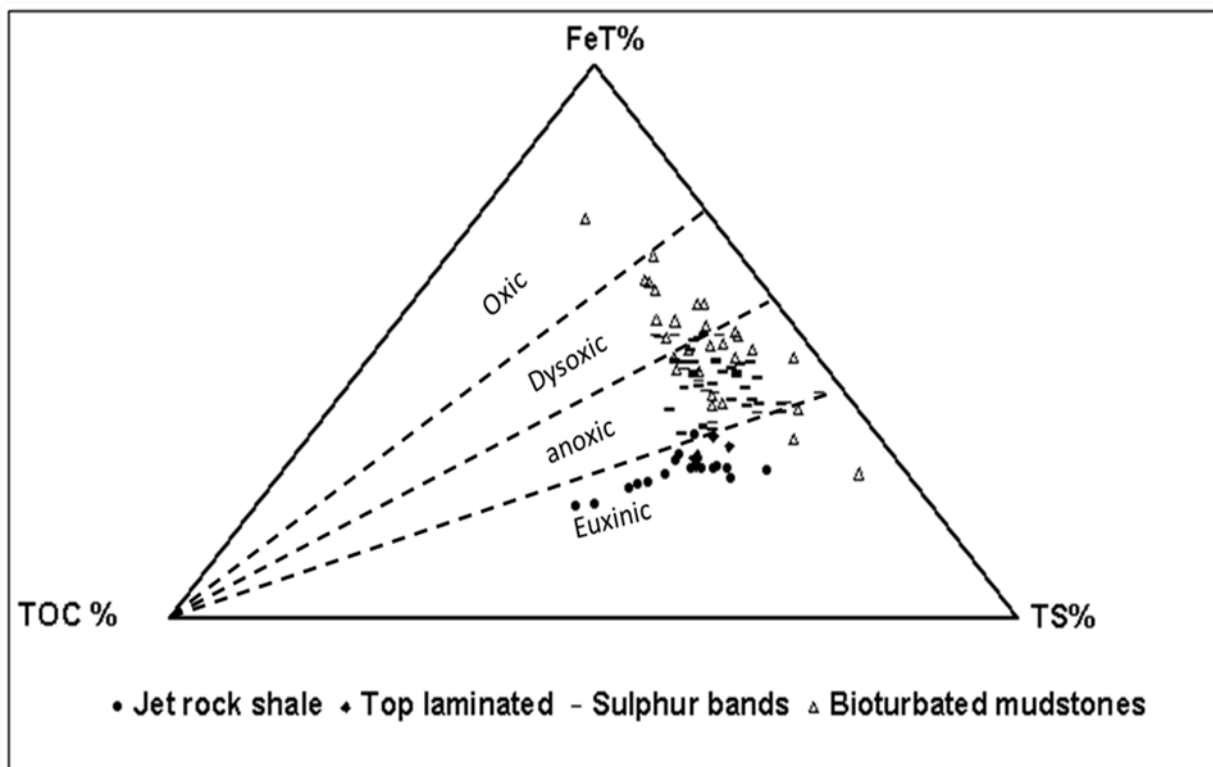


Figure 5. 3: Ternary TOC-TS-FeT diagram showing the relative distribution of the three elements. Construction and principles of interpretation of the diagram based on Dean and Arthur (1989) and Arthur and Sageman (1994).

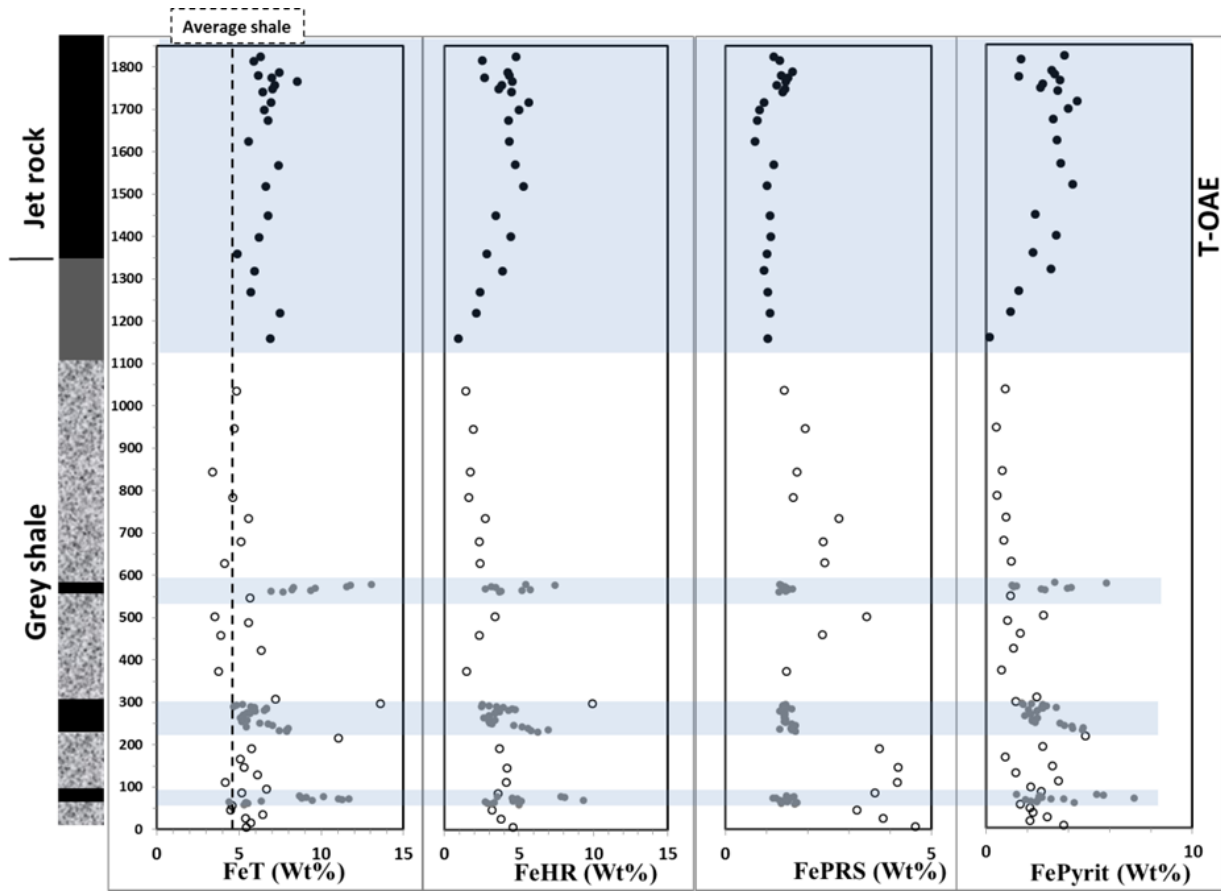


Figure 5.4: Composite stratigraphy with iron speciation data. The total Fe content (in wt%) and the relative proportion of Fe residing in unreactive and reactive phases at Port Mulgrave section

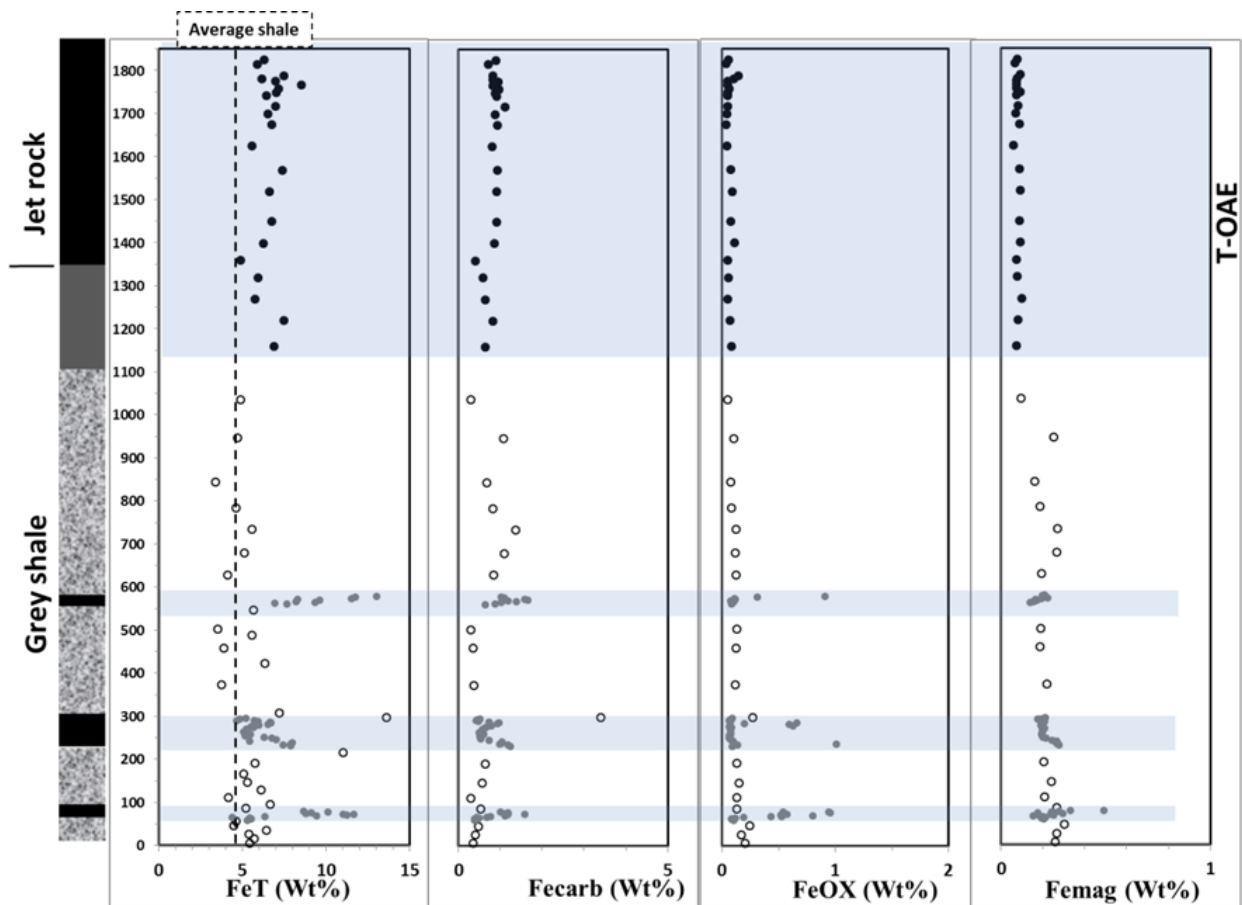


Figure 5.5: Composite stratigraphy with iron speciation data of the Port Mulgrave section

The Fe data confirm that the study section is overall enriched in iron. The average value of total iron (FeT) is 6.7 wt% which is significantly higher than average shale (4.7 wt%, Turekian and Wedepohl, 1961).

The Chlorobactane and Isorenieratane records, derived from photosynthetic green sulfur bacteria indicating photic zone euxinia (PZE), identify sulfidic conditions in the shallow ocean during deposition of most of the sulphur beds and the entire exartum subzone (Jet Rock). Concentrations of PZE markers fluctuate strongly, from zero to $93.1 \mu\text{g g}^{-1}$ TOC for Isorenieratane (Figure 5.6). Below the Toarc-OAE interval, PZE markers are restricted to the dark laminated units of the sulphur beds with highest quantities ($19.01 \mu\text{g/g}$ TOC) in the lower Sulphur Band. The mm-scale analysis of the lower sulphur bed reveals substantial variation in shallow water redox conditions during times of deposition. Moreover, the top laminated unit of the Grey shale (bed 31 and 32 of the semicelatum subzone) and the entire Exartum subzone reveals consistent high levels of PZE markers.

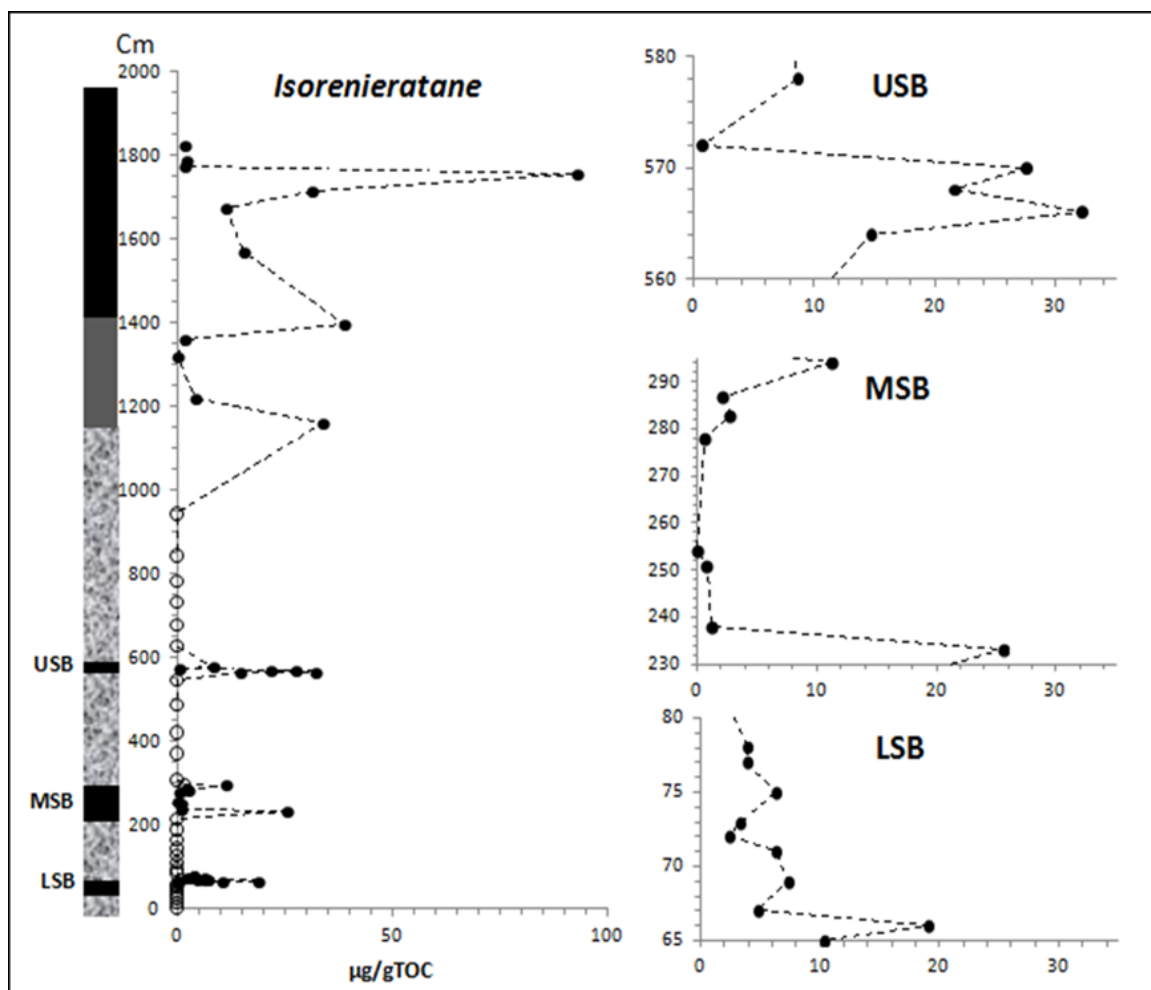


Figure 5.6: Stratigraphic records of isorenieratane abundances in $\mu\text{g/g TOC}$ across the study section at Port Mulgrave.

Transition metal concentrations are shown as depth profiles in Figure 5.7. To evaluate metal enrichment relative to the detrital fraction, and to avoid complications associated with dilution by biogenic fluxes such as calcium carbonate and organic matter, metal concentrations have been normalized to Al. Any deviation from average shale composition (from Taylor, 1964) is readily seen in element/Al-ratio records. In addition, enrichment factors (EF) ($\text{EF} = \frac{[\text{element}/\text{Al}]_{\text{sample}}}{[\text{element}/\text{Al}]_{\text{shale}}}$) for individual elements are shown (Table 5.1).

Table 5. 1: Averages of element enrichment factor values for each interval through the study section. MST = Mudstone, LSB= Lower sulphur bed, MSB=Middle sulphur bed, USB=Upper sulphur bed, TL=Top Laminated unit, and the bed numbers follow those of Howarth (1962, 1973).

Stratigraphic interval	Cu (E.F)	SD	Zn (E.F)	SD	Mo (E.F)	SD	V (E.F)	SD	Mn (E.F)	SD
Jet Rock (bed 37-39)	1.22	0.20	1.36	0.44	6.88	1.53	1.20	0.09	1.17	0.10
Jet Rock (bed 34-36)	1.93	0.72	1.32	0.50	7.99	3.09	1.44	0.30	0.84	0.45
Top laminated unit	0.91	0.28	0.89	0.18	4.01	0.79	1.01	0.10	0.84	0.22
4-MST	0.52	0.02	0.96	0.06	2.57	0.53	0.89	0.03	1	0.10
USB	1.42	0.59	1.23	0.61	3.98	0.87	0.94	0.06	1.09	0.10
3-MST	0.63	0.16	0.88	0.08	2.35	0.70	0.91	0.08	1.02	0.16
MSB	0.80	0.34	0.94	0.20	3.32	1.11	0.91	0.07	0.96	0.06
2-MST	0.73	0.61	1.09	0.50	5.70	6.16	1.00	0.07	1.02	0.09
LSB	0.95	0.70	0.87	0.21	17.38	10.43	0.98	0.13	1.11	0.22
1-MST	0.84	0.61	0.95	0.27	6.98	1.53	0.97	0.16	2.59	3.81

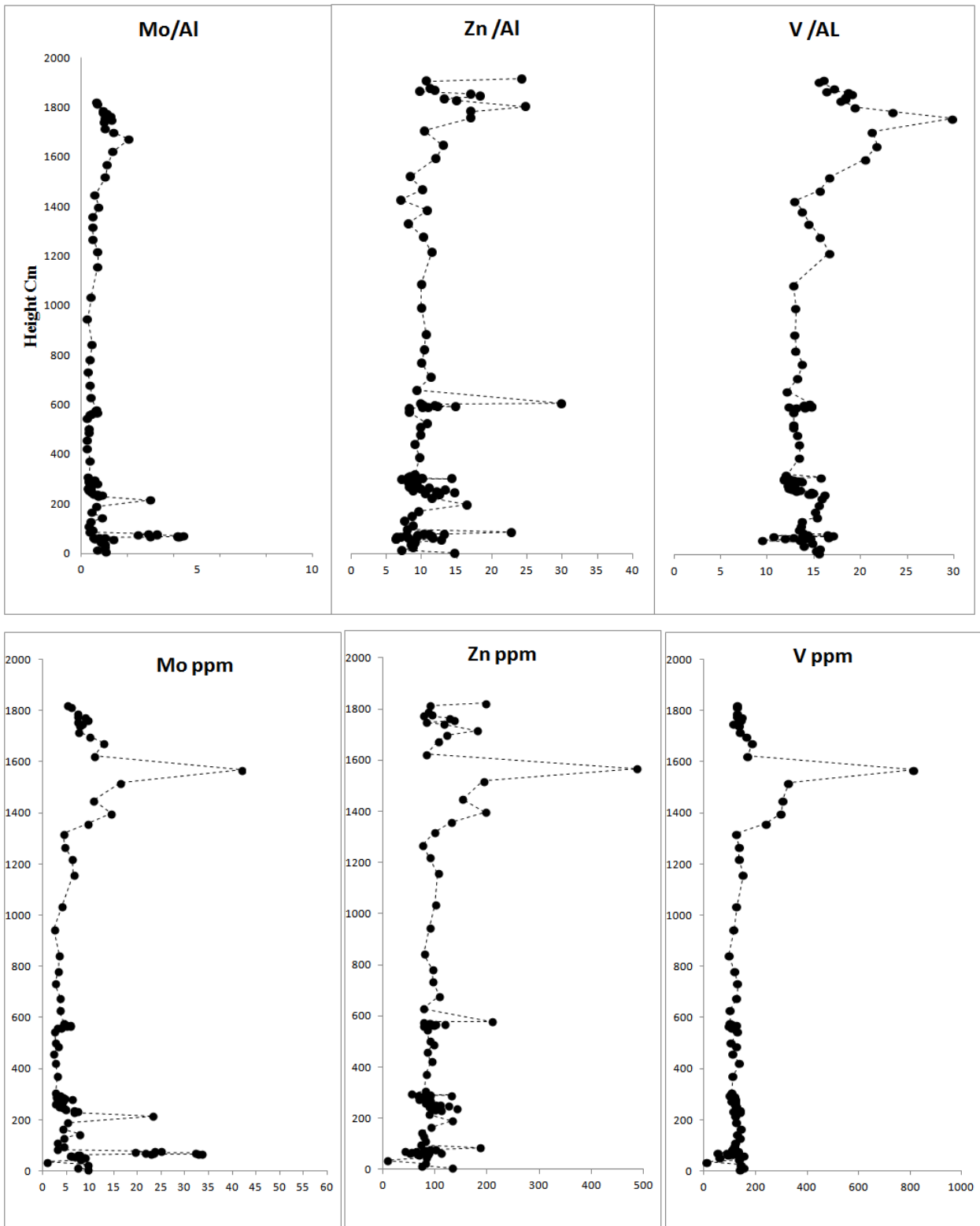


Figure 5.7: Sedimentary content of Mo/Al (10^4), V/Al (10^4) and Zn (10^4) plotted versus height from base of Gray Shale Members at Port Mulgrave section.

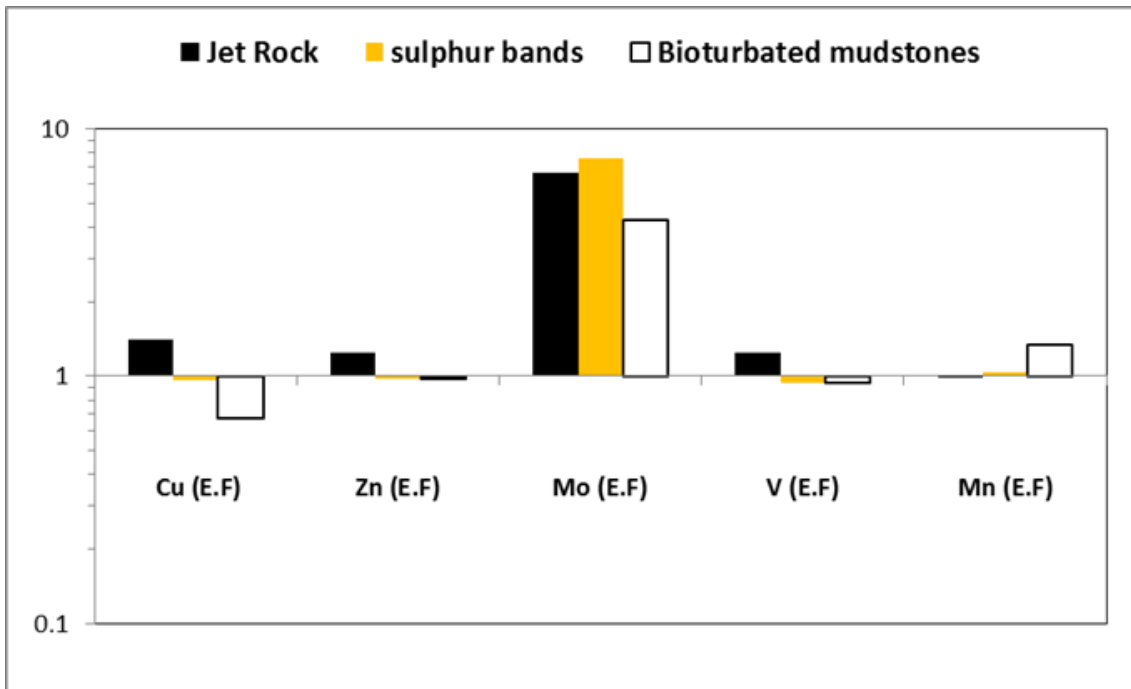


Figure 5.8: Mean enrichment factors (E.F.) of Cu, Zn, Mn, V and Mo relative to average shale for the study section at Port Mulgrave.

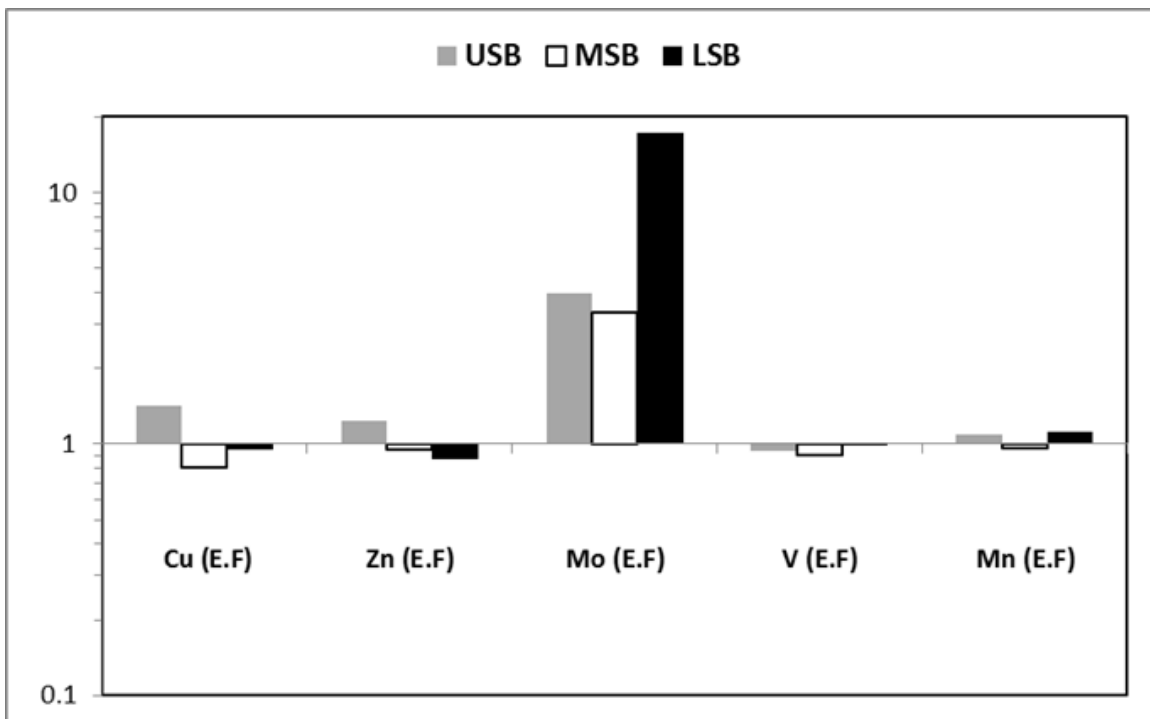


Figure 5.9: Mean enrichment factors (E.F.) of Cu, Zn, Mn, V and Mo relative to average shale for the Sulphur bands at Port Mulgrave.

The element/Al records of Cu, Mo, V and Zn fluctuate throughout the study section (Figure 5.7). The concentration of Mo ranges between 42 ppm and 0.9 ppm with a mean of 8 ppm. Generally the Mo is low within the bioturbated mudstones intervals (< 4 ppm) apart from the first bioturbated interval at the base of the section where Mo fluctuates between 7 to 10 ppm. Within the Sulphur Bands, Mo concentrations increase sharply, especially at the lower sulphur bed where it exceeds 30 ppm. The maximum Mo concentration is recorded in the *Exartum* subzone of the Jet Rock unit reaching 42 ppm. This depth trend in Mo concentration is followed by other trace elements, such as zinc and vanadium. Tracing the trace metal concentration within the Lower Sulphur bed at mm-scale sampling resolution, reveals systematic variation coupled with TOC concentration. The middle part of the Lower sulphur bed shows relative depletion in the trace metal concentration corresponded with low TOC and a spike in the $\delta^{13}\text{C}_{\text{org}}$ and $\delta^{34}\text{S}_{\text{pyrite}}$ towards heavy values.

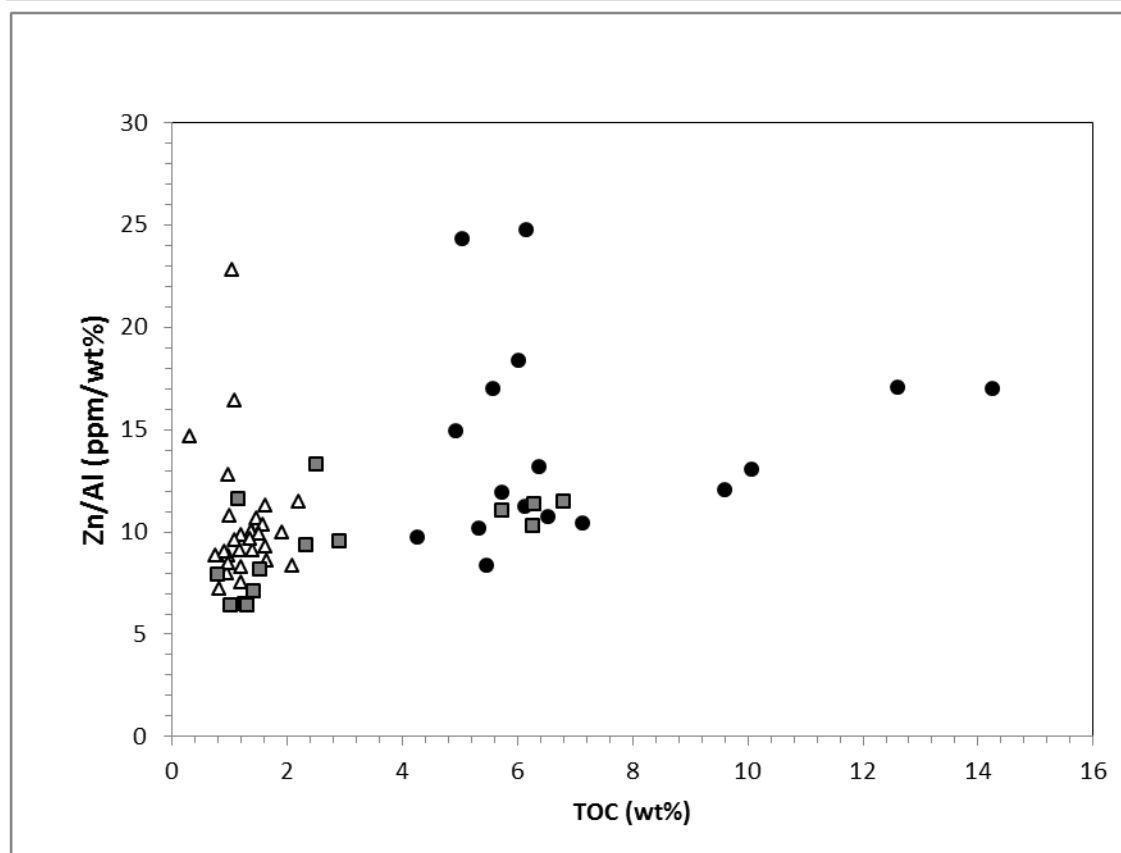
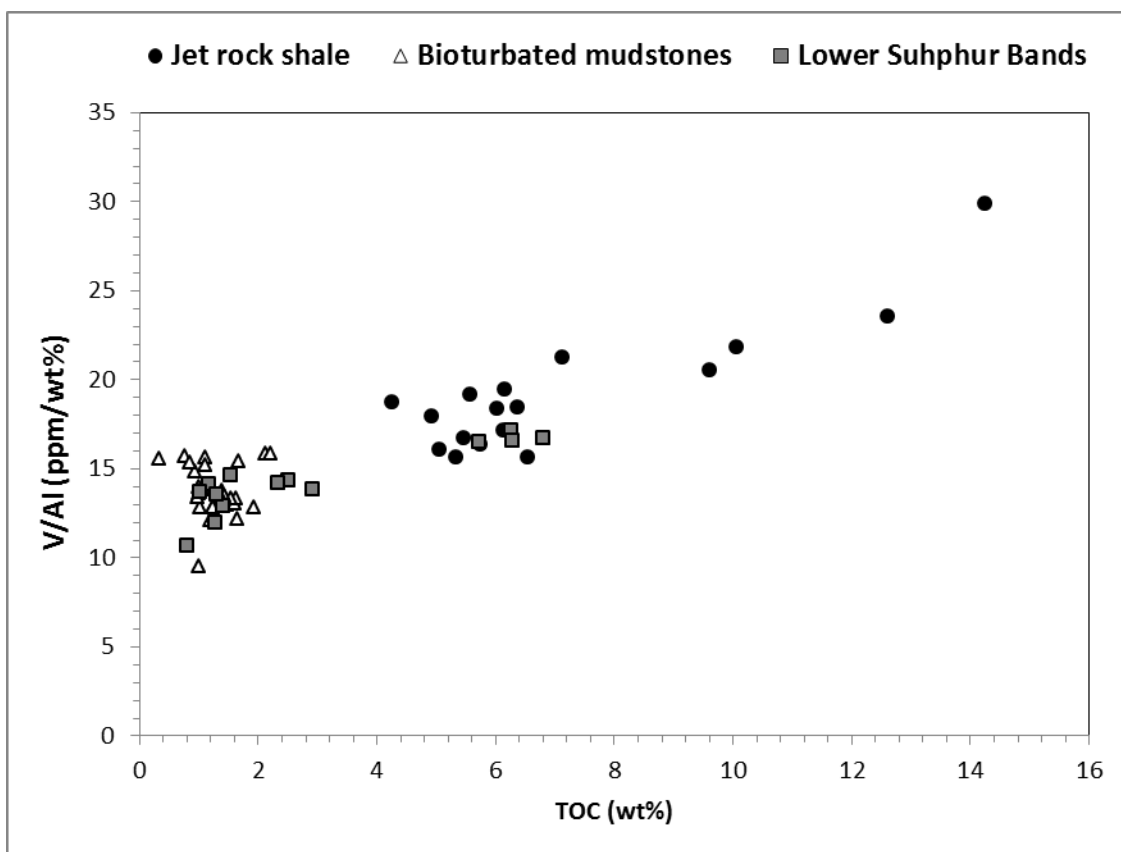


Figure 5.10: Cross-plots of element/Al against TOC for the study section at Port Mulgrave.

Lateral geochemical variation of the Sulphur Bands.

The Lower Sulphur Band at Hawsker Bottoms section is characterised by consistently low organic carbon content with an average of 0.9 wt.%. The middle Sulphur Band showed the similar trend of TOC at the both location. At Hawsker Bottoms the TOC ranges between 1.6 to 3.6 with an average of 2.3 wt.% while at Port Mulgrave section the TOC ranges between 1.13 to 4.68 with an average of 2.5. TOC profile across the Middle Sulphur Band at both locations shows high TOC content at the base that decrease in the central part and increases again at the top part. On the other hand, the Upper Sulphur Band has the same TOC profile at both locations with an average TOC of 2.0 and 2.5 at Hawsker Bottoms and Port Mulgrave respectively.

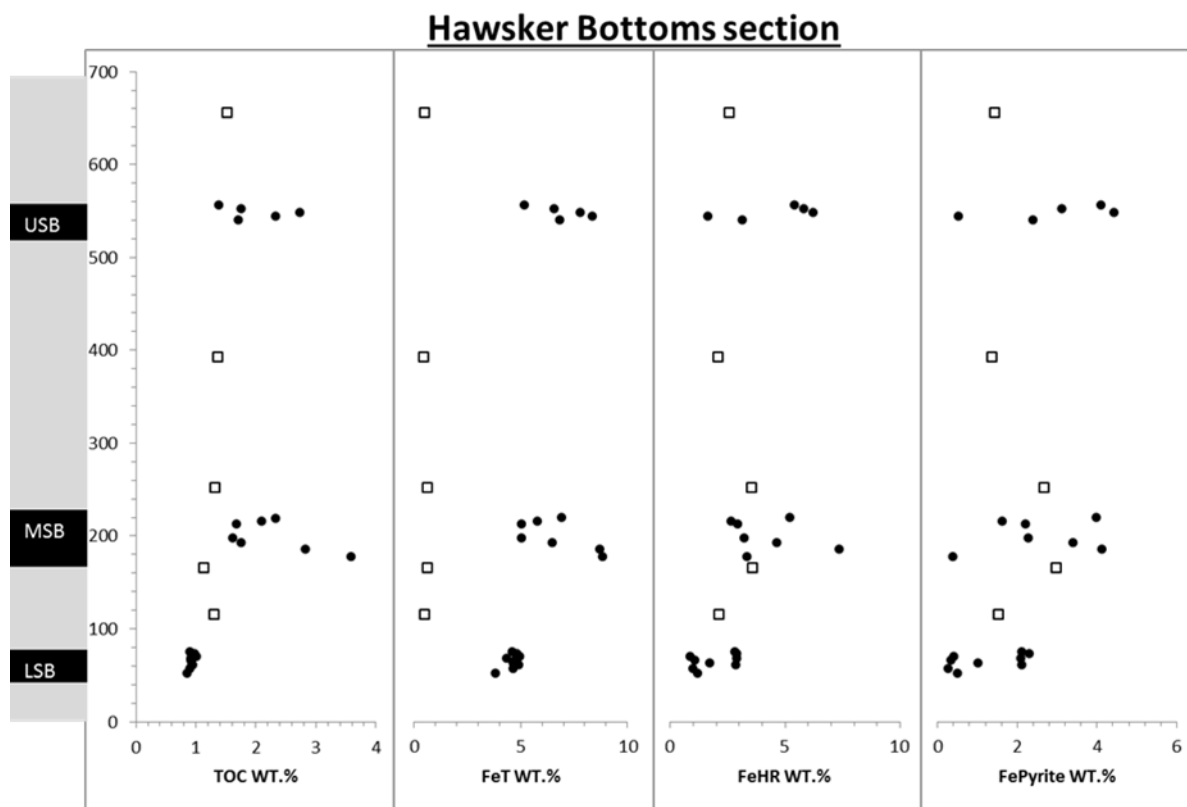


Figure 5. 11: TOC and Iron speciation profile of section at Hawsker Bottoms.

Moreover, the Lower Sulphur Band at Hawsker Bottom site is characterised with lower total iron content that ranges between 3.8 to 5.0 with an average of 4.6 wt%, compare with and average FeT of 8.05 recorded at Port Mulgrave site. The Middle and Upper Sulphur Bands show very similar iron content at both locations. Highly reactive iron (Fe_{HR}) on average accounts for approximately 42% of the total iron for the Lower Sulphur Band at Hawsker compare to more than 64% at Port Mulgrave site.

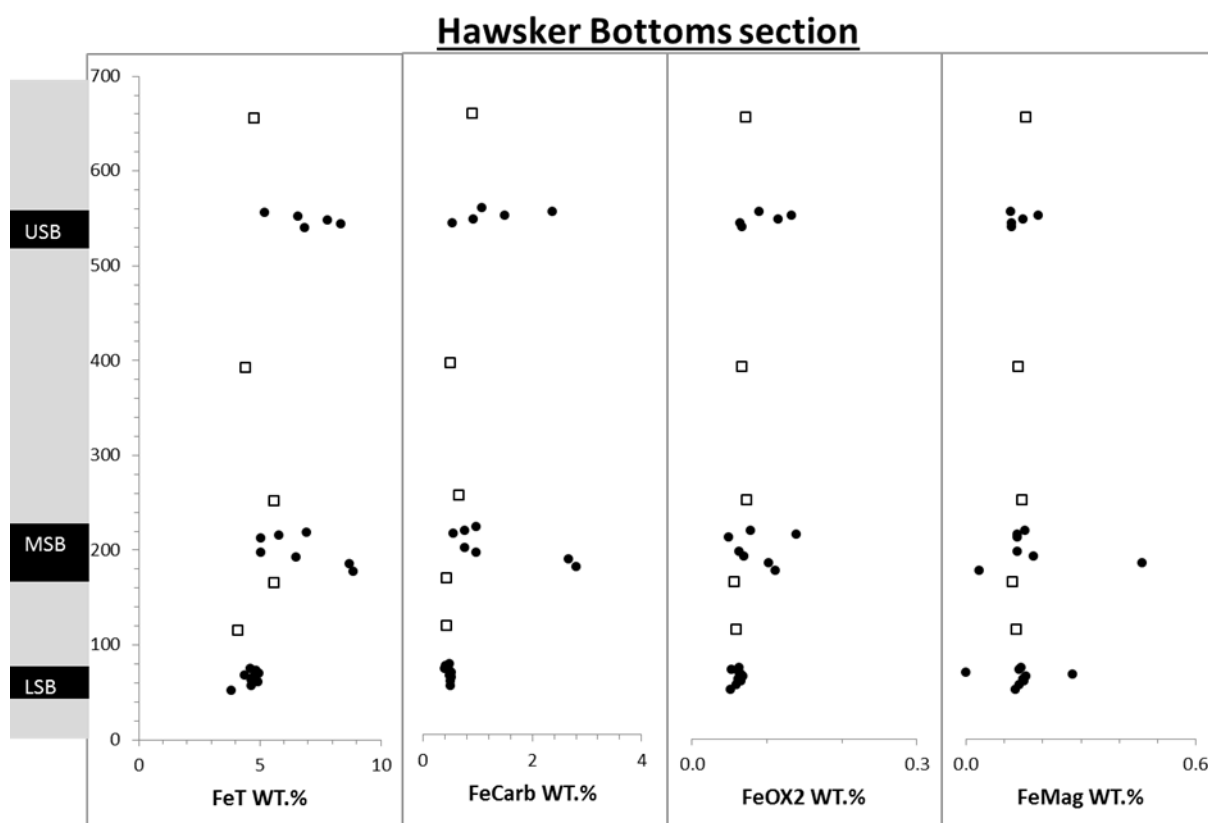


Figure 5. 12: iron speciation of section at Hawsker Bottoms.

Over the sampled interval at Hawsker Bottom, Fe_{Pyrite}/Fe_{HR} ratios also vary along the section (Figure 5.20) with values ranging between 0.12 and 0.77 (average value of 0.61). The Lower Sulphur Band is characterised with variable Fe_{Pyrite}/Fe_{HR} ratios ranging from 0.28 to 0.79 (average of 0.56). Middle and Upper Sulphur Bands are characterised with relatively higher Fe_{Pyrite}/Fe_{HR} ratios averaging at 0.61 and 0.62 respectively.

Averages of the element composition, Mo/TOC, as well as element/Al ratio concentrations of the Sulphur Bands and the interbedded bioturbated mudstones at both locations are presented in Table 5.2. Despite the very similar trace metal enrichment at the two sites, Lower Sulphur Band shows different Mo enrichment between the two locations. At more proximal setting in the Port Mulgrave section the Lower Sulphur Band is very enriched in Mo that fluctuate between 5.87 to 33.63 ppm (average of 19.27 ppm) which is far above the average shale value (2.6 ppm) that recorded by Turekian and Wedepohl (1961). Towards more distal setting at Hawsker Bottoms, the the Lower Sulphur Band is characterised with lower enrichment of Mo that ranges between 4.4 to 6.2 ppm (average of 5.20 ppm).

Table 5. 2: Averages values for individual units showing a comparison of the elemental distribution and ratios at both Hawsker Bottoms and Port Mulgrave section.

Hawsker Bottom section							
Interval	Zn ppm	Mo ppm	V ppm	V/Al	Zn/Al	Mo/Al	Mo/TOC
4-MST	87.51	3.07	119.32	11.78	8.64	0.30	2.01
USB	77.65	5.22	112.55	13.29	9.13	0.63	2.86
3-MST	74.10	5.05	122.74	12.51	7.54	0.52	3.74
MSB	76.10	7.02	119.88	13.72	8.67	0.81	3.11
2-MST	68.14	5.05	130.99	13.22	6.88	0.51	4.15
LSB	80.58	5.20	133.58	14.63	8.77	0.57	5.61
Port Mulgrave section							
Interval	Zn ppm	Mo ppm	V ppm	V/Al	Zn/Al	Mo/Al	Mo/TOC
4-MST	92.09	3.35	117.29	13.03	10.24	0.38	2.11
USB	104.51	4.71	111.88	13.72	13.16	0.58	1.93
3-MST	83.19	2.95	117.31	13.34	9.39	0.34	2.18
MSB	93.68	4.47	122.88	13.24	10.09	0.49	2.08
2-MST	100.46	6.97	128.36	14.61	11.67	0.83	4.77
LSB	75.90	19.21	118.85	14.36	9.31	2.54	8.71

At both locations Mo/TOC ratios of the Lower Sulphur Band (figure 5.13) are relatively high with an average of 5.61 and 8.71 ppm/wt% recorded at Hawsker Bottom and Port Mulgrave respectively.

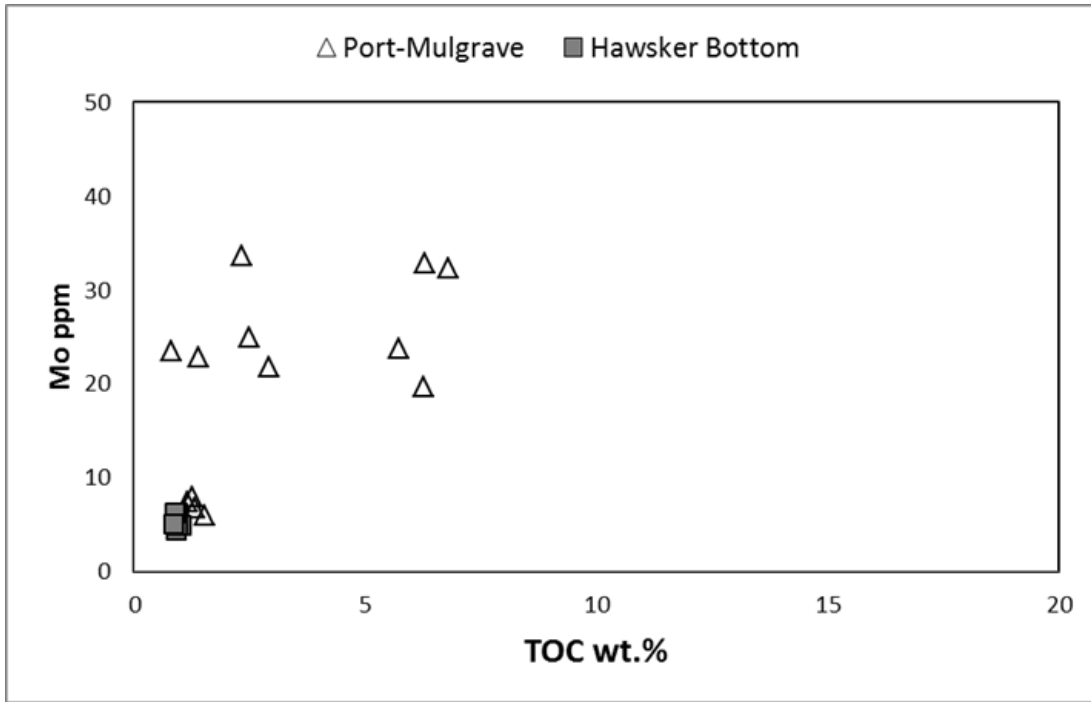


Figure 5. 13: Cross-plot of MO ppm and TOC %wt for the Lower Sulphur Band at Port-Mulgrave (empty triangles) and the Hawsker Bottoms (grey squares).

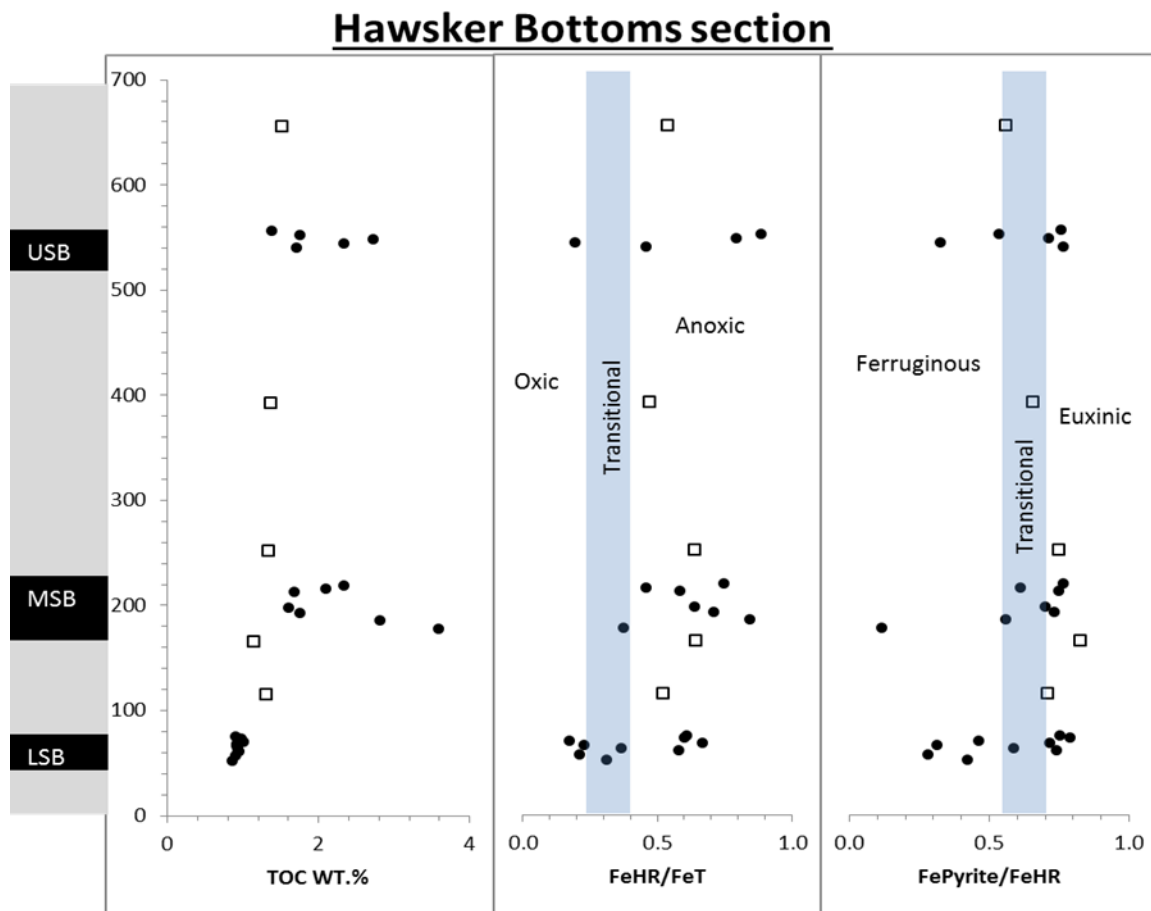


Figure 5. 14: TOC and Iron redox proxies of the lower Grey Shale at Hawsker Bottoms section.

5.3 Discussion

5.3.1 Redox dynamic throughout the study section

The geochemical data including iron, sulphur and carbon chemistry through the Lower Toarcian section of the lower Whitby mudstone formation reveals a marine basin dominated by anoxic and ferrous iron-rich (ferruginous) conditions. The redox indices indicate fluctuating redox conditions throughout the studied section, where the iron speciation data, Trace metals concentrations and molecular biomarkers reveals various and more dynamic palaeoxygenation conditions.

5.3.1.1 Iron data

The recent modification of iron speciation techniques has allowed the calculation of relative iron phases more precisely (regarding its biogeochemical reactivity). It has become one of the most valuable tools for investigating redox conditions in a variety of modern and ancient marine environments (Poulton and Raiswell, 2002; Lyons and Severmann 2006; Canfield et al., 2007). The distinctive feature of iron speciation as a paleoredox indicator from other parameters is its unique ability to differentiate between oxic, anoxic sulfidic, and anoxic non-sulfidic (ferruginous) water column conditions (Poulton et al., 2004b; Canfield et al., 2007), allowing a detailed evaluation of ocean redox.

Anoxia was common in subsurface water masses of lower Toarcian oceans (Farrimond et al., 1988; Jenkyns et al., 2001) and in this respect the Cleveland basin appears typical. The results of the iron speciation data (Figure 5.4) shows that total iron (Fe_T wt %) concentrations are slightly higher than average shale composition (Turekian and Wedepohl, 1961), but consistent with the ranges reported by McArthur et al. (2008) for the North Yorkshire section. Empirically, values of Fe_{HR}/Fe_T above 0.38 indicate anoxic bottom water conditions, whereas significantly lower values generally suggest oxic bottom water condition (Raiswell et al., 2001; Poulton and Raiswell, 2002).

Fe_{HR} enrichments relative to total Fe occur due to the water column formation of either pyrite in sulfidic basins, or non-sulfidized minerals (ferric oxides, magnetite or siderite) in anoxic ferruginous basins. The ratio Fe_{py}/Fe_{HR} can then be used to distinguish between deposition in sulfidic and anoxic non-sulfidic basins, where sulfidic marine waters commonly have Fe_{py}/Fe_{HR} ratios that approach >0.7-0.8 (Marz et al., 2008).

As our analyses are on outcrop samples (Staithees to Port Mulgrave section), a consideration for possible contributions from secondary alteration by oxidative weathering must be taken to the account. However, samples were obtained from fresh surfaces and any visible surface staining was avoided. Oxidation by post depositional weathering would cause the speciation within the actual highly reactive iron pool to change and as a consequence the Fe_{OX} fraction of the highly reactive iron will be increased. In our samples, Fe_{OX} contents are generally very low (Figure 5.5), indicating that we can readily discount any significant influence of secondary oxidative weathering for most of the succession.

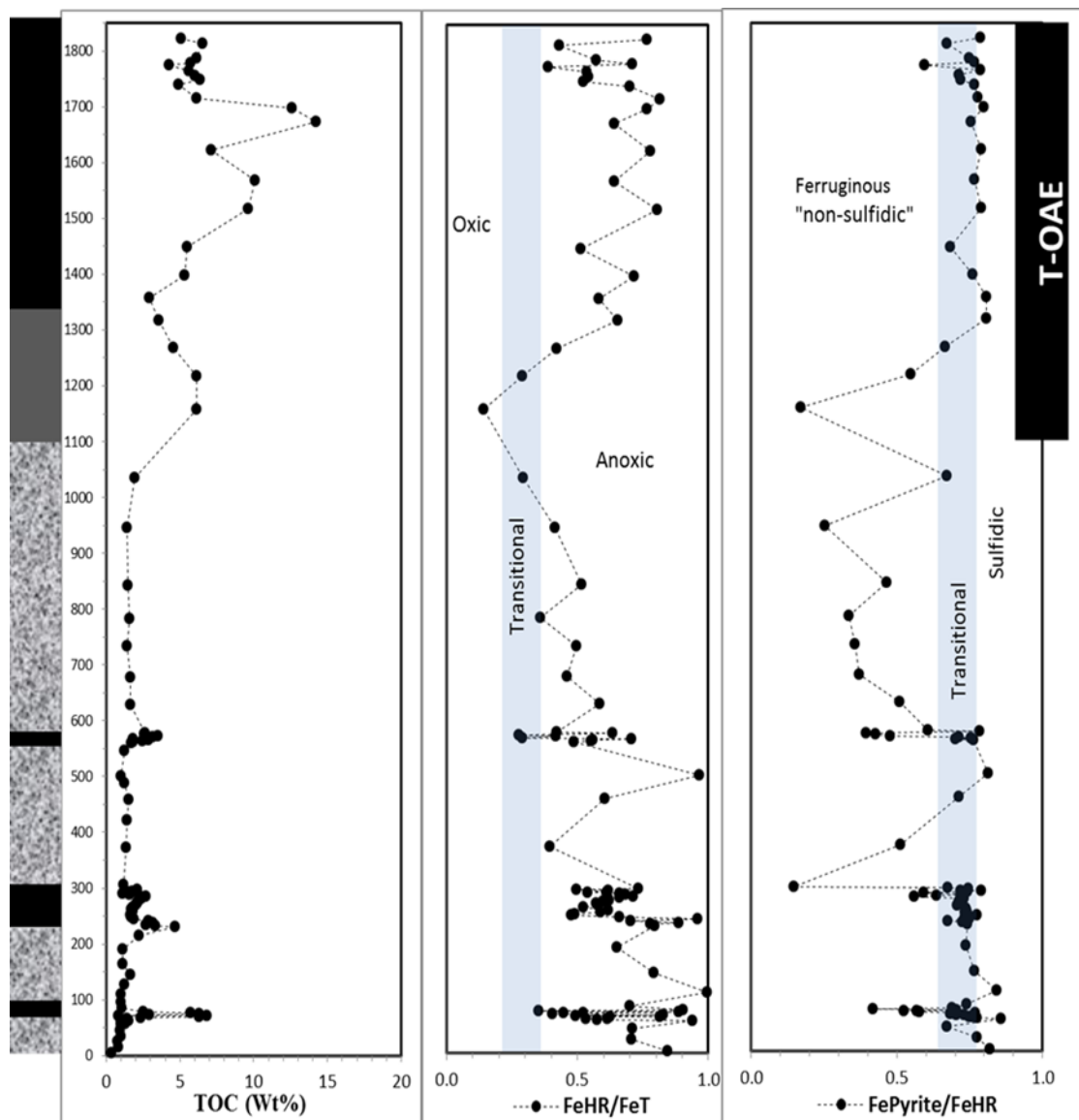


Figure 5.15: Composite stratigraphy with iron Paleoredox indicators for the study section at Port Mulgrave.

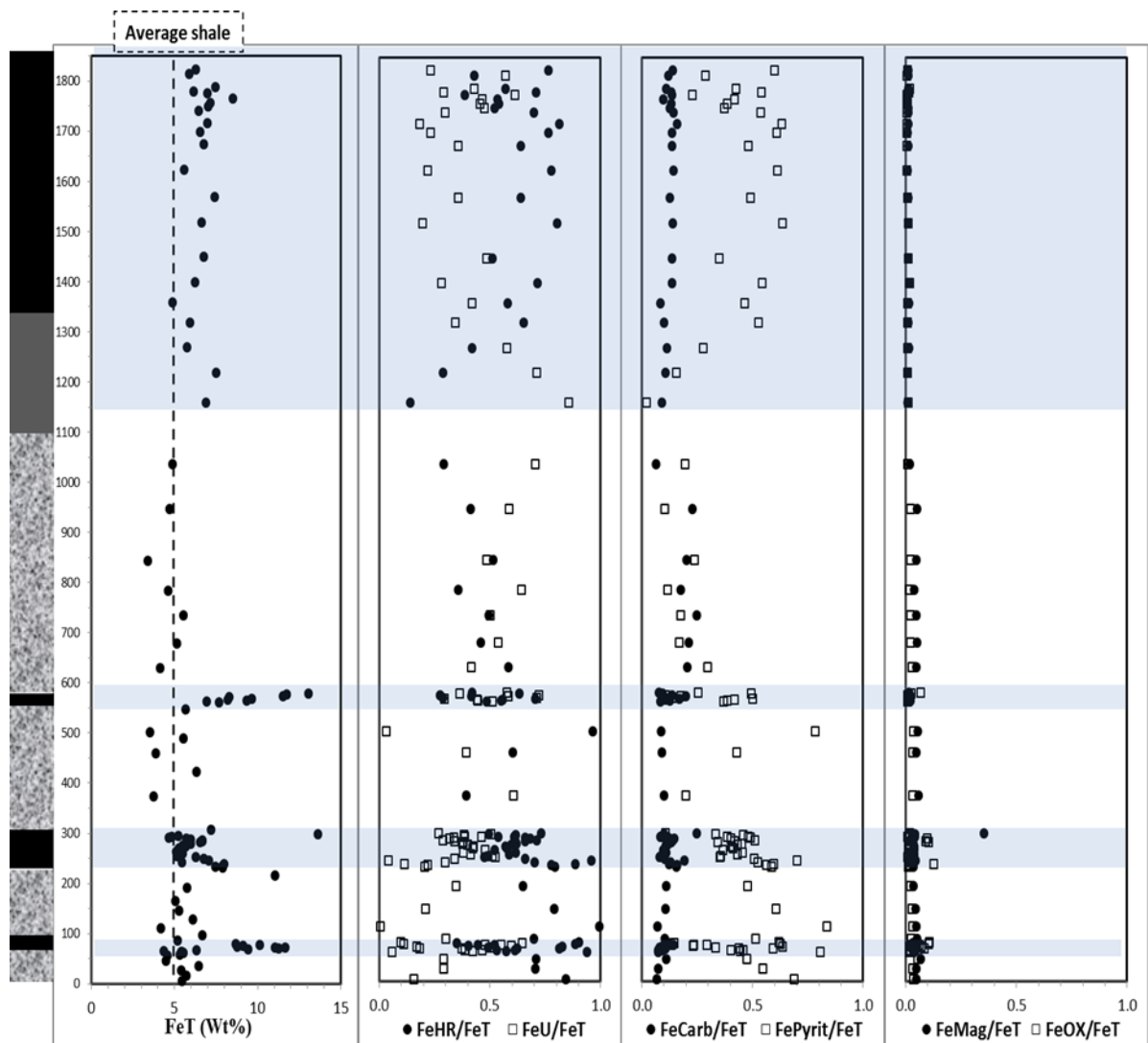


Figure 5.16: Composite stratigraphy with iron speciation data at Port Mulgrave section. The total Fe content in Wt. % and the relative proportion of Fe residing in unreactive and reactive phases, reduced phases and oxidized phases.

As Figure 5.15 shows, Fe_{HR}/Fe_T is variable throughout the section. Apart from the bioturbated mudstones, the rest of the section is fluctuating above the threshold value (0.38). The entire data set falls in the range above the modern oxic water column average of 0.26 (Poulton and Raiswell, 2002). At the Pliensbachian-Toarcian boundary (*paltum subzone till clevelandian subzone*) values of the Fe_{HR}/Fe_T regularly fall in the definitive anoxia region. At the Upper Sulphur band and above proceeding to the interval of Jet Rock Shale (*tenuicostatum tile middle semicelatum subzone*) Fe_{HR}/Fe_T fluctuates above and under the threshold value (0.38) and at some points falls in the equivocal range between definitive anoxia and modern oxic sediment (0.26). Moreover the F_{py}/Fe_{HR} values documented in this interval have an average of 0.42 which is far below the threshold value for euxinic condition

($F_{py}/F_{HR} \geq 0.7$), pointing to anoxic ferruginous water column conditions (Poulton and Canfield, 2001). Anoxia is more intense and permanent in the deepest waters, represented by the Jet Rock member where the F_{HR}/F_T values are consistently far above the threshold value.

Although the biomarker and trace elements data indicates that the bioturbated mudstones at the base of the study section represent oxic to dysoxic condition, the iron speciation data suggest that the lower third of the study section at the base of the Grey shales is a transition zone that was characterized by anoxic ferruginous condition which shows very high enrichment of F_{HR} . This enrichment of iron could be sourced from the ironstones on the basin margin or from the underneath sediment through the advection of the underground water (Newton, 2001) and riverine flux (lateritic weathering of the hinterland). This Ferruginous condition was punctuated with short-lived periods of euxinic conditions indicated by high F_{py}/F_{HR} ratio (> 0.8) which could be interpreted as more sulphur was added to the system to shift the anoxic (ferruginous) condition to euxinic condition. Above this interval and below the T-OAE (*upper clevelandian till middle semicelatum subzone*) the system was pulled back towards suboxic-oxic condition indicated by the sedimentary fabric of the bioturbated mudstones which record presence of benthic fossils (Caswell et al., 2008) and very low F_{HR}/F_T (< 0.38). The system then progressed from ferruginous non-sulfidic to sulfidic condition through the T-OAE zone (*Exeratum subzone*), where the Fe speciation data showed consistently high F_{pyrite}/F_{HR} ratio suggesting periods of pronounced sulphidic conditions in bottom waters.

The presence and fluctuation of both ferruginous and euxinic conditions recorded in the study section indicates how dynamic the palaeoredox condition was. At the Pliensbachian-Toarcian boundary (*paltum subzone till clevelandian subzone*) ferruginous waters were persistent and sulfidic waters transient lasting for a short period of time spanning the sulphur bands, which is estimated to last 5 – 10 Ka (McArthur et al., 2008). These perturbations which pushed the water masses toward euxinia are the mechanisms behind the formation of the sulphur bands at the base of the Gray shale. The dominance of sulfidic or non-sulfidic (ferruginous) condition must be related to the equilibrium between sulphur and iron in seawater (Poulton et al., 2004a). Enrichment of these elements is controlled by hydrothermal fluxes and seawater sulphate level (Kump and Seyfried, 2005)

5.3.1.2 Biomarkers

Photic zone anoxia (PZA) during the early Toarcian is indicated by biomarkers derived from green sulphur bacteria, such as isorenieratane and its diagenetic products, aryl isoprenoids (Schouten et al., 2000; Bowden et al., 2006). The diaryl isoprenoids are derived from isorenieratane, which is an undisputed biomarker for Chlorobiaceae (green sulphur bacteria). In contradiction to previous work by Sælen et al., 2000, this study has found isorenieratane in every sample of the Jet Rock. The occurrence of isorenieratane throughout the Jet Rock indicates that recurrent euxinia had extended into the euphotic zone (Koopman et al., 1996). Consistent isorenieratane presence was recorded in the equivalent interval of lower Toarcian in Germany (Posidonia Black Shale) by Schouten et al. (2000).

The presence and widespread distribution of isorenieratane indicates that a sulfidic photic zone was a common occurrence, before and during the T-OAE at North Yorkshire section. Isorenieratane maximum abundance is near the maximum in TOC, implying that strengthening euxinia was responsible for increasing organic carbon burial. This occurrence of diagenetic products of the carotenoid isorenieratane (isorenieratane and other aryl isoprenoids) in Toarcian black shales has been regarded as supporting evidence for the Kuspert hypothesis as they point to strong stratification of the epicontinental seas (van de Schootbrugge et al., 2005). The presence of isorenieratane within short intervals of the sulphur bands before the main T-OAE indicates that euxinia was developed during short periods at the Pliensbachian-Toarcian. This is in agreement with the iron speciation data and the isotopic data suggesting severe environmental changes triggered by repeated mechanisms.

5.3.1.3 Sulphur isotope record

The sulphur isotopic composition of pyrite from the study section is quite variable (Figure 5.6). It ranges from -20 ‰ to almost -47‰. Such a significant isotopic variation in sulphur isotopes always tend to develop in association with extensive processes of sulphate reduction, with the product sulphide being depleted in the heavier isotope by approximately 30‰ as long as sulphate is available (Habicht et al. 2002).

Sulphur is removed from the oceanic sulphate pool in two ways. Firstly as evaporated sulphate minerals, which is episodic and less important, the second process is by biological reduction of sulphate to sulphide in organic-rich marine sediments. Most of the sulphide gets reoxidized and the rest reacts with iron to form pyrite, which is buried in the sediments (Berner 1970). The lighter ^{32}S isotope forms slightly weaker bonds than the heavier isotope

and therefore has a more rapid rate of reduction and thus pyrite sulphur (produced by sulphide) is thus depleted in ^{34}S relative to the sea water sulphate (Newton and Bottrell, 2007).

In a closed system, sulphate becomes extensively depleted and therefore the isotopic difference between sulphide and sulphate diminishes. Therefore pyrite formed in euxinic water columns, should be isotopically light relative to diagenetic pyrite formed in sediments, which tend to more closely represent closed systems. While in open system, where there is supply of sulphate from the open ocean the isotopic differences between the sulphide and sulphate stays high and therefore isotopically heavier.

Sulphur isotope analyses of sedimentary sulfides within the studied section display a distinctive stratigraphic pattern of variability, with the lower part at the Pliensbachian-Toarcian boundary (*paltum subzone till clevelandian subzone*) preserving a large range of isotopic compositions (fluctuating between -20‰ and -47‰), and represents the most depleted interval with the most negative value. The overlying Jet Rock Shale (Exartum subzone) contains much more pyrite and preserves sulphur isotope compositions that cluster toward more enriched values where $\delta^{34}\text{S}_{\text{pyrite}}$ clustered around -21‰. Although the paleoredox proxies clearly suggest persistent euxinic condition for the Jet Rock Shale, the relatively heavier $\delta^{34}\text{S}_{\text{pyrite}}$ values compare to the Grey shale could suggest mass-balance effect of local sulphate limitation.

5.3.1.4 Trace elements

Redox conditions control the mobility of many trace elements, and the relative enrichment or depletion of these redox-sensitive trace elements in the sediments is used as a redox indicator of the overlying water. Certain trace metals (e.g Mo, V, and Zn) have proven to be particularly diagnostic for anoxic/sulfidic conditions during deposition of organic matter-rich sediments (Jones and Manning, 1994; Brumsack, 2006; Tribovillard et al., 2006; Chris et al., 2008). In many examples of organic rich sediments deposited under such extreme conditions, redox-sensitive trace metals such as Molybdenum and Zinc may be strongly enriched (by factors of >100) in comparison to average marine shale (März et al., 2008). The elements Mo, V and Zn are regarded as particularly reliable as paleoredox indicators as these metals all have in common the tendency to form insoluble phases under anoxic and sulfidic depositional conditions (Brumsack, 2006; Tribovillard et al., 2006).

Overall, element/Al ratios of Mo and V show enrichments that fluctuate throughout the study section, with highest values recorded in the Jet rock shales (figure 5.7). Notable trace metal enrichments occur with molybdenum (Mo), which is relatively enriched (8 ppm) and above the average shale value which is about 1 ppm (Brumsack, 2006). Basically, molybdenum displays much stronger enrichments under sulphidic conditions (Algeo and Maynard, 2004; Algeo and Lyons, 2006) where it is transformed to thiomolybdate, and becomes particle reactive under sulphidic conditions allowing its drawdown into sediments. This only occurs when sulphide reaches a critical level, which has been estimated to be about 11 μM (Zheng et al., 2000). Under sulphidic conditions, sorption of Mo to sinking organic matter and transport to the sediment surface is expected to be much more effective than under anoxic non-sulphidic conditions, resulting in higher enrichments.

According to Tribovillard et al. (2006), Vanadium can be reduced and accumulated under denitrifying conditions while Zn and Mo are enriched mainly under sulphate-reducing conditions. Thus, in the case of V enrichment without Mo enrichment, the authors postulate suboxic/anoxic depositional conditions without free H_2S , whereas sediments exhibiting concurrent enrichments in V and Mo reflect euxinic conditions at the sediments-water interface or in the water column (Algeo and Maynard, 2004; Tribovillard et al., 2004). At the Pliensbachian-Toarcian boundary (*paltum subzone till clevelandian subzone*) Mo and Zn fluctuate between relatively high enrichment within the sulphur bands and relatively lower enrichment within the bioturbated mudstone units. This suggests fluctuated palaeoredox condition as also indicated by the iron speciation and biomarkers data. This shift in ocean redox resulted in the rapid and extensive removal of Mo and Zn from the water column (in the form of sulfides), leading to the observed sharp peaks (Figure 5.11). On the other hand, V in this interval shows no particular enrichment responding to the Sulphur bands, which reflects the negligible role for the sulfidic condition to drawdown of V. At the base of T-OAE zone in the Jet rock shale (bed 33 & 34) there is relatively higher enrichment of trace elements. This enrichment decreases towards the top of the T-OAE. Taking seawater as the dominant source for Mo, V and Zn, the relative depletion in trace elements may reflect the global onset of the black shale deposition and the widespread development of anoxia, or it may reflect hydrographic factors where the water mass restriction developed and slowed the deepwater renewal of trace metals. Both of these mechanisms would have resulted in depletion of redox sensitive trace metals in the water column.

Mo versus TOC

Recent studies have identified a range of new applications of trace-metal concentration data in the analysis of paleoceanographic systems. In restricted anoxic marine systems, trace metal /TOC ratios can provide insight into the degree of water mass restriction and estimates of deepwater renewal times (Algeo and Rowe 2011). The transition from weakly sulfidic to strongly sulfidic facies is commonly accompanied by a decline in trace metal accumulation rates, because hydrographic factors (i.e., limited deepwater renewal) come to dominate over redox influences. Ultimately, deepwater renewal and aqueous molybdenum depends on basin geometry where the sub pycnoclinal water mass is renewed less readily in larger basins with shallower sills, such as the Black Sea, than in smaller basins with deeper sills (Algeo and Lyons, 2006).

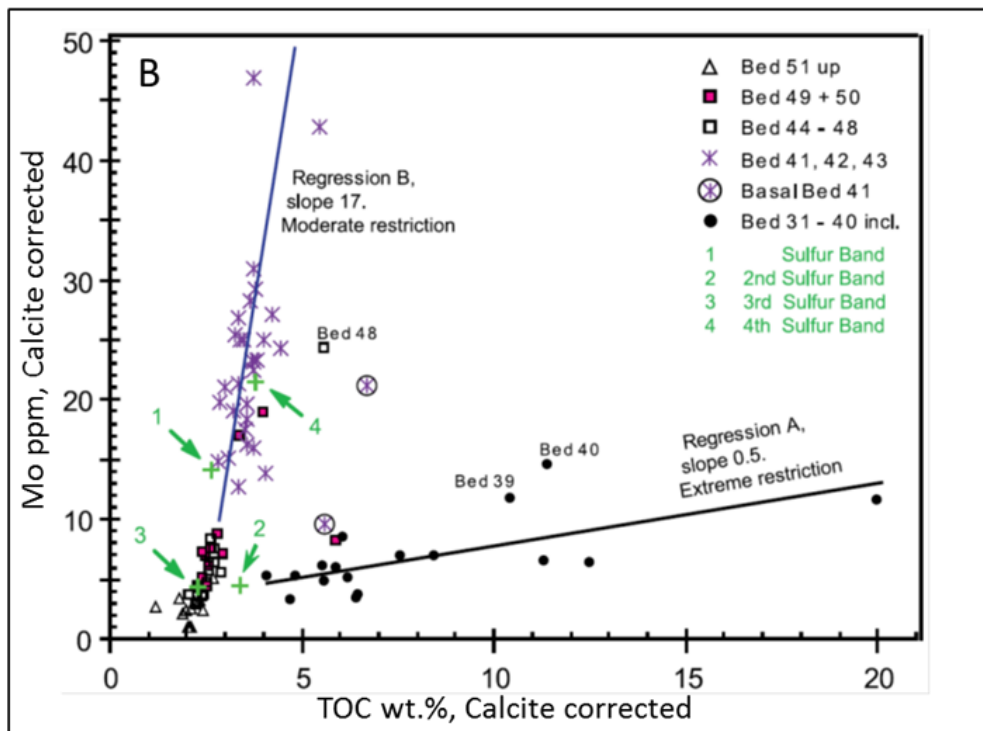
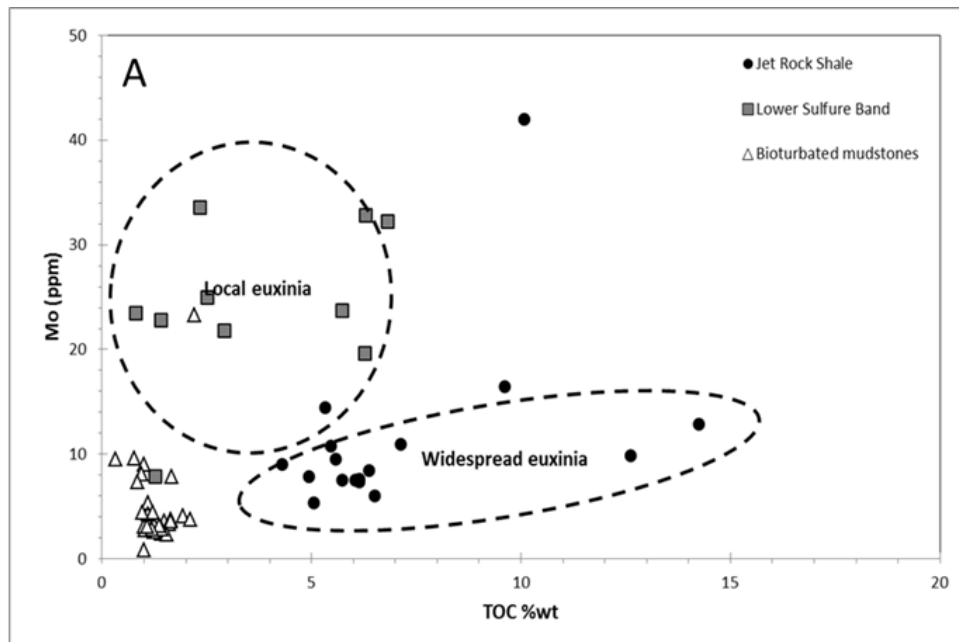


Figure 5.17: A) Cross-plot of MO ppm and TOC %wt from this study; B) Cross-plot of MO ppm and TOC %wt from McArthur et al., 2008 . Samples from the Jet rock suggest widespread euxinia, while the underlying Sulphur Beds indicate more local euxinic conditions

The Mo versus TOC cross plot (Figure 5.23), displays a similar plot to that generated by McArthur et al. (2008). The upper half of the *semicelatum* Subzone and most of the *exaratum* Subzone (Bed 31 to 38) are characterized by relatively lower ratios of Mo/TOC (low regression slop) and as this interval encompasses the Early Toarcian OAE, and is superimposed on the main negative excursion in $\delta^{13}\text{C}_{\text{TOC}}$, it could be suggested to indicate

that complete restriction occurred during this interval, which was termed the interval of maximum restriction (IMR) by McArthur et al. (2008). However, persistent euxinia would be expected to gradually lower the Mo concentration of seawater as expanded sinks exceeded riverine sources (Algeo and Lyons, 2006). On the other hand the bioturbated mudstones including the intervals of the sulphur bands are characterized with higher ratios of Mo/TOC (high regression slope), which could suggest lesser water restriction and a more dynamic scenario.

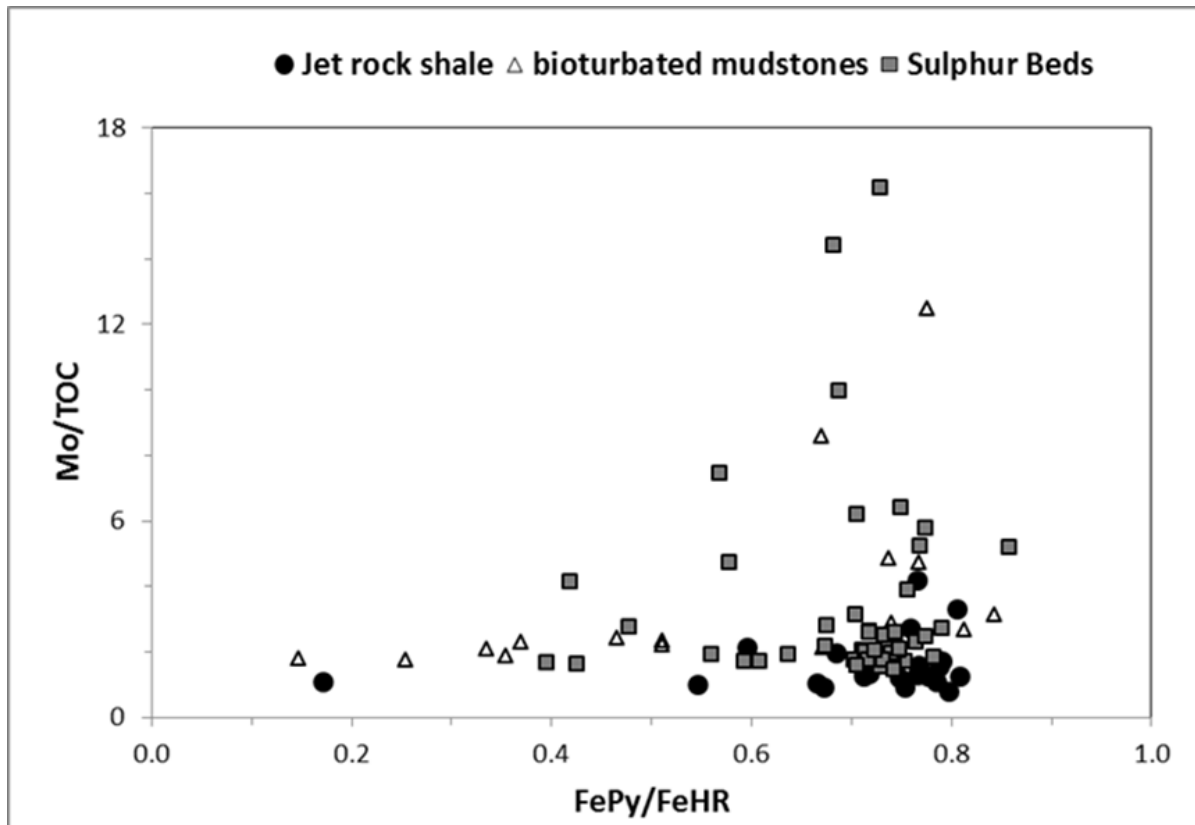


Figure 5.18: Mo/TOC versus FePy/FeHR for the study section at Port Mulgrave.

The role of redox versus hydrographic influences on trace metal accumulation in marine systems can be investigated through cross-plots of Mo/TOC versus paleoredox parameters that are highly sensitive to euxinic conditions (e.g DOP) (Algeo and Rowe, 2011). In this study the ratio of Fe_{Py}/Fe_{HR} which is a powerful redox proxy for indicating sulfidic deposition condition is used (Figure 5.18). Mo/TOC is potentially subject to both redox and hydrographic influences (McArthur, et al., 2008) and its relationship to Fe_{Py}/Fe_{HR} can assist in identifying the relative importance of both factors.

Uniform Mo/TOC values within a marine system that shows spatial or temporal variation in redox conditions are evidence for control of trace metal accumulation by hydrographic factors. Stratigraphic variation in Mo/TOC values independent of Fe_{Py}/Fe_{HR} is evidence for changes in aqueous Mo concentrations. On the other hand, covariation between Mo/TOC and Fe_{Py}/Fe_{HR} is evidence for either a direct or indirect redox control on trace metal accumulation. A direct redox control results in increasing Mo/TOC with more reducing conditions (Zheng et al., 2000), but such an effect generally should be manifested only in the oxic to weakly sulphidic part of the redox spectrum (Algeo and Rowe, 2011). Under more reducing conditions, hydrographic controls tend to become dominant (Algeo and Lyons, 2006).

As can be seen in Figure 5.13, the cross plots of Mo versus TOC through the T-OAE zone (*upper semicelatum - Exeratum subzone*) exhibits uniformly low Mo/TOC ratios. This is indicative of extreme water mass restriction, while from McArthur et al. (2008), the overlying *Falciferum zone* exhibits higher Mo/TOC ratios that covary positively with the degree of pyritization (DOP). On the other hand, the underlying Grey shale at the Pliensbachian-Toarcian boundary (*paltum subzone till semicelatum subzone*) has Mo/TOC values that are higher. Although most of this interval is considered to represent anoxic to dysoxic conditions (apart of the Sulphur beds where periodic euxinia was clearly detected), higher Mo/TOC could suggest more ventilation and less restriction in the water column. The lower sulphur bed at the Pliensbachian-Toarcian boundary showed exceptionally high Mo/TOC values. The very high Mo content in this bed could suggest a different scenario that developed over short a period of time. The drawdown and replenishment of Mo must have occurred within a small and local reservoir where elevated Mo/TOC indicates brief periods of euxinia.

5.3.2 Detailed iron geochemistry across the Sulphur Bands

The Sulphur Bands represent three brief periods of restriction and pyrite formation in the earliest Toarcian. They are deposited over a wide area and their lateral equivalent were recorded in at Dotternhausen section in Germany, where four thin units of organic-rich shale occur in the *paltum and uppermost clevelandicum* Subzone (Rohl et al., 2001).

At Port Mulgrave detailed (Cm-scale) multiproxy records from of the Lower Sulphur Band (Figure 5.19) reveal a dynamic system, with sulfidic water conditions that were intermittently interrupted by anoxic non-sulfidic water column conditions. Over all, the three sulphur beds are enriched in reactive iron, much of which is in form of pyrite. This high enrichment of iron is believed to be sourced from the Main Seam unit of Cleveland Ironstone Formation that lies directly underneath the Lower Sulphur bed (Newton, 2001). The Cleveland basin marginal sediments in the early Torcian consisted of ooidal ironstones providing a huge reservoir of highly reactive iron (Powell, 2010).

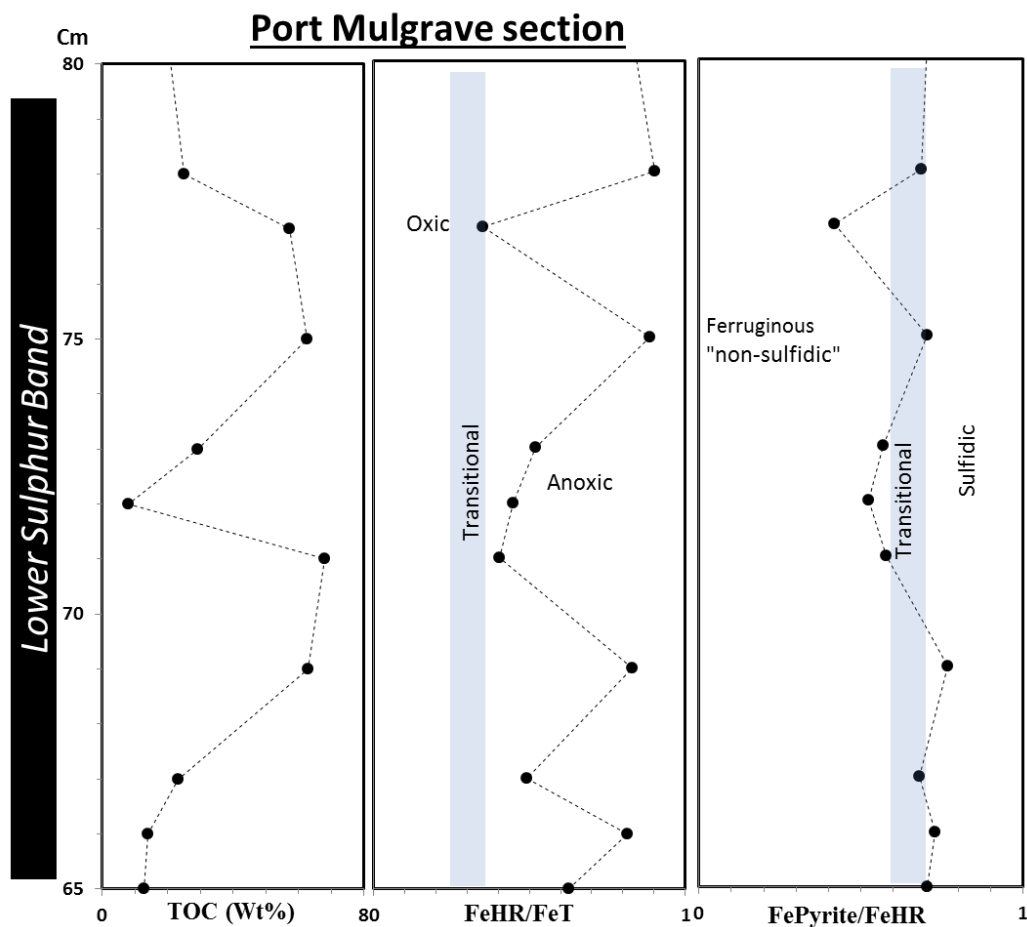


Figure 5.19: Detailed iron speciation profile across the Lower Sulphur Band at Port Mulgrave

The particular enrichment of the Lower sulphur band may reflect its position at the beginning of the transgression and therefore its relative proximity to the sediment source. All the sulphur bands show evidence of storm activity in the form of small scale hummocky cross stratification (Wignall, 1994). This storm activity could have played a role in redistributing the weathered marginal ironstones to the deeper parts of the basin and provided an initial input of iron oxides to the basin. Moreover, the anoxic bottom water reduced and released the iron oxides into solution as Fe^{+2} at the sea floor and then diffused along the layer of anoxic bottom waters to distribute extra reactive iron over a wider area.

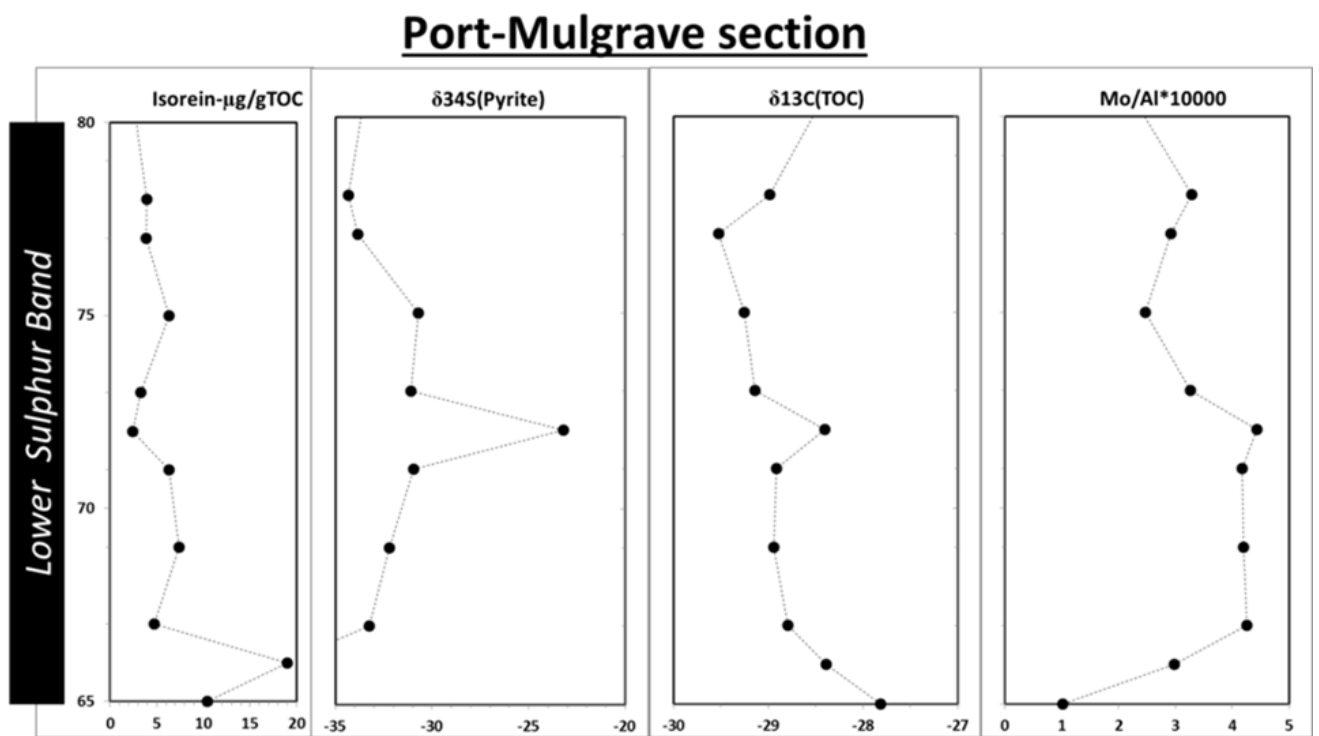


Figure 5.20: Detailed chemostratigraphic plots of $\delta^{34}\text{S}(\text{Pyrite})$ and $\delta^{13}\text{C}$ isotopes, Mo/Al ratio and maxima of isorenieratane abundances across the Lower Sulphur Band at Port Mulgrave section.

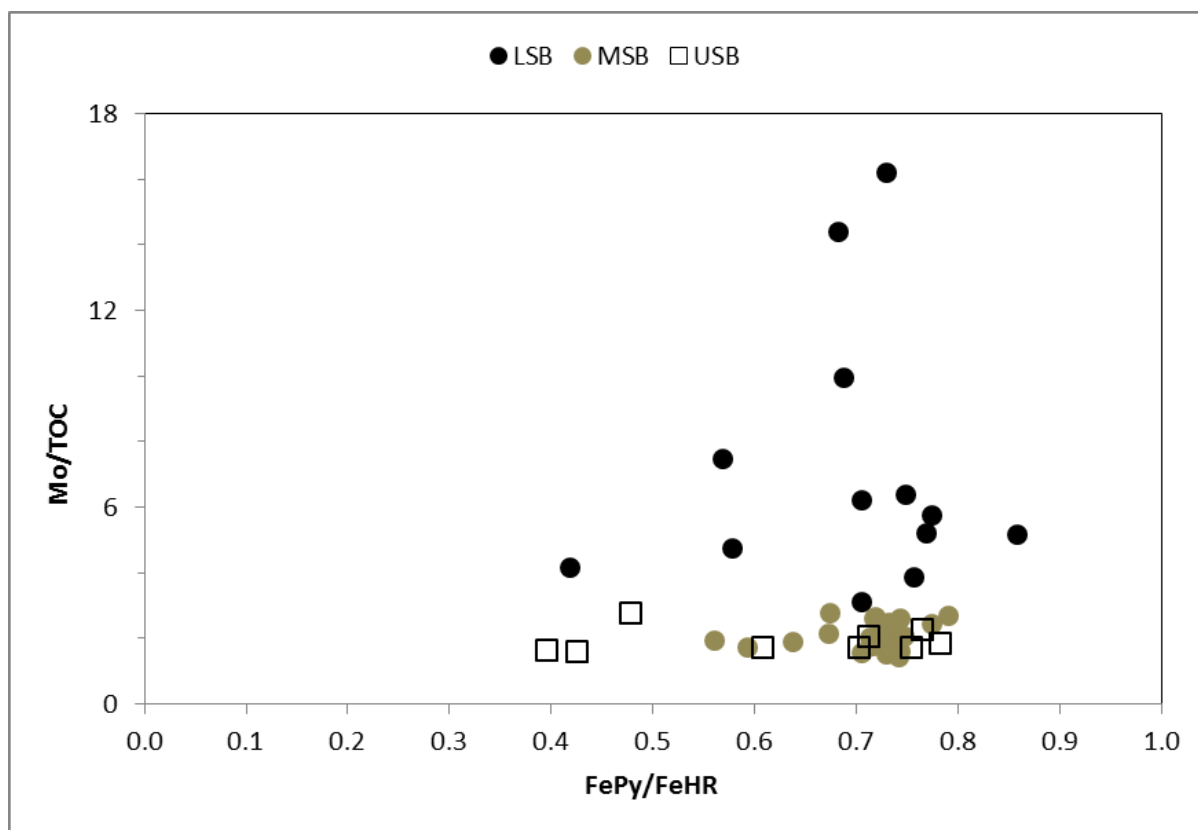


Figure 5.21: Cross plot of Mo/TOC versus FePy/FeHR through the three sulphur beds at Port Mulgrave section.

Based on the Sr isotope analysis by McArthur et al., (2000) and the cyclostratigraphic timescale of Suan et al., (2008), the Sulphur Bands at north Yorkshire are estimated to last from 5 to 10 Ka (McArthur et al., 2008). Working up from the base of the Lower Sulphur Band, the first 5 cm is characterised by high FePyrite/FeHR, high Mo enrichment and intensive presence of Isorenieratane ($9.47\mu\text{g/g}_{\text{TOC}}$) suggesting sulfidic water condition that lasted approximately 2.5 Ka (based on McArthur et al., 2000 estimation). Then the system was pushed back to non-sulfidic anoxic water column conditions lasted for approximately 2 Ka indicated by a decrease in the $\text{Fe}_{\text{Pyrite}}/\text{Fe}_{\text{HR}}$ ratio to less than 0.6 over the central 4 cm. Afterwards, the system turned to extreme euxinia with higher $\text{Fe}_{\text{HR}}/\text{Fe}_{\text{T}}$ where the sulfidic water condition also extended to the photic zone, which is indicated by the presence of the isoreineratene biomarker. Despite this fluctuation between ferruginous and sulfidic condition throughout the Lower Sulphur Band, the $\text{Fe}_{\text{HR}}/\text{Fe}_{\text{T}}$ continued above the threshold of anoxic water condition (0.38) throughout.

The middle part of the Lower sulphur bed witnesses major change, where the concentration of Mo dropped below the threshold of euxinic condition ($\text{H}_2\text{S} < 11\mu\text{M}$), and

transition from sulfidic bottom water to anoxic ferruginous non-sulfidic bottom water. This was associated with distinctive short-lived $\delta^{34}\text{S}$ excursion ($\sim 10\%$) suggesting limited sulphate availability and hence a decrease in sulphide in the water column.

Despite the bioturbated central 15 cm of the Middle Sulphur Band (Figure 5.28 and 5.29), the detailed geochemical analyses across it revealed consistent anoxic sulfidic conditions. The $\text{Fe}_{\text{HR}}/\text{Fe}_{\text{T}}$ remains high (above 0.38) in all sample (24 samples) as can be seen in Figure 5.23 (> 0.38).

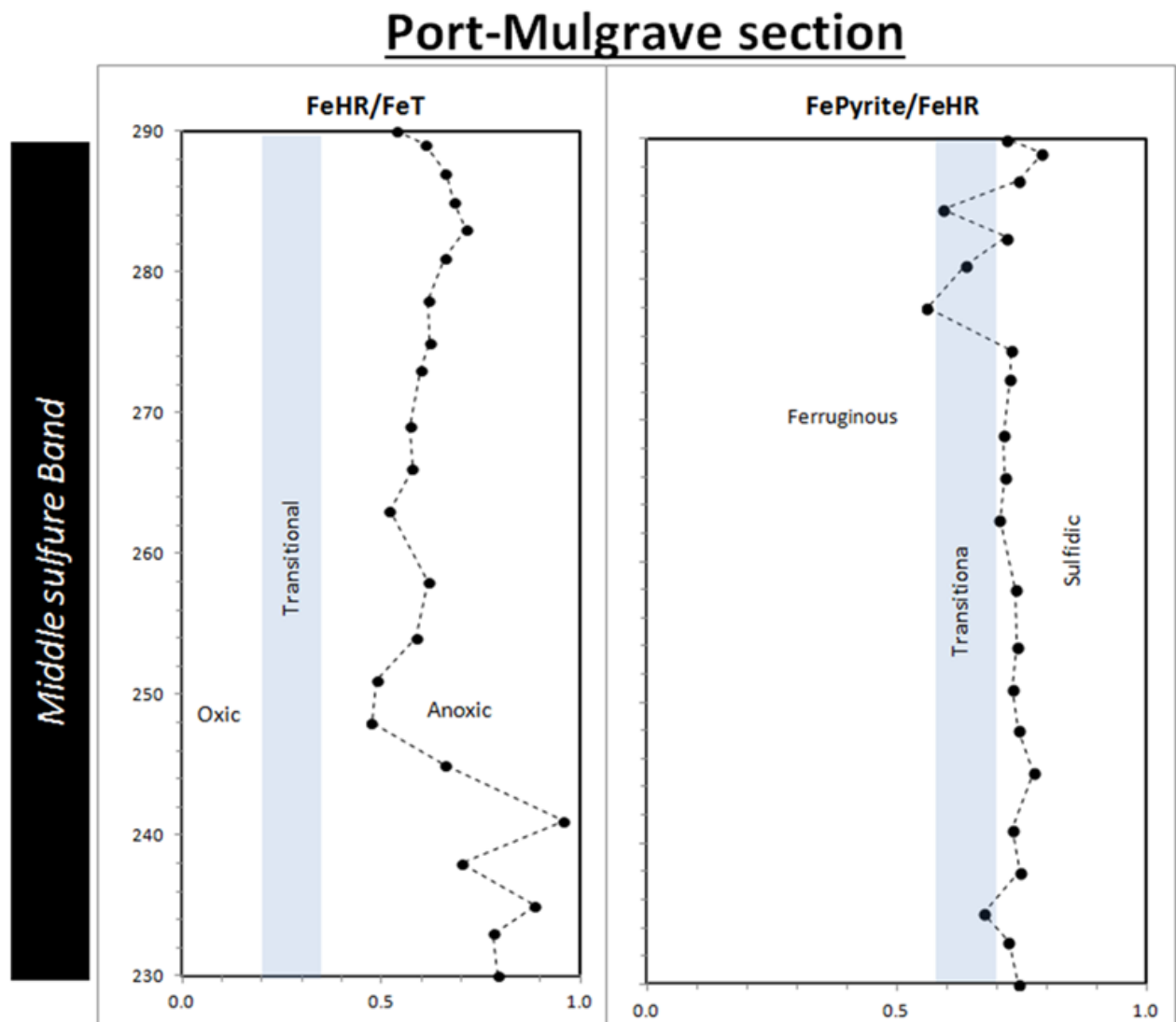


Figure 5. 22: Detailed iron speciation profile across the Middle sulphure Band at Port Mulgrave.

Port-Mulgrave section

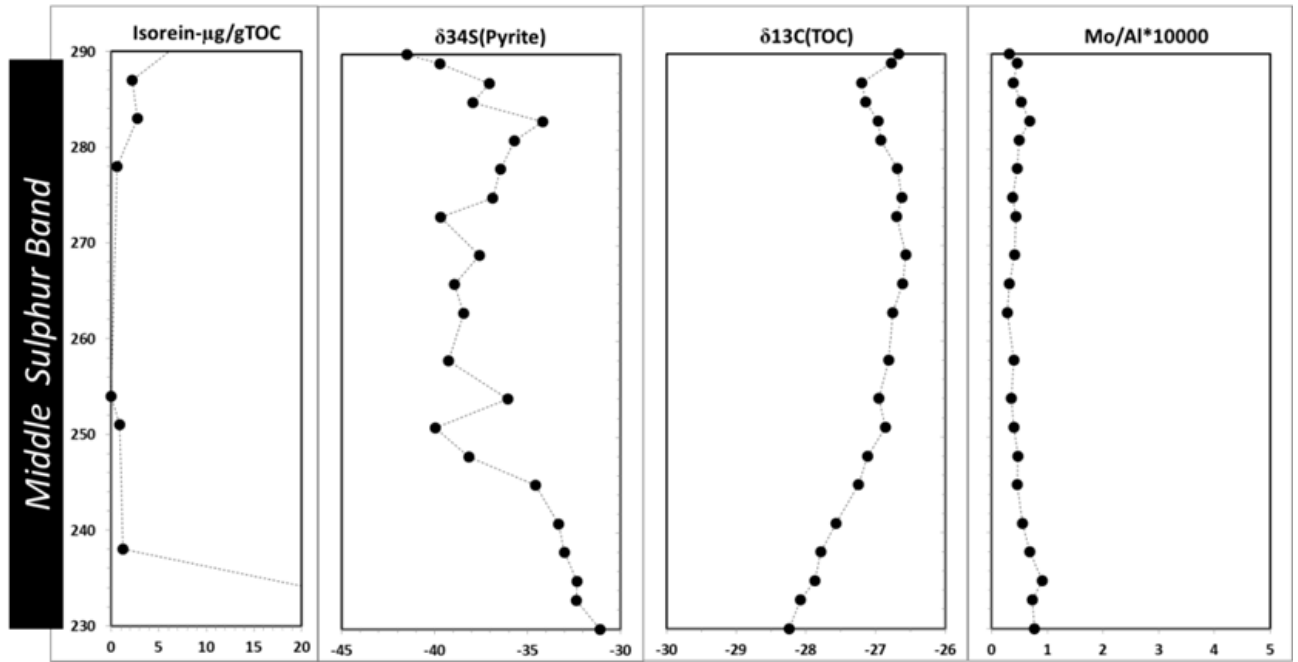


Figure 5.23: Detailed chemostratigraphic plots of $\delta^{34}\text{S}_{(\text{Pyrite})}$ and $\delta^{13}\text{C}$ isotopes , Mo/Al ratio and maxima of isorenieratane abundances across the Middle Sulphur Band.

The basal 10 cm of the MSB is characterised by high Fe_{HR} which could be linked to the availability of the reducible iron at the beginning of the event. Overall the $\text{Fe}_{\text{pyrit}}/\text{Fe}_{\text{HR}}$ profile across the MSB is above 0.7 which is the upper limit of the ferruginous condition and suggesting that dominant anoxic sulfidic condition prevailed throughout the MSB and no cycling between sulfidic and non-sulfidic (ferruginous) is observed unlike the case of LSB. Moreover, Isorenieratane was observed throughout the band suggesting sulfidic water conditions that extended to the euphotic zone. Lower Mo enrichment is recorded in MSB compared to LSB which could be related to decrease supply from content source or reflect deeper water column and thus the Mo deposited over wider area and not concentrate on shallower shelf zone as could be the case with the LSB.

Port-Mulgrave section

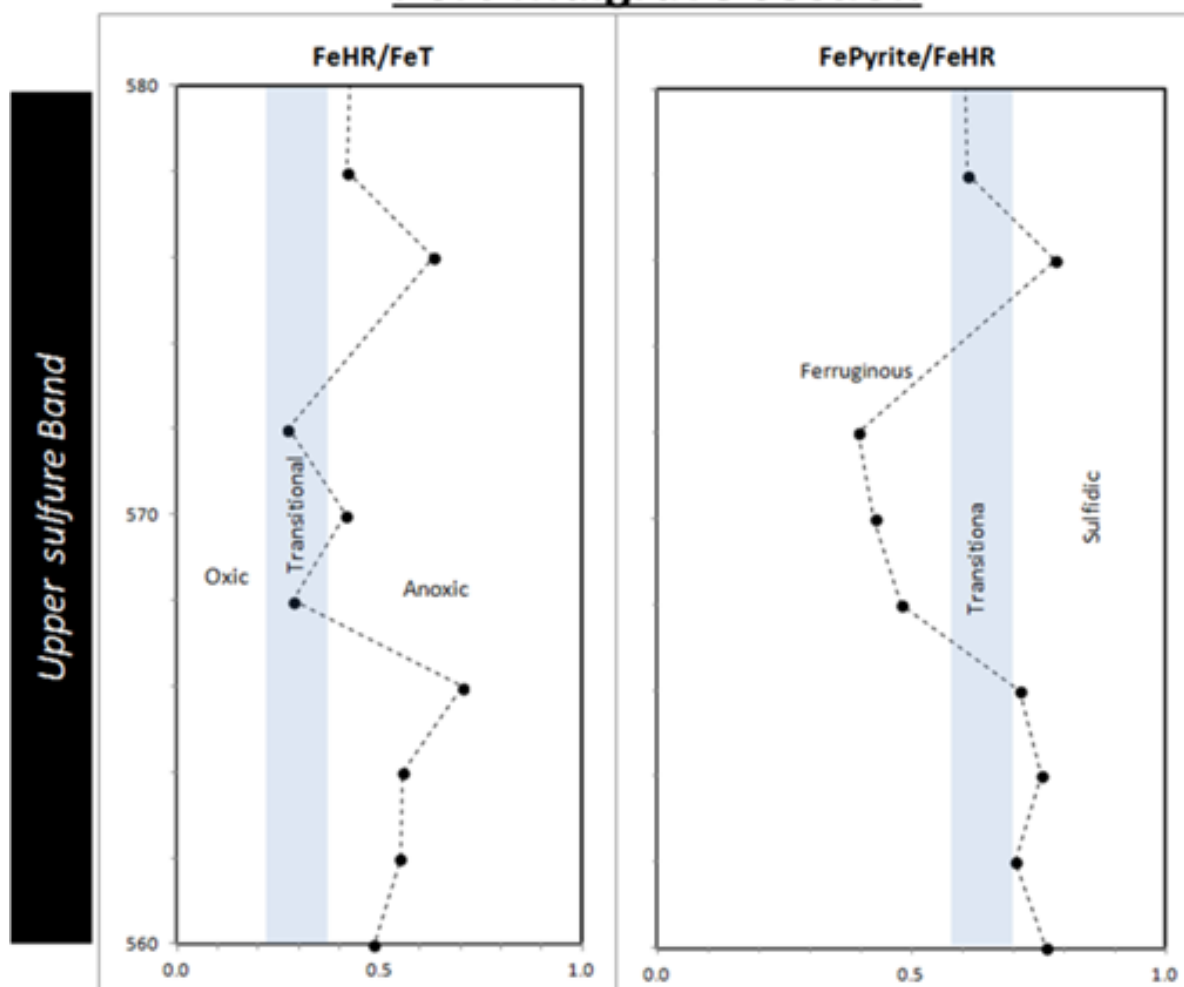


Figure 5.24: Detailed iron speciation profile across the USB at Port Mulgrave section.

Similar scenario to the LSB is observed in the USB. At the start of deposition of the USB (Figure 5.24 and 5.25), and within the lower 5 cm the Fe_{HR}/Fe_T ratios are higher than 0.38 and the Fe_{pyrite}/Fe_{HR} ratios above 0.7 indicating that bottom waters were anoxic sulfidic. Then both of the Fe_{HR}/Fe_T and Fe_{pyrite}/Fe_{HR} ratios were decreased in the central 3 cm of the USB to less than the threshold of anoxia and thus anoxic-dysoxic condition is suggested for this interval. Then the anoxic sulfidic water condition dominates the upper 6 cm. Unlike the LSB the USB has lower Mo enrichment. Moreover, the Mo/TOC ratios for the USB and MSB are different from the LSB (Figure 5.26) and resemble that for the Jet Rock shale, which could suggest that there is stronger stratification over regional area during the deposition compared to less stratified and more local condition for the LSB.

Port-Mulgrave section

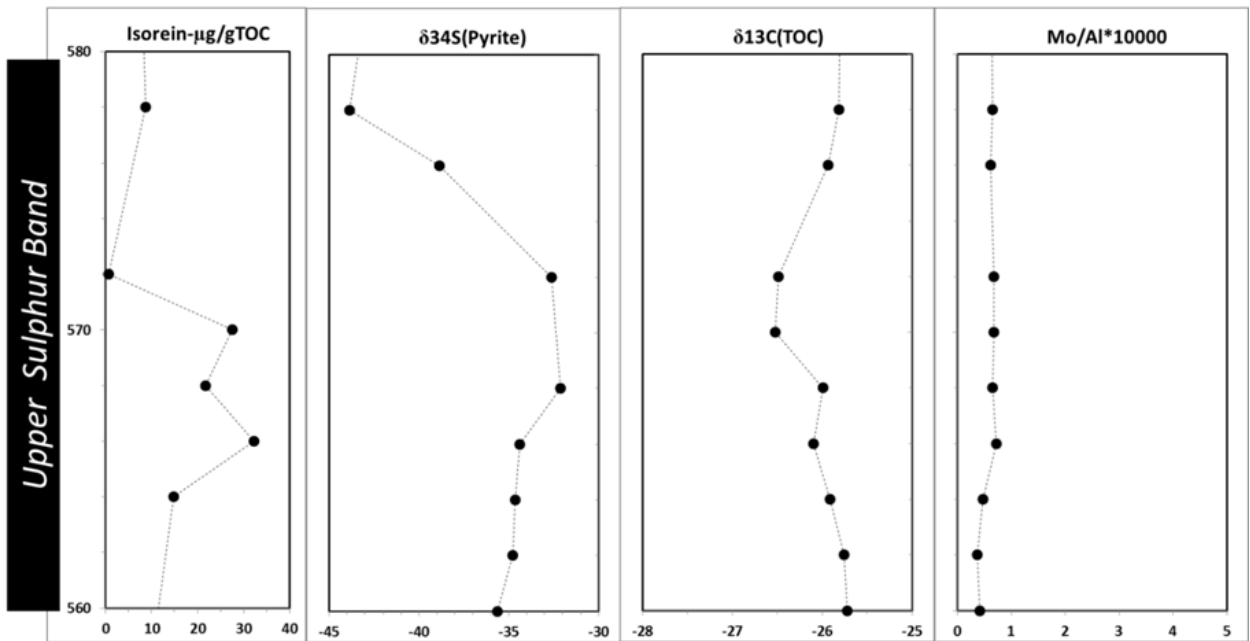


Figure 5.25: Detailed chemostratigraphic plots of $\delta^{34}\text{S}$ (Pyrite) and $\delta^{13}\text{C}$ isotopes , Mo/Al ration and maxima of isorenieratane abundances across the Upper Sulphur Band at Port Mulgrave section.

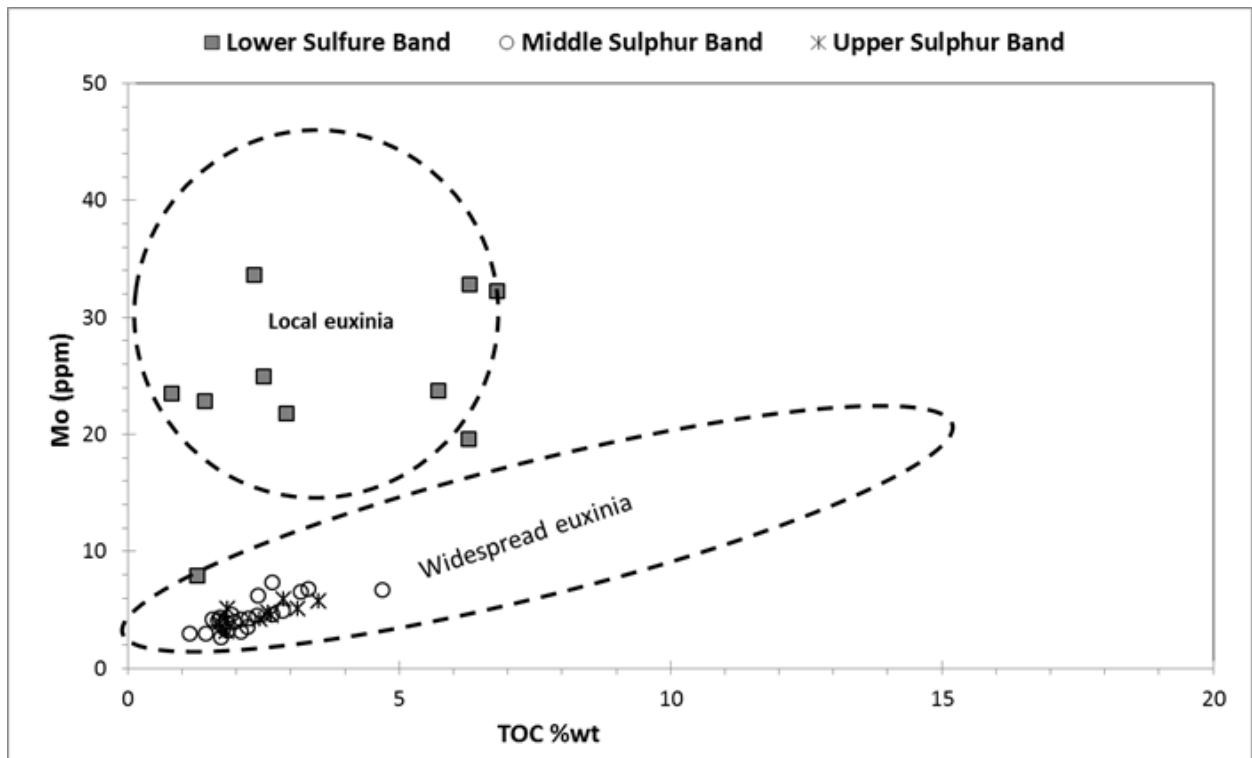


Figure 5. 26: Cross-plot of MO ppm and TOC %wt for the Sulphur Bands at Port Mulgrave section showing the different Mo/TOC of the Lower Sulphure Bands compare to the Upper and Middle once

5.3.3 Regional redox of the Sulphur Bands

The Sulphur Bands represent basal transgressive black shales that deposited in shallow shelf setting. Despite the very thin and short lived nature of the Sulphur Band, its development at the Piensbachian-Toarcian boundary is recorded over wide area within the European Epeiric Sea. At Dotternhausen in Germany four thin units of organic-rich shale occur in the *paltum* and uppermost *clevelandicum* Subzones which tempting to equate those units of Sulphur Bands of North Yorkshire. Stratigraphically the Sulphur Bands shows no thickness or variations (Figure 5.27).

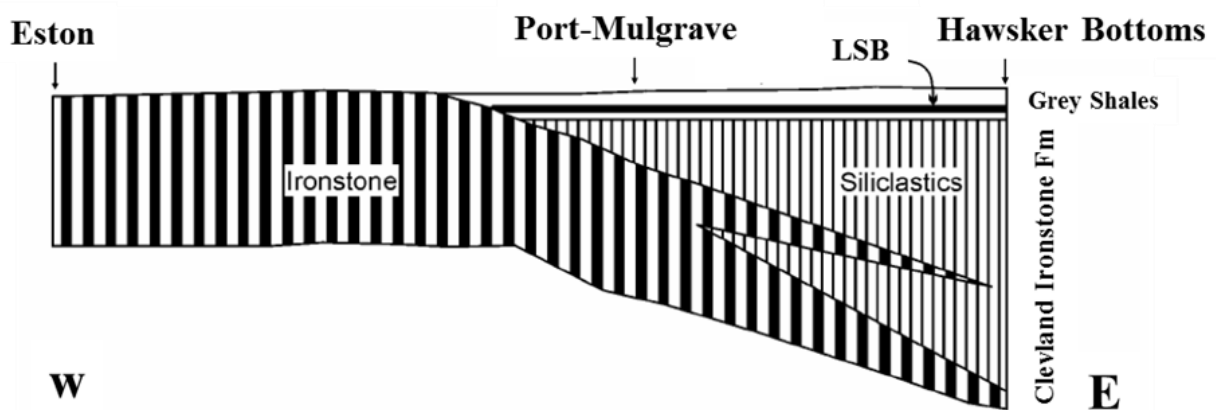


Figure 5.27: Schematic W-E cross section of the Cleveland Ironstone Formation and the lowest part of the overlying Grey Shale (Rob Newton PhD thesis, after Howard, 1985).

Previous studies have been concerned with boundary intervals at Late Piensbachian as it relates to sea level change (Hallam, 1997), as well as contrasting water mass and basinal restriction (Sælen et al., 2000; McArthur et al., 2008). The Piensbachian-Toarcian boundary represents significant increase of bottom water temperatures from about 14°C in the late Piensbachian to about 20°C in the earliest Early Toarcian, as seen in abrupt shift toward lower values of the $\delta^{18}\text{O}_{\text{brachiopod}}$ (Suan et al., 2008).

Important environmental change in paleo-climate warming and enhanced hydrological cycle across this interval is also suggested by $^{87}\text{Sr}/^{86}\text{Sr}$, $\delta^{18}\text{O}$ and Mg/Ca ratios of belemnite rostra, from England, Spain and Germany (Bailey et al., 2003; Rosales et al., 2004; van de Schootbrugge et al., 2005a). All of these may have affected deposition of the Grey Shales and the overlying Jet Rock shale during the period of major basin subsidence

characterised by deep open waters (Powell, 2010). However, the fluctuating redox condition at the base of Grey Shale still needs to be more understood, particularly in terms of the spatial extension of these small cyclic redox conditions within the Sulphur Bands.

As redox conditions at Port Mulgrave indicate that the bottom water during deposition of the sulphur bands were anoxic, non-sulfidic to sulfidic (Figure 5.15), iron speciation data from the Sulphur Bands at Hawsker Bottoms, a more distal site in Cleveland Basin, indicate that bottom water conditions were mainly anoxic (FeHR/FeT , > 0.38), to sulfidic ($\text{Fepyrite}/\text{FeHR}$, > 0.7) throughout their deposition (Figure 5.14).

The profile indicates that the LSB has variable redox condition between the two sites. At Port Mulgrave the LSB deposited under more sulfidic condition as can be suggested from the iron speciation data and the presence of Isorieneratane (Figure 5.19 and 5.20). On the other hand, the lateral extent of the LSB at the more distal setting in Hawsker Bottom is characterised by oxic-dysoxic to anoxic non-sulfidic (ferruginous) condition through its lower and middle part, while possibly sulfidic condition developed at its upper section. There was no Isorieneratane detected in the LSB at Hawsker Bottoms indicating that water column anoxia did not extend into the photic zone as is the case in Port-Mulgrave section. Moreover, the LSB at Port-Mulgrave is highly enriched in Mo compared to its lateral extent at Hawsker Bottoms which could be due to geographical position at more proximal setting close to the terrestrial flux from land where higher flux of organic matter gives rise to more transition elements under more reducing condition (Tribovillard et al., 1994).

Despite the lateral variation in the redox condition of the LSB at both localities, the MSB and LSB shows similar paleoredox trend at both locations with fluctuation between anoxic ferruginous to sulfidic.

5.3.4 Carbon isotopic excursion before the T-OAE

The $\delta^{13}\text{C}_{\text{org}}$ profile (Figure 5.38) displays a complex excursion developed at the Pliensbachian-Toarcian boundary. This complex negative $\delta^{13}\text{C}_{\text{org}}$ excursion consists of three peaks corresponding to the three sulphur bands at the base of the Gray Shale Member. The first component of the CIE occurs in the *upper P. hawskerense* Subzone at the Pliensbachian-Toarcian boundary, culminating in a value of $\sim -29.6\%$ within the Lower Sulphur Band and magnitude of approximately -4% . The earliest Toarcian samples (base of *Paltum Subzone*) are characterized by sudden return to pre-excursion values of $\sim -26.1\%$, which are then

gradually decreased again forming the second and third negative CIE spanning the Middle and Upper Sulphur Bands with weaker excursion with magnitude of $\sim -3\text{‰}$ and $\sim -1\text{‰}$, respectively. The return to pre-excursion values after the Upper Sulphur Band persists until the onset of the larger negative carbon-isotope excursion in the Late *D. tenuicostatum* zone that is associated with the Early Toarcian OAE. This complex excursion at the Pliensbachian-Toarcian boundary has similar characters to the main negative CIE that is well known from the Early Toarcian OAE, so that the proposed mechanisms to explain its presence would be similar.

The Paleocene-Eocene thermal maximum (PETM) is a globally brief interval that in some respects shares similar characteristic features to the Early Toarcian OAE (Cohen et al., 2007). Both events are characterized by a massive influx of isotopically light carbon, benthic faunal extinctions, extensive carbonate dissolution and evidence for a large and rapid global warming event (Bowen et al. 2006). There were at least five significant and similar events between 56 and 53 Ma, of which the PETM is the most pronounced. The five events are characterized by elevated sedimentation rates and marl-rich horizon with low $\delta^{13}\text{C}$ (Nicolo et al., 2010). They therefore may have had a similar generic cause and could represent massive inputs of isotopically light carbon during a long-term warming trend and accelerated hydrologic cycle that increased continental erosion and development of expanded condensed clay layers and marl rich horizons spanning the multiple excursions. Similarly, the repeated carbon isotopic excursion at the Pliensbachian-Toarcian boundary but prior to the main carbon isotopic excursion of the T-OAE seems to represent a comparable scenario. The repetitive nature of these excursions suggests a dynamic source must have repeatedly injected large quantities of ^{13}C depleted carbon into the ocean or atmosphere.

The carbon-isotope perturbation at the Pliensbachian-Toarcian boundary is coincident with the first phase of extinction in marine benthos at the stage boundary (Caswell et al., 2008) well before the main phase of anoxia associated with the Early Toarcian OAE, which could suggest the event was not simply a localized event. The apparent abrupt onset of the stage boundary CIE, and the initiation of an extinction step near the same level, supports the idea of a catastrophic event such as release of methane hydrate.

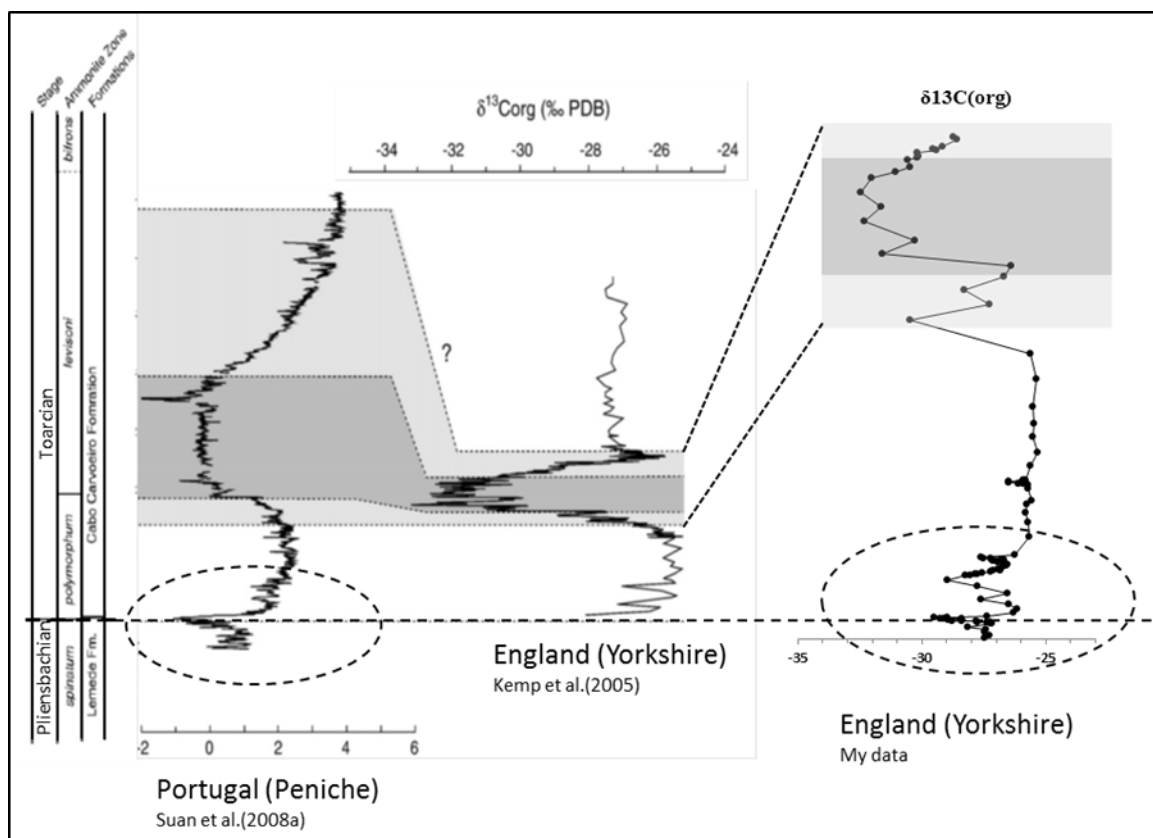


Figure 5.28: Comparison between carbon-isotope records of Port Mulgrave section in North Yorkshire and Peniche section in Portugal.

The identification of multiple perturbations with similar causes and consequences would lead us to think of a source that is capable of repeated carbon injections. A similar pattern of negative carbon-isotope excursions has been observed at the stage boundary in the SW European section at Peniche, Portugal (Figure 5.28). The isotopic excursion is of interest when considering the genesis and development of the later Toarcian Oceanic Anoxic Event (OAE), as well as the second-order global extinction event that spans the stage boundary.

The carbon isotopic excursions which represent sudden environment change that produced the Sulphur bands will likely provide a useful chemostratigraphic marker for the Pliensbachian-Toarcian boundary. Moreover, the gradual increase of the sulphidic condition for the middle and upper sulfure bands suggests more global condition and that the carbon perturbation could have affected the entire ocean system and should be registered in appropriate material in coeval strata in all parts of the world.

5.3.5 Conceptual model

The paleogeography of black shale depositional environments during T-OAE is a matter of discussion. Most of the Toarcian black shales were deposited on epi- and pericontinental shelves in environments proximal to Pangaea. In this study, two phases of important paleoenvironmental changes occurred at the Lower Toarcian, both of which are characterized with enhanced organic carbon accumulation, negative shift in the carbon isotopes and development of anoxic and euxinic bottom water condition. These two stratigraphic limited intervals also correlate with periods of high extinction rates of benthic marine fauna (Little and Benton, 1995; Caswell et al., 2008) and are associated with an increase in paleotemperature of bottom waters (Suane et al., 2008).

The possible trend for this mode of redox state observed could be as a result of local processes, which were triggered by changes in global climate. In this context a higher influx of organic matter from accelerated hydrological cycle delivered more nutrients and freshwater to shallow shelf-seas during continental weathering and runoff (Bailey et al., 2003), which is supported by very high TOC (> 3wt%), Mo (21 ppm) and high HI throughout the LSB in more proximal settings within the Cleveland Basin. In contrast to the low TOC, Mo and HI characterising the LSB at more distal setting which suggest possible distance from source, low productivity, and residence time of organic materials (Demaison & Moore, 1980).

Results of this study fit a model as showing in Figure (5.28). During the early Toarcian in Cleveland Basin, development of density stratification starts to occur at local extent at proximal setting, as a result of increased fresh water inputs by enhanced hydrological cycle, and thus combined with periodic high productivity, led to local expansion of anoxic-euxinic conditions. This anoxic condition prevailed during the deposition of the LSB and then the system fluctuates back to more oxic dysoxic condition represented in the bioturbated mudstones above the LSB. The second anoxic event derived by the same mechanism were stronger and tend to be more regional where the euxinic waters covered most of the Cleveland Basin which again lasted for short period of time before the system switch again to oxic-dysoxic condition.

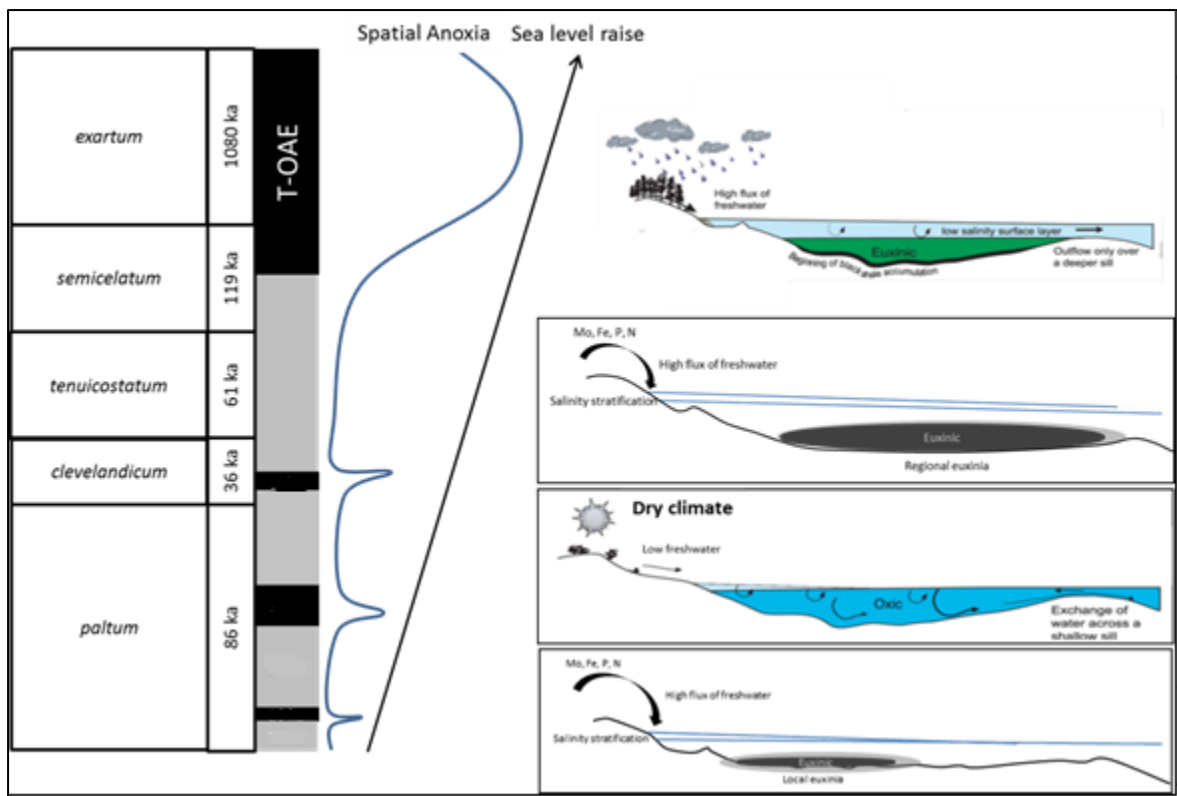


Figure 5.29: Schematic paleoceanographic model of the lowermost Early Toarcian. Showing the development of the driving mechanism for the Sulphur Bands which then accumulates in the T-OAE. Biozone duration from McArthur et al. (2000).

The development of and intensity of redox conditions across the Basin preceding the T-OAE could have been caused by a combination of restriction on circulation, coupled with local density stratification. Wide spreading of anoxia higher up across the T-OAE could represent more global forcing mechanisms which were capable of driving global environmental change. These mechanisms may have included; the eruption of the Karoo-Ferrar continental flood basalt and/or the massive dissociation of continental margin clathrates with a resulting increased hydrological cycle and a transient greenhouse climate with increased CO₂ concentrations and paleotemperatures.

5.4 Conclusions

- The Grey Shale Member represents an important marine sedimentary record of a gradual transition from an oxygenated sea to one characterized by anoxic bottom waters. These intervals of oxic and anoxic deposition for the Grey Shale are characterized by the deposition of three pyrite rich black shales, known as the sulphur bands, and indicating deposition under anoxic bottom water conditions.
- The bioturbated mudstone intervals surrounding the Sulphur bands, are characterized with Fe_{Py}/Fe_{HR} less than the upper limit of ferruginous condition and Fe_{HR}/Fe_T above the threshold of anoxic condition. The presence of bioturbation indicates that bottom waters were periodically oxic, with strong mixing of water column signals for Fe_{HR} and trace metals. Therefore the sequence of mudstone and Sulphur Band deposition throughout the Grey Shales can be described by a seasonal oxic/dysoxic fluctuation model coupled to gradual climatic warming and fluctuations in sediment supply.
- Repetitive, short periods of intense oceanic anoxia (often euxinic) occurred preceding the global T-OAE. These short periods of anoxia were localised in occurrence, with potentially catastrophic effects on marine biology.
- Despite the well laminated appearance of the Sulphur Bands, very detailed analysis indicates that there are fluctuation in the paleoredox condition across these units cycling between euxinic to anoxic non sulfidic to dysoxic condition.
- There is lateral variation in the redox condition of the Lower Sulphur Band between Port-Mulgrave and Hawsker Bottom section, where bottom water condition at Hawsker Bottoms were mainly dysoxic to anoxic, with less sulphide in contrast to a more sulfidic condition at more proximal setting in Port-Mulgrave.
- The style of anoxia in the Jet Rock is fundamentally different from that in the Grey Shales. A peak in global temperatures, a long period of sediment starvation and a greater water depth, all combined to create a stratified anoxic water column with organic rich sediments beneath.
- The results highlight that the Earth system was highly dynamic during even the early stages of global warming, with extreme periods of localised anoxia occurring well-before the global OAE.

CHAPTER 6 - FT-NIRS ANALYSIS OF MARINE ROCK SAMPLES FROM A RANGE OF DEPOSITIONAL ENVIRONMENTS

6.1 Introduction

Marine sedimentary rocks and sediments preserve abundant environmental information for reconstructing the climatic and oceanic history. One tendency in the current biogeochemical and pala-oceanographic studies is to investigate long sediment sections at very high resolution in order to unlock internal details of the long term record, such as small events that may hold vital information about the evolution and forcing mechanisms of environmental change in the past. This inevitably increases the number of samples to be analysed, significantly increasing the amount of resources and time needed. Another related challenge for multi-component analysis is the limited coring material available. Therefore, there is an urgent demand for new fast, non-destructive, and inexpensive analytical tools, such as core scanner systems (Chang et al., 2005; Leach et al., 2008).

Near infrared reflectance spectroscopy (NIRS) is one rapid and non-destructive analytical technique for characterization and quantification of material property, and it has been widely used to monitor the quality of raw material in agricultural, pharmaceutical, and other industries (Williams and Norris, 1987; McClure, 1994). NIRS measures the interactions between incident near-IR light and the material's surface. Multivariate calibration techniques, including principle components regression (PCR) and partial least squares regression (PLSR), are often used to relate near-IR spectra with measured properties of material (Martens and Naes, 1989).

The conventional bulk geochemical methods to determine the OC richness and hydrocarbon potential of source rocks is the Rock Eval analytical pyrolysis (Tissot and Welte, 1978) combined with Carbon-Sulphur Analyser (e.g LECO CS- 244). Despite progress in scanning technologies some of the most fundamental parameters in marine research and petroleum geology, total organic carbon (TOC), total sulphur (TS), is still not routinely determined. This comes as a surprise as scanning techniques have been shown to provide high accuracy data (e.g Balsam and Deaton, 1996; Chang et al., 2005; Leach et al., 2008), providing scope for further research.

Furthermore, scanning techniques pose no health and safety issues unlike some conventional methods that require the use of concentrated acids and carcinogenic indicators. An analytical scanning technique that has been used extensively with high success, including non-destructive quantification of organic compounds, is Infrared (IR) spectroscopy (Mckelvy et al., 1996). Further advancement in IR spectroscopy gave rise to a quicker and more sensitive Fourier Transform Infrared (FT-IR) Spectrometer (Rintoul et al., 1998). Many researchers have combined spectra from FT-IR with Partial Least Squares Regression (PLSR) to obtain accurate and useful information. Ballard (2007) demonstrated the adaptability of the technique to real-time logging by using it to construct mineralogical log for shale gas reservoir. This alongside portability and non-destructive ability of the technique is an advantage over the conventional combustion technique (LECO CS- 244). Breen et al. (2008) used the technique for bulk mineralogical characterisation of oil field reservoir rocks and sandstones and described the method as suitable for analysing complex multi-component spectra.

This study further demonstrates that FT-NIRS can be applied to old marine sediments to accurately determine TOC, total sulphur (TS) and potentially even total organic sulphur (TOS).

6.1.1 Principles of Near Infra-Red Spectroscopy

Infra-red (IR) spectroscopy is traditionally used to provide characteristic information on the structure of a sample, by measuring the energy (from light) absorbed by molecules as they vibrate (Bokobza, 2002). The IR analysis of a molecular structure can describe both simple diatomic molecules, and more complicated polyatomic compounds, which represent different functional group structures by individual characteristic absorptions (Duckett and Gilbert, 2000). Therefore, vibrations can either describe the movement of atomic bonds and interactions of functional groups, or describe the vibrations of a whole molecular structure (Williams and Fleming, 1995).

The near infra-red region of the electromagnetic spectrum ranges between wavelengths of 700-2500nm ($4000-12500\text{cm}^{-1}$). To understand the fundamental basis of NIRS, the concept and theory of vibrational energy must be introduced. For absorption to take place, the molecules from a structure must have a dipole moment where the atoms of a molecule have an unequal share of electrons (Duckett & Gilbert, 2000). Within a linear or

branched molecule (figure 6.1), atomic bonds behave like springs constantly displacing the shared electrons between the equilibrium positions (Hollas, 2004).

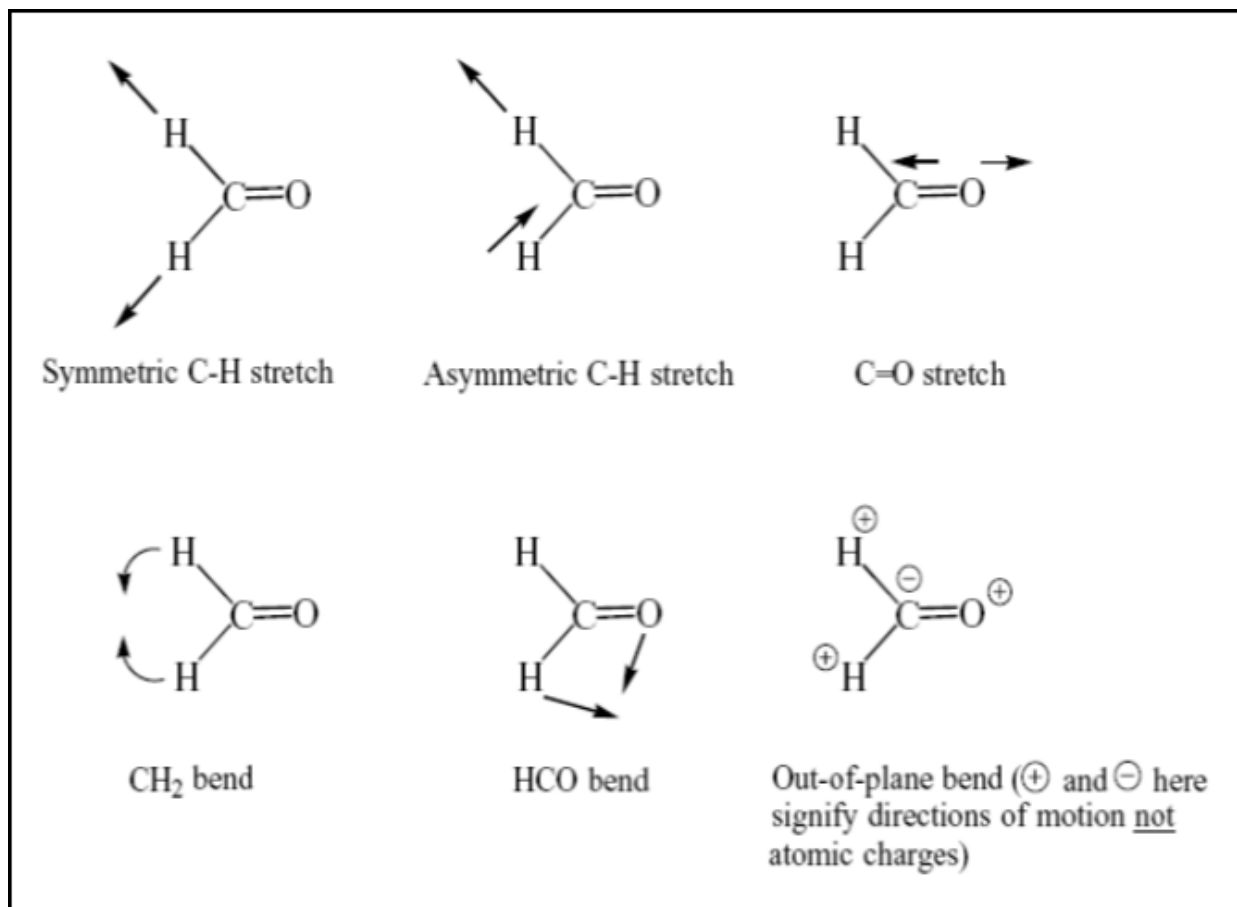


Figure 6. 1: the vibrational behaviour of bond stretching and bending in a molecule

These skeletal vibrations vary in oscillating wave function (intensity and frequency) depending upon the quantity or radiation light emitted from the source, and absorbed as each bond stretched or bends (McMillian and Hofmeister, 1988).

Linear diatomic molecules are the simplest group to describe by vibrational theory, as they have fast dipole moment changes and strong vibrational systems. Examples of these compounds include C-H, N-H and O-H, which are found in both the Near IR and Mid IR regions (Williams & Fleming 1995). These covalent bonds each have individual and characteristic wavelength absorption bands, found in the fingerprint region of the spectrum. Polyatomic group vibrations occur from functional groups, which are characterised by their position on the spectrum (McMillian & Hofmeister, 1988). The localized vibrational frequencies are found above or below the fundamental skeletal modes with lighter groups of

lower atomic mass having higher frequencies than those groups, which are heavier (Duckett and Gilbert, 2000).

Table 6. 1: Abbreviated table of group frequencies for Organic Groups (www.cem.msu.edu)

Bond	Wavenumber/ Cm⁻¹	Type of Compound	Intensity
C-H	2850-2970 1340-1470	Saturated alkanes, limited value as most organic compounds contain C-H	Strong
C-H	3010-3095	Unsaturated alkenes or aromatic	Medium
C-H	3300	Terminal Alkynes	Strong
C-H	3010-3100 690-900	Aromatic rings Aromatic rings	Medium Strong
O=C-H	2800 and 2700	Aldehyde, two weak peaks	Variable
O-H O-H (free)	3400-3000 ~ 3600	Alcohols and Phenols. If hydrogen bonding present peak will be broad 3000-2500 (e.g. carboxylic acids)	Variable, sometimes broad
N-H	3300 - 3500	Amines: Primary-several peaks, Secondary-one peak, tertiary-no peaks	Medium
C=C	1610-1680 1500-1600	Alkenes Aromatic rings	Variable Variable
C-O	1050-1300	Alcohols, ethers, carboxylic acids and esters	strong

As energy from each transition corresponds to individual spectrum peaks (characterised in Table 6.1), IR spectroscopy is therefore a very strong tool for identifying unknown compounds within a sample. However when used in NIRS, the spectral information obtained often requires quantitative analysis for calibration (Kawata, 2002). A strong mathematically model must be developed, due to aromatic overtone and combination vibrations which lower the intensity of fundamental frequencies and absorption.

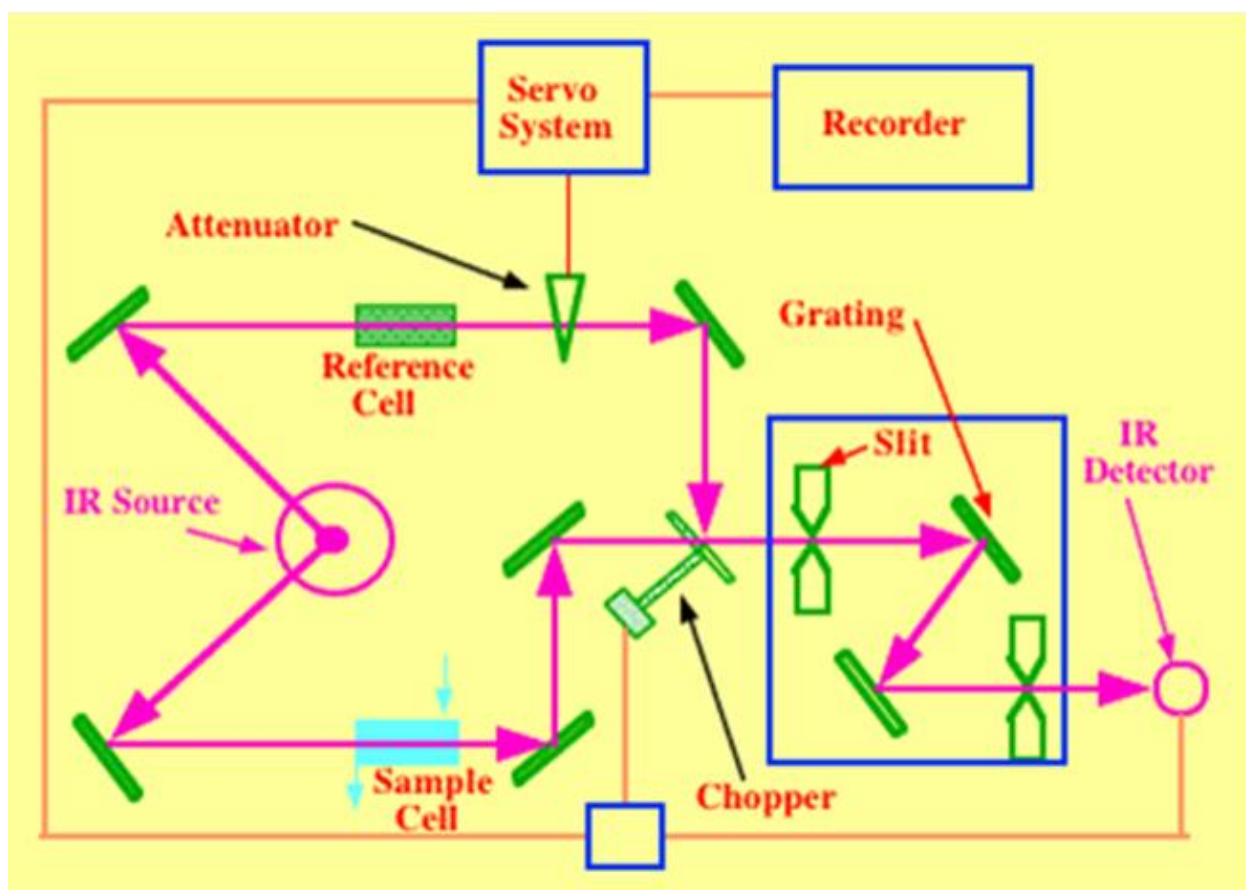


Figure 6. 2: Internal workings of an FT-IR/NIR spectrometer ((www.chromatography-online.org))

The configuration of the apparatus used in IR spectroscopy is shown in Figure 6.2. Instruments used to measure the vibrational properties of the sample structure in basic IR spectrometers include a source lamp filament, which is used to emit a continuous beam of radiation over a range of wavelengths (Smith, 1979). A radiation beam of uniform intensity is focussed through a monochromator which splits the beam into component wavelengths using a dispersion grating, or beam-splitting mirror which is half reflective and half transmitting (Smith, 1979). Each constituent wavelength is then focused on the sample, which is held in a cell that will not absorb radiation or cause light scatter due to the particulate nature of the sample. When the reflected radiation has passed the sample, it is collected, amplified and interpreted as a spectrum by the detector as a function of absorbance (Kawata, 2002).

6.1.2 Fourier Transform Infrared Spectroscopy

Fourier Transform infrared (FT-IR) spectroscopy was developed in order to overcome the limitations encountered with dispersive instruments. The significant speed and high sensitivity of FT-IRS over the use of dispersive instruments stemmed from its multiplex advantage that permits the entire wave number range to be measured at once, and its throughput effect that allows all infrared radiation that passed through a sample to reach the detector at once (Griffiths and De Haseth, 2007).

The FTIR spectrometer obtains infrared spectra by first collecting an interferogram of a sample signal with an interferometer, which measures all of infrared frequencies simultaneously. An FTIR spectrometer acquires and digitizes the interferogram (figure 6.3), performs the FT function, and outputs the spectrum. In addition, the “interferometric” approach of FT-IR allows it to routinely characterise and analyse complex samples in milligram quantities (Rintoul *et al.*, 1998; Griffiths and De Haseth, 2007).

When the interferogram signal is transmitted through or reflected from the sample surface, the specific frequencies of energy are adsorbed by the sample due to the excited vibration of function groups in molecules. The infrared signal after interaction with the sample is uniquely characteristic of the sample. The beam finally arrives at the detector and is measure by the detector. Then the detected interferogram has to be “decoded” with a well-known mathematical technique in term of Fourier Transformation. The computer can perform the Fourier transformation calculation and present an infrared spectrum, which plots adsorbance (or transmittance) versus wavenumber.

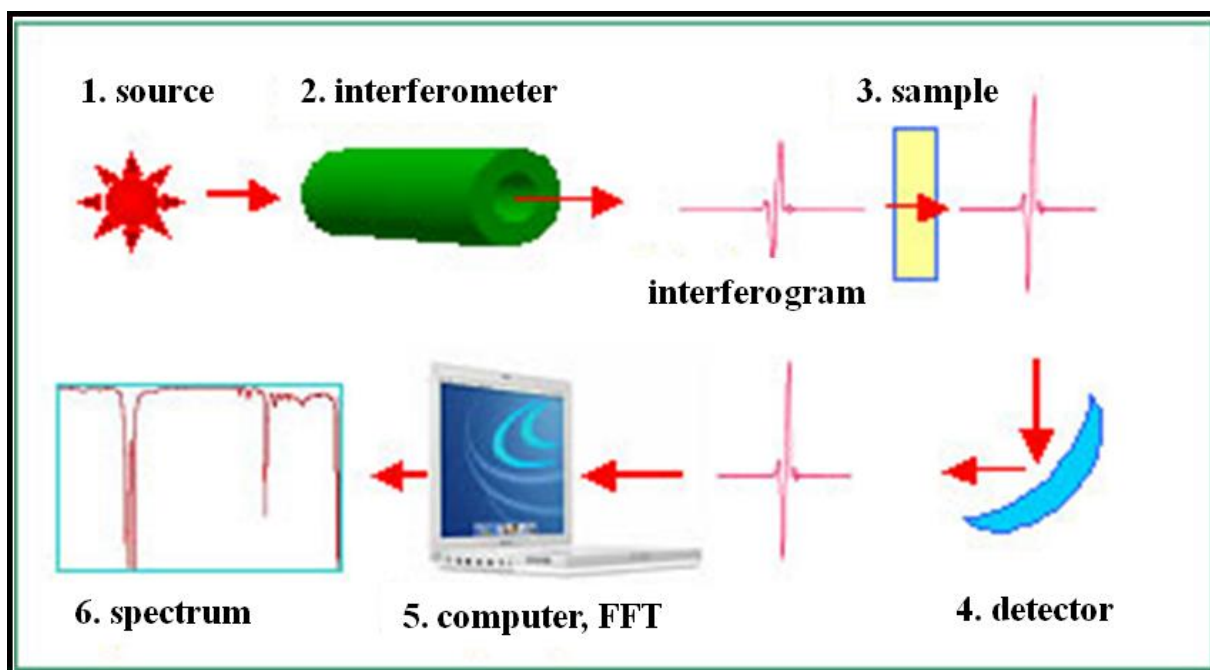


Figure 6. 3: Schematic illustration of FTIR system (www.norhtwestern.edu)

FT-IRS improved on the traditional transmission method employed in IR Spectroscopy with the development of reflection and emission techniques (Madejova, 2003; Griffiths and De Haseth, 2007). Reflectance techniques such as Diffuse Reflectance Infra-red Fourier Transform (DRIFT), Attenuated Total Reflectance (ATR) and Specular Reflectance have since been applied to many analytical studies. The preferential use of Reflection-FT-IR over other methods resulted from the little time and effort required for sample preparation (Madejova and Komadel, 2001; Madejova, 2003). Other advantages of FTIR over conventional IR analyses include the high level of photon flux, or “*optical throughput*” (Kawata, 2002) collected by the detector, and the high detection efficiency of the spectrometer due to the simultaneous detection of a wide range of mid-IR wavelengths (Kawata, 2002). As the wavelengths do not need to be scanned in order, the entire wavelength interval can be measured in a few seconds at most (Williams and Fleming, 1995). FTIR can also be used to measure wavelengths detectable with low energies due to the highly scattering or absorbing nature of the samples being analysed (Griffiths, 1978)

Madejova (2003) used transmission and reflection (DRIFT and ATR) techniques in the NIR and MIR region to characterise clay minerals and discovered that the various techniques can help distinguish clay minerals. Ballard (2007) realised the accuracy and swiftness of FT-IRS in predicting mineralogy for numerous data points within a wellbore and used it to produce instantaneous mineralogy log for a shale gas well: a principle which can be

applied to produce automated logging system for TOC concentration in sedimentary sections or wellbore if accurate calibrations can be developed from the analyses of several sample sets.

FT-IRS has been successfully used for both qualitative and quantitative analysis. Quantitative analysis in FT-IR is based on Beer's law, which states that the absorbance of a substance in a sample has a direct relationship with its concentration (Smith, 1996; Griffiths and De Haseth, 2007). While few workers have employed DRIFT technique in the quantification of TOC in sediment, ATR has rarely been used despite the comparative advantage it poses over DRIFT in terms of sample size and sample preparation. This could possibly be attributed to the poor signal to noise ratio (SNR) as observed for ATR relative to DRIFT during investigation of combination bands in some Kaolin samples (Frost and Johansson, 1998). Chang *et al.* (2005) explained the need for further investigation after NIR-DRIFT failed to accurately predict TOC concentration during geochemical analyses of some marine sediment. MIR-DRIFT spectroscopy was successfully used for quantitative reconstruction of TOC, total inorganic carbon (TIC), total nitrogen (TN) and opal in lake sediment (Vogel *et al.*, 2008). Leach *et al.* (2008) demonstrated that FT-IR in the NIR region can be used for routine determination of TOC in marine sediments from different environments and suggested a possible transformation of the technique into an automated well logging system. A diffuse reflectance method called "Updrift" was adopted for the study to minimise scatter and specular reflectance from powders during the scanning process.

NIR has been preferentially used for quantitative analysis as MIR sometimes requires KBr dilution to mitigate strong absorptions present in the MIR region which could lead to poor results (Olinger and Griffiths, 1993; Reeves *et al.*, 2001). The spectral distortion and non-linearities that result from the strong absorption probably makes quantification without KBr dilution of samples difficult in the MIR region (Reeves *et al.*, 2001). Furthermore, NIR has more intense and highly sensitive detectors relative to MIR and does not require mounting of samples on salt cells (Griffiths and De Haseth, 2007). Griffiths and De Haseth, (2007) also revealed that the ease of interpretation of MIR spectra is limited by its lesser amenability to multivariate statistical analysis.

6.1.3 Partial Least Square Regression

Partial Least Squares (PLS) (also called Projection to Latent Structures) technique for modelling blocks of complicated data sets was first developed by Herman Wold in 1975 (Wold *et al.*, 2001). The word “Partial” implies the method is a partial regression (Wold *et al.*, 2001). Svante Wold and Herald Martens in 1980 came up with modification of the multivariate analysis called PLSR that uses PLS model with two blocks (X and Y) which is suitable for science and technology data (Wold *et al.*, 2001).

The combination of FT-IRS with multivariate statistical analysis such as PLSR has helped solved many analytical problems (Rintoul *et al.*, 1998). PLSR models the structure and relationship between two matrices X and Y using two-block predictive PLS model to give better results relative to conventional multiple regression methods (Wold *et al.*, 2001).

The analyte components of IR spectra are usually quantified using PLSR: a process during which PLSR analyses the spectra and detects variations caused by changing component concentration in the investigated system (Wold *et al.*, 2001; Breen *et al.*, 2008). PLSR is a factor analysis method that calculates a weighted average spectrum by using concentration information from sample components (Smith, 1996). Moreover, construction of predictive models during computation that involves numerous complex collinear measurements (factors) has been successfully carried out using PLSR, and such models can be used to predict properties of samples that fall within the property domain of the “source” calibration set (population of samples whose properties were used for model construction) during future analyses (McCarty *et al.*, 2002; Leach *et al.*, 2008).

The application of PLSR in many analytical studies has proved effective in extracting information from spectra (Rintoul *et al.*, 1998) and making more accurate predictions from calibration models (Janik *et al.*, 1995; Reeves *et al.*, 2001; Breen *et al.*, 2008, Leach *et al.*, 2008; Vogel *et al.*, 2008).

6.1.4 Sample material

A total of 337 marine rock samples were collected from several locations. 193 samples are outcrop samples collected from two geologically and geographically different locations in England: Wessex Basin in the South West and Cleveland Basin in the North East

of England. Another 144 mudstone and shale samples were archived at CEG Newcastle covering different ages and a wide range of depositional settings.



Figure 6. 4: schematic map of the sampling locations: D = Lyme Regis outcrop at Dorset, P= Port Mulgrave

The 97 samples obtained from the Lower Jurassic Blue Lias Formation of Wessex Basin were collected from Lyme Regis, Dorset while the remaining 96 from Lower Toarcian Whitby Mudstone Formation of Cleveland Basin were collected from the North Yorkshire, Staithes. The Whitby Mudstone and Blue Lias Formations form part of the British Jurassic rocks with the former containing major organic-rich shale sequences and the latter containing minor sequences (Morris, 1980). The sediments of these Formations are thermally immature, marine in origin with mixed type II kerogen (Peters, 1986; Bowden *et al.*, 2006; West and Gallois, 2011) and TOC values vary between 0.5 to 12.2% for Blue Lias in Dorset area

(Deconinck *et al.*, 2003) and 1.5 to 14.5% for Whitby Mudstone in North Yorkshire (Helsebbo *et al.*, 2000).

All of the samples were subject to various geochemical analyses, including colour, total organic carbon (TOC), and total sulphur (TS). Additionally, the grey shale and Blue Lias samples were analysed for the determination of total reduced S (100% pyrite Sulphur as no AVS were detected).

6.1.5 Aims of the study

The main aim of this study was to determine whether data generated by FT-NIRS could be used to either replace or complement data generated by standard Leco analyses. Successful application would mean that future studies on marine rocks could benefit from time and cost savings offered by FT-NIRS in comparison to other, more complex geochemical analyses.

The project focuses on the development of FT-NIRS techniques that can be used for routine determination of TOC, TS and TOS in sediment. The aim of the project is to produce and compare calibrations from the FT-IR reflectance techniques using Near Infrared (NIR) (700-2500 nm) region of the electromagnetic spectrum, and measure their accuracy in quantifying the TOC, TS and TOS in sediment. This was achieved by scanning 373 outcrop samples through the FT-IR spectrometer in the reflection mode to obtain spectra. The spectra were combined with a multivariate statistical analysis (partial least squares regression) on statistical software (Unscrambler X) to construct the calibration models.

6.2 Methodology

This work was carried out using 337 rock samples. The samples selected offer a wide range of variability in TOC (0.3 to 19), TS (0.53 to 17.9) and TOS (0.13 to 14.05). The TOC and TS values for the samples as measured using a Leco CS-244 analyser, while the TOS is calculated as the difference between the TS and the pyrite Sulphur (S_{pyrite}). The S_{pyrite} is measured using the chromium reduction method of Canfield *et al.* (1986) as part of this study (See chapter 3 for more details). Most of the samples are mudstones and shales. The TOC ranges between 0.4 to 19 wt. % for the Blue Lias Formation in Lyme Regis and 0.3 to 14 wt. % for the Whitby Mudstone Formation in North Yorkshire. The school samples are from a

range of different basins and have TOC that ranges between 0.33 to 13.20 wt. % with an average of 3.15 wt. %.

Although FT-IR is capable of analysing samples using transmission and emission spectroscopy, these methods require more effort and time for sample preparation than the reflection techniques (Madejova, 2003). Hence, the project was restricted to the reflection techniques (DRIFT) that would satisfy the intent of developing a more rapid technique for quantification within the stipulated time frame for this study.

6.2.1 Sample Preparation

By using NIR spectroscopy, little preparation of the powdered rock samples was required due to the use of Updrift Diffuse Reflectance apparatus, which allows easy loading of very small quantities of sample (approximately 0.1 g) onto the instrument. These procedures were partly extracted from the work of Leach et al. (2008). Every sample was crushed in an agate pestle and mortar and sieved to < 100 microns to ensure full homogenisation and allow reproducibility of spectra during analysis. The powdered samples were then weighed, freeze dried and subsequently stored in air-tight glass vials prior to analysis.

Aliquots of the homogenised samples were consecutively transferred to the sample compartment for scanning.

6.2.2 Instrumentation and Analyses

A Thermo Nicolet Nexus 870 FT-IR spectrometer was used to scan the powdered samples. The instrumental set up included a diffuse reflectance NIRS sampling accessory which covers a near infrared wavelength range of 850-2500 nm. The samples were placed on the Updrift diffuse reflectance apparatus, covering a small quartz window which minimises scatter from heterogeneous powdered samples. After analysis the window was thoroughly cleaned to avoid cross contamination of samples, which could be kept for further analysis due to the non-destructive nature of the analyses.

The spectrometer contained a standard white light source, which passed light through a quartz beam-splitter. In turn each wavelength was passed through the sample and onto the InGaAs (Indium Gallium Arsenide) detector. The data was collected at 1nm resolution and each spectrum was the result of 64 co-added scans. In order to calibrate the spectrometer, a background spectrum was collected at 30 minute intervals to compensate for background

moisture and CO₂ concentration variation within each sample run. A Spectrolon disk was used as a background material during calibration as it is resistant to hygroscopic atmospheric changes. Once the samples are scanned, all spectra were transferred and stored as GRAMS 32 files to be statistically treated using the Camo ‘Unscrambler X’ software.

6.2.3 NIR Data Pre-Treatment

6.2.3.1 Multiplicative Scatter Correction

Multiplicative scatter correction (MSC) is a transformation method used to compensate for additive and/or multiplicative effects in spectral data. Due to the nature of light scattering associated with the analysis of powders whilst using NIRS and DRIFT (Fuller and Griffiths, 1978), the correction of scatter is based on reducing noise produced from sample particles of different sizes (Matrens and Naes, 1989). An adjusted spectrum can be produced by correcting a spectral area, which contains no peaks, and is therefore only affected by the light beam (Naes et al, 2004). By comparing a reference spectra to a measured plot, the baseline and slope of the spectrum can be adjusted, whilst maintaining useful chemical information (Andres and Bona, 2005). However, because a background signal is always present, which usually contains a poor signal to noise ratio, it is difficult to obtain the “ideal” spectra.

6.2.3.2 Savitzky-Golay smoothing

The Savitzky-Golay algorithm is used as first order derivative to reduce and smooth the data points of the spectrum. The Savitzky-Golay algorithm fits a polynomial to each successive curve segment, thus replacing the original values with more regular variations. Using derivatives as a means of data pre-treatment will correct for the spectral baseline and scatter from samples (Andres and Bona, 2005). By deriving new spectra, any additional baseline will be removed from the original spectrum, with the possibility of the new data creating an image very different to that of the original (Andres & Bona, 2005). However by measuring the tangent of the new curve the spectral signal is smoothed, effectively removing spectral noise, while keeping chemical information.

6.2.4 Development of the calibration models

The production of multivariate calibration and prediction models are highly specific for data produced from NIRS, due to the multi-component nature of data described by the spectral output (Lewi, 1992). Computed mathematical models are based on multiple independent variables, which construct a matrix equation used to predict a range of dependant variables (Hawthorn and Waychunas, 1988). Although there are a vast number of statistical methods, which can be used to develop, calibrate and validate the models produced, this study uses Partial Least Squares Regression (PLSR) and Root Mean Squared Error of Prediction (RMSEP) to create a model which will identify the predictive powers of NIRS for the TOC, TS and TOS. This is achieved by validating these models both internally by leave-one-out cross validation and externally by the prediction of 'unknown' values.

Numerical calibration models were constructed using partial least squares regression (PLSR). In PLSR computation, the complex relationship between a very large number of X variables (in this case numerous wavelengths of a spectrum) and one single Y variable (in this case a geochemical parameter of interest) is compressed into a small number of linear combinations of the original X variables, and only these components are used in the calibration (Naes et al., 2004). Possibly the most important advantage of PLSR in comparison to simpler regression methods (e.g. Multiple Linear Regression) is that many co-linear, independent X variables can be handled, which is essential in NIRS analysis because of the large number of spectral data points which often correlate with each other (Martens and Naes, 1989).

The relationship between FT-NIR spectra and geochemical composition of samples was tested using four steps. The first step was to use a partial least squares regression between a geochemical component of interest (e.g. TOC) and spectra for all rock samples for which data was known (e.g. for which TOC had been measured using traditional geochemical techniques). This first step determined whether there was any underlying relationship between FT-NIR spectra and geochemical composition of the sample. This initial PLSR calibration model was validated using a leave-one-out internal cross validation. Following this initial calibration, the data set was split into three groups. Two thirds of the samples were then used as a smaller calibration set and the remaining third used as a validation set. This smaller calibration set was then subject to further PLSR with full internal cross validation. The smaller calibration set was then used to independently predict the remaining one third of

the data as if their geochemistry was not known. Because the data for the ‘unknown’ samples were, in fact available, the prediction ability could be tested for accuracy by regression of the FT-NIRS predicted values for ‘unknown’ samples against their measured values, and by using the determination coefficient (r^2) value between the values.

All calibration steps were assessed for accuracy using the correlation (r^2 between measured and FT-NIRS predicted geochemistry) and the root mean squared error of prediction (RMSEP) which gives an assessment of how calibrations are likely to perform for the prediction of the geochemical parameters in samples with unknown values (See Naes et al., 2004 for a review). In a final step, the calibration model generated in step 1 (using all available data) was used to predict the geochemistry of any samples, which were truly ‘unknowns’ (e.g. which had no available previously measured geochemistry).

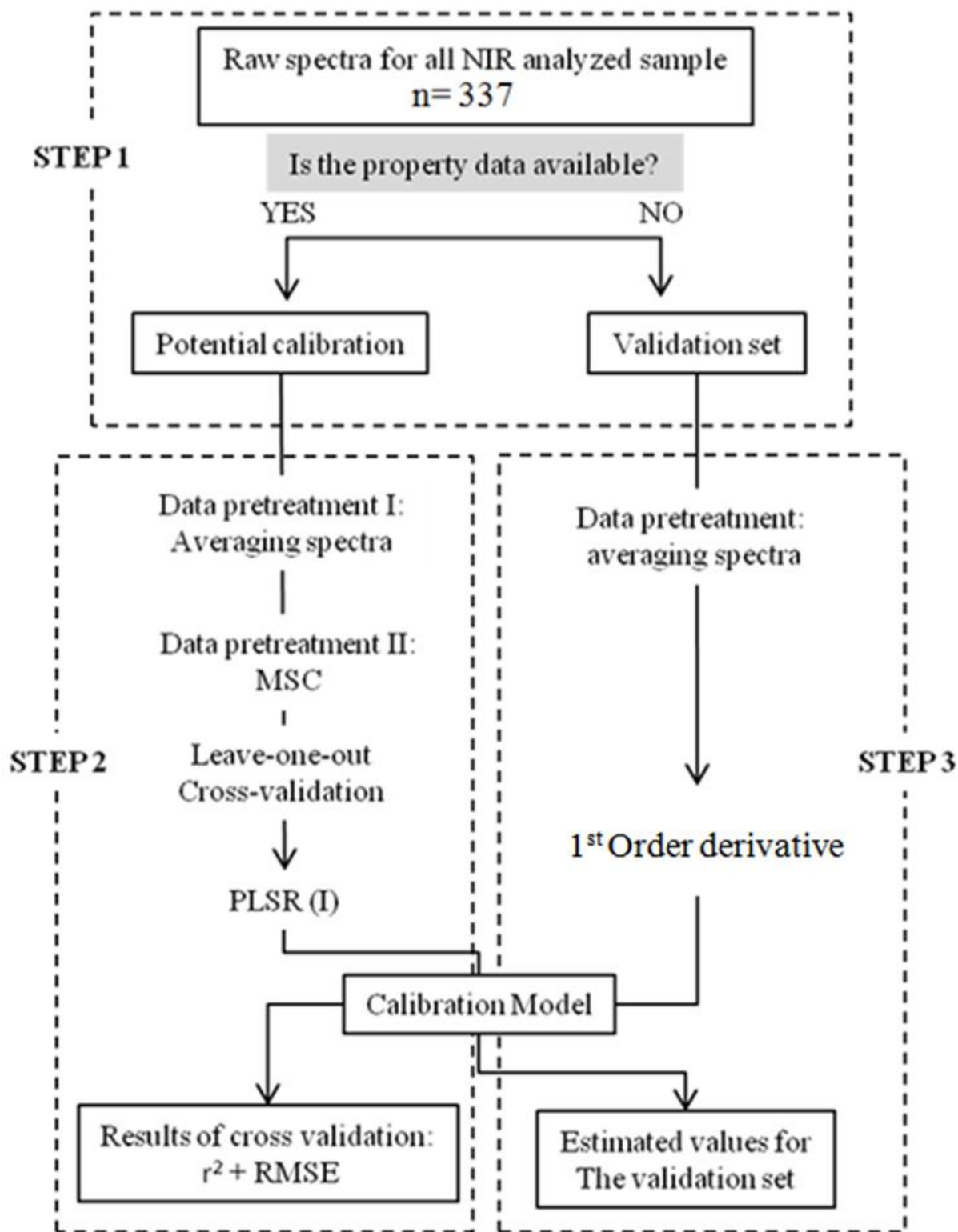


Figure 6. 5: A flow chart summarizing the 3 major steps used for the NIRS-PLSR calibration and validation procedures in this study

Calibration models were built between FT-NIR spectra and the following geochemical parameters:

- Total organic carbon (TOC)
- Total sulphur (TS)
- Total organic sulphur (TOS)

6.3 Results and discussion

6.3.1 Sediment TOC, TS and Organic S Distribution

A total of 373 rock samples have been subjected to TOC analysis using LECO. The TOC data set shows an uneven distribution of TOC that ranges from 0.03 to 18.7 wt%. The TOC values of individual samples with sampled Formations and corresponding locations are given in Appendix A. Figure 6.6 is a histogram of the TOC distribution of all samples. The distribution skewed to the left with most samples plotting in the 1- 3 wt. % range. There are sparse and intermittent distribution between 12 and 19 wt. %.

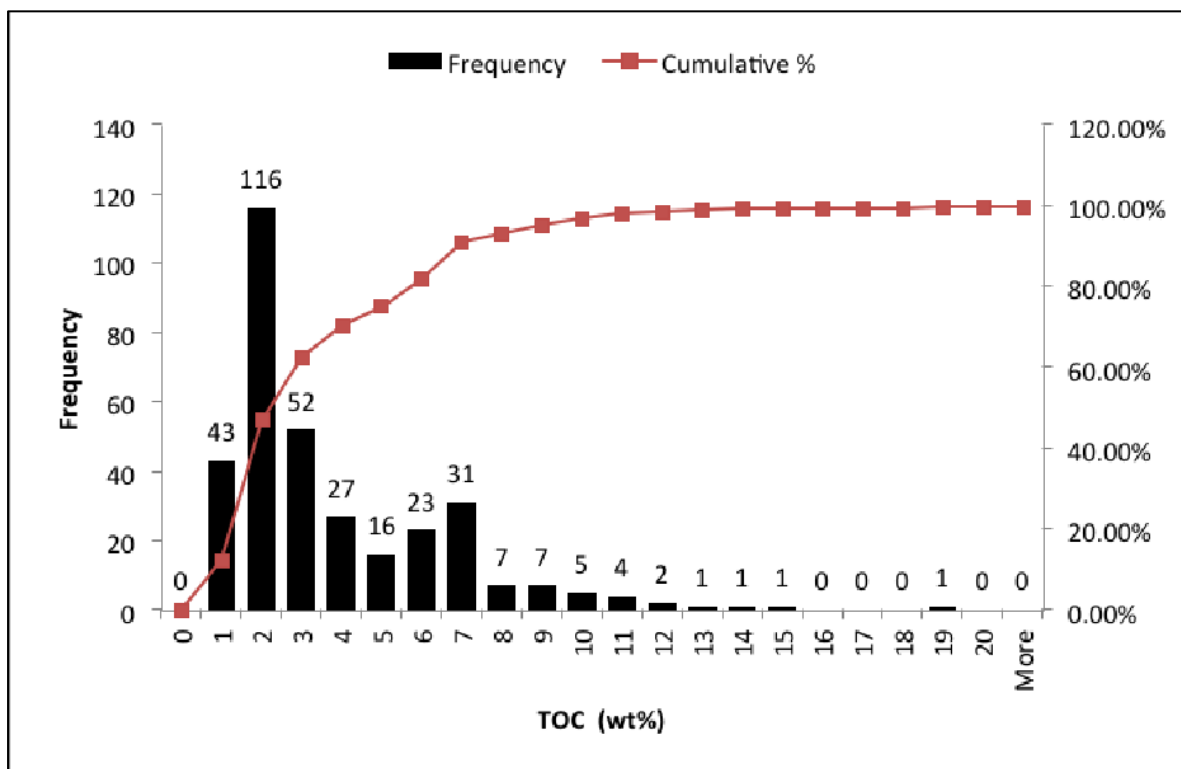


Figure 6. 6: Histogram representing all analyzed sediment TOC concentrations

Table 6. 2: TOC characteristic of all analyzed sediments samples.

ELEMENTARY STATISTICS OF SEDIMENT TOC					
Type	Population	Mean (wt. %)	Standard Deviation (wt. %)	Range (wt. %)	Median (wt. %)
All Samples	337	3.50	2.52	0.30-18.71	2.40
Blue Lias	97	3.92	3.19	0.36-18.71	1.90
Whitby mudstone	96	3.06	2.57	0.30-14.26	2.77
School archive	144	3.1	2.55	0.33- 18.20	2.04

The statistical description of the TS and Pyrite S analysed sediment samples (n=193 excluding the school archived samples) illustrates an uneven distribution of TS wt% with major distribution tilting to the left. Most of the samples plotting in the 3-7 wt% range (figure 6.7). Pyrite S data ranges from 0.00 to 8.25 wt% clustering around the range of 0 to 3 wt%.

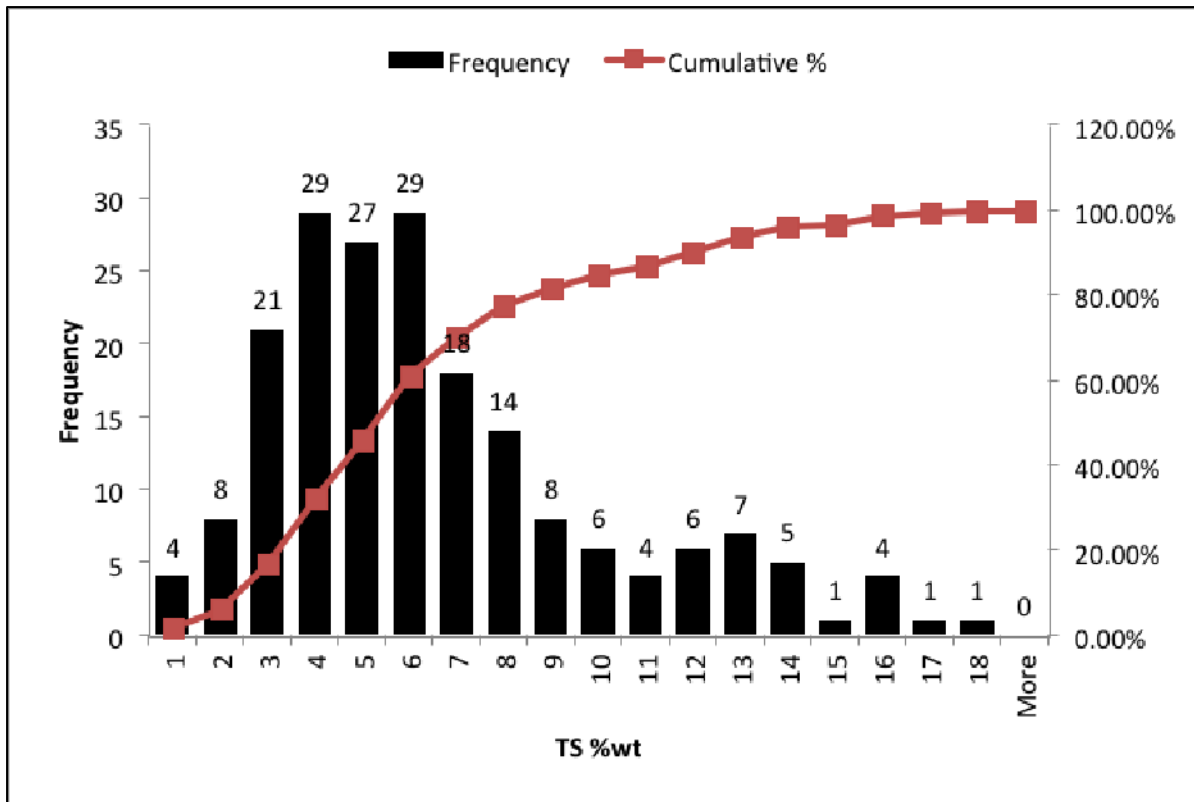


Figure 6. 7: Histogram representing the analyzed sediment TS wt % concentrations.

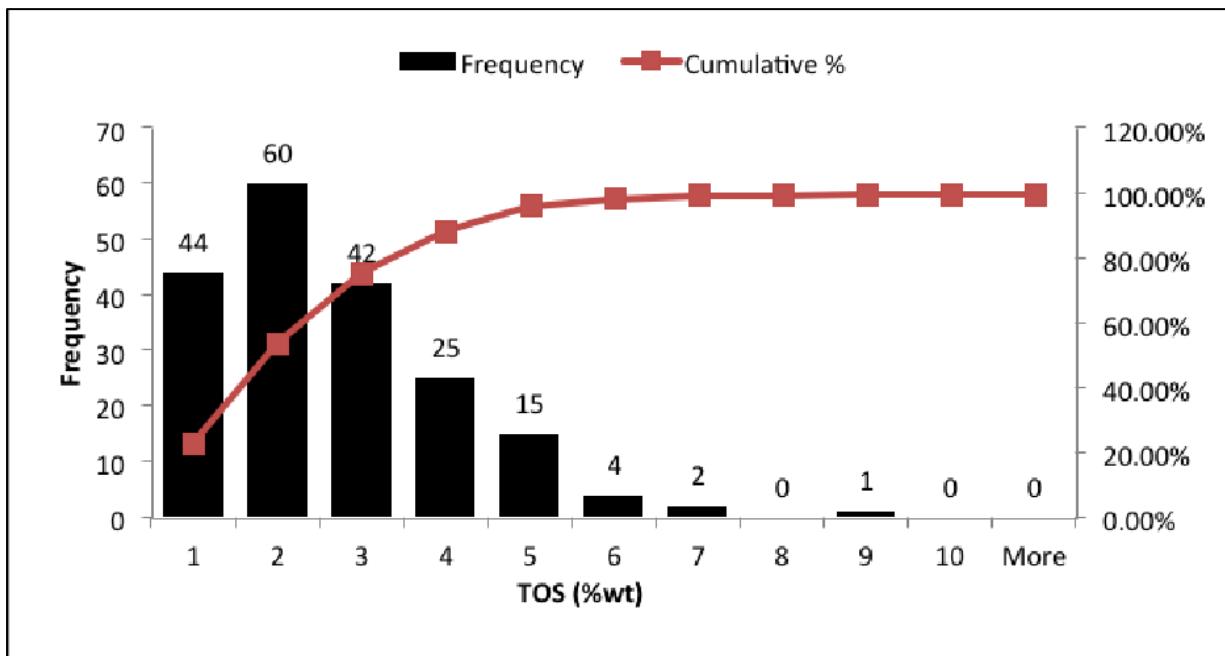


Figure 6. 8: Histogram representing the analysed sediment TOS %wt concentrations

6.3.2 PCA Score plots

Principle Component Analysis was used to construct score plots from all samples provided. The samples are shown in Figure 9 to be mainly distributed along the first Principle Component axis. 16 samples of the archived school set tend to behave differently and are plotted out of the main population.

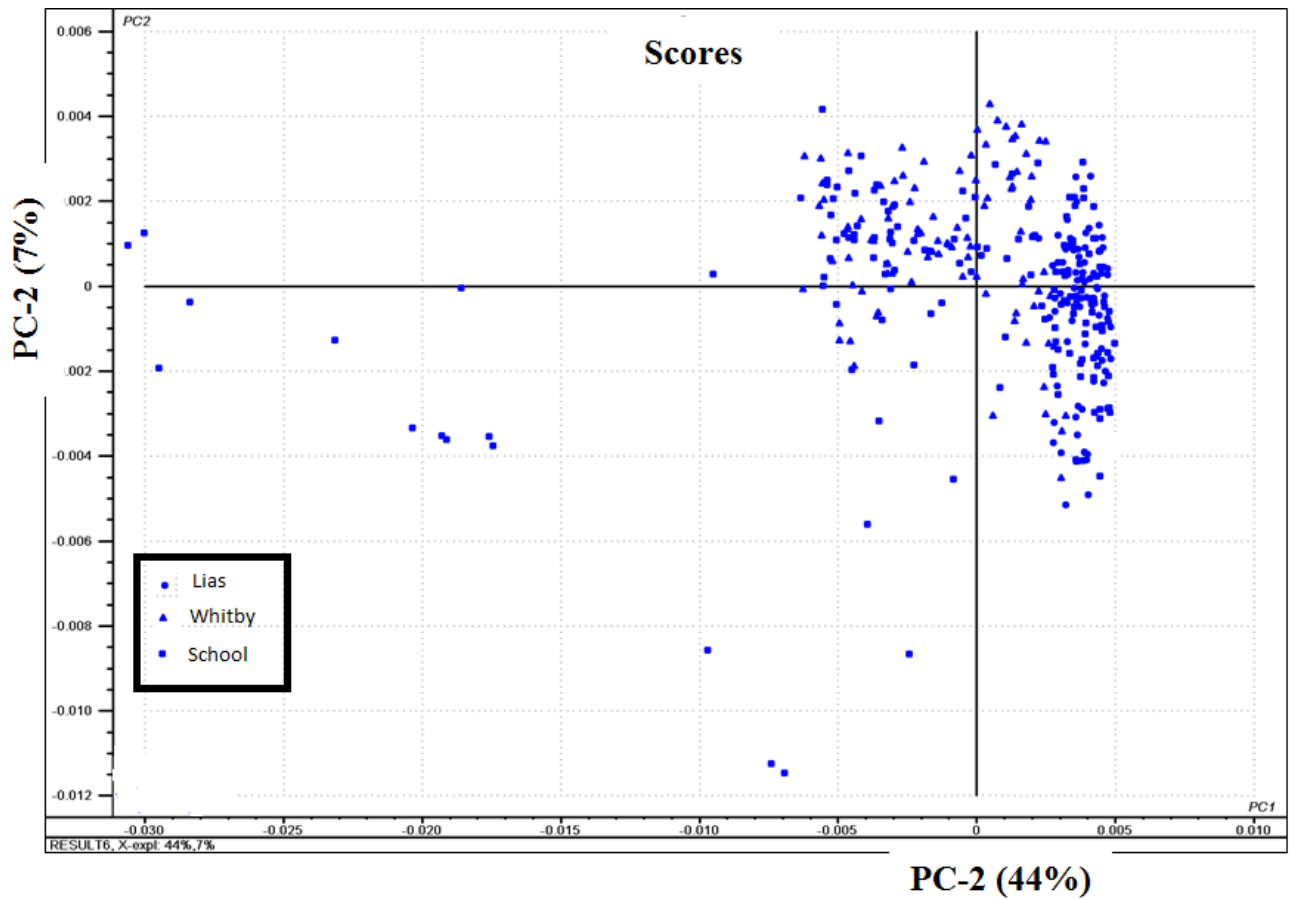


Figure 6.9: PCA scores plot of NIR spectra of all samples

6.3.3 Calibrated Validation Models.

TOC Model

The validation models in Figures 6.11 were produced using PLSR of the TOC %wt data set, developed by selecting the Blue Lias samples as calibration set. It has been tested by “leave on out” cross validation and one sample has been removed as it exceptionally has got very high TOC (sample 26-S2). Any outliers found within the data series were automatically removed from the set by the computer package, and the model refined.

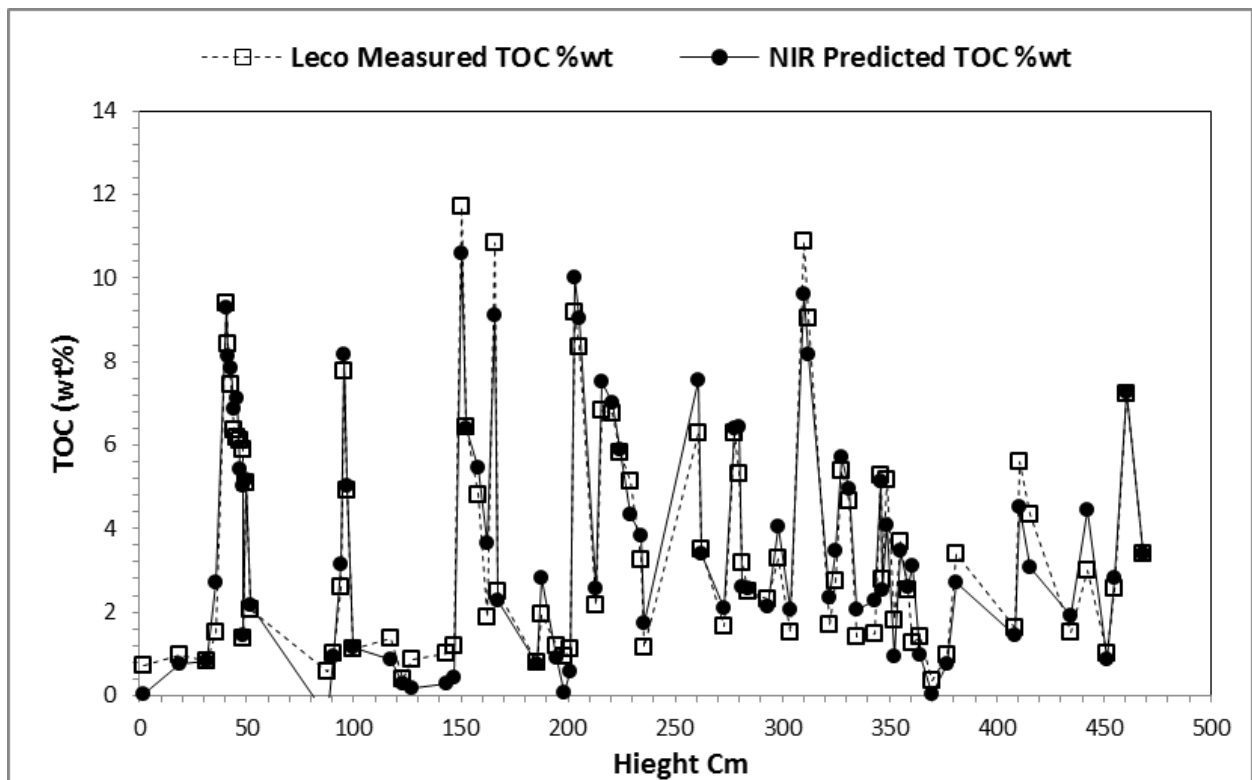


Figure 6.10: Combustion technique measured and FT-NIRS predicted TOC for the Blue Lias samples plotted against the stratigraphic height at the study section

Figure 6.11 shows that the relationship between measuring and predicting the TOC %wt data set provides very strong calibrated validation model with determination coefficient of 93%. Cross validating the data set gives an RMSE of 0.55%.

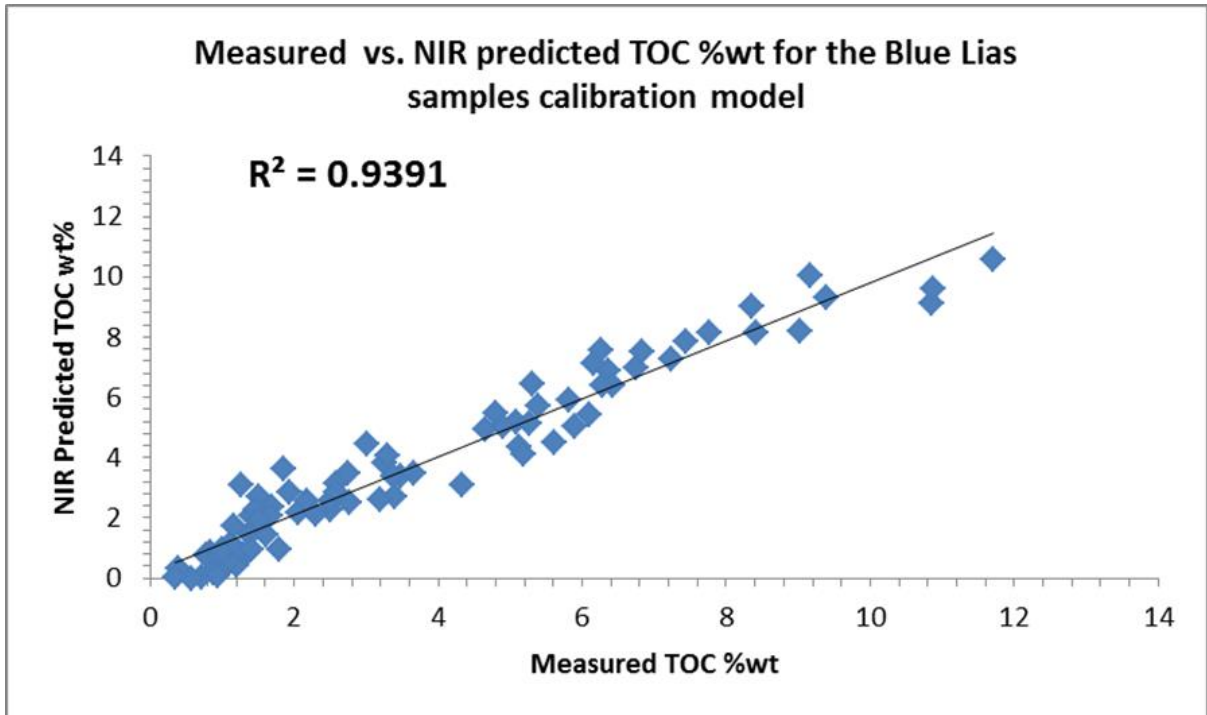


Figure 6. 11: The predicted and measured TOC %wt PLSR relationship for the Blue Lias samples.

TS Model

For the Total sulphur (TS), the Whitby samples were chosen to produce the calibration model. After testing the model by “leave on out” cross validation the XY plot of the measured versus predicted TS% values (figure 6.12) provides very strong calibrated validation model ($R^2 = 0.91$).

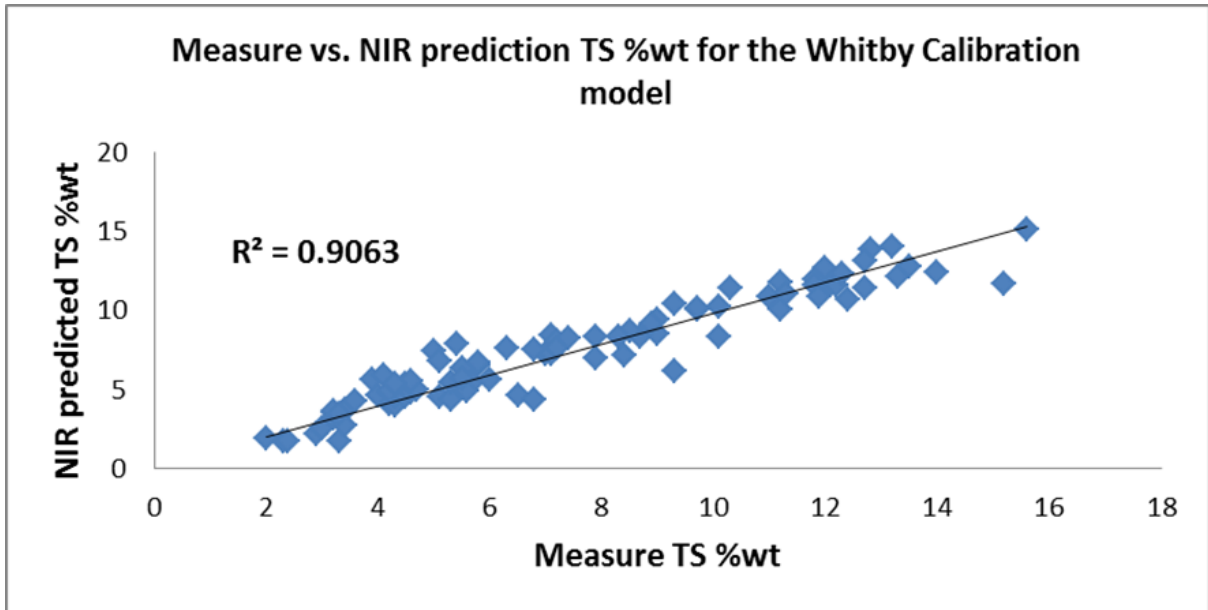


Figure 6. 12: The predicted and measured TS %wt PLSR relationship for the Whitby samples.

TOS Model

The Whitby samples were chosen again to build up the calibration model for predicting Total organic sulphur in the samples. The calibration and validation model for the prediction of TOS wt% is less strongly correlating than that of the other parameters. The relationship between measured and predicted TOS %wt data set provides determination coefficient of 86%.

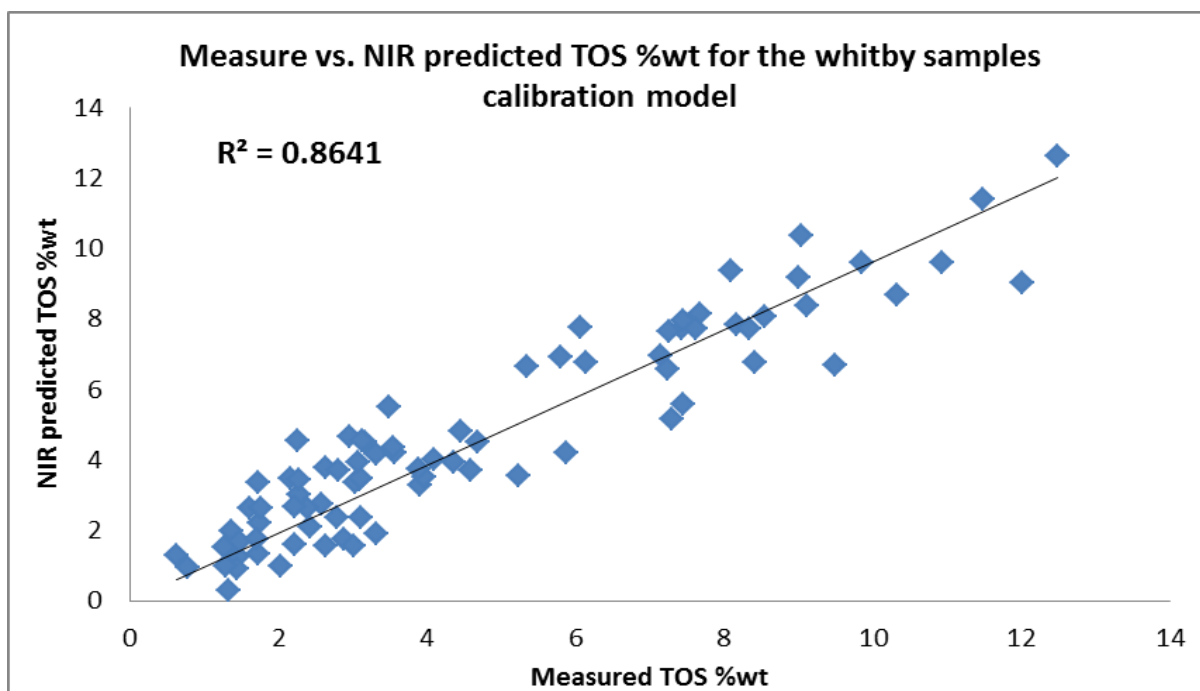


Figure 6. 13: The predicted and measured TOS %wt PLSR relationship for the Whitby samples.

The preliminary calibration models obtained for the individual data set were subjected to PLSR using leave-one out internal cross validation. Overall, the calibrated models suggests a strong relationship between the TOC content of the sample and the information collected from the NIR Spectroscopy indicated from high determination coefficient ($r^2 = 97$) and low root mean square error of the calibration (RMSE = 0.634). The calibration model for the TS and TOS shows good calibration with the NIR Spectra with slightly higher errors (table 6.3).

Table 6. 3: Summary of correlated results

Constituent	Number of samples	R ²	RMSE	Data pre-treatment	Outliers removed from model
TOC (%wt)	97	0.939	0.634	1 st order derivative	13
TS (%wt)	96	0.906	0.643	1 st order derivative	7
TOS (%wt)	96	0.864	1.063	1 st order derivative	7

6.3.4 External Cross Validation

TOC prediction-validation model;

The external cross validation for the optimised calibration model was carried out by splitting the data set (n = 193) into one calibration set (97 sample of the Blue Lias samples) and one validation set (96 samples of the Whitby samples). The latter were selected and predicted as “unknown” samples using the model obtained after subjecting the calibration set to leave-one-out Internal cross validation (Figures 6.14)

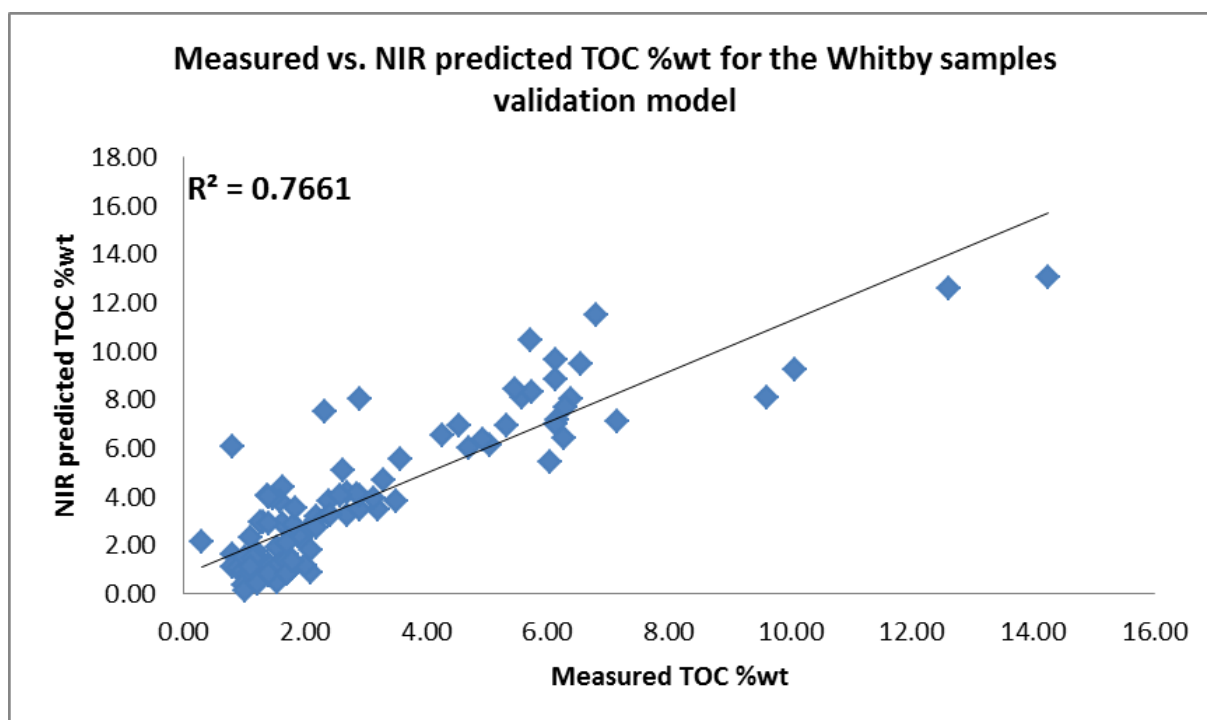


Figure 6. 14: Plot of Leco measured TOC against PLS regressed TOC for the test (validation) set (96 samples) for the Whitby samples.

Using external cross validation, the model shows good prediction for the measured TOC %wt of the Whitby set. Therefore, the determination coefficient of 0.77 indicates that the FT-NIR scanning method has potential for determining the TOC, at least in this case.

Applying the same calibration model to predict various samples (variation in term of lithology, richness and geological age) showed poor prediction with determination coefficient of 0.50 (Figure 6.16), suggesting weaker ability of the FT-NIR scanning method to predict TOC values for ancient sediment samples despite being of similar range of TOC.

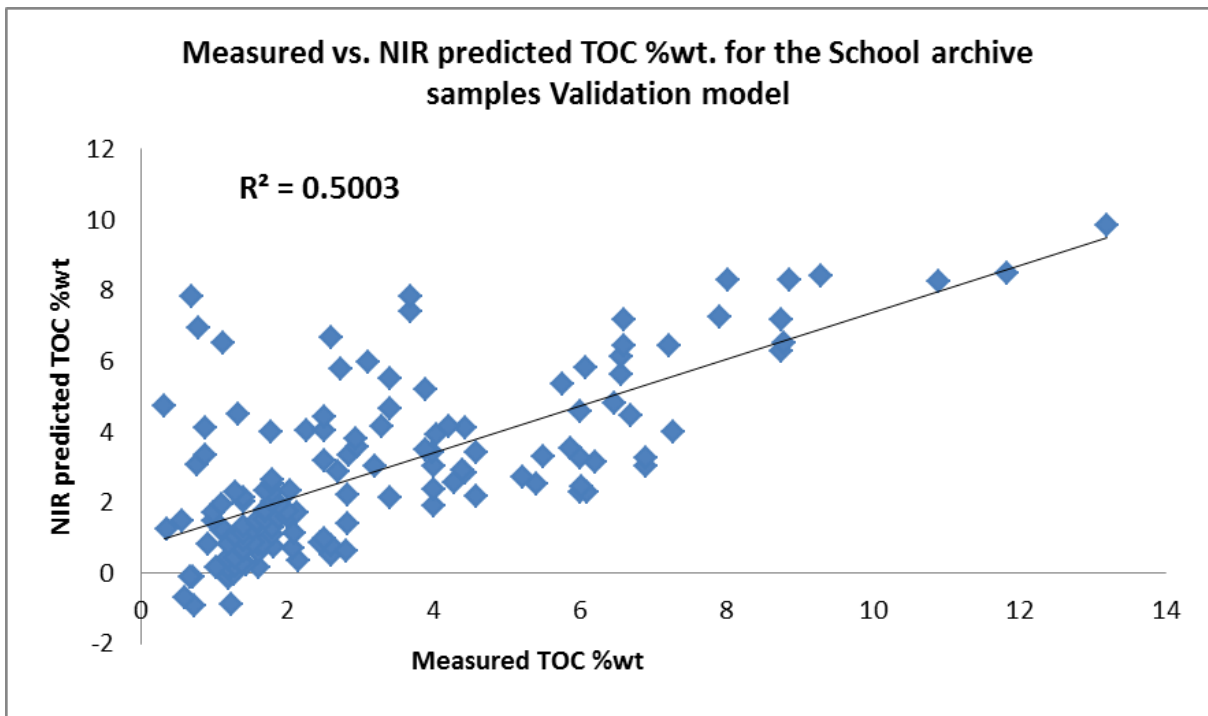


Figure 6. 15: Plot of Leco measured TOC against PLS regressed TOC for the test (validation) set (144 samples) for the School archived samples

TS prediction-validation model;

The optimised calibration model for TS is used to predict the 97 samples of the Blue Lias. The predicted values for the TS from this model are good indicated from the determination coefficient of 0.77 between the measured and predicted values.

The Whitby samples set is characterised with high TS values where most of the the TS values are above 2% wt. Therefor, when the model is used to predict the Blue lias set of sample which has some very low TS values (<2% wt) the predicted results show consist higer values compare to the real measurments using the traditional techniques. In order to minimise this effect a linear equation for the measured and predicted values is obtained ($y=0.9093x+6.0364$) and the offsect is minimized (Figure 6.16).

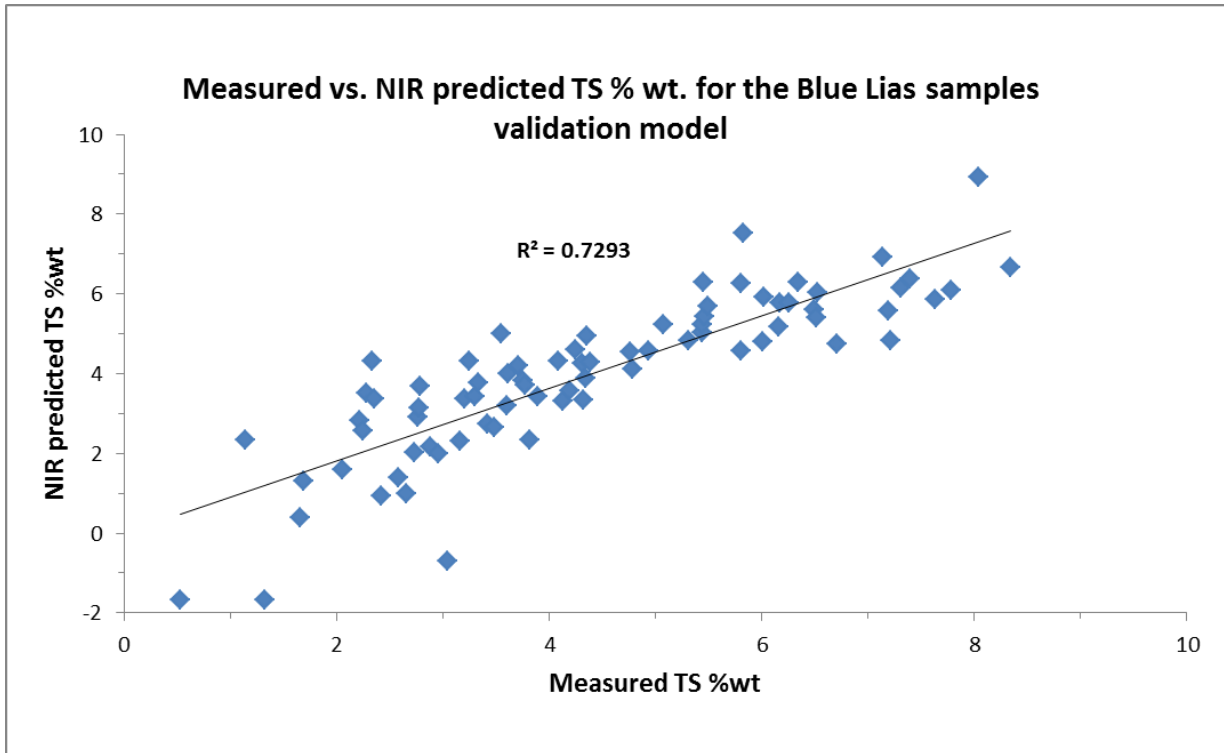


Figure 6.16: Plot of Leco measured TS against PLS regressed T for the test (validation) set (97 samples) for the Blue Lias samples.

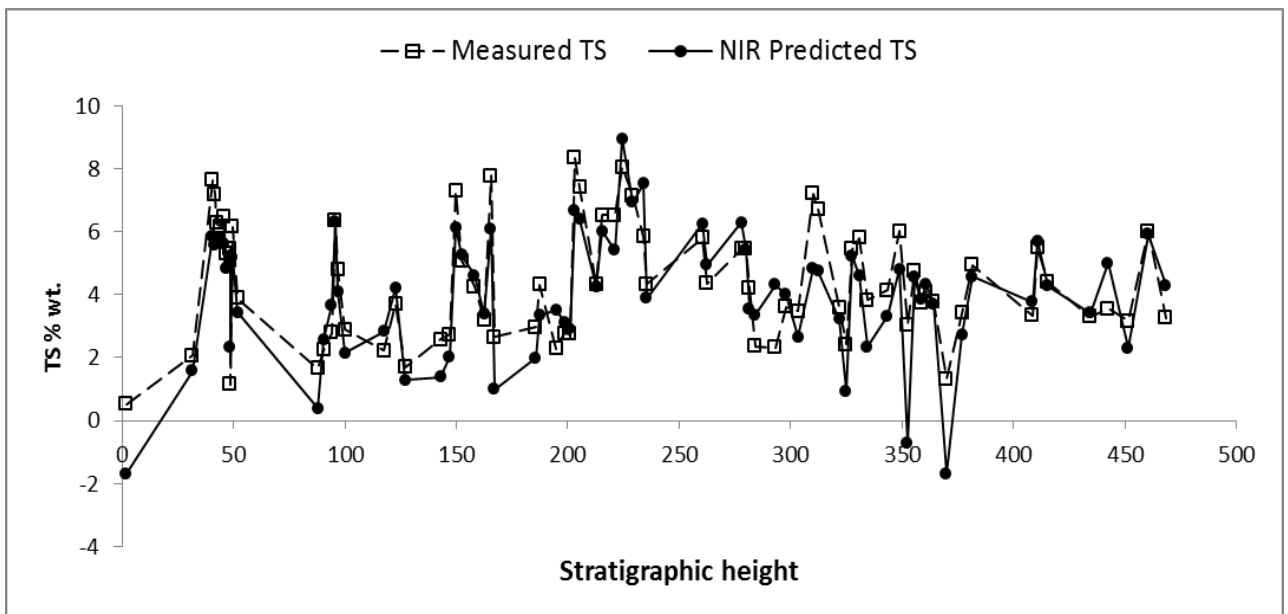


Figure 6.17: Combustion technique measured and FT-NIRS predicted TS for the Blue Lias samples plotted against the stratigraphic height at the study section

TOS prediction-validation model;

The prediction of the TOS using the optimized calibrated model showed very poor results, where the predicted TOS values which obtained using this model dose not correlation well with the measured values giving a determination coefficient of 0.35 (Figure 6.18)

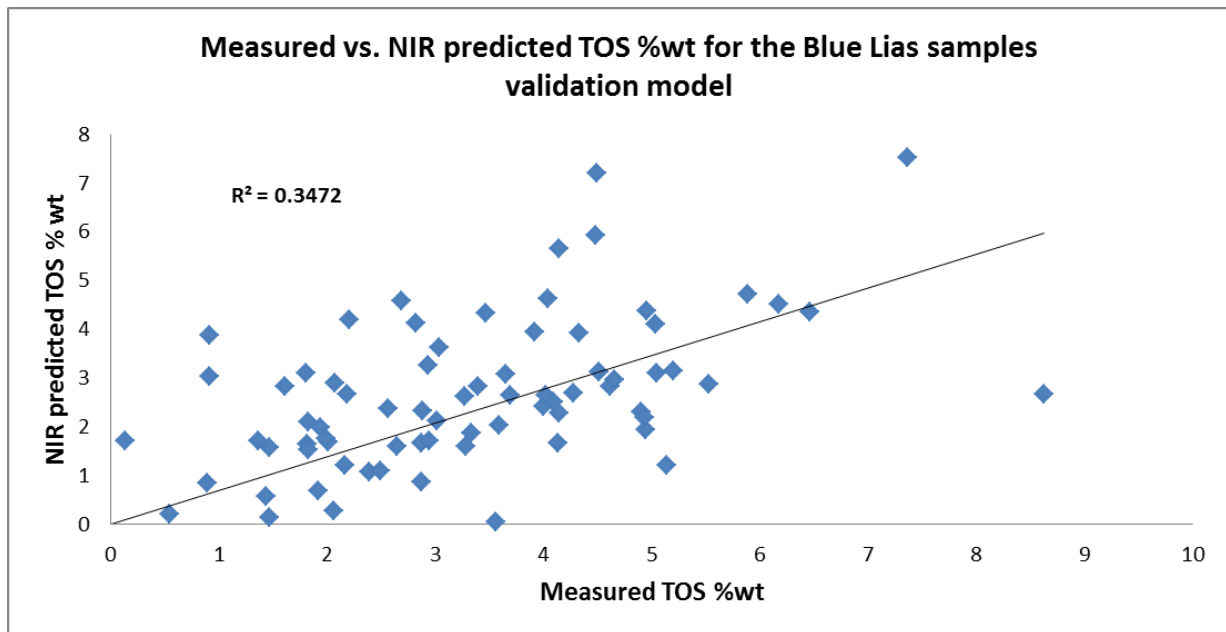


Figure 6.18: Plot of Leco measured TOS against PLS regressed T for the test (validation) set (97 samples) for the Blue Lias samples.

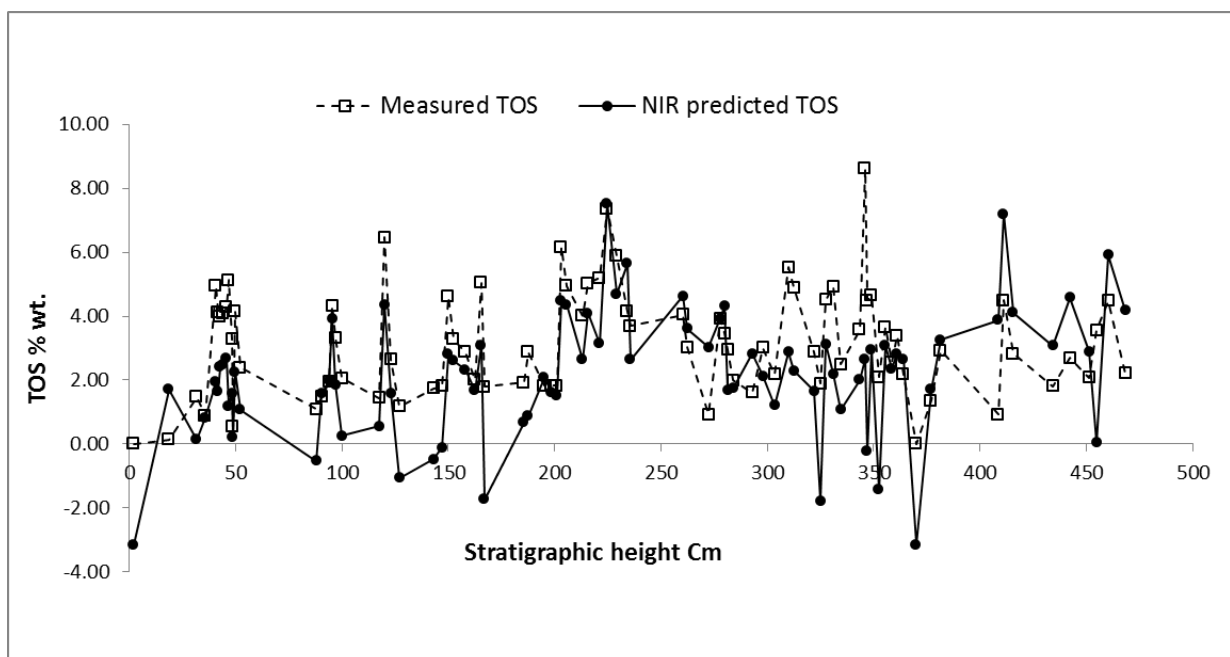


Figure 6.19: Combustion technique measured and FT-NIRS predicted TOS for the Blue Lias samples plotted against the stratigraphic height at the study section.

In general, the evaluation of FT-NIR calibration models was based on the correlation coefficient (r^2) and RMSE. For industry applications, calibrations are expected to generate r^2 of 0.98 or more, but the criteria for evaluating the success of sediment or soil samples have not been developed (Cheng et al., 2005). However, due to the complicated nature of the sediment samples, the evaluating criteria for r^2 are expected to be lower than industry application. The results showed that FT-NIR was able to predict the TOC ($r^2 = 0.76$) when it applied to similar set of sediment samples. Although TOC is a primary property (holding direct response to the NIR) in soils and sediments (Leach et al., 2008), it could not be accurately estimated for ancient sediment samples from different locations ($r^2 = 0.50$). Acceptable cross-validation results were also obtained in the prediction of TS ($r^2 = 0.77$). On the other hand, the FT-NIR could not be able to estimate the TOS accurately in this study ($r^2 = 0.35$).

This study focused on the development of a tool for routine characterisation of TOC, TS and TOS in sediment which was achieved with DRIFT technique using the NIR region of electromagnetic spectrum. Despite the successful optimisation of a NIR-DRIFT-PLS model for the TOC data when applied on similar set of samples, some low areas were observed where further development would be required to achieve desirable results. Firstly, the optimised model for the TOC used data set with highest value of about 12 wt. % because of the scanty nature of the data above this value. This impacted the predictive ability of the model, as values above this threshold were poorly predicted. For the TS optimised model, the TS values for the Whitby samples set were all above 2 wt. %. Therefore using this model to predict lower values will not be very accurate.

6.4 CONCLUSION

- This study has demonstrated the robustness of the combination of Reflection-FT-IRS and PLSR as a viable replacement technique for Leco analytical method in the quantification of sediment TOC concentration and could be potential to measure TS as well. By analysing a large set of shale and mudstones sample using NIRS, and comparing the spectral output with the same data provided by conventional methods, the level of correlation between the predicted NIR values and the conventionally measured known values was quantified.
- The evaluation of the calibration models constructed from the spectral data obtained from the analysis of 193 Shale samples collected from Dorset and Staithes using FT-NIR-PLS assured that this technique could be potential screening tool to predict organic carbon content of ancient sediments.
- Although FT-NIR estimated the TS with acceptable accuracy, there is not direct affect for the TS on the NIR spectra and more study is needed to understand it.
- Despite that, TOC has been successfully estimated by FT-NIR in soils and sediments, it application to estimate the TOC on ancient sediments characterised with different geological and geochemical properties could not be accurately estimated in this study. To improve the models, the number of samples analysed could be increased, or the range over which they preside reduced

CHAPTER 7 – SUMMARY AND OUTLOOK

The overall aim of the research presented in this thesis has been to increase knowledge and understanding of the paleoredox changes at the Lower Whitby Mudstone Formation of the Cleveland Basin in North Yorkshire, which is a world renowned location for the Early Toarcian (T-OAE). Most previous work has been on the Upper *semicelatum* and *exaratum* subzone where TOC concentrations are highest (the putative T-OAE). Few studies have explored the well-preserved sediments below this event that document the interval leading to large-scale (global) anoxia, which is the focus of this project. Very intensive geochemical analysis was carried out to investigate in details the underlying Grey Shale Member at cm-scale resolution and concluded the following:

- The lower and middle part of the Grey Shale Member were deposited during marine transgression and represent change in the shale facies from normal facies that dominated the Cleveland Ironstone Formations below to restricted shale facies with higher organic content (average TOC = 1.63 wt%). The kerogen has a mixed type II and type III composition, with a mean Hydrogen Index value of 243.8 (mgHC/gTOC). Optically this interval is characterised by some terrestrial contribution up to 25% of the total kerogen assemblage. Despite the different TOC values observed in the sulphur bands compare to the surrounding bioturbated mudstone units, the relative ratio of the main kerogen categories are similar compare to that observed in the Jet Rock Shale.
- The Upper part of the Grey Shale (top laminated unit) and the Jet Rock Shale (the putative T-OAE) were characterised by very high TOC content (up to 14.3) with an average of 7.1 (wt%). The kerogen has Type II composition, with a mean Hydrogen Index of 392 (mgHC/gTOC). Optically this interval is characterised by a dominance of AOM (almost 95% of the total kerogen content), terrestrial components (phytoclads and palynomorphs) are consistently very low. According to the blue light fluorescence study, the organic matter within the Upper *semicelatum* and *exaratum* subzone is well preserved while below this interval the organic matter is biodegraded

and poorly preserved except within the Sulphur bands where the organic matter is less biodegraded and shows a moderate degree of fluorescence.

- The biomarker analysis of the saturated hydrocarbon showed that the Carbon Preference Index (CPI) values and the measurements of the stereoisomeric ratios ($22S/22S+22R$ for C32 hopanes and $20S/20S+20R$ for regular steranes) of the extended hopanes and steranes series indicate that the sediments studied have reached a level of thermal maturity that approaches the oil window.
- The high TOC contents of the *exaratum* subzone (Jet Rock Shale) is coupled with the well-developed lamination, very fluorescent nature of the organic matter and low pristane/Phytane ratios and consistent Isorenieratane presence with relatively high concentration (up to 93 ng/ μ gTOC) suggesting anoxic stratified water condition that prevailed during the deposition of these shales, with free sulphide being present in the photic zone (Photic Zone Anoxia).
- The Grey Shale Member represents an important marine sedimentary record of a gradual transition from an oxygenated sea to one characterized by anoxic bottom waters. These intervals of oxic and anoxic deposition for the Grey Shale are characterized by the deposition of three pyrite rich black shales of the Sulphur Bands, which indicates deposition under anoxic bottom water conditions. Despite the well laminated appearance of these Sulphur Bands, very detailed analysis indicates that there are fluctuations in the paleoredox conditions across these units, cycling between dysoxic, anoxic and euxinic conditions.
- At the lower part of the Grey shale, the bioturbated mudstone intervals surrounding the Sulphur Bands are characterized with Fe_{Py}/Fe_{HR} less than the Upper limit of ferruginous condition (≤ 0.7) and Fe_{HR}/Fe_T above the threshold of anoxic condition (0.38). The presence of bioturbation indicates that bottom waters were periodically oxic, with strong mixing of water column signals for Fe_{HR} and trace metals. Therefore the sequence of mudstone and Sulphur Band deposition throughout the Grey Shales can be described by a seasonal oxic/dysoxic fluctuation model coupled to gradual climatic warming and fluctuations in sediment supply.

- The Sulphur Bands represent repetitive short periods of intense oceanic anoxia (often euxinic) occurred preceding the global T-OAE. These short periods of anoxia were localised in occurrence, with potentially catastrophic effects on marine biology. There is lateral variation in the redox condition of the Lower Sulphur Band between Port Mulgrave and Hawsker Bottom section.
- The transition boundary of the Pleinsbachian-Toarcian in this study characterised with a sharp negative $\delta^{13}\text{C}_{\text{org}}$ isotope excursions of somewhat complex character and with a magnitude of up to ~ -4 ‰. These excursions are recorded in the Sulphur Bands which could suggest stages of increased palaeotemperature which of course needs further investigations. This excursion across the Pleinsbachian–Toarcian boundary at North Yorkshire in Cleveland Basin can be correlated with a similar phenomenon of lesser magnitude in the carbonate sedimentary record from coastal Portugal, suggesting a perturbation in the carbon cycle synchronous on at least a regional scale.
- The patterns of enrichments of trace elements in black shales have been described based on their reactivity under different redox conditions, with notable trace metal enrichments (Mo) and presence of isorenieratane recorded for the LSB at Port Mulgrave due to more sulphide in the water column, in contrast to lower enrichment of these trace metals and the absence of isorenieratane at Hawsker Bottoms.
- The Sulphur Bands are characterised with high ratio of Mo/TOC compare to the Jet Rock Shales. Plotting the Mo (ppm) values against the TOC (wt%) suggesting that the Sulphur Bands was associated with less restriction while the Jet Rock Shale represent a time of maximum restriction.
- The development of and intensity of redox conditions across the Basin preceding the T-OAE could have been caused by a combination of restriction on circulation, coupled with local density stratification. Wide spreading of anoxia higher up across

the T-OAE could represent more global forcing mechanisms which were capable of driving global environmental change. These mechanisms may have included; the eruption of the Karoo-Ferrar continental flood basalt and/or the massive dissociation of continental margin clathrates with a resulting increased hydrological cycle and a transient greenhouse climate with increased CO₂ concentrations and paleotemperatures.

- Despite the successful application of FT-NIR Spectroscopy to measure the total organic content (TOC), this study showed relatively poor results. Especially when applying the technique on ancient sediments from wider range of depositional environments.

Future work

- One of the future goals to integrate this thesis is to study the Pleinsbachian-Toarcian boundary in details at another locations at more regional scale in order to understand more any influence of any global processes that could triggered the carbon cycle at this transition boundary
- Reconstructing the palaeotemperature record from the Late Pliensbachian–Early Toarcian interval could be used to decipher which mechanism is the most applicable to this carbon isotopic excursion at the stage boundary, since massive methane dissociation should be associated with a temperature maximum (as is seen at the Palaeocene–Eocene Thermal Maximum). There for intensive study applying plaeotemperature parameters (e.g Oxygen-isotope analysis) is recommended.

REFERENCES

- Alaoui G., Leger M. N., Gagne J. and Tremblay L. (2011) Assessment of Estuarine Sediment and Sedimentary Organic Matter Properties by Infrared Reflectance Spectroscopy. *Chemical Geology* **286**, 290-300
- Algeo T. J. and Maynard J. B. (2004) Trace-element behaviour and redox facies in core shales of Upper Pennsylvanian Kansas-type cyclotherms. *Chemical Geology* **206**, 289-318
- Algeo T. J. and Lyons T. W. (2006) Mo-total organic carbon covariation in modern anoxic marine environments: Implication for analysis of paleoredox and paleohydrographic conditions. *Paleoceanography* **21**, 1016-1029
- Algeo T. J. and Rowe H. (2011) Paleooceanographic applications of trace-metal concentration data. *Chemical Geology* **325**, 6-18
- Aller R. C., Mackin J. E. and Cox R. T. (1986) Diagenesis of Fe and S in Amazon inner shelf muds - apparent dominance of Fe reduction and implications for the genesis of ironstones. *Continental Shelf Research* **6**, 263-289
- Al-suwaidi A. H., Angelozzi G. N., Baudin F., Damborenea S. E., Hesselbo S. P., Jenkyns H. C., Mancenido M. O. and Riccardi A. C. (2010) First record of the Early Toarcian Oceanic Anoxic Event from the Southern Hemisphere, Neuquen Basin, Argentina. *Journal of the Geological Society London* **167**, 633-636
- Andres J. M. and Bona M. T. (2005) Analysis of coal by diffuse reflectance near-infrared spectroscopy. *Analytica Chimica Acta* **535**, 123-132
- Anderson T. F. and Raiswell R. (2004) Sources and mechanisms for the enrichment of highly reactive iron in euxinic Black Sea sediments. *American Journal of Science* **304**, 203-233
- Arens N. C. and Jahre A. H. (2000) Carbon isotope excursion in atmospheric CO₂ at the Cretaceous-Tertiary Boundary: Evidence from terrestrial sediments. *Palaios* **15**, 314-322
- Armstrong H. A., Turner B. R., Makhlof I. M., Weedon G. P., Williams M., Al Smadi A. and Abu Salah A. (2005) Origin, sequence stratigraphy and depositional environment of an upper Ordovician (Hirnantian) deglacial black shale, Jordan. *Palaeogeography, Palaeoclimatology, Palaeoecology* **220**, 273-289
- Arthur M. A. and Sageman B. B. (1994) Marine black shales – depositional mechanisms and environments of ancient-deposits. *Annual Review of Earth and Planetary Sciences* **22**, 499-551
- Bailey T. R., Rosenthal Y., McArthur J. M., van dea Schootbrugge B. and Thirlwall M. F. (2003) Paleooceanographic changes of the late Pliensbachian-Early Toarcian interval: a possible link to the genesis of an Oceanic Anoxic Event. *Earth and Planetary science letters* **212**, 307-320

- Ballard B. D. (2007) Quantitative Mineralogy of Reservoir Rocks using Fourier Transform Infrared Spectroscopy. *Society of Petroleum Engineers- 113023-STU*
- Balsam W. L. and Deaton B. C. (1996) Determining the composition of late Quaternary marine sediments from NUV, VIS, and NIR diffuse reflectance spectra. *Marine Geology* **134**, 31-55
- Barling J., Arnold G. L. and Anbar A. D. (2001) Natural mass-dependent variations in the isotopic composition of molybdenum. *Earth and Planetary Science Letters* **193**, 447–457
- Berner R. A. and Raiswell R. (1983) Burial of organic-carbon and pyrite sulfur in sediments over Phanerozoic time - a new theory. *Geochimica et Cosmochimica Acta* **47**, 855-862
- Berner R. A. (1980) Early diagenesis: A theoretical approach. *Princeton University Press*, Princeton, NJ
- Berner R. A. and Raiswell R. (1984) C/S Method for distinguishing fresh-water from marine sedimentary rocks. *Geology* **12**, 365-368
- Bertrand P. and Lallierverges E. (1993) Past sedimentary organic-matter accumulation and degradation controlled by productivity. *Nature* **364**, 786-788
- Bokobza L. (2002) Origins of Near- Infrared Absorption Bands. In: SIESLER, H.W., OZAKI, Y., KAWATA, S. & HEISE, H.M (eds) *Near Infrared Spectroscopy: Principles, Instruments, Applications*, WILEY-VCH, Weinheim, p11-39
- Boon J. J., Hines H., Burlingame A. L., Klok J., Rijpstra W. I. C., Leeuw J. W. Edmunds K. E. and Eglinton G. (1983) Organic geochemical studies of Solar Lake laminated cyanobacterial mats. In *Advances in Organic Geochemistry*, 207-227
- Bordenave M. L. (1993) Applied petroleum geochemistry, Imprimerie Nouvelle, Paris, 524
- Bottcher M. E. and Lepland A. (2000) Biogeochemistry of sulfur in a sediment core from the west-central Baltic Sea: Evidence from stable isotopes and pyrite textures. *Journal of Marine Systems* **25**, 299-312
- Bowden S. A., Farrimond P., Snape C. E. and Love G. D. (2006) Compositional differences in biomarker constituents of the hydrocarbon, resin, asphaltene and kerogen fractions: An Example from the Jet Rock (Yorkshire, UK). *Organic Geochemistry* **37**, 369 – 383
- Brassell S. C., Eglinton G., Marlowe I. T., Pflaumann U. and Samthein M. (1986) Molecular stratigraphy: A new tool for climatic assessment. *Nature* **320**, 129-133
- Breen C., Clegg F., Herron M. M., Hild G. P., Hillier S., Hughes T. L., Jones T. G. J., Matteson A. and Yarwood J. (2008) Bulk Mineralogical Characterisation of Oil field

Reservoir Rocks and Sandstone using Diffuse Reflectance Infrared Transform Fourier Spectroscopy and Partial Least Square analysis. *Journal of petroleum science and engineering* **60**, 1-17

- Brocks J. J., Love G. D., Summons R. E., Knoll A. H., Logan G. A. and Bowden S. A. (2005) Biomarker evidence for green and purple sulphur bacteria in a stratified Palaeoproterozoic sea. *Nature*, **437**, 866-870
- Brumsack H. J. (2006) The trace metal content of recent organic carbon-rich sediments: implications for Cretaceous black shale formation. *Palaeogeography, palaeoclimatology, palaeoecology* **232**, 344-361
- Buesseler K. O., Livingston H. D., and Casso S. A. (1991) Mixing between oxic and anoxic waters of the Black Sea as traced by Chernobyl caesium isotopes. *Deep-Sea Research Part A - Oceanographic Research Papers* **38**, 725-745
- Butler I. B. and Rickard D. (2000) Framboidal pyrite formation via the oxidation of iron (II) monosulfide by hydrogen sulphide. *Geochimica et Cosmochimica Acta* **64**, 2665-2672
- Calvert S. E. and Karlin R. E. (1991) Relationships between sulfur, organic carbon, and iron in the modern sediments of the Black Sea. *Geochimica et Cosmochimica Acta* **55**, 2483-2490
- Calvert S. E. and Pedersen T. F. (1993) Geochemistry of recent oxic and anoxic marine sediments: Implications for the geological record. *Marine Geology* **133**, 67-88
- Calvert S. E., Pedersen T. F., Naidu P. D. and von Stackelberg U. (1995) On the organic-carbon maximum on the continental slope of the eastern Arabian Sea. *Journal of Marine Research* **53**, 269-296
- Canfield D. E. (1989a) Sulfate reduction and oxic respiration in marine-sediments - Implications for organic-carbon preservation in euxinic environments. *Deep-Sea Research Part A - Oceanographic Research Papers* **36**, 121-138
- Canfield D. E. (1989b) Reactive iron in marine sediments. *Geochimica et Cosmochimica Acta* **53**, 619-632
- Canfield D. E., Lyons T.W. and Raiswell R. (1996) A model for iron deposition to euxinic Black Sea sediments. *American Journal of Science* **296**, 818-834
- Canfield D. E., Poulton S. W., and Narbonne G. M. (2007) Late-Neoproterozoic deep-ocean oxygenation and the rise of animal life. *Sciences* **315**, 92-95
- Canfield D. E., Poulton S. W., Knoll A. H., Narbonne G. M., Ross G., Goldberg T. and Strauss H. (2008) Ferruginous conditions dominated later Neoproterozoic deep-water chemistry. *Science* **321**, 949-952
- Canfield D. E., Raiswell R. and Bottrell S. (1992) The reactivity of sedimentary iron mineral toward sulphide. *American Journal of Science* **292**, 659-683

- Canfield D. E., Raiswell R. Westrich J. T., Reaves C. M. and Berner R. A. (1986) The use of Chromium reduction in the analysis of reduced inorganic sulfur in sediments and shales. *Chemical Geology* **54**, 149-155
- Canfield D. E. and Thamdrup B. (2009) Towards a consistent classification scheme for geochemical environments, or, why we wish the term 'suboxic' would go away. *Geobiology* **7**, 385-392
- Caswell B. A., Coe A. L. and Cohen A. S. (2008) New range data for marine invertebrate species across the early Toarcian (Early Jurassic) mass extinction. *Journal of the Geological Society, London* **166**, 859-872
- Chang C., You C., Huang C. and Lee T. (2005) Rapid determination of chemical and physical properties in marine sediment using a near-infrared reflectance spectroscopic technique. *Applied Geochemistry* **20**, 1637-1647
- Chen J., Luo P. and Li J. (1986) Using kerogen FTIR parameters for determination of organic facies. *Chinese Science Bulletin* **43**, 681 – 684
- Chowns T. M. (1966) Depositional environment of the Cleveland Ironstone series. *Nature* **21**, 1286-1287
- Clark J. P. and Philp R. P. (1989) Geochemical characterisation of evaporite and carbonate depositional environments and correlation of associated crude oils in the Black Creek Basin, Alberta. *Bulletin of Canadian Petroleum Geology* **37**, 401–416
- Cohen A. S., Coe A. L. and Kemp D. B. (2007) The Late Palaeocene_Early Eocene and Toarcian (Early Jurassic) carbon isotope excursions: a comparison of their time scales, associated environmental changes, causes and consequences. *Journal of the Geological Society* **164**, 1093-1108
- Crusius J., Calvert S., Pedersen T. and Sage D. (1996) Rhenium and molybdenum enrichments in sediments as indicators of oxic, suboxic, and sulfidic conditions of deposition. *Earth and Planetary Science Letters* **145**, 65–78
- Cutter G. A. and Kluckhohn R. S. (1999) The cycling of particulate carbon, nitrogen, sulfur, and sulfur species (iron monosulfide, greigite, pyrite, and organic sulfur) in the water columns of Framvaren Fjord and the Black Sea. *Marine Chemistry* **67**, 149-160
- Emeis K. C., Angelo C., McKenzie J. A., Rio D. and Sprovieri R. (1991) The occurrence and significance of Pleistocene and Upper Pliocene sapropels in the Tyrrhenian Sea. *Marine Geology* **100**, 155-182
- Deconinck J., Helsebbo S. P., Debuisser N., Averbuch O., Baudin F. and Bessa J. (2003) Environmental Controls on Clay Mineralogy of an Early Jurassic Mudrock (Blue Lias Formation, Southern England). *International Journal of Earth Science* **92**, 255-266
- Demaison G. J. and Moore G. T. (1980) Anoxic environments and oil source bed genesis. *The American Association of Petroleum Geologists Bulletin* **64**, 1179-1209.

- Dickens G. R., Oneil J. R., Rea D. K. and Owen R. M. (1995) Dissociation of oceanic methane hydrate as a cause of the carbon-isotope excursion at the end of the Paleocene. *Paleoceanography* **10**, 965-971
- Didyk B. M., Simoneit B. R. T., Brassell S. C. and Eglinton G. (1978) Organic geochemical indicators of palaeoenvironmental conditions of sedimentation. *Nature* **272**, 216-222
- Duan Y., Wang Z. P., Zhang H., Zhang X. B., Qian Y. R. and Zheng G. D. (2006) Biomarker geochemistry of crude oils from Qaidam basin, northwestern China. *Journal of Petroleum Geology* **29**, 175 - 188
- Duckett S. and Gilbert B. (2000) Foundations of Spectroscopy. *Oxford Science Publications*, Oxford, p 23-33
- Ebukanson E. J. and Kinghorn R. R. F. (1985) Kerogen facies in the major Jurassic mudrock formations of southern England and the implications on the depositional environments of their precursors. *Journal of Petroleum Geology* **8**, 435-462
- Erickson B. E. and Helz G. R. (2000) Molybdenum(VI) speciation in sulfidic waters: stability and lability of thiomolybdates. *Geochimica et Cosmochimica Acta* **64**, 1149–1158
- Esbensen K. H., Guyot D., Westad F. and Houmoller L. P. (2002) Multivariate Data Analysis: In Practice: An Introduction to Multivariate Data Analysis and Experimental Design, 5th Edition. *Aalborg University* 105 – 279
- Espitalie J., Madec M. and Tissot B. (1980) Role of mineral matrix in kerogen pyrolysis: Influence on petroleum generation and migration. *American Association of Petroleum Geologist Bulletin* **64**, 59-66
- Farrimond P., Eglinton G. and Brassell S. C. (1989) Toarcian anoxic event in Europe: An organic geochemical study. *Marine and Petroleum Geology* **6**, 136-147
- Farrimond P., Stoddart D. P. and Jenkyns H. C. (1994) An organic geochemical profile of the Toarcian anoxic event in northern Italy. *Chemical Geology* **111**, 17-33
- Frimmel A., Oschmann W. and Schwark L. (2004) Chemostratigraphy of the Posidonia Black Shale, SW Germany I. Influence of sea-level variation on organic facies evolution. *Chemical Geology* **206**, 199–230
- Froelich P. N. (1979) Marine phosphorus geochemistry. Ph.D. thesis, University of Rhode Island, Kingston, 322p
- Frost R. L. and Johansson U. (1998) Combination bands in the infrared spectroscopy of kaolins-a DRIFT spectroscopic study. *Clays and Clay Minerals* **46**, 466-477
- Fuller M. P. and Griffiths P. R. (1978) Diffuse Reflectance Measurements by Infrared Fourier Transform Spectrometry. *Analytical Chemistry* **50**, 1906–1910

- Gad M.A., Catt J.A., Le riche H. H. (1969) Geochemistry of the Whitbian (Upper Lias) sediments of the Yorkshire coast. *Proceedings of the Yorkshire Geological Society* **37**, 105-139
- Gill B. C., Lyons T. W. and Jenkyns H. C. (2011) A global perturbation to the sulfur cycle during the Toarcian Oceanic Anoxic Event. *Earth and Planetary Science Letters* **312**, 484–496
- Greensmith J. T., Rawson P. F. and Shalabyy, S .E. (1980) An association of minor fining-upward cycles and aligned gutter marks in the Middle Lias (Lower Jurassic) of the Yorkshire. Yorkshire coast. *Proceedings of the Yorkshire Geological Society* **42**, 525-538
- Griffiths P. R. and De haseth J. A. (2007) Fourier Transform Infrared Spectrometry: (Second edition), WILEY, New Jersey 1-361
- Gröcke D. R., Hori R. S. and Arthur M. A. (2003) The global significance of a deep-sea isotopic event during the Toarcian oceanic anoxic event recorded in Japan. *EOS Transactions, American Geophysical Union* **84**,905
- Gröcke D. R., Hori R. S., Trabucho-Alexandre J., Kemp D. B. and Schwark L. (2011) An open ocean record of the Toarcian oceanic anoxic event. *Solid Earth* **2**, 245-257
- Habicht K. S., Gade M., Thamdrup B., Berg P. and Canfield D. E. (2002) Calibration of sulfate levels in the Archean Ocean. *Science* **298**, 2372-2374
- Hallam, A. (1981) A revised sea level curve for the early Jurassic. *Journal of the Geological Society* **138**, 735-743
- Hallam A. (1967a) The depth significance of shales with bituminous laminae. *Marine Geology* **5**, 481-493
- Hallam A. (1967b) An environmental study of the Upper Domerian and Lower Toarcian in Great Britain. **252**, 393-445
- Hallam A. (1978) Eustatic cycles in the Jurrasic. *Palaeogeography, Palaeoclimatology, Palaeoecology* **23**, 1-32
- Hallam A. (1997) Estimates of the amount and rate of sea-level change across the Rhaetian-Hettangian and Pliensbachian-Toarcian boundaries (latest Triassic to early Jurassic). *Journal of the Geological Society of London* **154**, 773-779
- Hallam A. and Bradshaw M. J. (1979) Bituminous shales and oolitic ironstones as indicators of transgression and regressions. *Journal of the Geological Society of London of London* **136**, 157-164
- Hallam A. (2001) A review of the broad pattern of Jurassic sea-level changes and their possible causes in the light of current knowledge. *Palaeogeography, Palaeoclimatology, Palaeoecology* **167**, 23–37

- Harries P. J. and Little C. T. S. (1999) The early Toarcian (Early Jurassic) and the Cenomanian-Turonian (Late Cretaceous) mass extinctions: similarities and contrasts. *Palaeogeography Palaeoclimatology Palaeoecology* **154**, 39-66
- Hartgers W. A., Sinninghe Damste J. S., Requejo A. G., Allan J., Hayes J. M., Ling Y., Xie T. M., Primack J. and De Leeuw J. W. (1994)b A molecular and carbon isotopic study towards the origin and diagenetic fate of diaromatic carotenoids. *Organic Geochemistry* **22**, 703-725
- Hawthorn F. C. and Waychunas G. A. (1988) Spectrum fitting methods, In:Hawthorn, F.C (ed) *Spectroscopic methods in Minerology and Geology, Reviews in Minerology* **18**, 63-79
- Hayes M. J., Strauss H. and Kaufman A. J. (1999) The abundance of ^{13}C in marine organic matter and isotopic fractionation in the global biogeochemical cycle of carbon during the past 800 Ma. *Chemical Geology* **161**, 103-125
- Helz G. R., Miller C. V., Charnock J. M., Mosselmans J. F. W., Patrick R. A. D. and Garner C. D. (1996). Mechanism of molybdenum removal from the sea and its concentration in black shales: EXAFS evidence. *Geochimica et Cosmochimica Acta* **60**, 3631–3642
- Helz G. R., Bura-Nakic E., Mikac N. and Ciglencecki I. (2011) New model for molybdenum behaviour in euxinic waters. *Chemical Geology* **284**, 323–332
- Hemingway J. E. and Riddler G. P. (1982) Basin inversion in North Yorkshire. *Transactions of the Institute of Mining and Metallurgy, Section B* **91**, 175–186
- Hermoso M., Minoletti F., Callonnec L. L., Jenkyns H. C., Hesselbo S. P., Rickaby R. E. M., Renard M., Rafelis M. and Emmanuel L. (2009) Global and local forcing of Early Toarcian seawater chemistry: A comparative study of different paleoceanographic settings (Paris and Lusitanian basins). *Paleoceanography* **24**, PA4208
- Hesselbo S. P., Jenkyns H. C., Duarte L.V. O and liveira L. C. V (2007)a Carbon-isotoperecord of the Early Jurassic (Toarcian) Oceanic Anoxic Event from fossil wood and marine carbonate (Lusitanian Basin, Portugal). *Earth and Planetary Science Letters* **253**, 455-470
- Hesselbo S. P., McRoberts C. A. and Palfy J. (2007)b Triassic-Jurassicboundaryevents: problems,progress,possibilities. *Palaeogeography Palaeoclimatology Palaeoecology* **244**, 1-10
- Hesselbo S. P. (2008) Sequence stratigraphy and inferred relative sea-level change from the onshore British Jurassic. *Proceedings of the Geologists' Association* **119**, 19-34
- Hesselbo S. P., Gröcke D. R., Jenkyns H. C., Bjerrum C. J., Farrimond P., Morgans H. S. and Green O. R. (2000) Massive dissociation of gas hydrate during a Jurassic oceanic anoxic event. *Nature* **406**, 392-395

- Hesselbo S.P. and Pienkowski G. (2011) Stepwise atmospheric carbon-isotope excursion during the Toarcian Oceanic Anoxic Event (Early Jurassic, Polish Basin). *Earth and Planetary Science Letters* **301**, 365-372
- Hollas M. J. (2004) *Modern Spectroscopy*. (4th Edition), Wiley, pp59-62, 137-151
- Howard A. S. (1985) Lithostratigraphy of the Staithes Sandstone and Cleveland Ironstone formations (Lower Jurassic) of north-east Yorkshire. *Proceedings of the Yorkshire Geological Society* **45**, 261-275.
- Howarth M. K. (1962) The Jet Rock series and the Alum Shale series of the Yorkshire coast. *Proceedings of the Yorkshire Geological Society* **33**, 381-422
- Hunt M. J., (1996) The Source Rock: quality of organic matter. *Petroleum Geochemistry and Geology* second edition 329-332
- Hutton A. C., Kantsler A. J. Cook A. C. and McKirdy D. M. (1980) Organic matter in oil shales. *APEA Journal* **20**, 44-67
- Ibrahim B. A. (1995) A geochemical study of the Jet Rock, the Kimmeridge Clay and the associated concretions. *M.Phil. Thesis, University of Newcastle upon Tyne*, 95 pp
- Ivimey-Cook H. C. and Powell, J. H. (1991) Late Triassic and early Jurassic biostratigraphy of the Felixkirk Borehole, North Yorkshire. *Proceedings of the Yorkshire Geological Society* **48**, 367-374
- Jackson M. J. and Raiswell R. (1991) Sedimentology and carbon sulfur geochemistry of the Velkerri Formation, a Midproterozoic potential oil source in Northern Australia. *Precambrian Research* **54**, 81-108
- Jenkyns H. C. (1985) The Early Toarcian and Cenomanian-Turonian anoxic events in Europe - comparisons and contrasts. *Geologische Rundschau* **74**, 505-518
- Jenkyns H. C. (1988) The early Toarcian (Jurassic) anoxic event - stratigraphic, sedimentary, and geochemical evidence. *American Journal of Science* **288**, 101-151
- Jenkyns H. C. and Clayton C. J. (1997) Lower Jurassic epicontinental carbonates and mudstones from England and Wales: chemostratigraphic signals and the early Toarcian anoxic event. *Sedimentology* **44**, 687-706
- Jenkyns H. C., Grocke D. R. and Hesselbo S. P. (2001) Nitrogen isotope evidence for water mass denitrification during the early Toarcian (Jurassic) oceanic anoxic event. *Palaeogeography* **16**, 592-603
- Jones B. and Manning D. A. C. (1994) Comparison of geochemical indices used for the interpretation of palaeoredox conditions in ancient mudstones. *Chemical Geology* **111**, 111-129

- Katz M. E., Pak D. K., Dickens G. R. and Miller K. G. (1999) The source and fate of massive carbon input during the latest Paleocene thermal maximum. *Science* **286**, 1531-1533
- Kawata S. (2002) Instrumentation for Near-Infrared Spectroscopy. In: SIESLER, H.W., OZAKI, Y., KAWATA, S. & HEISE, H.M (eds) *Near Infrared Spectroscopy: Principles, Instruments, Applications*, WILEY-VCH, Weinheim, p43-54
- Keller G. and Lindinger M. (1989) Stable isotope, TOC and CaCO₃ record across the Cretaceous/Tertiary boundary at ElKef, Tunisia. *Palaeogeography, Palaeoclimatology, Palaeoecology* **73**, 243–65
- Kemp D. B., Cohen A. S. and Schwark L. (2005) Astronomical pacing of methane release in the Early Jurassic Period. *Nature* **437**, 396-399
- Knox R. W. O'B., Howard A. S., Powell J. H. and Van Buchem F. (1991) Lower and Middle Jurassic sediments in the Cleveland Basin, N.E. England: shallow-marine and paralic facies seen in their sequence stratigraphic context. 13th International Sedimentological Congress, Field Guide No. 5.
- Koopmans M. P., Koster J., Van Kaam-Peters H. M. E., Schouen S., Hartgers W. A., De Leeuw J. W. and Sinninghe-Damste J. S. (1996)a Diagenetic and catagenetic of isorenieratene: Molecular indicators for photic zone anoxia. *Geochimica et Cosmochimica Acta* **60**, 4467-4496
- Koopmans M. P., Schouen S., Kohnen M. E. L. and Sinninghe-Damste J. S. (1996)b Restricted utility of aryl isoprenoids as indicators for photic zone anoxia. *Geochimica et Cosmochimica Acta* **60**, 4873-4876
- Kump L. R., Pavlov A. and Arthur M. A. (2005) Massive release of hydrogen sulphide to the surface ocean and atmosphere during intervals of oceanic anoxia. *Geology* **33**, 397-400
- Langford F. F. and Blanc-Valleron M. M. (1990) Interpreting Rock Eval pyrolysis data using graphs of pyrolyzable hydrocarbons vs. total organic carbon. *The American Association of Petroleum Geologists, Bulletin* **74**, 799–804
- Leach C. J., Wagner T., Jones M., Juggins S. and Stevenson A. C. (2008) Rapid determination of total organic carbon concentration in marine sediments using fourier transform near-infrared spectroscopy (FT-NIRS). *Organic Geochemistry* **39**, 910 – 914
- Leventhal J. S. (1983) An interpretation of carbon and sulfur relationships in Black Sea sediments as indicators of environments of deposition. *Geochimica et Cosmochimica Acta* **47**, 133-137
- Leventhal J. S. (1995) Carbon-sulfur plots to show diagenetic and epigenetic sulfidation in sediments. *Geochimica et Cosmochimica Acta* **59**, 1207-1211

- Lewi P. J. (1992) Multivariate Data Display. In: Brereton (ed) Multivariate pattern recognition in chemometrics, illustrated by case studies. *Data handling in science and technology* **9**, 56-59
- Little C. T. S. and Benton M. J (1995). Early Jurassic mass extinction: a global long-term event. *Geology* **23**, 495–498
- Littler K., Hesselbo S. P. and Jenkyns H. C. (2009) A carbon-isotope perturbation at the Pliensbachian–Toarcian boundary: evidence from the Lias Group, NE England. *Geological Magazine* **147**, 181-192
- Li C., Love G. D., Lyons T. W., Fike D. A., Sessions A. L. and Chu X. (2010) A stratified redox model for the Ediacaran Ocean. *Science* **328**, 80-83
- Lyons T. W. (1997) Sulfur isotopic trends and pathways of iron sulfide formation in upper Holocene sediments of the anoxic Black Sea. *Geochimica et Cosmochimica Acta* **61**, 3367-3382
- Lyons T. W. and Berner R. A. (1992) Carbon sulfur iron systematics of the uppermost deep-water sediments of the Black Sea. *Chemical Geology* **99**, 1-27
- Lyons T. W. and Severmann S. (2006) A critical look at iron paleoredox proxies: new insights from modern euxinic marine basins. *Geochimica et Cosmochimica Acta* **70**, 5698-5722
- Mackenzie A. S. (1984a) Applications of biological markers in petroleum geochemistry. In *Advances in Petroleum Geochemistry*, London: Academic, 115-214
- Mackenzie A. S. (1984b) Organic reactions as indicators of the burial and temperature histories of sedimentary sequences. *Clay Minerals* **19**, 271-86
- Madejova J. (2003) FT-IR Techniques in Clay Mineral studies. *Vibrational spectroscopy* **31**, 1-10
- Madejova J. and Komadel P. (2001) Baseline Studies of the Clay Minerals Society Source Clays: Infrared Methods. *Clays and clay minerals* **49**, 410-432
- Mailliot S., Mattioli E., Bartolini A. and Baudin F. (2009) Late Pliensbachian–Early Toarcian (Early Jurassic) environmental changes in an epicontinental basin of NW Europe (Causses area, central France): a micropaleontological and geochemical approach. *Palaeogeography, Palaeoclimatology, Palaeoecology* **273**, 346–364
- Martens H. and Næs T. (1989) *Multivariate calibration*. John Wiley and Sons Ltd, Chichester, UK.
- März C., Poulton S. W., Beckmann B., Kuster K., Wagner T. and Kasten S. (2008) Redox sensitivity of P cycling during marine black shale formation: dynamics of sulfidic and anoxic, non-sulfidic bottom waters. *Geochimica et Cosmochimica Acta* **72**, 3703-3717

- Matrens H. and Naes T. (1991) *Multivariate Calibration*. John Wiley and Sons, Guildford, pp59-119, 237-258
- McArthur J. M. (2007) Comment on “Carbon-isotope record of the Early Jurassic (Toarcian) Oceanic Anoxic Event from fossil wood and marine carbonate (Lusitanian Basin, Portugal)” by Hesselbo S., Jenkyns H.C., Duarte L.V. and Oliveira L.C.V. *Earth and Planetary Science Letters* **259**, 634-639
- McArthur J. M., Donovan D. T., Thirlwall M. F., Fouke B. W. and Matthey D. (2000) Strontium isotope profile of the early Toarcian (Jurassic) oceanic anoxic event, the duration of ammonite biozones and belemnite palaeotemperatures. *Earth and Planetary Science Letters* **179**, 269-285
- McArthur J. M. and Wignall P. B. (2007) Comment on “Non-uniqueness and interpretation of the seawater $^{87}\text{Sr}/^{86}\text{Sr}$ curve” by Dave Waltham and Darren R. (*Geochimica et Cosmochimica Acta*, 70, 2006, 384–394). *Geochimica et Cosmochimica Acta* **71**, 3382-3386
- McArthur J. M., Algeo T.J., van de Schootbrugge B., Li Q. and Howarth R. J. (2008) Basinal restriction, black shales, Re-Os dating, and the Early Toarcian (Jurassic) oceanic anoxic event. *Paleoceanography* **23**, 4217- 4228
- McClure W. F. (1994) Near-Infrared spectroscopy: the giant is running strong. *Analytical Chemistry* **66**, 43-53
- McElwain J. C., Murphy J. W. and Hesselbo S. P. (2005) Changes in carbon dioxide during an oceanic anoxic event linked to intrusion into Gondwana coals. *Nature* **435**, 479-482
- Mckelvy M. L., Britt T. R., Davis B. L., Gille J. K., Lentz L. A., Leugers A., Nyquist R. A. and Putzig C. L. (1996) Infrared Spectroscopy. *Analytical chemistry* **68**, 93-160
- McMillian P. F. and Hofmeister A. M. (1988) Infrared and Raman Spectroscopy. In: HAWTHORN, F.C (ed) *Spectroscopic methods in Mineralogy and Geology, Reviews in Mineralogy* **18**, 99-120
- Meyers S. R. (2007) Production and preservation of organic matter: The significance of iron. *Paleoceanography* **22**, PA4211.
- Meyer K. M. and Kump L. R. (2008) Oceanic euxinia in earth history: causes and consequences. *Annual Review of Earth and Planet Sciences* **36**, 251-288
- Middelburg J. J. and de Lange G. J. (1988) Particulate manganese and iron framboids in Kau Bay, Halmahera (eastern Indonesia). *Marine Chemistry* **23**, 353-364
- Morford J. L. and Emerson S. (1999) The geochemistry of redox sensitive trace metals in sediments. *Geochimica et Cosmochimica Acta* **63**, 1735-1750

- Morris K. A. (1979) A classification of Jurassic marine shale sequences: an example from the Toarcian (Lower Jurassic) of Great Britain. *Palaeogeography, Palaeoclimatology, Palaeoecology* **26**, 117-126
- Morris K. A. (1980) Comparison of major sequences of organic-rich mud deposition in the British Jurassic. *Journal of the Geological Society*, **137**, 157-170
- Morten S. M. and Twitchett R. J. (2009) Fluctuations in the body size of marine invertebrates through the Pliensbachian–Toarcian extinction event. *Palaeogeography, Palaeoclimatology, Palaeoecology* **284**, 29-38
- Moses G. P. G. (1995) Calibration, analysis and interpretation of depositional cycles in the Early Toarcian of Yorkshire, UK. *Geological Society, London, Special Publications* **85**, 67-74
- Mossmann J. R., Aplin A. C., Curtis C. D. and Coleman M. L. (1991) Geochemistry of inorganic and organic sulfur in organic-rich sediments from the Peru margin. *Geochimica et Cosmochimica Acta* **55**, 3581-3595
- Muramoto J. A., Honjo S., Fry B., Hay B. J., Howarth R. W., and Cisne J. L. (1991) Sulfur, iron and organic carbon fluxes in the Black Sea: sulfur isotopic evidence for origin of sulfur fluxes. *Deep-Sea Research Part A -Oceanographic Research Papers* **38**, S1151-S1187
- Murphy N. J., Sauer M. J. and Armstrong J. P. (1995) Toarcian source rock potential in the North Celtic Sea Basin, offshore Ireland. *Geological Society Special Publication* **93**, 193-207
- Murray J. W. and Izdar E. (1989) The 1988 Black Sea Oceanographic Expedition: overview and new discoveries. *Oceanography* **2**, 15-16
- Murray H. W., Jannasch H. W., Honjo S., Anderson R. F., Reeburgh W. W., Top Z., Friederich G. E., Codispoti L. A. and Izdar E. (1989) Unexpected changes in the oxic/anoxic interface in the Black Sea. *Nature* **338**, 411-413
- Nägler T.F., Siebert C., Lüschen H. and Böttcher M. E. (2005) Sedimentary Mo isotope record across the Holocene fresh–brackish water transition of the Black Sea. *Chemical Geology* **219**, 283– 295
- Nara F. W., Watanabe T., Kakegawa T., Seyama H., Horiuchi K., Nakamura T., Imai A., Kawasaki N and Kawi T. (2010) Climate control of sulfate influx to Lake Hovsgol, northwest Mongolia, during the last glacial–postglacial transition: Constraints from sulfur geochemistry. *Palaeogeography, Palaeoclimatology, Palaeoecology* **298**, 278–285
- Naes T., Isaksson T., Fearn T. and Davies T. (2004) A user friendly guide to Multivariate Calibration and Calibration, NIR Publications, Chichester, pp105-114, 156-160

- Negri A., Ferretti A., Wagner T., and Meyers P. A. (2009)a Organic-carbon-rich sediments through the Phanerozoic: Processes, progress, and perspectives. *Palaeogeography, Palaeoclimatology, Palaeoecology* **273**, 213–217
- Negri A., Ferretti A., Wagner T., and Meyers P. A. (2009)b Phanerozoic organic-carbon-rich marine sediments: Overview and future research challenges. *Palaeogeography, Palaeoclimatology, Palaeoecology* **273**, 218–227
- Neubert N., Nägler T. F. and Böttcher M. E. (2008) Sulphidity controls molybdenum isotope fractionation into euxinic sediments: Evidence from the modern Black Sea. *Geology* **36**, 775–778
- Newton R. and Bottrell S. (2007) Stable isotopes of carbon and sulphur as indicators of environmental change: past and present. *Journal of the Geological Society London* **164**, 691–708
- Newton R. J., Bottrell S. H., Dean S. P., Hatfield D., and Raiswell R. (1995) An evaluation of the use of the chromous chloride reduction method for isotopic analyses of pyrite in rocks and sediment. *Chemical Geology* **125**, 317-320
- Newton R. J., Reeves E. P., Kafousia N., Wignall P. B., Bottrell S. H. and Sha J. G. (2011) Low marine sulfate concentrations and the isolation of the European epicontinental sea during the Early Jurassic. *Geology* **39**, 7-10
- Nicolo M. J., Dickens G. R., Hollis C. J. and Zachos J. C. (2007) Multiple early Eocene hyperthermals: Their sedimentary expression on the New Zealand continental margin and in the deep sea. *Geology* **35**, 699-702
- Nicolo M. J., Dickens G. R. and Hollis C.J. (2010) South Pacific intermediate water oxygen depletion at the onset of the Paleocene-Eocene thermal maximum as depicted in New Zealand margin sections: *Paleoceanography* **25**, 4210-4222
- O'Brien N. R. (1990) Significance of lamination in Toarcian (Lower Jurassic) shales from Yorkshire, Great Britain. *Sedimentary Geology* **67**, 25-34
- Olinger J. M. and Griffiths P. R. (1993) Effects of Sample dilution and Particle size/morphology on Diffuse Reflectance Spectra of Carbohydrate systems in the Near- and Mid-infrared. Part1: single analytes. *Applied spectroscopy* **47**, 687-694
- Pálffy J. and Smith P. L. (2000) Synchrony between Early Jurassic extinction, oceanic anoxic event, and the Karoo-Ferrar flood basalt volcanism. *Geology* **28**, 747-750
- Pancost R. D., Crawford N. and Maxwell J. R. (2002) Molecular evidence for basin-scale photic zone euxinia in the Permian Zechstein Sea. *Chemical Geology* **188**, 217–227
- Paropkari A. L., Babu C. P. and Mascarenhas A. (1992) A critical evaluation of depositional parameters controlling the variability of organic carbon in Arabian Sea sediments. *Marine Geology* **107**, 213-226

- Payne J. L., Lehrmann D. J., Wei J., Orchard M. J., Schrag D. P. and Knoll A. H. (2004) Large perturbations of the carbon cycle during recovery from the End-Permian extinction. *Science* **305**, 506–509
- Pearce C. R., Cohen A. S., Coe A. L. and Burton K. W. (2008) Molybdenum isotope evidence for global ocean anoxia coupled with perturbations to the carbon cycle during the Early Jurassic. *Geology* **36**, 231-234
- Pearson M. J., Hill A. M., Fallick A. E. and Ecuivillon S. (1996) Sulphur incorporation in Jurassic marine mudrocks and their bitumens at low thermal maturity, Cleveland Basin, England. *Geochimica et Cosmochimica Acta* **60**, 4181- 4192
- Pedersen T. F. and Calvert S. E. (1990) Anoxic vs. Productivity: What Controls the Formation of Organic-Carbon-Rich Sediments and Sedimentary Rocks? *The American Association of Petroleum Geology Bulletin* **74**, 454-466
- Peters K. E., Walters C. C. and Moldowan J. M. (1993) *The Biomarker Guide: Volume 2, Biomarkers and Isotopes in Petroleum Exploration and Earth History*. Cambridge, UK: Cambridge University Press
- Peters K. E. Moldowan, J. M. Schoell M. and Hemphkins W. B. (1986) Petroleum isotopic and biomarker composition related to source rock organic matter and depositional environment. *Organic Geochemistry* **10**, 17–27
- Peters K. E. and Moldowan M. J. (1991) Effects of source, thermal maturity, and biodegradation on the distribution and isomerization of homohopanes in petroleum. *Organic Geochemistry* **17**, 47–61
- Peters K. E. and Moldowan J. M. (1993) *The biomarker guide: Interpreting molecular fossils in petroleum and ancient sediments*. pp.363. Prentice-Hall, Englewood Cliffs (United States)
- Peters K. E., Fraser T. H., Amris W., Rustanto B. and Hermanto E. (1999) Geochemistry of crude oils from eastern Indonesia. *American Association of Petroleum Geologists Bulletin* **83**, 1927 - 1942
- Peters K. E., Walters C. C. and Moldowan J. M. (2005) *The Biomarker Guide: Volume 1, Biomarkers and Isotopes in the Environment and Human History*. Cambridge, UK: Cambridge University Press
- Philp R. P. (1994) Geochemical characteristics of oil derived predominantly from terrigenous source materials. *The Geological Society, London* **77**, 71–91
- Piper D. Z. and Calvert S. E. (2009) A marine biogeochemical perspective on black shale deposition. *Earth Science Reviews* **95**, 63–96
- Prauss M., Ligouis B. and Luterbacher H. (1991) Organic matter and palynomorphs in the 'Posidonienschiefer' (Toarcian, Lower Jurassic) of southern Germany. *Geological Society Special Publication* **58**, 335-351

- Poulton S. W. and Canfield D. E. (2005) Development of a sequential extraction procedure for iron: implications for iron partitioning in continentally derived particulates. *Chemical Geology* **214**, 209–221
- Poulton S. W. and Canfield D. E. (2011) Ferruginous conditions: a dominant feature of the ocean through earth's history. *Elements* **7**, 107-112
- Poulton S. W. and Raiswell R. (2002) The low temperature geochemical cycle of iron from continental fluxes to marine sediment deposition. *American Journal of Science* **302**, 744-805
- Poulton S. W., Fralick P. W. and Canfield D. E. (2004) The transition to a sulphidic ocean-1.84 billion years ago. *Nature* **431**, 173-177
- Poulton S. W., Fralick P. W. and Canfield D. E. (2010) Spatial variability in oceanic redox structure 1.8 billion years ago. *Nature* **431**, 486-490
- Powell J. H. (1984) Lithostratigraphical nomenclature of the Lias Group in the Yorkshire Basin. *Proceedings of the Yorkshire Geological Society* **45**, 51-57
- Powell J. H. (2010) Jurassic sedimentation in the Cleveland Basin: a review. *Proceedings of the Yorkshire Geological Society* **58**, 21-72
- Pye K. and Krinsley D. H. (1985) Microfabric, mineralogy and early diagenetic history of the Whitby Mudstone Formation (Toarcian), Cleveland Basin, UK. *Geological Magazine* **123**, 191-203
- Raiswell R. and Berner R. A. (1987) Organic carbon losses during burial and thermal maturation of normal marine shales. *Geology* **15**, 853-856
- Raiswell R., Buckley F., Berner R. A. and Anderson T. F. (1988) Degree of pyritization of iron as a paleoenvironmental indicator of bottom-water oxygenation. *Journal of Sedimentary Petrology* **58**, 812-819
- Raiswell R. and Canfield D. E. (1996) Rates of reaction between silicate iron and dissolved sulfide in Peru Margin sediments. *Geochimica et Cosmochimica Acta* **60**, 2777-2787
- Raiswell R. (2006) An evaluation of diagenetic recycling as a source of iron for banded iron formation. In: Kesler SE, Ohmoto H (eds) Evolution of Early Earth's Atmosphere, Hydrosphere and Deposits. *Geological Society of America Memoir* **198**, 223-238
- Raiswell R. and Anderson T. F. (2005) Reactive iron enrichment in sediments deposited beneath euxinic bottom waters: constraints on supply by shelf recycling. *Geological Society, London, Special Publications* **248**, 179-194
- Raiswell R. and Canfield D. E. (1998) Sources of iron for pyrite formation in marine sediments. *American Journal of Science* **298**, 219-245

- Raiswell R., Canfield D. E. and Berner R. A. (1994) A comparison of iron extraction methods for the determination of degree of pyritisation and the recognition of iron-limited pyrite formation. *Chemical Geology* **111**, 101-110
- Raiswell R., Newton R. and Wignall P. B. (2001) An indicator of water-column anoxia: resolution of biofacies variations in the Kimmeridge Clay (Upper Jurassic, U.K.). *Journal of Sediment Research* **71**, 286–294
- Reeves J. B., McCarty G. W. and Reeves, V. B. (2001) Mid-Infrared Diffuse Reflectance Spectroscopy for the Quantitative Analysis of the Agricultural Soils. *Journal of Agricultural and Food Chemistry* **49**, 766-772
- Reichert G. J., Lourens L. J. and Zachariasse W. J. (1998) Temporal variability in the northern Arabian Sea Oxygen Minimum Zone (OMZ) during the last 225000 years. *Paleoceanography* **13**, 607-621
- Riccardi A., Kump L. R., Arthur M. A. and D'Hondt S. (2007) Carbon isotopic evidence for chemocline upward excursions during the end-Permian event. *Palaeogeography, Palaeoclimatology, Palaeoecology* **248**, 73–81
- Rickard D. (1970) The origin of framboids. *Lithos* **3**, 269–293
- Rickard D., Schoonen M. A. A. and Luther G. W. (1995) Chemistry of iron sulphides in sedimentary environments. *Geochemical Transformations of Sedimentary Sulfur* **612**, 168-193
- Rintoul L., Panylotou H., Kokot S., George G., Cash G., Frost R., Bui T. and Fredricks P. (1998) Fourier Transform Infrared Spectroscopy: A versatile technique for real world samples. *Analyst* **123**, 371-377
- Röhl H.-J., Schmid-Röhl A., Oschmann W., Frimmel A. and Schwark L. (2001) The Posidonia Shale (Lower Toarcian) of SW-Germany: an oxygen depleted ecosystem controlled by sea level and palaeoclimate. *Palaeogeography, Palaeoclimatology, Palaeoecology* **165**, 27-52
- Rullkötter J. and Marzi R. (1987) Natural and artificial maturation of biological markers in a Toarcian shale from northern Germany. *Advances in Organic Geochemistry* **13**, 639-645
- Sabatino N., Neri R., Bellanca A., Jenkyns H., Baudin F., Parisi G. and Masetti D. (2009) Carbon-isotope records of the Early Jurassic (Toarcian) oceanic anoxic event from the Valdorbia (Umbria–Marche Apennines) and Monte Mangart (Julian Alps) sections: palaeoceanographic and stratigraphic implications. *Sedimentology* **56**, 1307–1328
- Sælen G., Doyle P. and Talbot M. R. (1996) Stable-isotope analyses of Belemnite rostra from the Whitby Mudstone Fm, England: surface water conditions during deposition of a marine black shale. *Palaios* **11**, 97-117

- Sælen G., Raiswell R., Talbot M. R., Skei J. M. and Bottrell S. H. (1993) Heavy sedimentary sulfur isotopes as indicators of super-anoxic bottom-water conditions. *Geology* **21**, 1091-1094
- Sælen G., Tyson R. V., Talbot M. R. and Telnaes N. (1998) Evidence of recycling of isotopically light CO₂(aq) in stratified black shale basins: contrasts between the Whitby Mudstone and Kimmeridge Clay formation, UK. *Geology* **26**, 747-750
- Sælen G., Tyson R. V., Telnaes N. and Talbot M. R. (2000) Contrasting water mass conditions during deposition of the Whitby Mudstone (Lower Jurassic) and Kimmeridge Clay (Upper Jurassic) formations, UK. *Palaeogeography, Palaeoclimatology, Palaeoecology* **163**, 163-196
- Sari A., Allyev S. A. and Koralay D. B. (2007) Source Rock Evaluation of the Eocene Shales in the Gökçesu Area (Bolu/Turkey). *Energy Sources* **29**, 1025–1039
- Savrda C. E. and Bottjer D. J. (1987) The exaerobic zone, a new oxygen deficient marine biofacies. *Nature* **327**, 54-56
- Savrda C. E. and Bottjer D. J. (1991) Oxygen related biofacies in marine strata: An overview and update. *The Geological Society Special Publication* **58**, 201-219
- Schlanger S.O. and Jenkyns H. C. (1976) Cretaceous oceanic anoxic event: causes and consequences. *Geologie En mijnbouw* **55**, 179-184
- Schouten S., van Kaam-Peters H. M. E., Rijpstra W. I.C. and Damste J. S. S. (2000) Effects of an oceanic anoxic event on the stable carbon isotopic composition of Early Toarcian carbon. *American Journal of Science* **300**, 1- 22
- Schulte S., Rostek F., Bard E., Rullkötter J. and Marchal O. (1999) Variations of oxygen-minimum and primary productivity record in sediments of the Arabian Sea. *Earth and Planetary Science Letters* **173**, 205–221
- Scott C., Lyons T. W., Bekker A., Shen Y., Poulton S. W., Chu X. and Anbar A. D. (2008) Tracing the stepwise oxygenation of the Proterozoic ocean. *Nature* **452**, 456-459
- Severmann S. and Anbar A. D. (2009) Reconstructing paleoredox conditions through a multitracer approach: the key to the past is the present. *Elements* **5**, 359-364
- Simms M. J., Chidlaw N., Morton N. and Page K. N. (2004) British Lower Jurassic stratigraphy. *Geological Conservation Review Series*, No. 30, Joint Nature Conservation Committee, Peterborough, 458 pages
- Smith A. L. (1979) *Applied Infrared Spectroscopy*, John Wiley and Sons, Canada, p8-17
- Sinninghe Damste J. S., Schouten S. and van Duin A. C. T. (2001) Isorenieratene derivatives in sediments: Possible controls on their distribution. *Geochimica et Cosmochimica Acta* **65**, 1557-1571

- Staubwasser M. and Sirocko F. (2001) On the formation of laminated sediments on the continental margin off Pakistan: the effects of sediment provenance and sediment redistribution. *Marine Geology* **172**, 43-56
- Suan G., Mattioli E., Pittet B., Lecuyer C., Marx B., Duarte L. V., Philippe M., Reggiani L. and Martineau F. (2010) Secular environmental precursors to Early Toarcian (Jurassic) extreme climate changes. *Earth and Planetary Science Letters* **290**, 448–458
- Suan G., Nikitenko B. L., Rogov M. A., Baudin F., Spangenberg J. E., Knyazev V. G., Glinskikh L. A., Goryacheva A. A., Adatte T., Riding J. B., Follmi K. B., Pittet B., Mattioli E. and Lecuyer C. (2011) Polar record of Early Jurassic massive carbon injection. *Earth and Planetary Science Letters* **312**, 102–113
- Suan G., Pittet B., Bour I., Mattioli E., Duarte L. V., and Mailliot S. (2008) Duration of the Early Toarcian carbon isotope excursion deduced from spectral analysis: Consequence for its possible causes. *Earth and Planetary Science Letters* **267**, 666–679
- Suits N. S. and Wilkin R. T. (1998) Pyrite formation in the water column and sediments of a meromictic lake. *Geology* **26**, 1099-1102
- Summons R. E. and Powell T. G. (1987) Identification of aryl isoprenoids in source rocks and crude oils: biological markers for the green sulphur bacteria. *Geochimica et Cosmochimica Acta* **51**, 557–566
- Svensen H., Planke S., Chevallier L., Malthe-Sørensen A., Corfu B. and Jamtveit B. (2007) Hydrothermal venting of greenhouse gases triggering Early Jurassic global warming. *Earth and Planetary Science Letters* **256**, 554-566
- Sweeney R. E. and Kaplan I. R. (1980) Stable isotope compositions of dissolved sulfate and hydrogen sulphide in the Black Sea. *Marine Chemistry* **9**, 145-152
- Sweeney R. E., Kalil E. K. and Kaplan I. R. (1980) Characterisation of domestic and industrial sewage in southern California coastal sediments using nitrogen, carbon, sulphur and uranium tracers. *Marine Environmental Research* **3**, 225-243
- Taylor K. G. (1998) Spatial and temporal variations in early diagenetic organic matter oxidation pathways in Lower Jurassic mudstones of eastern England. *Chemical Geology* **145**, 47-60.
- Tissot B. P. and Welte D. H. (1984) Petroleum formation and occurrence. (2nd edition) Springer-Verlag, 699pp
- Trabucho -Alexandre J., Hay W. W. and de Boer P. L. (2011) Phanerozoic black shales and the Wilson cycle. *Solid Earth Discussions* **3**, 743-768
- Tribovillard N. P., Desprairies A., Lallier E., Bertrand P., Moureau N., Ramadani A. and Ramanampiso L. (1994). Geochemical study of organic matter rich cycles from

- Kimmeridg Clay Formation of Yorkshire (UK): Productivity versus anoxia. *Palaeogeography, Palaeoclimatology, Palaeoecology* **108**, 165-181
- Tribovillard N. P., Riboulleau A., Lyons T. W. and Baudin F. (2004) Enhanced trapping of molybdenum by sulphurized organic matter of marine origin as recorded by various Mesozoic Formations. *Chemical Geology* **213**, 385-401
- Tribovillard N. P., Algeo T. J., Lyons T. W. and Riboulleau A. (2006) Trace metals as paleoredox and paleoproductivity proxies: An update. *Chemical Geology* **232**, 12-32
- Tuweni A. O. and Tyson R. V. (1994) Organic facies variations in the Westbury Formation (Rhaetic, Bristol Channel, SW England). *Organic Geochemistry* **21**, 1001-1014
- Tyson R. V. (1993) Palynofacies analysis, In: Jenkins, D.G. (ed.) *Applied micropalaeontology*, Kluwer, Dordrecht, pp. 153-191
- Tyson R. V. (1995) Sedimentary Organic Matter. Organic Facies and Palynofacies, *Chapman and Hall*, London, 625pp.
- Tyson R. V. and Pearson T. H. (1991) Modern and ancient continental shelf anoxia: an overview. In *Modern and Ancient Continental Shelf Anoxia* **58**, 1-24
- Tyson R. V. and Follows B. (2000) Palynofacies prediction of distance from sediment source : a case study from the Upper Cretaceous of the Pyrenees. *Geology* **28**, 569-571
- Tyson R. V., Wilson R. C. L. and Downie C. (1979) A stratified water column environmental model for the type Kimmeridge Clay. *Nature* **277**, 377-380
- van Breugel Y., Baas M., Schouten S., Mattioli E. and Sinninghe J.S. (2006) Isorenieratane record in black shales from the Paris Basin, France: Constraints on recycling of respired CO₂ as a mechanism for negative carbon isotope shifts during the Toarcian oceanic anoxic event. *Paleoceanography* **21**, PA 4220, 1-8
- van Buchem F. S. P. and Knox R. W. O'B. (1998) Lower and Middle Jurassic Depositional Sequences of Yorkshire (U.K.). In *Mesozoic and Cenozoic Sequence Stratigraphy of European Basins* (eds P. C. de Graciansky, J.Hardenbol, T. Jacquin and P. R. Vail), pp. 545-59. Special Publication of the Society for Sedimentary Geology (SEPM) no. 60
- Vandenbroucke M. and Largeau C. (200) Kerogen origin, evolution and structure. *Organic Geochemistry* **38**, 719-833
- Van De Schootbrugge B., McArthur J. M., Bailey T.R., Rosenthal Y., Wright J. D. and Miller K. G. (2006) Toarcian oceanic anoxic event: An assessment of global causes using belemnite C-isotope records. *Palaeogeography* **20**, PA 3008
- Veizer J., Ala D., Azmy K., Bruckschen P., Buhl D., Bruhn F., Carden G. A. F., Diener A., Ebner S., Godderis Y., Jasper T., Korte C., Pawellek F., Podlaha O. and Strauss, H.

- (1999) $^{87}\text{Sr}/^{86}\text{Sr}$, $\delta^{13}\text{C}$ and $\delta^{18}\text{O}$ evolution of Phanerozoic seawater. *Chemical Geology* **161**, 59-88
- Vernadsky, V.I., McMenamin, M.A.S., Langmuir, D.B., 1998. The Biosphere. *Copernicus, New York, NY*. 192 pp
- Vinogradov A.P., Grinenko V. A. and Ustinov V. I. (1962) Isotopic composition of sulphur compounds in the Black Sea. *Geochemistry* **10**, 851-873
- Vogel H., Rosen P., Wagner B., Melles M. and persson P. (2008) Fourier Transform Infrared Spectroscopy, A new Cost Effective Tool for Quantitative Analysis of Biogeochemical Properties in Long Sediment Records. *Journal of Paleolimnology* **40**, 689-702
- Volkman J. K., Everitt D. A. and Allen D. I. (1986) Some analyses of lipid classes in marine organisms, sediments and seawater using thin-layer chromatography-flame ionisation detection. *Journal of Chromatography* **356**, 147-162
- Wang Q. W. and Morse J. W. (1996) Pyrite formation under conditions approximating those in anoxic sediments I. Pathway and morphology. *Marine Chemistry* **52**, 99-121
- Wang F. and Chapman P. M. (1999) Biological implications of sulfide in sediment: a review focusing on sediment toxicity. *Environmental Toxicology and Chemistry* **18**, 2526-2532
- Waples D. W. (1980) Time and temperature in petroleum formation: application of Lopatin's method to petroleum exploration. *American Association of Petroleum Geology Bulletin* **64**, 916-926
- Waples D. W. (1985) *Geochemistry in Petroleum Exploration*. Boston, IHRDC, 232P.
- Weeks S. J., Currie B., Bakun A. and Peard K. R. (2004) Hydrogen sulphide eruptions in the Atlantic Ocean off southern Africa: implications of a new view based on SeaWiFS satellite imagery. *Deep Sea Research Part I: Oceanographic Research Papers* **51**, 153–72
- West I. and Gallois R. (2011) Lyme Regis West ward –Monmouth, Pinhay Bay and Landslide: *Geology of the Wessex of Southern England*.
<http://www.soton.ac.uk/~imw/Lyme-Regis-Westward.htm> Accessed 23/04/12
- Wignall P. B. (1991a) A model for transgressive black shales in a sequence stratigraphic framework. *American Association of Petroleum Geologists Bulletin* **75**, 693
- Wignall P. B. (1991b) Model for transgressive black shales. *Geology* **19**, 167-170
- Wignall P. B., Newton R. J. and Little C. T. S. (2005). The timing of paleo-environmental change and cause-and-effect relationships during the Early Jurassic mass extinction in Europe. *American Journal of Science* **305**, 1014–1032

- Wignall P. B. (1994) Black shales. *Oxford University Press*, Oxford, 130pp
- Wignall P. B. and Bond P. G. (2008) The end-Permian and Early Jurassic mass extinction in the British Isles. *Proceedings of the Geologists Association* **119**, 73-84
- Wignall P. B. and Hallam A. (1991) Biofacies, stratigraphic distribution and depositional models of British onshore Jurassic black shales. *Modern and Ancient Continental Shelf Anoxia* **58**, 291-309
- Wignall P. B. and Myers K. J. (1988) Interpreting benthic oxygen levels in mudrocks: a new approach. *Geology* **16**, 452-455
- Wijnsman J. W. M., Middelburg J. J. and Heip C. H. R. (2001) Reactive iron in Black Sea sediments: implication for iron cycling. *Marine Geology* **172**, 167-180
- Wilkin R. T. and Arthur M. A. (2001) Variations in pyrite texture, sulfur isotope composition, and iron systematics in the Black Sea: evidence for Late Pleistocene to Holocene excursions of the O₂-H₂S redox transition. *Geochimica et Cosmochimica Acta* **65**, 1399-1416
- Wilkin R. T., Arthur M. A. and Dean W. E. (1997a) History of water-column anoxia in the Black Sea indicated by pyrite framboid size distributions. *Earth and Planetary Science Letters* **148**, 517-525
- Wilkin R. T. and Barnes H. L. (1997b) Pyrite formation in an anoxic estuarine basin. *American Journal of Science* **297**, 620-650
- Wilkin R. T., Barnes H. L. and Brantley S. L. (1996) The size distribution of framboidal pyrite in modern sediments: An indicator of redox conditions. *Geochimica et Cosmochimica Acta* **60**, 3897-3912
- Williams D. H. and Fleming I. (1995) *Spectroscopic Methods in Organic Chemistry*, (5th edition) McGraw-Hill, Cambridge, pp30-45, 170
- Williams P. C. and Norris K. H. (1987) Qualitative applications of nearinfrared reflectance spectroscopy. In: Williams P. C. and Norris K. H (Eds.), *Near-infrared technology in the agricultural and food industries* (pp. 241– 246). St. Paul, MN: American Association of Cereal Chemists
- Wold S., Sjostrom M. and Eriksson L. (2001) PLS-regression: a basic Tool for Chemometrics. *Chemometrics and intelligent laboratory systems* **58**, 109-130
- Yao W. and Millero F. (1996) Oxidation of hydrogen sulfide by hydrous Fe(III) oxides in seawater. *Marine Chemistry* **52**, 1-16

Zheng Y., Anderson R. F., Van Geen A. and Kuwabara J. (2000) Authigenic molybdenum formation in marine sediments: A link to pore water sulphide in the Santa Barbara Basin. *Geochimica et Cosmochimica Acta* **64**, 4165-4175

DATA APPENDIX

APPENDIX A1: Port-Mulgrave section

Formation	Subzone	Sample name	Stratigraphic height (Cm)	Lithology	Fabric	Colour Index	TOC wt%	TC wt%	TIC wt%	CaCO3%	TS wt%
Jet Rock Shale	H.Exaratum	JET17	1823	Shale	Laminated	5	5.05	7.645	2.6	21.6	11.8
Jet Rock Shale	H.Exaratum	JET16	1814	Shale	Laminated	5	6.536	7.269	0.7	6.1	10.3
Jet Rock Shale	H.Exaratum	JET15	1787	Shale	Laminated	5	6.132	7.673	1.5	12.8	14.0
Jet Rock Shale	H.Exaratum	JET14	1779	Shale	Laminated	5	5.741	7.542	1.8	15.0	11.0
Jet Rock Shale	H.Exaratum	JET13	1774	Shale	Laminated	5	4.261	7.309	3.0	25.4	14.9
Jet Rock Shale	H.Exaratum	JET12	1765	Shale	Laminated	5	5.58	7.26	1.7	14.0	11.8
Jet Rock Shale	H.Exaratum	JET11	1756	Shale	Laminated	5	6.036	11.932	5.9	49.1	15.2
Jet Rock Shale	H.Exaratum	JET10	1748	Shale	Laminated	5	6.38	10.665	4.3	35.7	11.2
Jet Rock Shale	H.Exaratum	JET9	1740	Shale	Laminated	5	4.931	6.846	1.9	16.0	12.4
Jet Rock Shale	H.Exaratum	JET8	1716	Shale	Laminated	4	6.148	8.242	2.1	17.5	12.7
Jet Rock Shale	H.Exaratum	JET7	1698	Shale	Laminated	4	12.617	14.198	1.6	13.2	12.7
Jet Rock Shale	H.Exaratum	JET6	1673	Shale	Laminated	4	14.255	16.097	1.8	15.4	12.8

Jet Rock Shale	H.Exaratum	JET5	1623	Shale	Laminated	6	7.135	8.56	1.4	11.9	10.1
Jet Rock Shale	H.Exaratum	JET4	1568	Shale	Laminated	5	10.071	11.365	1.3	10.8	13.3
Jet Rock Shale	H.Exaratum	JET3	1518	Shale	Laminated	5	9.614	10.761	1.1	9.6	12.1
Jet Rock Shale	H.Exaratum	JET2	1448	Shale	Laminated	5	5.466	6.817	1.4	11.3	11.3
Jet Rock Shale	H.Exaratum	JET1	1398	Shale	Laminated	6	5.327	6.081	0.8	6.3	9.7
Gray Shale	D.Semicelatum	TL.5	1358	Shale	Laminated	6	2.9032	3.2569	0.4	2.9	7.1
Gray Shale	D.Semicelatum	TL.4	1318	Shale	Laminated	6	3.562	3.796	0.2	2.0	9.7
Gray Shale	D.Semicelatum	TL.3	1268	Shale	Laminated	6	4.534	5.341	0.8	6.7	9.3
Gray Shale	D.Semicelatum	TL.2	1218	Shale	Laminated	5	6.141	6.595	0.5	3.8	12.3
Gray Shale	D.Semicelatum	TL.1	1158	Shale	Laminated	5	6.128	6.734	0.6	5.1	12.2
Gray Shale	D.Semicelatum	4-MST7	1035	Mudston	Massive	6	1.9273	2.1731	0.2	2.0	5.7
Gray Shale	D.Semicelatum	4-MST6	945	Mudston	Massive	6	1.4107	2.1027	0.7	5.8	3.6
Gray Shale	D.Semicelatum	4-MST5	843	Mudston	Massive	6	1.4787	1.936	0.5	3.8	3.9
Gray Shale	D.Semicelatum	4-MST4	783	Mudston	Massive	6	1.5991	2.0921	0.5	4.1	4.2
Gray Shale	D.Semicelatum	4-MST3	733	Mudston	Massive	6	1.3921	2.1431	0.8	6.3	3.4
Gray Shale	D.Semicelatum	4-MST2	678	Mudston	Massive	6	1.633	2.1027	0.5	3.9	3.4
Gray Shale	D.Semicelatum	4-MST1	628	Mudston	Massive	6	1.6381	2.1437	0.5	4.2	4.5
Gray Shale	Clevelandicum	USB10	578.0	Shale	Laminated	4.0	2.638	2.7	0.1	0.9	17.9
Gray Shale	Clevelandicum	USB9	576.0	Shale	Laminated	4.0	2.590	3.014	0.4	3.5	16.2
Gray Shale	Clevelandicum	USB7	572.0	Shale	Laminated	4.0	3.513	4.1	0.6	4.9	8.9
Gray Shale	Clevelandicum	USB6	570	Shale	Laminated	4.0	3.137	3.7	0.6	4.8	9.0
Gray Shale	Clevelandicum	USB5	568.0	Shale	Laminated	4.0	1.842	2.23	0.4	3.2	7.4
Gray Shale	Clevelandicum	USB4	566	Shale	Laminated	4.0	2.867	3.29	0.4	3.5	8.3
Gray Shale	Clevelandicum	USB3	564	Shale	Laminated	4.0	2.428	2.83	0.4	3.4	6.8
Gray Shale	Clevelandicum	USB2	562	Shale	Laminated	4.0	1.814	2	0.2	1.6	7.2

Gray Shale	Clevelandicum	USB1	560	Shale	Laminated	5.0	1.705	1.87	0.2	1.4	5.5
Gray Shale	Paltum	3-MST8	546	Mudston	Massive	6.0	1.23	1.47	0.2	2.0	2.4
Gray Shale	Paltum	3-MST7	501	Mudston	Massive	6.0	1.022	1.31	0.3	2.4	2.0
Gray Shale	Paltum	3-MST6	488	Mudston	Massive	6.0	1.2285	1.39	0.2	1.3	2.3
Gray Shale	Paltum	3-MST5	458	Mudston	Massive	6.0	1.5342	1.59	0.1	0.5	3.2
Gray Shale	Paltum	3-MST4	422	Mudston	Massive	6.0	1.4255	1.57	0.1	1.2	3.0
Gray Shale	Paltum	3-MST3	372	Mudston	Massive	6.0	1.37	1.58	0.2	1.8	2.9
Gray Shale	Paltum	3-MST2	307	Mudston	Laminated	6.0	1.2	1.35	0.2	1.3	4.3
Gray Shale	Paltum	3-MST1	297	Mudston	Massive	6.0	2.1121	3.79	1.7	14.0	5.0
Gray Shale	Paltum	MSB24	294	Shale	Laminated	6.0	1.7	2.2	0.4	3.6	3.3
Gray Shale	Paltum	MSB23	292	Shale	Laminated	6.0	1.4	1.8	0.4	2.9	3.2
Gray Shale	Paltum	MSB22	290	Shale	Laminated	6.0	1.1	1.7	0.6	4.9	3.4
Gray Shale	Paltum	MSB21	289	Shale	Laminated	6.0	1.6	2.1	0.6	4.8	6.5
Gray Shale	Paltum	MSB20	287	Shale	Laminated	5.0	2.2	2.3	0.1	1.1	5.1
Gray Shale	Paltum	MSB19	285	Shale	Laminated	5.0	2.7	3.0	0.3	2.5	7.0
Gray Shale	Paltum	MSB18	283	Shale	Laminated	5.0	2.4	2.6	0.2	2.0	7.9
Gray Shale	Paltum	MSB17	281	Shale	Laminated	5.0	2.4	2.5	0.2	1.3	5.8
Gray Shale	Paltum	MSB16	278	Shale	Laminated	5.0	2.2	2.5	0.3	2.4	5.5
Gray Shale	Paltum	MSB15	275	Shale	Laminated	5.0	2.1	2.3	0.2	1.7	5.3
Gray Shale	Paltum	MSB14	273	Shale	Laminated	5.0	2.1	2.2	0.1	1.0	4.6
Gray Shale	Paltum	MSB13	269	Shale	Laminated	5.0	2.0	2.0	0.0	0.3	4.1
Gray Shale	Paltum	MSB12	266	Shale	Laminated	5.0	1.8	1.9	0.1	0.5	4.7
Gray Shale	Paltum	MSB11	263	Shale	Laminated	6.0	1.7	1.8	0.1	0.7	3.2
Gray Shale	Paltum	MSB10	258	Shale	Laminated	5.0	1.8	1.9	0.1	0.8	4.6
Gray Shale	Paltum	MSB9	254	Shale	Laminated	5.0	1.8	1.9	0.1	1.1	4.3
Gray Shale	Paltum	MSB8	251	Shale	Laminated	5.0	1.7	1.9	0.2	2.0	5.6
Gray Shale	Paltum	MSB7	248	Shale	Laminated	5.0	1.7	2.1	0.4	3.7	6.8
Gray Shale	Paltum	MSB6	245	Shale	Laminated	5.0	1.9	2.1	0.2	1.5	6.3
Gray Shale	Paltum	MSB5	241	Shale	Laminated	4.0	2.9	3.2	0.3	2.5	7.2

Gray Shale	Paltum	MSB4	238	Shale	Laminated	4.0	3.2	3.4	0.2	2.0	7.9
Gray Shale	Paltum	MSB3	235	Shale	Laminated	4.0	2.7	3.1	0.5	4.0	10.1
Gray Shale	Paltum	MSB2	233	Shale	Laminated	4.0	3.3	3.6	0.3	2.6	7.1
Gray Shale	Paltum	MSB1	230	Shale	Laminated	4.0	4.7	5.0	0.4	3.0	8.5
Gray Shale	Paltum	2-MST8	215	Mudston	Massive	5.0	2.2	4.1	1.9	15.9	9.0
Gray Shale	Paltum	2-MST7	190	Mudston	Massive	5.0	1.1	4.7	3.6	30.3	8.4
Gray Shale	Paltum	2-MST6	165	Mudston	Massive	5.0	1.1	2.8	1.7	13.8	13.3
Gray Shale	Paltum	2-MST5	145	Mudston	Massive	5.0	1.7	2.6	1.0	7.9	9.3
Gray Shale	Paltum	2-MST4	128	Mudston	Massive	5.0	1.2	1.7	0.5	4.3	4.3
Gray Shale	Paltum	2-MST3	110	Mudston	Massive	6.0	1.0	1.3	0.3	2.3	3.3
Gray Shale	Paltum	2-MST2	95	Mudston	Massive	6.0	1.0	1.3	0.3	2.7	5.4
Gray Shale	Paltum	2-MST1	85	Mudston	Massive	6.0	1.1	1.3	0.2	1.8	0.9
Gray Shale	Paltum	LSB14	78	Shale	Laminated	4.0	2.507	2.8	0.3	2.4	11.2
Gray Shale	Paltum	LSB13	77	Shale	Laminated	4.0	5.726	6.5	0.8	6.3	13.2
Gray Shale	Paltum	LSB12	75	Shale	Laminated	4.0	6.273	7.0	0.7	6.2	11.9
Gray Shale	Paltum	LSB11	73	Shale	Laminated	4.0	2.915	3.8	0.9	7.8	12.0
Gray Shale	Paltum	LSB10	72	Shale	Laminated	4.0	0.802	0.9	0.1	0.7	15.2
Gray Shale	Paltum	LSB9	71	Shale	Laminated	4.0	6.809	7.1	0.3	2.6	15.6
Gray Shale	Paltum	LSB8	69	Shale	Laminated	4.0	6.296	7.1	0.8	6.4	15.5
Gray Shale	Paltum	LSB7	67	Shale	Laminated	4.0	2.333	2.9	0.6	4.7	13.5
Gray Shale	Paltum	LSB6	66	Shale	Laminated	4.0	1.410	1.6	0.2	1.7	8.7
Gray Shale	Paltum	LSB5	65	Shale	Laminated	4.0	1.275	2.3	1.0	8.6	5.4
Gray Shale	Paltum	LSB4	63	Shale	Laminated	4.0	1.160	1.3	0.2	1.4	6.0
Gray Shale	Paltum	LSB3	62	Shale	Laminated	4.0	1.542	2.8	1.3	10.6	5.3
Gray Shale	Paltum	LSB2	60	Shale	Laminated	4.0	1.020	1.1	0.1	0.8	5.4
Gray Shale	Paltum	LSB1	58	Shale	Laminated	4.0	1.305	2.9	1.6	13.7	5.1
Gray Shale	Paltum	1-MST6	55	Shale	Massive	5.0	1.0	1.0	0.0	0.1	4.5
Gray Shale	Paltum	1-MST5	45	Shale	Massive	5.0	0.9	1.0	0.1	0.7	4.2
Gray Shale	Paltum	1-MST4	35	Shale	Massive	6.0	1.0	1.1	0.1	0.5	4.0

Gray Shale	Paltum	1-MST3	25	Shale	Massive	6.0	0.8	0.8	0.0	0.3	4.2
Gray Shale	Paltum	1-MST2	15	Shale	Massive	6.0	0.8	1.0	0.2	1.6	5.2
Gray Shale	Paltum	1-MST1	5	Shale	Massive	7.0	0.3	1.0	0.7	5.9	5.8

APPENDIX A2: Port-Mulgrave section

Formation	Subzone	Sample name	Stratigraphic height (Cm)	TOC wt%	S1	S2	Tmax	HI	PI
Jet Rock Shale	H.Exaratum	JET17	1823	5.05	3.89	21.84	420	432	0.15
Jet Rock Shale	H.Exaratum	JET16	1814	6.536	3.73	26.1	433	399	0.13
Jet Rock Shale	H.Exaratum	JET15	1787	6.132	4.09	26.08	432	425	0.14
Jet Rock Shale	H.Exaratum	JET14	1779	5.741	4.39	27.76	436	484	0.14
Jet Rock Shale	H.Exaratum	JET13	1774	4.261	3.31	18.39	431	432	0.15
Jet Rock Shale	H.Exaratum	JET12	1765	5.58	3.8	26.8	432	479	0.12
Jet Rock Shale	H.Exaratum	JET11	1756	6.036	5.15	24.51	433	406	0.17
Jet Rock Shale	H.Exaratum	JET10	1748	6.38	6.72	28.26	434	443	0.19
Jet Rock Shale	H.Exaratum	JET9	1740	4.931	4.16	17.62	430	357	0.19
Jet Rock Shale	H.Exaratum	JET8	1716	6.148	4.66	21.55	429	351	0.18
Jet Rock Shale	H.Exaratum	JET7	1698	12.617	7.02	41.81	434	331	0.14
Jet Rock Shale	H.Exaratum	JET6	1673	14.255	7.87	42.39	433	297	0.16
Jet Rock Shale	H.Exaratum	JET5	1623	7.135	3.8	26.47	432	371	0.13
Jet Rock Shale	H.Exaratum	JET4	1568	10.071	5.34	32.06	431	318	0.14

Jet Rock Shale	H.Exaratum	JET3	1518	9.614	4.88	32.2	429	335	0.13
Jet Rock Shale	H.Exaratum	JET2	1448	5.466	3.12	22.7	430	415	0.12
Jet Rock Shale	H.Exaratum	JET1	1398	5.327	2.07	20.61	431	387	0.09
Gray Shale	D.Semicelatum	TL.5	1358	2.9032	0.73	9.2	436	317	0.07
Gray Shale	D.Semicelatum	TL.4	1318	3.562	1.15	11.68	436	328	0.09
Gray Shale	D.Semicelatum	TL.3	1268	4.534	2.16	18.84	431	416	0.10
Gray Shale	D.Semicelatum	TL.2	1218	6.141	3.33	20.92	434	341	0.14
Gray Shale	D.Semicelatum	TL.1	1158	6.128	3.79	23.43	433	382	0.14
Gray Shale	D.Semicelatum	4-MST7	1035	1.9273	0.35	3.98	437	207	0.08
Gray Shale	D.Semicelatum	4-MST6	945	1.4107	0.2	2.38	439	169	0.08
Gray Shale	D.Semicelatum	4-MST5	843	1.4787	0.18	2.42	437	164	0.07
Gray Shale	D.Semicelatum	4-MST4	783	1.5991	0.21	2.71	438	169	0.07
Gray Shale	D.Semicelatum	4-MST3	733	1.3921	0.22	2.28	440	164	0.09
Gray Shale	D.Semicelatum	4-MST2	678	1.633	0.25	2.39	439	146	0.09
Gray Shale	D.Semicelatum	4-MST1	628	1.6381	0.26	3.23	439	197	0.07
Gray Shale	Clevelandicum	USB10	578.0	2.638	1.01	12.24	429	464	0.08
Gray Shale	Clevelandicum	USB9	576.0	2.590	0.58	7.11	427	275	0.08
Gray Shale	Clevelandicum	USB7	572.0	3.513	0.85	10.63	436	303	0.07
Gray Shale	Clevelandicum	USB6	570	3.137	0.49	4.93	433	157	0.09
Gray Shale	Clevelandicum	USB5	568.0	1.842	0.50	4.87	435	264	0.09
Gray Shale	Clevelandicum	USB4	566	2.867	0.55	7.15	436	249	0.07
Gray Shale	Clevelandicum	USB3	564	2.428	0.45	4.43	435	182	0.09
Gray Shale	Clevelandicum	USB2	562	1.814	0.56	4.89	435	270	0.10
Gray Shale	Clevelandicum	USB1	560	1.705	0.22	2.24	440	131	0.09
Gray Shale	Paltum	3-MST8	546	1.23	0.22	1.57	436	128	0.12
Gray Shale	Paltum	3-MST7	501	1.022	0.28	3.08	438	301	0.08
Gray Shale	Paltum	3-MST6	488	1.2285	0.21	2.6	439	212	0.07

Gray Shale	Paltum	3-MST5	458	1.5342	0.18	2.43	438	158	0.07
Gray Shale	Paltum	3-MST4	422	1.4255	0.35	2.8	441	196	0.11
Gray Shale	Paltum	3-MST3	372	1.37	0.23	2.38	441	174	0.09
Gray Shale	Paltum	3-MST2	307	1.2	0.24	2.32	438	193	0.09
Gray Shale	Paltum	3-MST1	297	2.1121	0.48	5.17	437	245	0.08
Gray Shale	Paltum	MSB24	294	1.7	0.38	5.30	435	306	0.07
Gray Shale	Paltum	MSB23	292	1.4	0.29	4.06	437	282	0.07
Gray Shale	Paltum	MSB22	290	1.1	0.42	4.30	434	381	0.09
Gray Shale	Paltum	MSB21	289	1.6	0.57	6.09	435	390	0.09
Gray Shale	Paltum	MSB20	287	2.2	0.89	10.94	427	497	0.08
Gray Shale	Paltum	MSB19	285	2.7	1.16	13.42	435	505	0.08
Gray Shale	Paltum	MSB18	283	2.4	1.01	13.33	430	558	0.07
Gray Shale	Paltum	MSB17	281	2.4	1.06	11.98	431	503	0.08
Gray Shale	Paltum	MSB16	278	2.2	1.06	10.99	435	493	0.09
Gray Shale	Paltum	MSB15	275	2.1	0.92	10.55	432	507	0.08
Gray Shale	Paltum	MSB14	273	2.1	0.85	9.65	430	464	0.08
Gray Shale	Paltum	MSB13	269	2.0	0.63	8.24	432	420	0.07
Gray Shale	Paltum	MSB12	266	1.8	0.57	6.85	433	372	0.08
Gray Shale	Paltum	MSB11	263	1.7	0.51	5.19	434	304	0.09
Gray Shale	Paltum	MSB10	258	1.8	0.50	7.86	432	437	0.06
Gray Shale	Paltum	MSB9	254	1.8	0.47	7.10	433	401	0.06
Gray Shale	Paltum	MSB8	251	1.7	0.48	7.72	435	465	0.06
Gray Shale	Paltum	MSB7	248	1.7	0.53	7.57	438	448	0.07
Gray Shale	Paltum	MSB6	245	1.9	0.55	8.88	434	467	0.06
Gray Shale	Paltum	MSB5	241	2.9	0.98	16.79	431	589	0.06
Gray Shale	Paltum	MSB4	238	3.2	1.30	20.17	433	634	0.06
Gray Shale	Paltum	MSB3	235	2.7	0.43	4.31	427	162	0.09
Gray Shale	Paltum	MSB2	233	3.3	1.92	23.53	431	707	0.08
Gray Shale	Paltum	MSB1	230	4.7	2.96	35.81	431	765	0.08

Gray Shale	Paltum	2-MST8	215	2.2	0.48	5.58	432	252	0.08
Gray Shale	Paltum	2-MST7	190	1.1	0.14	1.28	436	116	0.10
Gray Shale	Paltum	2-MST6	165	1.1	0.18	1.50	439	136	0.11
Gray Shale	Paltum	2-MST5	145	1.7	0.42	3.99	436	240	0.10
Gray Shale	Paltum	2-MST4	128	1.2	0.35	2.43	438	201	0.13
Gray Shale	Paltum	2-MST3	110	1.0	0.23	1.47	437	148	0.14
Gray Shale	Paltum	2-MST2	95	1.0	0.18	1.68	439	173	0.10
Gray Shale	Paltum	2-MST1	85	1.1	0.25		437		
Gray Shale	Paltum	LSB14	78	2.507	0.76	6.46	437	258	0.11
Gray Shale	Paltum	LSB13	77	5.726	1.69	21.67	425	378	0.07
Gray Shale	Paltum	LSB12	75	6.273	2.43	27.87	437	444	0.08
Gray Shale	Paltum	LSB11	73	2.915	88.00	9.44	426	324	
Gray Shale	Paltum	LSB10	72	0.802	0.16	0.58	433	72	0.22
Gray Shale	Paltum	LSB9	71	6.809	2.10	22.88	426	336	0.08
Gray Shale	Paltum	LSB8	69	6.296	2.72	27.83	434	442	0.09
Gray Shale	Paltum	LSB7	67	2.333	0.56	6.64	424	285	0.08
Gray Shale	Paltum	LSB6	66	1.410	0.28	2.40	428	170	0.10
Gray Shale	Paltum	LSB5	65	1.275	0.17	1.16	431	91	0.13
Gray Shale	Paltum	LSB4	63	1.160	0.29	2.18	431	188	0.12
Gray Shale	Paltum	LSB3	62	1.542	0.23	2.30	436	149	0.09
Gray Shale	Paltum	LSB2	60	1.020	0.23	1.99	431	195	0.10
Gray Shale	Paltum	LSB1	58	1.305	0.23	1.65	436	126	0.12
Gray Shale	Paltum	1-MST6	55	1.0	0.30	1.51	437	153	0.17
Gray Shale	Paltum	1-MST5	45	0.9	0.22	1.53	426	163	0.13
Gray Shale	Paltum	1-MST4	35	1.0	0.22	1.64	437	166	0.12
Gray Shale	Paltum	1-MST3	25	0.8	0.15	1.01	437	131	0.13
Gray Shale	Paltum	1-MST2	15	0.8	0.08	1.14	437	136	0.07
Gray Shale	Paltum	1-MST1	5	0.3	0.15	1.28	435	388	0.10

APPENDIX A2: Hawsker Bottom section

unit interval	Height (Cm)	Sample Name	S1	S2	PI	TC	wt% TOC	Tmax	HI
Fourth mudstone unit	655	4-MST-26	0.73	3.27	0.18	2.0	1.5	437.0	214
Upper Sulphur Band	556	USB-21	0.69	4.63	0.13	2.4	1.4	444.0	334
Upper Sulphur Band	552	USB-22	0.89	7.80	0.10	3.3	1.8	442.0	444
Upper Sulphur Band	548	USB-23	1.59	8.61	0.16	3.3	2.7	434.0	315
Upper Sulphur Band	544	USB-24	1.71	4.15	0.29	2.1	2.3	437.0	177
Upper Sulphur Band	540	USB-25	1.92	2.87	0.40	1.6	1.7	436.0	167
Third mudstone unit	392	3-MST-20	0.69	2.93	0.19	1.6	1.4	450.0	214
Third mudstone unit	252	3-MST-19	0.81	3.37	0.19	1.7	1.3	446.0	253
Middle Sulphur Band	219	MSB-18	1.59	7.81	0.17	2.6	2.3	446.0	334
Middle Sulphur Band	215	MSB-17	1.30	6.25	0.17	2.2	2.1	445.0	298
Middle Sulphur Band	212	MSB-16	1.22	5.11	0.19	1.9	1.7	448.0	304
Middle Sulphur Band	197	MSB-15	1.12	4.92	0.19	1.9	1.6	446.0	305
Middle Sulphur Band	192	MSB-14	0.92	5.49	0.14	2.2	1.8	445.0	312
Middle Sulphur Band	185	MSB-13	2.06	13.40	0.13	4.1	2.8	442.0	474
Middle Sulphur Band	177	MSB-12	2.63	16.84	0.14	4.8	3.6	443.0	468
Second mudstone unit	165	2-MST-11	0.37	2.60	0.12	1.3	1.1	446.0	227
Second mudstone unit	115	2-MST-10	0.45	2.47	0.15	1.3	1.3	447.0	190
Lower Sulphur Band	75	LSB-1	0.47	2.97	0.14	1.0	0.9	450.0	325
Lower Sulphur Band	73	LSB-2	0.47	2.68	0.15	0.9	1.0	447.0	273
Lower Sulphur Band	70	LSB-3	0.35	1.75	0.17	0.9	1.0	447.0	172
Lower Sulphur Band	68	LSB-4	0.24	1.47	0.14	0.9	0.9	447.0	160
Lower Sulphur Band	66	LSB-5	0.32	1.62	0.16	0.9	0.9	443.0	176
Lower Sulphur Band	63	LSB-6	0.41	1.37	0.23	0.9	0.9	442.0	147
Lower Sulphur Band	61	LSB-7	0.20	1.50	0.12	1.0	0.9	447.0	158
Lower Sulphur Band	57	LSB-8	0.42	1.43	0.23	0.8	0.9	448.0	159

Lower Sulphur Band	52	LSB-9	0.59	1.32	0.31	0.9	0.9	442.0	153
--------------------	----	-------	------	------	------	-----	-----	-------	-----

APPENDIX B: Port-Mulgrave section

Trace elements

Formation	Subzone	Sample name	Stratigraphic height (Cm)	Cu µg/g	Zn µg/g	Mo µg/g	V µg/g	Mn µg/g	Al µg/g	P µg/g
Jet Rock Shale	H.Exaratum	JET17	1823	37.44	195.83	5.36	129.86	239.64	80659.60	611.47
Jet Rock Shale	H.Exaratum	JET16	1814	41.59	89.60	6.02	130.81	254.35	83643.94	594.14
Jet Rock Shale	H.Exaratum	JET15	1787	44.30	86.22	7.37	131.89	279.44	76802.07	622.77
Jet Rock Shale	H.Exaratum	JET14	1779	46.08	93.92	7.49	129.27	267.41	78981.95	526.54
Jet Rock Shale	H.Exaratum	JET13	1774	47.98	77.63	9.03	149.76	488.13	79834.41	487.80
Jet Rock Shale	H.Exaratum	JET12	1765	58.52	127.76	9.56	143.93	316.24	75237.15	634.94
Jet Rock Shale	H.Exaratum	JET11	1756	49.85	135.54	7.50	135.80	239.53	73849.25	581.12
Jet Rock Shale	H.Exaratum	JET10	1748	45.90	83.35	8.46	116.66	269.69	63346.76	593.31
Jet Rock Shale	H.Exaratum	JET9	1740	51.71	116.30	7.86	139.41	257.17	77791.32	529.84
Jet Rock Shale	H.Exaratum	JET8	1716	51.85	180.05	7.62	141.22	340.11	72714.79	666.01
Jet Rock Shale	H.Exaratum	JET7	1698	102.18	121.58	9.87	167.87	309.62	71373.07	620.31
Jet Rock Shale	H.Exaratum	JET6	1673	93.12	106.04	12.88	186.72	395.35	62428.28	841.63

Shale										
Jet Rock										
Shale	H.Exaratum	JET5	1623	69.02	83.48	10.94	170.96	408.76	80341.51	653.58
Jet Rock										
Shale	H.Exaratum	JET4	1568	445.23	486.35	41.97	813.58	1426.09	373000.86	2858.87
Jet Rock										
Shale	H.Exaratum	JET3	1518	156.38	192.92	16.42	328.22	632.88	159954.31	1330.05
Jet Rock										
Shale	H.Exaratum	JET2	1448	93.34	152.59	10.76	305.09	482.62	182602.13	1008.79
Jet Rock										
Shale	H.Exaratum	JET1	1398	123.24	195.56	14.46	300.86	620.08	192035.52	1034.45
Gray Shale	D.Semicelatum	TL.5	1358	58.90	130.64	9.62	240.66	561.64	185503.96	1373.60
Gray Shale	D.Semicelatum	TL.4	1318	31.58	99.31	4.41	126.03	240.21	91346.27	629.54
Gray Shale	D.Semicelatum	TL.3	1268	52.22	76.41	4.74	136.23	295.26	93797.26	1011.03
Gray Shale	D.Semicelatum	TL.2	1218	37.30	89.70	6.21	137.38	268.50	87531.81	662.13
Gray Shale	D.Semicelatum	TL.1	1158	60.02	105.08	6.56	153.15	309.00	91849.41	514.74
Gray Shale	D.Semicelatum	4-MST7	1035	23.51	99.89	4.11	128.26	200.07	99993.46	636.74
Gray Shale	D.Semicelatum	4-MST6	945	23.73	89.79	2.44	117.78	274.26	89966.66	1162.22
Gray Shale	D.Semicelatum	4-MST5	843	19.75	79.75	3.56	96.99	207.40	74657.14	641.19
Gray Shale	D.Semicelatum	4-MST4	783	24.45	94.45	3.36	118.96	283.75	91005.76	1192.63
Gray Shale	D.Semicelatum	4-MST3	733	26.15	95.87	2.64	131.26	320.14	95317.72	1414.80
Gray Shale	D.Semicelatum	4-MST2	678	25.13	108.32	3.73	127.47	304.87	95713.87	1316.18
Gray Shale	D.Semicelatum	4-MST1	628	21.74	76.56	3.61	100.27	222.28	82468.15	634.76
Gray Shale	Clevelandicum	USB10	578.0	84.27	208.44	4.55	101.82	342.51	69686.50	376.47
Gray Shale	Clevelandicum	USB9	576.0	68.83	76.70	4.76	108.99	408.29	77943.77	410.30
Gray Shale	Clevelandicum	USB7	572.0	57.11	87.89	5.78	126.86	548.95	85565.55	490.23
Gray Shale	Clevelandicum	USB6	570	44.74	89.58	5.06	111.75	483.61	75343.02	462.41
Gray Shale	Clevelandicum	USB5	568.0	43.11	117.53	5.10	97.64	422.96	78914.56	450.67
Gray Shale	Clevelandicum	USB4	566	47.41	100.45	5.90	115.35	481.34	82086.36	471.60
Gray Shale	Clevelandicum	USB3	564	101.87	96.56	4.18	115.55	481.32	88037.61	441.61

Gray Shale	Clevelandicum	USB2	562	36.96	85.75	3.14	108.92	471.60	84623.39	413.15
Gray Shale	Clevelandicum	USB1	560	35.55	77.72	3.90	120.06	391.13	93595.81	382.54
Gray Shale	Paltum	3-MST8	546	23.25	83.80	2.57	129.59	209.23	100923.20	575.47
Gray Shale	Paltum	3-MST7	501	31.83	89.54	2.73	106.57	180.99	82836.67	493.76
Gray Shale	Paltum	3-MST6	488	29.52	96.59	3.38	125.74	200.25	97902.20	445.69
Gray Shale	Paltum	3-MST5	458	23.38	83.66	2.31	112.28	150.24	84332.76	349.34
Gray Shale	Paltum	3-MST4	422	30.30	93.81	2.81	138.51	232.82	102854.52	575.35
Gray Shale	Paltum	3-MST3	372	27.25	82.24	3.20	114.36	167.29	84976.11	426.77
Gray Shale	Paltum	3-MST2	307	24.38	81.34	2.81	107.84	241.28	89142.82	429.33
Gray Shale	Paltum	3-MST1	297	31.51	54.54	3.77	103.62	1123.25	65475.50	2063.77
Gray Shale	Paltum	MSB24	294	27.67	81.98	3.73	120.19	312.41	101258.24	472.08
Gray Shale	Paltum	MSB23	292	23.38	89.77	2.96	111.18	326.24	89028.92	433.38
Gray Shale	Paltum	MSB22	290	21.76	131.42	2.97	109.65	355.62	92217.98	430.40
Gray Shale	Paltum	MSB21	289	27.64	89.94	4.21	115.55	278.56	90116.31	438.18
Gray Shale	Paltum	MSB20	287	39.34	66.24	3.56	113.86	297.65	91619.26	435.06
Gray Shale	Paltum	MSB19	285	39.78	72.79	4.59	114.14	304.18	85410.28	424.64
Gray Shale	Paltum	MSB18	283	43.88	74.40	6.21	112.92	314.30	90658.07	440.54
Gray Shale	Paltum	MSB17	281	36.24	80.70	4.52	124.36	304.25	90328.87	479.52
Gray Shale	Paltum	MSB16	278	36.86	75.46	4.31	121.02	307.70	92817.02	449.54
Gray Shale	Paltum	MSB15	275	29.36	68.70	3.16	107.75	276.53	83313.54	449.96
Gray Shale	Paltum	MSB14	273	30.43	88.76	4.21	122.87	291.90	96348.84	482.01
Gray Shale	Paltum	MSB13	269	24.17	89.99	3.93	123.41	266.91	95914.76	492.22
Gray Shale	Paltum	MSB12	266	28.37	90.72	3.25	122.45	269.80	99912.02	484.23
Gray Shale	Paltum	MSB11	263	22.32	86.62	2.69	124.69	275.57	96435.87	518.26
Gray Shale	Paltum	MSB10	258	29.75	81.59	3.99	122.30	281.48	98750.67	532.52
Gray Shale	Paltum	MSB9	254	25.59	108.94	3.46	126.61	276.41	98219.09	554.10
Gray Shale	Paltum	MSB8	251	26.27	99.85	4.12	127.47	295.74	100915.25	526.98
Gray Shale	Paltum	MSB7	248	28.87	124.55	4.37	126.13	311.84	92845.83	548.75
Gray Shale	Paltum	MSB6	245	48.38	88.73	4.64	131.88	381.83	100115.12	669.11

Gray Shale	Paltum	MSB5	241	50.58	108.14	4.96	131.19	404.33	88927.75	575.14
Gray Shale	Paltum	MSB4	238	63.97	140.77	6.56	143.07	438.58	95601.34	551.74
Gray Shale	Paltum	MSB3	235	53.99	99.87	7.39	117.46	425.83	81131.56	532.94
Gray Shale	Paltum	MSB2	233	66.23	98.06	6.83	137.11	478.63	92555.59	623.11
Gray Shale	Paltum	MSB1	230	73.66	110.38	6.71	141.92	501.11	87687.05	653.46
										20131.0
Gray Shale	Paltum	2-MST8	215	83.64	88.66	23.30	122.66	545.92	77301.82	6
Gray Shale	Paltum	2-MST7	190	37.97	132.95	5.33	126.36	268.42	80832.77	308.41
Gray Shale	Paltum	2-MST6	165	6.01	92.26	4.27	145.72	165.37	95906.67	285.02
Gray Shale	Paltum	2-MST5	145	29.12	73.98	7.86	132.29	238.63	85752.24	319.67
Gray Shale	Paltum	2-MST4	128	23.95	76.94	4.41	141.02	172.28	102115.72	269.77
Gray Shale	Paltum	2-MST3	110	24.78	80.51	3.09	123.85	170.65	90852.89	302.52
Gray Shale	Paltum	2-MST2	95	17.96	72.23	4.39	121.54	355.38	90400.40	491.73
Gray Shale	Paltum	2-MST1	85	23.01	186.13	3.08	113.41	427.34	81725.51	1384.63
Gray Shale	Paltum	LSB14	78	85.29	100.89	24.95	108.93	489.13	75911.12	0.00
Gray Shale	Paltum	LSB13	77	85.20	89.74	23.72	133.69	630.85	81092.62	511.99
Gray Shale	Paltum	LSB12	75	54.45	81.23	19.59	135.79	591.34	79152.67	388.48
Gray Shale	Paltum	LSB11	73	22.76	63.40	21.76	92.23	633.84	66627.00	450.14
Gray Shale	Paltum	LSB10	72	5.91	41.87	23.50	56.67	496.98	52946.51	364.34
Gray Shale	Paltum	LSB9	71	37.87	88.64	32.27	129.49	681.11	77345.99	303.65
Gray Shale	Paltum	LSB8	69	77.76	88.55	32.78	129.40	713.15	78063.42	283.98
Gray Shale	Paltum	LSB7	67	48.74	73.76	33.60	112.20	511.61	78844.14	260.42
Gray Shale	Paltum	LSB6	66	24.83	54.43	22.82	98.61	319.90	76546.92	249.10
Gray Shale	Paltum	LSB5	65	14.53	50.21	7.89	93.07	237.62	77596.82	250.99
Gray Shale	Paltum	LSB4	63	20.55	110.45	7.42	135.08	266.01	95372.13	265.49
Gray Shale	Paltum	LSB3	62	21.41	87.10	5.97	156.23	308.37	106555.88	268.80
Gray Shale	Paltum	LSB2	60	20.49	64.61	5.87	138.58	282.11	101165.89	255.62
Gray Shale	Paltum	LSB1	58	18.78	67.75	6.75	143.98	305.35	106153.28	259.28
Gray Shale	Paltum	1-MST6	55	68.40	82.89	9.04	61.71	98.87	64793.67	215.94

Gray Shale	Paltum	1-MST5	45	30.15	82.71	8.08	136.48	247.49	91784.92	365.82
Gray Shale	Paltum	1-MST4	35	2.91	7.29	0.87	12.01	20.60	8592.62	23.35
Gray Shale	Paltum	1-MST3	25	25.95	80.91	9.61	143.60	277.96	91584.46	286.30
Gray Shale	Paltum	1-MST2	15	26.17	73.19	7.35	155.35	319.06	101370.61	289.60
Gray Shale	Paltum	1-MST1	5	25.56	132.15	9.53	140.38	301.64	90257.20	283.08

APPENDIX B: Hawsker Bottom section

Trace elements

Unit interval	Height (Cm)	Sample Name	Cu µg/g	Zn µg/g	Mo µg/g	V µg/g	Al (wt%)
Fourth mudstone unit	655	4-MST-26	27.15	87.51	3.07	119.3	10.1
Upper Sulphur Band	556	USB-21	44.07	79.96	6.13	100.7	7.9
Upper Sulphur Band	552	USB-22	49.08	74.82	7.02	111.4	7.8
Upper Sulphur Band	548	USB-23	50.22	77.43	6.07	118.4	8.5
Upper Sulphur Band	544	USB-24	41.11	70.24	3.24	108.9	8.7
Upper Sulphur Band	540	USB-25	26.06	85.43	3.81	123.8	9.8
Third mudstone unit	392	3-MST-20	29.60	82.94	5.02	133.0	10.3
Third mudstone unit	252	3-MST-19	21.33	65.26	5.09	112.4	9.3
Middle Sulphur Band	219	MSB-18	45.76	80.11	6.90	105.8	8.6
Middle Sulphur Band	215	MSB-17	35.66	60.19	6.85	113.9	9.4
Middle Sulphur Band	212	MSB-16	26.95	70.97	5.93	118.4	9.9
Middle Sulphur Band	197	MSB-15	26.21	84.76	5.11	112.9	9.4
Middle Sulphur Band	192	MSB-14	40.38	69.31	5.69	112.2	8.9
Middle Sulphur Band	185	MSB-13	64.09	74.29	8.84	119.1	7.6
Middle Sulphur Band	177	MSB-12	77.21	92.52	9.37	145.3	8.3
Second mudstone unit	165	2-MST-11	31.20	65.99	5.20	129.3	9.8
Second mudstone unit	115	2-MST-10	21.22	70.29	4.89	132.7	10.0
Lower Sulphur Band	75	LSB-1	25.71	89.65	4.81	134.8	8.8
Lower Sulphur Band	73	LSB-2	25.10	78.03	5.40	139.9	9.5
Lower Sulphur Band	70	LSB-3	24.34	107.13	4.88	153.3	10.0
Lower Sulphur Band	68	LSB-4	21.82	81.49	4.81	130.9	9.0
Lower Sulphur Band	66	LSB-5	24.02	63.77	4.39	132.6	9.0
Lower Sulphur Band	63	LSB-6	24.85	61.37	4.88	131.1	9.0

Lower Sulphur Band	61	LSB-7	28.04	62.56	6.22	135.3	9.3
Lower Sulphur Band	57	LSB-8	24.37	95.51	6.20	127.0	8.9
Lower Sulphur Band	52	LSB-9	23.91	78.37	5.02	115.6	8.5

APPENDIX C: Port-Mulgrave section

Iron speciation

Formation	Subzone	Sample name	Stratigraphic height (Cm)	Fe carb wt%	Fe OX2 wt%	Fe mag wt%	FePRS wt%	FeT wt%	Fe pyrite (wt%)
Jet Rock Shale	H.Exaratum	JET17	1823	0.901	0.058	0.0789	1.175	6.319	3.81
Jet Rock Shale	H.Exaratum	JET16	1814	0.723	0.041	0.0701	1.327	5.919	1.71
Jet Rock Shale	H.Exaratum	JET15	1787	0.836	0.147	0.0935	1.632	7.484	3.19
Jet Rock Shale	H.Exaratum	JET14	1779	0.841	0.106	0.0797	1.355	6.183	3.36
Jet Rock Shale	H.Exaratum	JET13	1774	0.964	0.054	0.0778	1.521	6.999	1.61
Jet Rock Shale	H.Exaratum	JET12	1765	0.844	0.051	0.0749	1.476	8.546	3.59
Jet Rock Shale	H.Exaratum	JET11	1756	0.973	0.068	0.0759	1.255	7.170	2.77
Jet Rock Shale	H.Exaratum	JET10	1748	0.891	0.050	0.0947	1.447	7.041	2.64
Jet Rock Shale	H.Exaratum	JET9	1740	0.926	0.051	0.0755	1.395	6.454	3.47
Jet Rock Shale	H.Exaratum	JET8	1716	1.132	0.056	0.0832	0.941	6.985	4.42

Jet Rock Shale	H.Exaratum	JET7	1698	0.898	0.046	0.0717	0.833	6.564	4.01
Jet Rock Shale	H.Exaratum	JET6	1673	0.936	0.041	0.0915	0.781	6.782	3.28
Jet Rock Shale	H.Exaratum	JET5	1623	0.816	0.044	0.0630	0.737	5.599	3.44
Jet Rock Shale	H.Exaratum	JET4	1568	0.947	0.079	0.0904	1.187	7.419	3.64
Jet Rock Shale	H.Exaratum	JET3	1518	0.930	0.092	0.0943	1.027	6.637	4.22
Jet Rock Shale	H.Exaratum	JET2	1448	0.928	0.081	0.0904	1.095	6.786	2.39
Jet Rock Shale	H.Exaratum	JET1	1398	0.865	0.116	0.0948	1.115	6.252	3.40
Gray Shale	D.Semicelatum	TL.5	1358	0.421	0.054	0.0765	1.026	4.910	2.30
Gray Shale	D.Semicelatum	TL.4	1318	0.608	0.061	0.0792	0.950	5.972	3.16
Gray Shale	D.Semicelatum	TL.3	1268	0.654	0.057	0.1007	1.042	5.755	1.61
Gray Shale	D.Semicelatum	TL.2	1218	0.827	0.075	0.0823	1.095	7.521	1.19
Gray Shale	D.Semicelatum	TL.1	1158	0.646	0.088	0.0778	1.036	6.917	0.17
Gray Shale	D.Semicelatum	4-MST7	1035	0.318	0.055	0.0985	1.227	4.889	0.96
Gray Shale	D.Semicelatum	4-MST6	945	1.095	0.109	0.2528	1.336	4.734	0.50
Gray Shale	D.Semicelatum	4-MST5	843	0.691	0.082	0.1624	1.365	3.398	0.81
Gray Shale	D.Semicelatum	4-MST4	783	0.830	0.084	0.1880	1.321	4.649	0.56
Gray Shale	D.Semicelatum	4-MST3	733	1.385	0.127	0.2733	1.267	5.576	0.98
Gray Shale	D.Semicelatum	4-MST2	678	1.106	0.121	0.2695	1.344	5.155	0.88
Gray Shale	D.Semicelatum	4-MST1	628	0.859	0.126	0.1977	1.342	4.143	1.23
Gray Shale	Clevelandicum	USB10	578.0	1.036	0.911	0.2117	1.335	13.072	3.35
Gray Shale	Clevelandicum	USB9	576.0	1.112	0.315	0.1982	1.364	11.778	5.84
Gray Shale	Clevelandicum	USB7	572.0	1.588	0.117	0.2252	1.457	11.562	1.26
Gray Shale	Clevelandicum	USB6	570	1.669	0.123	0.1964	1.415	8.311	1.47
Gray Shale	Clevelandicum	USB5	568.0	1.204	0.080	0.1679	1.500	9.654	1.33

Gray Shale	Clevelandicum	USB4	566	1.394	0.106	0.1748	1.637	8.229	4.14
Gray Shale	Clevelandicum	USB3	564	1.030	0.095	0.1647	1.532	9.378	3.94
Gray Shale	Clevelandicum	USB2	562	0.893	0.094	0.1579	1.464	6.959	2.70
Gray Shale	Clevelandicum	USB1	560	0.655	0.084	0.1430	1.300	7.677	2.86
Gray Shale	Paltum	3-MST8	546					5.674	1.19
Gray Shale	Paltum	3-MST7	501	0.314	0.134	0.1941	1.249	3.554	2.79
Gray Shale	Paltum	3-MST6	488					5.579	1.06
Gray Shale	Paltum	3-MST5	458	0.365	0.125	0.1898	1.423	3.903	1.68
Gray Shale	Paltum	3-MST4	422					6.359	1.35
Gray Shale	Paltum	3-MST3	372	0.388	0.118	0.2208	1.325	3.778	0.76
Gray Shale	Paltum	3-MST2	307					7.218	2.46
Gray Shale	Paltum	3-MST1	297	3.413	0.271	4.8186	2.862	13.631	1.46
Gray Shale	Paltum	MSB24	294	0.535	0.094	0.2153	1.469	5.229	1.74
Gray Shale	Paltum	MSB23	292	0.470	0.083	0.2057	1.415	4.850	2.23
Gray Shale	Paltum	MSB22	290	0.440	0.074	0.1926	1.406	4.674	1.80
Gray Shale	Paltum	MSB21	289	0.490	0.065	0.1782	1.396	5.737	2.77
Gray Shale	Paltum	MSB20	287	0.735	0.081	0.2000	1.504	5.976	2.94
Gray Shale	Paltum	MSB19	285	0.984	0.665	0.2087	1.431	6.699	2.71
Gray Shale	Paltum	MSB18	283	0.952	0.198	0.1942	1.610	6.710	3.43
Gray Shale	Paltum	MSB17	281	0.770	0.597	0.2024	1.416	6.556	2.76
Gray Shale	Paltum	MSB16	278	0.800	0.627	0.2044	1.332	6.013	2.08
Gray Shale	Paltum	MSB15	275	0.671	0.067	0.1920	1.452	5.527	2.50
Gray Shale	Paltum	MSB14	273	0.644	0.089	0.1971	1.416	5.694	2.47
Gray Shale	Paltum	MSB13	269	0.576	0.082	0.2089	1.459	5.287	2.16
Gray Shale	Paltum	MSB12	266	0.568	0.082	0.2066	1.436	5.234	2.16
Gray Shale	Paltum	MSB11	263	0.505	0.078	0.2002	1.438	5.109	1.88
Gray Shale	Paltum	MSB10	258	0.614	0.081	0.2007	1.476	5.503	2.50
Gray Shale	Paltum	MSB9	254	0.525	0.068	0.1968	1.444	5.182	2.25
Gray Shale	Paltum	MSB8	251	0.550	0.073	0.1991	1.471	6.300	2.25

Gray Shale	Paltum	MSB7	248	0.554	0.069	0.2025	1.615	6.774	2.40
Gray Shale	Paltum	MSB6	245	0.753	0.081	0.2191	1.704	7.067	3.61
Gray Shale	Paltum	MSB5	241	1.053	0.101	0.2479	1.640	5.464	3.83
Gray Shale	Paltum	MSB4	238	1.039	0.107	0.2701	1.590	7.999	4.20
Gray Shale	Paltum	MSB3	235	0.990	1.013	0.2725	1.327	7.898	4.72
Gray Shale	Paltum	MSB2	233	1.199	0.139	0.2695	1.613	7.470	4.22
Gray Shale	Paltum	MSB1	230	1.247	0.094	0.2784	1.710	7.924	4.67
Gray Shale	Paltum	2-MST8	215					11.065	4.84
Gray Shale	Paltum	2-MST7	190	0.650	0.131	0.2052	1.178	5.757	2.76
Gray Shale	Paltum	2-MST6	165					5.094	0.94
Gray Shale	Paltum	2-MST5	145	0.584	0.151	0.2432	1.490	5.315	3.22
Gray Shale	Paltum	2-MST4	128					6.140	1.44
Gray Shale	Paltum	2-MST3	110	0.305	0.136	0.2115	1.362	4.198	3.52
Gray Shale	Paltum	2-MST2	95					6.694	2.20
Gray Shale	Paltum	2-MST1	85	0.544	0.133	0.2690	1.288	5.207	2.69
Gray Shale	Paltum	LSB14	78	1.013	0.942	0.4921	1.494	8.694	5.39
Gray Shale	Paltum	LSB13	77	1.199	0.545	0.3324	1.670	10.164	1.50
Gray Shale	Paltum	LSB12	75	1.151	0.960	0.2810	1.629	9.126	5.71
Gray Shale	Paltum	LSB11	73	1.190	0.550	0.2430	1.243	8.810	2.61
Gray Shale	Paltum	LSB10	72	1.592	0.576	0.1789	1.172	11.050	2.60
Gray Shale	Paltum	LSB9	71	1.164	0.522	0.2983	1.496	11.685	2.72
Gray Shale	Paltum	LSB8	69	1.124	0.802	0.2411	1.478	11.283	7.19
Gray Shale	Paltum	LSB7	67	0.788	0.435	0.2548	1.322	9.449	3.17
Gray Shale	Paltum	LSB6	66	0.688	0.532	0.1806	1.401	6.350	3.77
Gray Shale	Paltum	LSB5	65	0.462	0.194	0.1556	1.524	4.398	1.94
Gray Shale	Paltum	LSB4	63	0.514	0.122	0.2040	1.510	5.469	2.51
Gray Shale	Paltum	LSB3	62	0.403	0.088	0.2126	1.741	5.434	2.19
Gray Shale	Paltum	LSB2	60	0.429	0.097	0.1945	1.357	5.536	2.47
Gray Shale	Paltum	LSB1	58	0.397	0.107	0.2081	1.689	5.323	4.29

Gray Shale	Paltum	1-MST6	55					4.613	1.67
Gray Shale	Paltum	1-MST5	45	0.498	0.247	0.3066	1.511	4.511	2.14
Gray Shale	Paltum	1-MST4	35					6.466	2.30
Gray Shale	Paltum	1-MST3	25	0.415	0.177	0.2668	1.529	5.420	2.98
Gray Shale	Paltum	1-MST2	15					5.720	2.15
Gray Shale	Paltum	1-MST1	5	0.369	0.205	0.2611	1.541	5.473	3.78

APPENDIX C: Hawsker Bottom section

Unit interval	Height (Cm)	Sample Name	Fe carb wt%	Fe OX2 wt%	Fe Mag wt%	Fe pyrit Wt%	FeT wt%
Fourth mudstone unit	655	4-MST-26	0.90	0.07	0.16	1.44	4.79
Upper Sulphur Band	556	USB-21	1.09	0.09	0.12	4.10	5.20
Upper Sulphur Band	552	USB-22	2.38	0.13	0.19	3.14	6.59
Upper Sulphur Band	548	USB-23	1.50	0.12	0.15	4.44	7.80
Upper Sulphur Band	544	USB-24	0.93	0.06	0.12	0.54	8.38
Upper Sulphur Band	540	USB-25	0.55	0.07	0.12	2.41	6.85
Third mudstone unit	392	3-MST-20	0.51	0.07	0.14	1.38	4.43
Third mudstone unit	252	3-MST-19	0.67	0.07	0.15	2.68	5.59
Middle Sulphur Band	219	MSB-18	0.99	0.08	0.15	3.99	6.94
Middle Sulphur Band	215	MSB-17	0.76	0.14	0.13	1.63	5.79
Middle Sulphur Band	212	MSB-16	0.56	0.05	0.13	2.22	5.04
Middle Sulphur Band	197	MSB-15	0.77	0.06	0.14	2.28	5.06
Middle Sulphur Band	192	MSB-14	0.99	0.07	0.18	3.41	6.52
Middle Sulphur Band	185	MSB-13	2.67	0.10	0.46	4.13	8.71
Middle Sulphur Band	177	MSB-12	2.80	0.11	0.03	0.39	8.86
Second mudstone unit	165	2-MST-11	0.44	0.06	0.12	2.99	5.60
Second mudstone unit	115	2-MST-10	0.44	0.06	0.13	1.53	4.12

Lower Sulphur Band	75	LSB-1	0.48	0.06	0.14	2.13	4.63
Lower Sulphur Band	73	LSB-2	0.42	0.05	0.14	2.30	4.84
Lower Sulphur Band	70	LSB-3	0.41	0.06	0.00	0.40	4.99
Lower Sulphur Band	68	LSB-4	0.48	0.07	0.28	2.10	4.37
Lower Sulphur Band	66	LSB-5	0.53	0.07	0.16	0.35	4.76
Lower Sulphur Band	63	LSB-6	0.50	0.06	0.15	1.01	4.65
Lower Sulphur Band	61	LSB-7	0.52	0.07	0.15	2.12	4.92
Lower Sulphur Band	57	LSB-8	0.51	0.06	0.14	0.28	4.67
Lower Sulphur Band	52	LSB-9	0.51	0.05	0.13	0.51	3.84

APPENDIX D: Port-Mulgrave section

Isotopes analysis:

Formation	Subzone	Sample name	Stratigraphic height (Cm)	S as FeS ₂ (wt%)	$\delta^{13}\text{C}_{\text{TOC}}$ (‰)	$\delta^{34}\text{S}$ (‰)
Jet Rock Shale	H.Exaratum	JET17	1823	4.37	-28.7522	-25.55
Jet Rock Shale	H.Exaratum	JET16	1814	1.96	-28.5639	-23.98
Jet Rock Shale	H.Exaratum	JET15	1787	3.67	-29.1582	-23.86
Jet Rock Shale	H.Exaratum	JET14	1779	3.85	-29.5667	-24.86
Jet Rock Shale	H.Exaratum	JET13	1774	1.85	-29.3875	-24.47
Jet Rock Shale	H.Exaratum	JET12	1765	4.13	-30.2013	-23.48
Jet Rock Shale	H.Exaratum	JET11	1756	3.18	-30.1541	-25.73
Jet Rock Shale	H.Exaratum	JET10	1748	3.03	-30.1798	-24.82
Jet Rock Shale	H.Exaratum	JET9	1740	3.98	-30.579	-25.33
Jet Rock Shale	H.Exaratum	JET8	1716	5.08	-30.4889	-22.61
Jet Rock Shale	H.Exaratum	JET7	1698	4.60	-31.0741	-23.05
Jet Rock Shale	H.Exaratum	JET6	1673	3.76	-32.046	-20.85
Jet Rock Shale	H.Exaratum	JET5	1623	3.95	-32.4533	-25.80

Jet Rock Shale	H.Exaratum	JET4	1568	4.18	-31.6361	-26.40
Jet Rock Shale	H.Exaratum	JET3	1518	4.85	-32.3382	-26.42
Jet Rock Shale	H.Exaratum	JET2	1448	2.74	-30.2664	-27.46
Jet Rock Shale	H.Exaratum	JET1	1398	3.91	-31.5761	-26.82
Gray Shale	D.Semicelatum	TL.5	1358	2.64	-26.4104	-35.93
Gray Shale	D.Semicelatum	TL.4	1318	3.63	-26.7049	-32.76
Gray Shale	D.Semicelatum	TL.3	1268	1.85	-28.291	-31.98
Gray Shale	D.Semicelatum	TL.2	1218	1.36	-27.2885	-26.66
Gray Shale	D.Semicelatum	TL.1	1158	0.19	-30.5005	-28.46
Gray Shale	D.Semicelatum	4-MST7	1035	1.11	-25.6461	-33.22
Gray Shale	D.Semicelatum	4-MST6	945	0.57	-25.3766	-32.95
Gray Shale	D.Semicelatum	4-MST5	843	0.94	-25.5151	-33.74
Gray Shale	D.Semicelatum	4-MST4	783	0.64	-25.4799	-30.60
Gray Shale	D.Semicelatum	4-MST3	733	1.13	-25.5215	-30.77
Gray Shale	D.Semicelatum	4-MST2	678	1.01	-25.3476	-32.13
Gray Shale	D.Semicelatum	4-MST1	628	1.42	-25.6208	-32.05
Gray Shale	Clevelandicum	USB10	578.0	3.84	-25.8111	-43.85
Gray Shale	Clevelandicum	USB9	576.0	6.71	-25.9384	-38.85
Gray Shale	Clevelandicum	USB7	572.0	1.45	-26.4882	-32.63
Gray Shale	Clevelandicum	USB6	570	1.69	-26.5205	
Gray Shale	Clevelandicum	USB5	568.0	1.53	-25.9892	-32.11
Gray Shale	Clevelandicum	USB4	566	4.75	-26.0978	-34.40
Gray Shale	Clevelandicum	USB3	564	4.53	-25.9123	-34.65
Gray Shale	Clevelandicum	USB2	562	3.10	-25.7566	-34.78
Gray Shale	Clevelandicum	USB1	560	3.29	-25.7247	-35.64
Gray Shale	Paltum	3-MST8	546	1.37	-25.7288	-39.01

Gray Shale	Paltum	3-MST7	501	3.21	-25.569	-39.30
Gray Shale	Paltum	3-MST6	488	1.22	-25.7477	-38.47
Gray Shale	Paltum	3-MST5	458	1.93	-25.8221	-31.26
Gray Shale	Paltum	3-MST4	422	1.55	-25.7399	-27.10
Gray Shale	Paltum	3-MST3	372	0.87	-25.6622	-31.85
Gray Shale	Paltum	3-MST2	307	2.82	-26.235	-29.36
Gray Shale	Paltum	3-MST1	297	1.68	-27.6012	-32.71
Gray Shale	Paltum	MSB24	294	2.00	-27.5039	-39.44
Gray Shale	Paltum	MSB23	292	2.57	-27.2381	-38.23
Gray Shale	Paltum	MSB22	290	2.07	-26.6727	-41.50
Gray Shale	Paltum	MSB21	289	3.18	-26.7721	-39.70
Gray Shale	Paltum	MSB20	287	3.37	-27.2009	-37.06
Gray Shale	Paltum	MSB19	285	3.11	-27.14	-37.92
Gray Shale	Paltum	MSB18	283	3.94	-26.9654	-34.18
Gray Shale	Paltum	MSB17	281	3.16	-26.9295	-35.69
Gray Shale	Paltum	MSB16	278	2.39	-26.6872	-36.45
Gray Shale	Paltum	MSB15	275	2.88	-26.6233	-36.88
Gray Shale	Paltum	MSB14	273	2.84	-26.6955	-39.68
Gray Shale	Paltum	MSB13	269	2.48	-26.5684	-37.60
Gray Shale	Paltum	MSB12	266	2.48	-26.617	-38.92
Gray Shale	Paltum	MSB11	263	2.16	-26.7577	-38.43
Gray Shale	Paltum	MSB10	258	2.87	-26.8107	-39.25
Gray Shale	Paltum	MSB9	254	2.58	-26.9554	-36.07
Gray Shale	Paltum	MSB8	251	2.59	-26.8572	-39.96
Gray Shale	Paltum	MSB7	248	2.75	-27.1107	-38.16
Gray Shale	Paltum	MSB6	245	4.14	-27.2449	-34.56
Gray Shale	Paltum	MSB5	241	4.40	-27.5718	-33.32
Gray Shale	Paltum	MSB4	238	4.82	-27.7831	-32.99
Gray Shale	Paltum	MSB3	235	5.42	-27.8665	-32.34

Gray Shale	Paltum	MSB2	233	4.84	-28.0755	-32.36
Gray Shale	Paltum	MSB1	230	5.36	-28.2416	-31.08
Gray Shale	Paltum	2-MST8	215	5.55	-28.9631	-33.54
Gray Shale	Paltum	2-MST7	190	3.17	-27.7755	-33.56
Gray Shale	Paltum	2-MST6	165	1.08	-26.5494	-46.96
Gray Shale	Paltum	2-MST5	145	5.39	-27.6142	-36.24
Gray Shale	Paltum	2-MST4	128	1.66	-26.4833	-42.34
Gray Shale	Paltum	2-MST3	110	4.04	-26.1768	-39.08
Gray Shale	Paltum	2-MST2	95	2.52	-26.31	-35.44
Gray Shale	Paltum	2-MST1	85	3.09	-27.3856	-32.02
Gray Shale	Paltum	LSB14	78	6.19	-28.9835	-34.32
Gray Shale	Paltum	LSB13	77	1.72	-29.5227	-33.83
Gray Shale	Paltum	LSB12	75	6.56	-29.257	-30.71
Gray Shale	Paltum	LSB11	73	2.99	-29.1423	-31.08
Gray Shale	Paltum	LSB10	72	2.98	-28.4049	-23.18
Gray Shale	Paltum	LSB9	71	3.12	-28.9154	-30.96
Gray Shale	Paltum	LSB8	69	8.25	-28.9405	-32.20
Gray Shale	Paltum	LSB7	67	3.64	-28.7959	-33.27
Gray Shale	Paltum	LSB6	66	4.33	-28.3894	-37.99
Gray Shale	Paltum	LSB5	65	2.22	-27.8132	-36.45
Gray Shale	Paltum	LSB4	63	2.88	-27.7573	-38.29
Gray Shale	Paltum	LSB3	62	2.51	-27.2245	-35.23
Gray Shale	Paltum	LSB2	60	2.84	-27.3678	-34.42
Gray Shale	Paltum	LSB1	58	4.93	-27.2131	-30.19
Gray Shale	Paltum	1-MST6	55	1.91	-27.1749	-40.62
Gray Shale	Paltum	1-MST5	45	2.46	-28.1535	-33.69
Gray Shale	Paltum	1-MST4	35	2.64	-27.4211	-36.60
Gray Shale	Paltum	1-MST3	25	3.42	-27.492	-32.80
Gray Shale	Paltum	1-MST2	15	2.47	-27.2972	

APPENDIX E1: Port-Mulgrave section

Normal alkanes

Stratigraphic height (Cm)	Sample	normal alkanes					Prystane	n-C18	Phytane	n-C19	n-C20	n-C21	n-C22	n-C23
		n-C13	n-C14	n-C15	n-C16	n-C17								
1823	Jet 17	38644	65235	84089	86122	89349	94224	68081	65518	61861	53588	54429	46099	44349
1787	Jet15	185	384	640	657	749	1054	527	738	545	512	469	444	446
				12244	14381	15969		12667			12062	11161		
1774	Jet 13	17085	68078	5	2	5	213947	5	167464	3677	7	1	92208	91452
1756	Jet 11	280	711	1263	1299	1156	1612	712	1052	784	698	623	590	583
				12829	14474	16155		12767		12098	13251	10896		
1716	Jet 8	39102	83606	8	4	3	224976	1	178536	1	3	0	87839	83389
		41882	60907	56191	55278	55668		43216		34279	29058	21958	17217	15930
1673	Jet 6	5	0	0	8	9	425218	2	367832	6	5	1	4	5
		10689	16681	23204	22242	22746		17404		14862	15553	12294		
1568	Jet 4	2	9	4	4	3	292568	2	228819	9	4	1	95575	86733
1398	Jet 1	344	533	705	689	781	1207	595	864	607	568	563	501	508
1358	TL.5	7298	20222	34734	41019	48327	53530	35427	19683	39775	28935	26839	29573	26538
		11773	13272	13358	12797	12370								
1318	TL.4	3	7	3	0	5	165155	98603	79376	91987	76159	69899	62705	60251
1218	TL.2													
1158	TL.1	20935	39507	54940	53493	52720	70364	39727	41636	44557	29100	26323	27427	22502
945	4-MST 6	2460	9830	18027	21507	25758	22673	20686	5198	20173	19005	19080	17978	19069
843	4-MST 5			4285	10201	15945	14503	14355	3613	14362	14217	14381	13701	14588
783	4-MST 4													
678	4-MST 2		2308	8401	12737	15863	13602	13027	3156	13142	12730	12965	12288	13146

628	4-MST 1		2982	11670	18355	24268	21457	20155	5400	18502	20462	20429	19658	21034
578.0	USB10		4915	18971	30981	44903	119170	36250	36695	39640	32582	37107	31322	32238
572.0	USB7													
570	USB6	31980	45360	65675	72477	85832	210741	58953	62331	57740	49939	46461	42285	42849
						10328								
568.0	USB5	41901	62894	83996	88631	7	238129	72191	73632	71330	61600	58861	54507	53877
						10329								
566	USB4	43903	64339	82283	85899	7	227449	73993	66543	73748	64338	60766	55019	55340
564	USB3						322	649	216	177		168	151	
501	3-MST 7		2396	10828	19456	27195	23895	23031	5168	20787	22446	22722	22147	22832
458	3-MST 5		8237	16685	19991	22744	23867	16702	4323	14440	15245	15435	14920	16180
297	3-MST 1	5421	14018	19733	20102	21912	37935	15977	10202	13192	13347	13007	12573	13047
294	MSB24					71	114	53	29			44	39	
287	MSB 20	29540	63674	80702	80134	83500	159256	63538	40944	56108	55173	55757	52924	56765
283	MSB18					124	245	89	76			70	63	
278	MSB 16	10820	20442	25469	25190	26953	51329	21019	14500	17991	19055	19320	18821	20173
254	MSB 9	8366	17046	21845	22962	25734	39610	20018	9704	17920	18051	18211	17562	18811
251	MSB8					21	34	16	8			14	13	
238	MSB 4	7474	20305	30065	30569	33120	66519	24539	21965	20271	20551	20046	19238	19920
233	MSB2					103	213	72	75			52	45	
	2-MST													
215	8	17914	31949	39547	36105	37099	100676	27811	33374	21076	22107	20865	22960	19595
	2-MST													
128	4	3537	14213	21372	22460	24432	28426	20417	5658	20353	20380	21234	20799	22956
	2-MST													
85	1	2441	2362	13731	14290	15864	26480	12549	7114	12030	12705	13013	12618	13104
78	LSB14	24431	43370	59536	57478	62517	169670	46703	58116	43136	36726	33451	29235	29927
				10755	10826	11515								
77	LSB13	45144	75191	3	6	7	310908	88590	113289	79201	68012	61035	52704	53438
75	LSB12													

			12537	18729	19988	22485		17290		15899	13976	12654	11197	11337
73	LSB11	82014	3	6	0	5	624739	6	230515	8	4	1	1	1
72	LSB10	7948	14495	21452	21950	24271	69772	18034	25355	16477	14963	14206	13076	13605
		10570	10377	11639	10071									
71	LSB9	0	1	6	0	99725	278806	72558	95629	65304	55685	49073	44033	43090
69	LSB8					74	247	46	83			19	14	
		10218	12346	15101	13965	14189		10478						
67	LSB7	9	3	1	4	0	395146	0	141502	92932	27380	77425	69186	61607
				10014										
66	LSB6	75492	88009	3	88605	91686	236729	65531	81639	59476	50813	45458	41706	40510
65	LSB5	14668	22912	31454	33875	35613	86591	27781	26952	25960	22773	21477	20817	21809
63	LSB 4	1093	3477	4578	5200	9581	4586	2590	4245	4682	5149	5249	6041	5909
62	LSB3	14850	22332	29013	30902	31112	44342	25743	12439	26105	25297	27217	26091	29218
	Bitume													
	n LSB	84061	84382	93992	78998	77435	197061	54519	65315	51054	41055	36421	30162	31458
35	1-MST 4		3548	7063	7849	8696	11287	7629	2585	7609	8108	9007	9219	10368

APPENDIX E1: Port-Mulgrave section

Stratigraphic height (Cm)	Sample	normal alkanes											
		<i>n</i> -C24	<i>n</i> -C25	<i>n</i> -C26	<i>n</i> -C27	<i>n</i> -C28	<i>n</i> -C29	<i>n</i> -C30	<i>n</i> -C31	<i>n</i> -C32	<i>n</i> -C33	<i>n</i> -C34	<i>n</i> -C35
1823	Jet 17	40560	35871	32496	27581	22424	26960	20571	16062	16393	16711	10990	13026
1787	Jet15	416	348	341	251	245	230	202	326	199	116	65	70
1774	Jet 13	83110	80920	69568	55417	50897	57809	44987	51461	46068	41190	27591	28696
1756	Jet 11	554	458	473	359	351	349	308	545	312	149	86	76
1716	Jet 8	79384	71819	61837	51603	46800	52682	41134	48939	42475	38320	30447	34674
1673	Jet 6	132478	99842	93555	107685	75124	71969	60780	45692	28376	31791	8936	1288
1568	Jet 4	75453	74180	55989	44936	41084	41901	32964	35191	30283	25669	18469	21174
1398	Jet 1	483	425	430	333	324	323	295	473	309	168	107	106
1358	TL.5	23716	25357	21221	22481	16584	23198	16208	15358	11165	12678	7140	6744
1318	TL.4	53236	53346	43232	40700	32474	35927	20131	21793	13262	14175	8423	9977
1218	TL.2												
1158	TL.1	21450	17172	16246	11571	9942	11423	8699	7554	6119	6490	4200	4077
945	4-MST 6	16437	17542	14533	15876	10555	13474	8472	7747	4968	7361	2697	3656
843	4-MST 5	12225	14677	11515	12743	8520	11178	6977	8158	4271	6309	2723	3315
783	4-MST 4												
678	4-MST 2	11076	13640	10249	11101	7412	9405	6044	3183	3645	5315	2270	2541
628	4-MST 1	17700	21142	15012	17904	12193	15576	10324	12151	7199	8904	4013	4389
578.0	USB10	29558	32664	27858	32566	24457	28341	20439	20638	13153	13801	10025	6388
572.0	USB7												
570	USB6	41086	43157	36884	42624	35528	33355	20475	22596	14004	10464	0	0
568.0	USB5	50961	52567	45461	51767	41395	38227	25669	23781	13546	7572	0	0
566	USB4	51839	54975	47028	55706	44211	45104	29392	30110	16461	9077	0	0

564	USB3	142	155	130	143	120	127	94	78	56	0	0	0
501	3-MST 7	20155	23186	18940	21352	14763	18047	11672	13044	7829	10523	4484	4731
458	3-MST 5	14042	16707	13695	15392	10781	13060	8789	9055	5119	7026	2998	3210
297	3-MST 1	11955	13267	10664	11441	8823	9694	6875	5753	3754	5106	2701	2455
294	MSB24	36	39	31	30	24	33	17	17	12	0	0	0
287	MSB 20	52067	59902	53350	55615	41039	49245	33294	30068	19486	26797	12311	12317
283	MSB18	66	76	66	69	56	70	37	45	29	9	5	
278	MSB 16	18472	21749	19427	20533	14898	17834	11724	10380	6432	8994	4230	4292
254	MSB 9	16899	19747	17236	18205	12891	15755	10488	9565	6198	8627	3751	3929
251	MSB8	16	19	17	18	15	16	11	10	7	0	0	0
238	MSB 4	19541	20967	18003	18792	16342	16186	12473	9289	6065	7952	4143	3717
233	MSB2	42	44	36	43	29	41	25	17	12	4	0	0
215	2-MST 8	18763	20583	17368	17446	13042	15623	10828	9990	6832	9064	4158	3903
128	2-MST 4	20374	24666	19858	22908	15406	19353	12908	12640	8983	13926	4760	5367
85	2-MST 1	11731	12974	11373	11433	8290	10253	6961	6586	4205	5966	2392	2639
78	LSB14	27893	28787	23653	29864	19775	20661	10215	13155	5636	3467	0	0
77	LSB13	51027	51984	44490	43212	30536	31240	16358	18385	8362	3668	0	0
75	LSB12												
73	LSB11	106876	109723	95999	103117	70299	76147	39682	50943	27519	22542	0	0
72	LSB10	13135	13738	11805	12396	8513	10454	5860	8853	4861	3693	0	0
71	LSB9	40593	41039	35505	34844	23948	24925	11264	16547	6557	5128	0	
69	LSB8	51	53	55	57	59	61	63	64	66	67	69	0
67	LSB7	60269	55776	55713	47215	49325	30533	32414	13035	18349	0	0	0
66	LSB6	38381	40292	34236	35868	25025	25327	13597	19502	11126	1016	0	0
65	LSB5	21050	24212	19241	23579	14910	17886	12190	14476	8834	0	0	0
63	LSB 4	7017	5237	6570	4452	5463	3742	3645	2610	3740	1368	1473	381
62	LSB3	26270	31272	22699	29393	18938	21169	14626	14500	9191	12298	3185	3954
	Bitumen												
	LSB	27074	28198	21664	24872	21676	19646	14168	14622	8702	7888	3038	2837

APPENDIX E2: Port-Mulgrave section

GC-MS: Steranes + isoreinaratens

Stratigraphic height (Cm)	Sample	ααSteranes						C27 Diast-S	C27 Diast-R	Isoreinaraten Isore- (ng/μTOC)
		27S	27R	28S	28R	29S	29R			
1823	Jet 17	35067	41201	7367	29303	43297	56439	328794	216122	1.80
1787	Jet15	265767	24596	61381	15373	224737	31563	186894	129712	2.32
1774	Jet 13	58865	69023	9849	44526	68419	92606	604584	408948	2.07
1756	Jet 11	157560	15087	57972	10158	97494	24430	142496	102174	93.09
1716	Jet 8	82770	92445	22739	63736	112350	136595	877292	556637	31.51
1673	Jet 6	138274	157848	34524	109384	172189	213957	1294583	873165	11.40
1568	Jet 4	84485	95775	20847	63970	108083	135987	860123	574362	15.57
1398	Jet 1	403368	38916	123513	28628	394998	58378	346389	244795	38.74
1358	TL.5	14166	15277	8375	10656	22819	27001	204097	129826	2.05
1318	TL.4									0.28
1218	TL.2									4.27
1158	TL.1	19567	20992	7829	14207	25389	31892	227793	150928	33.86
945	4-MST 6	3403	3840	1928	2349	4962	6098	48849	31205	0.00
843	4-MST 5	6122	4056	2660	2734	6076	8381	50093	33778	0.00
783	4-MST 4	8411	7469	0	4966	12147	15485			0.00
678	4-MST 2	6192	4105	2729	2708	6176	7814	54370	38003	0.00

628	4-MST 1	4943	5501	3655	3289	7280	8219	74077	44969	0.00
578.0	USB10	16199	18189	12068	12100	28997	36127	221984	134538	8.69
572.0	USB7									0.72
570	USB6	4975	5831	2104	4484	9525	12099	60995	40171	27.58
568.0	USB5	5639	6483	1306	4519	9980	12120	82235	54613	21.71
566	USB4	10909	12955	2808	10291	21504	26288	140961	95581	32.18
564	USB3									14.78
501	3-MST 7	2425	2703	2162	1778	4237	4339	36268	22848	0.00
458	3-MST 5	1964	2310	1576	1605	3481	3741	29736	18781	0.00
297	3-MST 1	4068	5298	2847	3543	7299	8568	52851	34162	1.82
294	MSB24									11.27
287	MSB 20	8015	4937	2867	3396	7362	9507	66213	44644	2.18
283	MSB18									2.77
278	MSB 16	14642	8290	5882	6298	14896	18645	112857	70968	0.64
254	MSB 9									0.00
251	MSB8	9667	5842	4018	4009	11150	12105	78195	52603	0.86
238	MSB 4	23852	15420	7107	11941	23330	30138	178628	126943	1.23
233	MSB2									25.67
215	2-MST 8	16609	11465	5126	6130	12041	18443	142340	103654	0.00
128	2-MST 4	5151	2897	2485	2322	5528	6610	53590	35860	0.00
85	2-MST 1	6632	3898	2726	2674	6424	7786	57987	37789	0.00
78	LSB14	6756	8488	1643	4451	9893	11545	118847	76118	3.94
77	LSB13	11705	16038	2311	9493	16206	21243	192747	132943	3.88
75	LSB12									6.29
73	LSB11	21921	24285	3989	13834	26344	35066	301568	196880	3.32
72	LSB10	7067	8541	1404	4799	7260	9933	97385	66939	2.39
71	LSB9	11059	12221	2656	7397	13385	16727	151615	99337	6.30
69	LSB8									7.39
67	LSB7	24333	25188	4734	15820	27784	34685	325373	210621	4.74

66	LSB6	6099	6381	1022	3340	8185	8772	103319	66764	19.02
65	LSB5	5857	6136	1670	4232	10302	8384	87408	55478	10.40
63	LSB 4	1163	1179	903	909	1814	2430	17859	9679	0.00
62	LSB3	3633	3979	983	2894	6898	6881	61125	40049	0.00
	Bitumen LSB		20087		10501		15845			
35	1-MST 4	1180	1443	1366	1036	2809	3369	26500	18724	0.00

APPENDIX E3: Port-Mulgrave section

GC-MS: Hopanes

Stratigraphic height (Cm)	Sample	Hopanes											
		29 α β	30 α β	31 α β (S)	31 α β (R)	32 α β (S)	32 α β (R)	33 α β (S)	33 α β (R)	34 α β (S)	34 α β (R)	35 α β (S)	35 α β (R)
1823	Jet 17	460195	1104054	46628	31981	34594	23783	29494	20399	19042	11911	13854	9018
1787	Jet15	24352	63364	29448	18982	19576	13842	17042	12280	12249	7692	8548	6572
1774	Jet 13	717383	1805743	76433	53040	60070	38342	51933	35498	32254	20980	25790	15243
1756	Jet 11	18947	53425	24779	15524	16164	11308	15288	11095	10483	6554	6584	4830
1716	Jet 8	1E+06	2938892	113534	76790	92399	62255	92856	62126	55534	36561	44406	24425
1673	Jet 6	2E+06	4934920	177340	126135	129061	91530	125840	88396	73596	48376	57596	32724
1568	Jet 4	1E+06	3094048	117952	79433	90903	61259	87069	60455	53016	34609	40659	23961
1398	Jet 1	41991	113572	48925	31165	34442	22988	33254	23051	23321	13721	16102	12487
1358	TL.5	829829	1403045	66196	44942	38403	26075	27801	18863	23333	13290	12225	8735
1318	TL.4												
1218	TL.2												
1158	TL.1	294161	773378	34249	23051	24411	16910	25659	17904	14624	9800	10750	6616

945	4-MST 6	500169	581712	31064	20969	15685	10570	10067	7050	6120	4034	1814	1463
843	4-MST 5	520936	686304	39166	26513	21015	14142	12998	10841	10715	6480	3788	1482
783	4-MST 4	91435	119207	62678	43536	34487	23882	20963	14168	14362	8187	5871	3846
678	4-MST 2	7E+06	760440	40677	28952	23325	15743	15507	9604	9717	7366	4172	2064
628	4-MST 1	600418	741855	39710	27548	20154	14170	13059	9470	8256	4879	2005	1748
578.0	USB10	909791	1497908	66055	45750	41785	27976	28016	20178	20408	12550	9703	6961
572.0	USB7												
570	USB6	30154	52853	22055	15348	13544	8843	9527	6776	6829	4572	3525	2252
568.0	USB5	50136	84666	36454	25545	22109	14174	14635	10621	10722	6681	5177	2964
566	USB4	75531	129220	56532	39482	33671	22299	23322	17064	17566	11838	8381	6472
564	USB3	184123	289810	129488	89073	73385	48953	52463	36640	40385	23616	18856	12549
501	3-MST 7	301145	508041	26259	18196	14477	9832	8344	5271	5784	3169	2066	1821
458	3-MST 5	385216	438985	22850	16180	12347	8112	6545	4413	5166	2551	1704	1302
297	3-MST 1	138233	286105	12768	8880	7306	4655	4472	2959	3485	2443	1282	1345
294	MSB24												
287	MSB 20	342660	533903	27159	19346	17122	10448	10033	7985	9361	5971	2940	3315
283	MSB18												
278	MSB 16	523508	829930	45264	31282	25526	16906	19248	12453	18483	9056	6440	4964
254	MSB 9												
251	MSB8	418047	649884	32962	23744	18940	12693	13806	9569	12007	6958	5002	3081
238	MSB 4	463150	847441	40629	26804	26038	15358	19299	13207	15913	8867	5496	3244
233	MSB2	185203	346789	154179	106661	91904	60996	71091	50794	54727	32534	25831	18961
215	2-MST 8	467387	892704	41575	28639	25812	17524	21775	13614	14099	9294	4517	4292
128	2-MST 4	480485	723753	34915	24636	18691	13913	12997	8667	9019	7282	3629	1975
85	2-MST 1	267547	417921	18954	13380	10957	7910	10263	8159	5800	2880	2912	2729
78	LSB14	34371	63784	28275	20115	17889	11389	12793	9091	8533	5178	4378	3404
77	LSB13	50342	97055	41108	29085	27127	18354	22603	16281	13349	8139	7375	5672
75	LSB12	77003	165257										
73	LSB11	83862	159430	66941	47121	41203	28082	33340	23963	20133	12331	12049	8440

72	LSB10	30027	61155	25029	18163	16450	10507	11520	8437	6610	4076	3863	2532
71	LSB9	52734	97923	39694	27742	24817	16273	19935	13921	11620	6921	6815	4912
69	LSB8	468369	899084	365596	250847	219580	146286	180950	123218	110229	62052	55058	36663
67	LSB7	105527	189277	82128	56647	48392	32818	39320	27789	25144	15307	13478	10244
66	LSB6	56000	89609	45110	30786	23602	15796	16614	12198	12466	7445	6862	4702
65	LSB5	70373	104789	53338	36870	28312	18626	18959	13962	14379	8674	7110	4258
63	LSB 4	99339	208217	11554	7854	5465	3507	3771	2442	4720	1911	1193	399
62	LSB3	55006	82072	40902	27967	23141	15342	14463	10527	11232	6757	5527	3047
	Bitumen												
	LSB	28372	48733	17855	12864	9326	7247	9038	6135	4805	3448	3187	2004
35	1-MST 4	239774	377659	18009	13084	11860	8265	6867	4723	5625	4006	1936	869

APPENDIX F: Port-Mulgrave section

Kerogen microscopy

Formation	Stratigraphic height (Cm)	Sample	AOM	Phytoclast	Palynomorphs	Light brown	Dark brown	Black	Laith	Equant
Jet Rock Shale	1779	JET14	297	2	1	43	2	10	39	16
Jet Rock Shale	1774	JET13	289	6	5	52	7	5	54	12
Jet Rock Shale	1740	JET9	298	2	0					
Jet Rock Shale	1698	JET7	300	0	0					
Jet Rock Shale	1623	JET5	296	3	1	27	14	9	39	11
Jet Rock Shale	1518	JET3	294	4	2	45	4	1	34	16
Jet Rock Shale	1398	JET1	293	3	4	42	6	2	38	12
Gray Shale	843	4-MST5	248	105	47	24	48	78	75	75
Gray Shale	678	4-MST2	258	103	39	18	49	83	85	65
Gray Shale	576	USB9	339	38	23	90	29	31	119	28
Gray Shale	570	USB6	343	26	31	71	12	17	84	16

Gray Shale	564	USB3	325	32	43	80	7	13	78	22
Gray Shale	546	3-MST8	264	99	37	67	30	53	86	64
Gray Shale	488	3-MST6	253	102	45	52	51	44	72	78
Gray Shale	422	3-MST4	261	83	56	41	49	60	87	63
Gray Shale	307	3-MST2	272	98	30	30	64	56	83	67
Gray Shale	294	MSB24	233	50	17					
Gray Shale	290	MSB22	229	57	14	22	41	87	98	51
Gray Shale	287	MSB20	251	36	13	38	60	52	119	31
Gray Shale	283	MSB18	264	27	9					
Gray Shale	278	MSB16	237	44	19					
Gray Shale	273	MSB14	231	53	16	21	45	84	88	67
Gray Shale	266	MSB12	240	51	9	36	75	39	89	61
Gray Shale	258	MSB10	238	48	14					
Gray Shale	251	MSB8	216	57	27					
Gray Shale	245	MSB6	201	61	38	40	42	68	94	56
Gray Shale	238	MSB4	234	46	20	60	47	43	99	51
Gray Shale	233	MSB2	220	51	29	39	51	60		
Gray Shale	69	LSB8	261	26	13					
Gray Shale	66	LSB6	227	56	17	37	57	56	81	69
Gray Shale	63	LSB4	206	79	15	34	64	52	133	17
Gray Shale	25	1-MST3	178	81	41	30	63	57	115	35

APPENDIX G: FT-NIR DATA

DORSET SHALE SAMPLES				
Formation	Sample	TOC %wt	TS %wt	TOS %wt
Blue Lias	20S-1	0.722	0.530	0.000
Blue Lias	20S-2	0.689	1.600	0.926
Blue Lias	20S-3	0.964	0.690	0.135
Blue Lias	22S-1	0.846	2.060	1.466
Blue Lias	22S-10	5.898	5.440	3.278
Blue Lias	22S-11	5.093	6.160	4.136
Blue Lias	22S-12	2.064	3.890	2.390
Blue Lias	22S-2	1.502	1.300	0.892
Blue Lias	22S-3	1.379	1.140	0.541
Blue Lias	22S-4	9.385	7.630	4.940
Blue Lias	22S-5	8.419	7.190	4.133
Blue Lias	22S-6	7.442	6.260	4.000
Blue Lias	22S-7	6.361	6.170	4.090
Blue Lias	22S-8	6.169	6.490	4.275
Blue Lias	22S-9	6.096	5.310	5.133
Blue Lias	24S-1	0.584	1.660	1.092
Blue Lias	24S-2	0.997	2.250	1.465
Blue Lias	24S-3	2.583	2.790	1.938
Blue Lias	24S-4	7.772	6.340	4.323
Blue Lias	24S-5	4.900	4.780	3.329
Blue Lias	24S-6	1.119	2.880	2.058
Blue Lias	26S-1	1.360	2.220	1.434
Blue Lias	26S-2	18.709	9.520	6.459
Blue Lias	26S-3	0.394	3.710	2.644
Blue Lias	26S-4	0.876	1.690	1.180
Blue Lias	28S-1	1.007	2.580	1.733
Blue Lias	28S-2	1.206	2.730	1.803
Blue Lias	28S-3	11.710	7.310	4.612
Blue Lias	28S-4	6.436	5.080	3.271
Blue Lias	28S-5	4.805	4.250	2.876
Blue Lias	28S-6	1.862	3.200	2.010
Blue Lias	28S-7	10.856	7.780	5.046
Blue Lias	28S-8	2.508	2.660	1.783
Blue Lias	30S-1	0.775	2.960	1.915
Blue Lias	30S-10	6.842	6.530	5.029
Blue Lias	30S-11	6.755	6.520	5.200
Blue Lias	30S-12	5.807	8.040	7.359
Blue Lias	30S-13	5.127	7.140	5.886
Blue Lias	30S-14	3.248	5.830	4.145

Blue Lias	30S-15	1.171	4.340	3.688
Blue Lias	30S-2	1.933	4.320	2.871
Blue Lias	30S-3	1.205	2.280	1.820
Blue Lias	30S-4	0.943	2.780	1.817
Blue Lias	30S-5	1.119	2.760	1.828
Blue Lias	30S-6	9.168	8.340	6.167
Blue Lias	30S-7	8.347	7.400	4.949
Blue Lias	30S-8	3.824	5.450	3.717
Blue Lias	30S-9	2.171	4.310	4.017
Blue Lias	32S-1	6.272	5.810	4.039
Blue Lias	32S-10	3.302	3.610	3.014
Blue Lias	32S-11	1.509	3.480	2.166
Blue Lias	32S-12	10.877	7.210	5.524
Blue Lias	32S-13	9.031	6.710	4.897
Blue Lias	32S-14	1.697	3.600	2.867
Blue Lias	32S-15	2.741	2.420	1.885
Blue Lias	32S-16	5.397	5.440	4.510
Blue Lias	32S-17	4.659	5.810	4.930
Blue Lias	32S-18	1.415	3.820	2.494
Blue Lias	32S-19	1.462	4.130	3.583
Blue Lias	32S-2	3.487	4.360	3.032
Blue Lias	32S-20	5.266	9.770	8.620
Blue Lias	32S-21	2.771	5.420	4.491
Blue Lias	32S-22	5.182	6.010	4.651
Blue Lias	32S-23	1.801	3.040	2.097
Blue Lias	32S-24	3.669	4.760	3.650
Blue Lias	32S-25	2.537	3.750	2.559
Blue Lias	32S-26	1.260	4.090	3.396
Blue Lias	32S-27	1.407	3.770	2.180
Blue Lias	32S-28	0.355	1.320	0.000
Blue Lias	32S-29	0.960	3.420	1.357
Blue Lias	32S-3	0.920	2.700	1.782
Blue Lias	32S-30	3.404	4.940	2.928
Blue Lias	32S-4	1.668	1.460	0.915
Blue Lias	32S-5	6.278	5.450	3.914
Blue Lias	32S-6	5.309	5.460	3.462
Blue Lias	32S-7	3.188	4.190	2.943
Blue Lias	32S-8	2.506	2.360	1.989
Blue Lias	32S-9	2.310	2.330	1.607
Blue Lias	34S-1	1.613	3.330	0.914
Blue Lias	34S-10	3.384	3.250	2.199
Blue Lias	34S-11	2.434	3.010	1.946
Blue Lias	34S-12	2.013	2.910	2.008
Blue Lias	34S-13	7.099	6.930	5.668

Blue Lias	34S-14	2.527	3.370	2.354
Blue Lias	34S-15	4.653	4.530	3.197
Blue Lias	34S-16	5.303	5.460	3.661
Blue Lias	34S-17	7.115	6.730	5.312
Blue Lias	34S-18	8.918	6.760	4.497
Blue Lias	34S-19	6.109	5.530	3.476
Blue Lias	34S-2	5.615	5.490	4.492
Blue Lias	34S-3	4.327	4.390	2.818
Blue Lias	34S-4	0.386	0.700	0.368
Blue Lias	34S-5	1.515	3.300	1.808
Blue Lias	34S-6	3.009	3.550	2.686
Blue Lias	34S-7	1.003	3.160	2.069
Blue Lias	34S-8	2.578	4.640	3.559
Blue Lias	34S-9	7.234	6.020	4.478

PORT-MULGRAVE SHALE SAMPLES				
Formation	Sample	TOC % wt	TS % wt	TOS % wt
Whitby Mudstone	JET17	5.050	11.846	7.475
Whitby Mudstone	JET16	6.536	10.338	8.373
Whitby Mudstone	JET15	6.132	14.013	10.346
Whitby Mudstone	JET14	5.741	11.001	7.149
Whitby Mudstone	JET13	4.261	14.910	13.059
Whitby Mudstone	JET12	5.580	11.781	7.654
Whitby Mudstone	JET11	6.036	15.163	11.983
Whitby Mudstone	JET10	6.380	11.242	8.208
Whitby Mudstone	JET9	4.931	12.418	8.433
Whitby Mudstone	JET8	6.148	12.703	7.628
Whitby Mudstone	JET7	12.617	12.736	8.135
Whitby Mudstone	JET6	14.255	12.807	9.045
Whitby Mudstone	JET5	7.135	10.110	6.160
Whitby Mudstone	JET4	10.071	13.314	9.129
Whitby Mudstone	JET3	9.614	12.088	7.242
Whitby Mudstone	JET2	5.466	11.295	8.552
Whitby Mudstone	JET1	5.327	9.659	5.753
Whitby Mudstone	TL.5	2.903	7.105	4.469
Whitby Mudstone	TL.4	3.562	9.740	6.111
Whitby Mudstone	TL.3	4.534	9.267	7.417
Whitby Mudstone	TL.2	6.141	12.285	10.921
Whitby Mudstone	TL.1	6.128	12.161	11.969
Whitby Mudstone	4-MST7	1.927	5.725	4.618
Whitby Mudstone	4-MST6	1.411	3.592	3.023
Whitby Mudstone	4-MST5	1.479	3.938	3.003

Whitby Mudstone	4-MST4	1.599	4.177	3.539
Whitby Mudstone	4-MST3	1.392	3.390	2.262
Whitby Mudstone	4-MST2	1.633	3.390	2.381
Whitby Mudstone	4-MST1	1.638	4.485	3.070
Whitby Mudstone	USB10	2.638	17.896	14.053
Whitby Mudstone	USB9	2.590	16.159	9.453
Whitby Mudstone	USB7	3.513	8.920	7.473
Whitby Mudstone	USB6	3.137	8.950	7.257
Whitby Mudstone	USB5	1.842	7.400	5.871
Whitby Mudstone	USB4	2.867	8.320	3.572
Whitby Mudstone	USB3	2.428	6.840	2.312
Whitby Mudstone	USB2	1.814	7.170	4.070
Whitby Mudstone	USB1	1.705	5.530	2.245
Whitby Mudstone	3-MST8	1.230	2.440	1.073
Whitby Mudstone	3-MST7	1.022	1.990	-1.216
Whitby Mudstone	3-MST6	1.229	2.330	1.108
Whitby Mudstone	3-MST5	1.534	3.240	1.313
Whitby Mudstone	3-MST4	1.426	2.960	1.410
Whitby Mudstone	3-MST3	1.370	2.890	2.017
Whitby Mudstone	3-MST2	1.200	4.290	1.468
Whitby Mudstone	3-MST1	2.112	5.030	3.355
Whitby Mudstone	MSB24	1.730	3.330	1.328
Whitby Mudstone	MSB23	1.440	3.230	0.664
Whitby Mudstone	MSB22	1.130	3.390	1.319
Whitby Mudstone	MSB21	1.560	6.459	3.277
Whitby Mudstone	MSB20	2.200	5.090	1.719
Whitby Mudstone	MSB19	2.660	6.990	3.880
Whitby Mudstone	MSB18	2.390	7.850	3.915
Whitby Mudstone	MSB17	2.380	5.841	2.676
Whitby Mudstone	MSB16	2.230	5.450	3.060
Whitby Mudstone	MSB15	2.080	5.270	2.394
Whitby Mudstone	MSB14	2.080	4.580	1.740
Whitby Mudstone	MSB13	1.960	4.130	1.650
Whitby Mudstone	MSB12	1.840	4.670	2.186
Whitby Mudstone	MSB11	1.710	3.180	1.022
Whitby Mudstone	MSB10	1.800	4.640	1.765
Whitby Mudstone	MSB9	1.770	4.253	1.669
Whitby Mudstone	MSB8	1.660	5.550	2.964
Whitby Mudstone	MSB7	1.690	6.817	4.066
Whitby Mudstone	MSB6	1.900	6.300	2.158
Whitby Mudstone	MSB5	2.850	7.216	2.816
Whitby Mudstone	MSB4	3.180	7.850	3.032
Whitby Mudstone	MSB3	2.660	10.126	4.705
Whitby Mudstone	MSB2	3.330	7.133	2.291

Whitby Mudstone	MSB1	4.680	8.450	3.090
Whitby Mudstone	2-MST8	2.210	9.048	3.496
Whitby Mudstone	2-MST7	1.100	8.440	5.272
Whitby Mudstone	2-MST6	1.100	13.320	12.236
Whitby Mudstone	2-MST5	1.660	9.310	3.919
Whitby Mudstone	2-MST4	1.210	4.270	2.613
Whitby Mudstone	2-MST3	0.990	3.343	-0.695
Whitby Mudstone	2-MST2	0.970	5.440	2.920
Whitby Mudstone	2-MST1	1.070	0.910	-2.178
Whitby Mudstone	LSB14	2.507	11.241	5.049
Whitby Mudstone	LSB13	5.726	13.196	11.479
Whitby Mudstone	LSB12	6.273	11.892	5.331
Whitby Mudstone	LSB11	2.915	12.004	9.009
Whitby Mudstone	LSB10	0.802	15.217	12.234
Whitby Mudstone	LSB9	6.809	15.583	12.463
Whitby Mudstone	LSB8	6.296	15.540	7.287
Whitby Mudstone	LSB7	2.333	13.533	9.892
Grey Shale	LSB6	1.410	8.699	4.365
Grey Shale	LSB5	1.275	5.445	3.221
Grey Shale	LSB4	1.160	5.994	3.110
Grey Shale	LSB3	1.542	5.263	2.749
Grey Shale	LSB2	1.020	5.395	2.559
Grey Shale	LSB1	1.305	5.145	0.215
Grey Shale	1-MST6	0.990	4.460	2.545
Grey Shale	1-MST5	0.940	4.150	1.690
Grey Shale	1-MST4	0.990	3.950	1.313
Grey Shale	1-MST3	0.770	4.235	0.819
Grey Shale	1-MST2	0.840	5.235	2.770
Grey Shale	1-MST1	0.330	5.800	1.461

School archived samples		
Reference	sample	TOC
Adrian Piper	CGD25	2.500
Adrian Piper	CW24	0.880
Adrian Piper	CW27	2.270
Adrian Piper	CW29	2.940
Adrian Piper	CW45	0.720
Adrian Piper	CW50	2.820
Adrian Piper	H2	1.900
Adrian Piper	H22	1.400
Adrian Piper	H34	1.800
Alastair Vincent	KE41	1.000
Alastair Vincent	LBM1	1.000
Alastair Vincent	LBT2	1.200

Alastair Vincent	LOK6	1.200
Ali Nategh	PJ43	3.900
Ali Nategh	PJ43R	3.900
Ali Nategh	PJ49	4.000
Ali Nategh	PJ50	6.100
Ali Nategh	PJ61-3	6.700
Ali Nategh	PJ61-4	6.000
Ali Nategh	PJ61-5	5.400
Ali Nategh	PJ61-6	6.900
Ali Nategh	RG42	2.700
Ali Nategh	RG43	1.800
Ali Nategh	RG44	1.700
Alastair Vincent	RNB13	1.400
Alastair Vincent	RNB17	4.400
Alastair Vincent	RNB7	1.600
Alastair Vincent	RNB9	3.300
Adrian Piper	SC40	3.990
Adrian Piper	SC45	2.730
Adrian Piper	SC48	1.810
Adrian Piper	SC57	2.840
Adrian Piper	SC69	1.620
Adrian Piper	SC70	2.040
Adrian Piper	SC77	11.820
Adrian Piper	STG1	1.200
Adrian Piper	STG11	1.300
Adrian Piper	STG11R	1.300
Adrian Piper	STG12	1.400
Adrian Piper	STG14	1.100
Adrian Piper	STG14R	1.100
Adrian Piper	STG15	1.100
Adrian Piper	STG16	1.200
Adrian Piper	STG18	6.000
Adrian Piper	STG18R	6.000
Adrian Piper	STG25	2.600
Adrian Piper	STG25R	2.600
Adrian Piper	STG27	1.700
Adrian Piper	STG28	2.500
Adrian Piper	STG28R	2.500
Adrian Piper	STG32	1.300
Adrian Piper	STG34	1.400
Adrian Piper	STG34R	1.400
Adrian Piper	STG35	1.700
Adrian Piper	STG36	1.800
Adrian Piper	STG39	2.000

Adrian Piper	STG4	1.400
Adrian Piper	STG41	1.800
Adrian Piper	STG41R	1.800
Adrian Piper	STG42	3.400
Adrian Piper	STG42R	3.400
Adrian Piper	STG44d	3.200
Adrian Piper	STG45	2.000
Adrian Piper	STG46	2.100
Adrian Piper	STG48	1.800
Adrian Piper	STG4R	1.400
Adrian Piper	STG6	1.700
Adrian Piper	STG8b	6.600
Adrian Piper	STG8bR	6.600
Adrian Piper	STG9	3.100
Alastair Vincent	UOB24	1.300
Alastair Vincent	UOB31	6.900
Alastair Vincent	UOB34	5.500
Alastair Vincent	UOB35	2.600
Adrian Piper	YN100	0.790
Adrian Piper	YN107	1.780
Adrian Piper	YN109	10.890
Adrian Piper	YN111	8.020
Adrian Piper	YN115	0.920
Adrian Piper	YN117	5.760
Adrian Piper	YN18	0.690
Adrian Piper	YN19	1.120
Adrian Piper	YN22	2.960
Adrian Piper	YN25	0.560
Adrian Piper	YN68	0.780
Adrian Piper	YN7	0.890
Adrian Piper	YN91	3.680
Adrian Piper	YN91R	3.680
Adrian Piper	YN92	1.330
Gorden Ross	Cblr10-a	0.800
Gorden Ross	Cblr13	0.330
Gorden Ross	Cblr14	1.390
Gorden Ross	Cblr15-a	6.800
Gorden Ross	Cblr15-b	5.210
Gorden Ross	Cblr17	0.370
Gorden Ross	Cblr18-19	2.500
Gorden Ross	Cblr21	2.160
Gorden Ross	Cblr23	0.600
Gorden Ross	Cblr25-a	1.230
Gorden Ross	Cblr25-b	8.780

Gorden Ross	Cblr26	1.200
Gorden Ross	Cblr26R	1.200
Gorden Ross	Cblr27	9.290
Gorden Ross	Cblr2-a	8.850
Gorden Ross	Cblr2-b	5.870
Gorden Ross	Cblr3	3.400
Gorden Ross	Cblr31	8.750
Gorden Ross	Cblr31-32	2.450
Gorden Ross	Cblr31R	8.750
Gorden Ross	Cblr32	6.020
Gorden Ross	Cblr33	1.240
Gorden Ross	Cblr36	4.580
Gorden Ross	Cblr36R	4.580
Gorden Ross	Cblr37	2.070
Gorden Ross	Cblr38	4.040
Gorden Ross	Cblr39	1.900
Gorden Ross	Cblr40	7.270
Gorden Ross	Cblr41	1.620
Gorden Ross	Cblr42	1.440
Gorden Ross	Cblr45-a	0.740
Gorden Ross	Cblr45-b	1.660
Gorden Ross	Cblr46	2.810
Gorden Ross	Cblr47	1.530
Gorden Ross	Cblr47R	1.530
Gorden Ross	Cblr49-50	4.000
Gorden Ross	Cblr5	0.670
Gorden Ross	Cblr50	4.000
Gorden Ross	Cblr53	7.220
Gorden Ross	Cblr56	1.040
Gorden Ross	Cblr57	4.200
Gorden Ross	Cblr58	2.130
Gorden Ross	Cblr60	6.560
Gorden Ross	Cblr60R	6.560
Gorden Ross	Cblr66	2.830
Gorden Ross	Cblr67	6.210
Gorden Ross	Cblr68	4.280
Gorden Ross	Cblr6-a	6.470
Gorden Ross	Cblr6-b	7.910
Gorden Ross	Cblr7	6.070
Gorden Ross	Cblr70	1.620
Gorden Ross	Cblr70R	1.620
Gorden Ross	Cblr72	1.280
Gorden Ross	Cblr8	4.440
Gorden Ross	Cblr8R	4.440